Experimental setup for a Rydberg atom–mechanical oscillator hybrid system

Dissertation
zur
Erlangung des Doktorgrades (Dr. rer. nat.)
der
Mathematisch-Naturwissenschaftlichen Fakultät
der
Rheinischen Friedrich-Wilhelms-Universität Bonn

von
Cedric Wolff Heinrich Wind
aus
Brühl

Bonn, February 2026

Angefertigt mit Genehmigung der Mathematisch-Naturwissenschaftlichen Fakultät der Rheinischen Friedrich-Wilhelms-Universität Bonn

Gutachter/Betreuer:	Prof. Dr. Sebastian Hofferberth
Gutachter:	Prof. Dr. Stefan Linden
Tag der Promotion:	27.03.2026
Erscheinungsjahr:	2026

Abstract

Hybrid quantum systems provide a promising route toward combining the complementary strengths of distinct physical platforms for quantum information processing. In this context, highly excited Rydberg atoms are particularly attractive due to their strong electric dipole moments, long lifetimes, and compatibility with both optical and microwave frequency regimes. Mechanical resonators, on the other hand, offer long coherence times and the ability to store quantum information in macroscopic degrees of freedom.

In this thesis, the development of a novel hybrid platform interfacing ultracold Rydberg atoms with high-overtone bulk acoustic wave resonators (HBARs) in a cryogenic environment is presented. The core components of the experimental apparatus have been designed, assembled, and characterized, including a room-temperature realization featuring the complete cold-atom preparation chain. A first-generation superconducting atom chip for trapping ultracold atoms in a cryogenic environment has been designed and fabricated, establishing the foundation for future experiments under cryogenic conditions.

The full experimental realization of the hybrid system, including the integration of the mechanical resonator, was delayed by the delivery of a custom-built cryostat. Nevertheless, the preparation of the cryogenic experiment has been completed, enabling rapid progress toward first experiments once cryogenic operation becomes available. At an operating temperature of 4 K, thermal phonon occupation of HBAR modes is significantly reduced compared to room temperature but remains above the quantum ground state, motivating the development of active cooling strategies.

Complementing the experimental work, the feasibility of cooling a mechanical mode toward its quantum mechanical ground state using a cloud of Rydberg atoms is investigated theoretically. In this approach, Rydberg atoms act as a dissipative resource that extracts phononic excitations from the mechanical resonator and removes them via radiative decay. Furthermore, the potential of Rydberg atom-mediated interactions to generate entanglement between spatially separated mechanical oscillators is analyzed. Together, these results establish a foundation for future experimental investigations of Rydberg atom–mechanical oscillator hybrid systems.

Parts of this thesis have been published on arXiv and are currently under peer-review:

[1] Cedric Wind, Chris Nill, Julia Gamper, Samuel Germer, Valerie Mauth, Wolfgang Alt, Igor Lesanovsky, and Sebastian Hofferberth, *Entanglement of mechanical oscillators mediated by a Rydberg tweezer chain*, 2025, arXiv: 2510.08371 [quant-ph]

Contents

CHAPTER 1

Introduction

The quantum technology landscape has undergone rapid development over recent decades giving rise to applications across a broad range of domains, from quantum sensing and metrology [2, 3], to secure quantum communication [4], and quantum simulation and quantum computing [5, 6].

Quantum sensing and quantum metrology have entered many aspects of modern life, including the realization of the International System of Units, which is defined through fixed numerical values of fundamental constants and implemented using quantum metrology [7], as well as precision timekeeping [8].

Quantum computing and simulations are today being demonstrated in prototype experiments [9, 10], and in the long term promise the capacity of solving computationally difficult problems, including problems in theoretical chemistry [11], materials science [12], and cryptography [13].

A variety of physical platforms have emerged to harness quantum mechanics for quantum computing and quantum technologies in general. These platforms include atomic [10, 14, 15], solid-state [16], and photonic [17, 18] architectures, each offering distinct advantages and limitations in terms of coherence, controllability, scalability, and interfacing with the external environment [19].

To exploit the complementary strength of different quantum systems, various hybrid architectures have been developed, where distinct (quantum) degrees of freedom such as atomic, mechanical, and electromagnetic modes are coupled [19, 20].

One example that shows the requirement of coupling two regimes are superconducting circuit-based qubits, such as transmon qubits [21]: They enable fast and high-fidelity gate operations, but operate in the microwave frequency regime, which is ill-suited for low-loss transmission over long distances. In contrast, optical photons experience minimal attenuation in optical fibers [22, 23], making microwave-to-optical frequency conversion a key requirement for connecting superconducting quantum processors to optical quantum networks [23].

To date, the most successful approaches to such microwave-to-optical quantum transduction are based on hybrid opto- and electromechanical systems [23–28]. These systems leverage mechanical motion, phonons, that couple both to optical cavity modes and to microwave resonators. The phonons can interact with optical fields via radiation pressure or photoelastic effects, and with microwave circuits through electrostatic forces, such as capacitance modulation induced by deformation, or through piezoelectric coupling [**chuPerspectiveHybridQuantum2020**, 25, 29].

Beyond their role in frequency conversion, hybrid electromechanical systems have attracted growing interest as a platform for quantum acoustics, where quantized mechanical motion is coherently

controlled and can be interfaced with other quantum systems [**chuPerspectiveHybridQuantum2020**]. In the last decade, it has become possible to fabricate mechanical resonators with exceptionally high quality factors and gigahertz-scale resonance frequencies providing access to long-lived phononic modes that are well-matched to superconducting transmon qubits [30, 31]. Such mechanical system finds potential applications in the investigation of fundamental aspects of quantum mechanics at mesoscopic scales and open pathways toward the realization of mechanical quantum memories [**chuPerspectiveHybridQuantum2020**].

Among the various mechanical platforms explored in this context, high-overtone bulk acoustic resonators (HBARs) have emerged as a promising candidate that was recently used in a hybrid architecture with a superconducting transmon qubit to realize the first mechanically encoded qubit [32]. These HBARs feature a piezoelectric top layer that couples the mechanical mode to the microwave near field of the nearby transmon qubit.

Neutral laser-cooled atom systems provide another well-understood platform for many quantum technology applications [10, 33, 34] and a promising constituent of hybrid quantum architectures [20]. Neutral atoms feature transitions across the electromagnetic spectrum, with optical transitions between low-lying electronic states, and microwave transitions between hyperfine states or neighboring highly excited states. Especially, atoms excited to high principal quantum numbers, so-called Rydberg atoms, exhibit strong electric dipole transitions in the microwave regime between adjacent Rydberg levels, together with lifetimes that are strongly enhanced compared to those of low-lying excited states [35, 36]. This combination of strong, long-range interactions and extended lifetimes makes Rydberg atoms attractive not only for the implementation of long-range two-qubit gates in quantum computing [10, 37], but also for a variety of hybrid quantum information processing proposals [37–40]. These proposed applications range from long-term storage and optical readout of quantum information to their use as transducers for microwave-to-optical conversion.

Experimentally, several hybrid platforms combining ultracold Rydberg atoms with superconducting microwave resonators have been realized, demonstrating coherent interactions between Rydberg atoms and the microwave circuit [39, 41, 42].

Beyond interfacing Rydberg atoms with microwave resonators, their combination with mechanical oscillators provides additional opportunities. Theoretical proposals suggest a wide range of potential applications, including the generation of non-classical states of light [43], cooling and coherent control of mechanical modes [44, 45], and the realization of hybrid interfaces linking superconducting transmon qubits with neutral atomic systems [46]. To date, Rydberg atom–mechanical oscillator hybrid systems have not been realized experimentally.

In this thesis, we report on the development of a novel experimental platform that will interface Rydberg atoms with HBARs in a cryogenic environment at 4 K. Operating at cryogenic temperatures is a key enabling element of this Rydberg–HBAR hybrid system. At cryogenic temperatures, internal losses in the HBAR are suppressed, boosting the quality factor of the mechanical resonances [47–51]. Furthermore, blackbody-induced transitions of Rydberg atoms, which typically limit their lifetime at room temperature, are strongly suppressed at 4 K, extending the lifetime of highly excited Rydberg states to their natural lifetime [35].

Within this work, we have developed and assembled the core components of the Rydberg–HBAR hybrid system. A room-temperature version of the experimental apparatus has been realized that includes the full cold-atom preparation chain, and all essential components required for cryogenic operation have been prepared. In particular, a first-generation superconducting atom chip for trapping ultracold atoms in a cryogenic environment has been designed and fabricated.

The full experimental realization of the hybrid platform, including the integration of the HBAR, was ultimately prevented by delays in the delivery of a custom-built cryostat, which constitutes a critical component of the apparatus. Nevertheless, the cryogenic experiment has been prepared, and the designed and fabricated atom chip establishes a foundation for first experiments once cryogenic operation becomes available.

With an environment at 4 K, the thermal phonon occupation of HBAR modes is strongly reduced compared to room-temperature operation, but it is not yet frozen out. Reaching the quantum regime therefore requires additional cooling of the mechanical mode toward its ground state. As a result, a short-term objective of the hybrid platform is the cooling of a mechanical mode toward its quantum mechanical ground state utilizing the Rydberg atom–HBAR coupling.

In parallel to the construction of the experimental apparatus, we have theoretically investigated the feasibility of this mechanical mode cooling using a cloud of Rydberg atoms. In this approach, Rydberg atoms act as a dissipative resource that extracts phononic excitations from the mechanical resonator and removes them via radiative decay. Furthermore, we theoretically investigated the use of Rydberg atom-mediated interactions to entangle two distant mechanical oscillators.

This thesis is organized as follows. In Chapter 2, we introduce the hybrid Rydberg atom-–mechanical oscillator system and its individual constituents, outline the relevant theoretical concepts, and estimate the achievable coupling strengths. An overview of the experimental apparatus and the preparation of cold atomic ensembles is presented in Chapter 3. The preparation of the cryogenic experiment, including the design and fabrication of the superconducting atom chip, is detailed in Chapter 4. In Chapter 5, we discuss prospective applications of the hybrid architecture. Specifically, we discuss the cooling of a mechanical oscillator mode using Rydberg atoms and present the investigation of the feasibility of entangling two mechanical modes of spatially separated HBARs mediated by a chain of Rydberg atoms.

CHAPTER 2

A Rydberg atom–mechanical oscillator hybrid system

This thesis focuses on the development of a novel hybrid platform interfacing Rydberg atoms with a mechanical oscillator, specifically a high-overtone bulk acoustic wave resonator (HBAR).

In this chapter, we introduce the theoretical framework underlying the proposed hybrid platform. We begin by introducing the two constituents and their relevant properties. We then present the hybrid architecture, detailing the experimental geometry. Finally, we examine the atom–oscillator coupling mechanism, derive the expected interaction strength, and assess the feasibility of reaching the strong-coupling regime.

2.1 Rydberg atoms

The first constituent of the hybrid platform are so-called Rydberg atoms. Rydberg atoms are neutral atoms with a valence electron excited to a high[1] principal quantum number n [35]. The large n is accompanied by exaggerated properties [35, 52] compared to ground state atoms and atoms in low excited states, including large spatial extent, large polarizability, strong dipole transitions between neighboring Rydberg levels, and long lifetimes.

For high-n Rydberg states, the hyperfine splitting is typically much smaller than the transition linewidth and can be neglected. We therefore label Rydberg states[2] by $|n\,L\,J\,m_J\rangle$, where L is the orbital angular momentum, J is the total angular momentum, and m_J is the magnetic sublevel of J. When the specific J or m_J is not relevant, we omit them from the notation.

This section summarizes the features of Rydberg atoms most relevant for the hybrid architecture.

Binding energy and transition frequency The binding energies of Rydberg states in alkali atoms are described by the Rydberg–Ritz formula [35, 53]

$$E_{nLJ} = -\frac{R^*}{(n-\delta_{nLJ})^2} = -\frac{R^*}{(n^*)^2}, \tag{2.1}$$

[1] A minimal principal quantum number for a Rydberg state is not well-defined in the literature. In this work we typically consider $n \sim 60$ to 90.

[2] When a numerical value is specified for J, we write it as a subscript following spectroscopic notation.

where R^* is the specific Rydberg constant, δ_{nLJ} the quantum defect, and n^* the effective principal quantum number. The quantum defect captures deviations from the hydrogenic spectrum due to incomplete shielding of the nucleus by inner electrons. It depends primarily on the orbital angular momentum L and only weakly on the principal quantum number n and total angular momentum J.

For rubidium, the atomic species relevant to this work, transitions from the ground state to low-lying ($n < 7$) states fall in the optical regime, while direct transitions to Rydberg states lie in the UV range.

In contrast, the transition frequency between neighboring Rydberg states $|n\mathrm{S}\rangle$ and $|n\mathrm{P}\rangle$ scales as

$$\hbar\omega_{n\mathrm{S}\leftrightarrow n\mathrm{P}} = E_{n\mathrm{P},\,J=\{1/2,\,3/2\}} - E_{n\mathrm{S},\,J=1/2} \propto (n^*)^{-3/2}, \tag{2.2}$$

placing the transition in the microwave regime [52].

This ability to access widely separated regions of the electromagnetic spectrum through different atomic transitions makes Rydberg atoms addressable by visible lasers via two-photon excitation while simultaneously enabling them to interface with microwave fields.

Enhanced transition dipole moment Neighboring Rydberg states $|n\,L\,J\,m_J\rangle$ and $|n'L'J'm'_J\rangle$ with similar principal quantum numbers ($n \approx n'$) and orbital angular momenta differing by one ($L' = L \pm 1$) exhibit substantial radial wavefunction overlap. As a consequence, the magnitude of the transition dipole moment scales as

$$d_{n'L'J'm'_J\leftrightarrow nLJm_J} = \left\| \langle n'L'J'm'_J|\boldsymbol{d}|nLJm_J\rangle \right\| \propto (n^*)^2, \tag{2.3}$$

where $\boldsymbol{d} = -e\,\boldsymbol{r}$ is the electric-dipole operator. Conversely, the wavefunction overlap between a Rydberg state and low-lying states is small, diminishing the corresponding transition dipole moment by $(n^*)^{-3/2}$ [52].

The strongly enhanced transition dipole moment between neighboring Rydberg states—compared to ground-state transitions—makes Rydberg atoms sensitive microwave antennas. These strong dipole transitions in the microwave regime are the central feature enabling coupling to the HBAR in our architecture.

Comparing the n^* scalings of the transition frequency in Eq. (2.2) with that of the transition dipole moment in Eq. (2.3), we deduce a frequency scaling of the transition dipole moment of

$$d_{n\mathrm{S}\leftrightarrow n\mathrm{P}} \propto (\omega_{n\mathrm{S}\leftrightarrow n\mathrm{P}})^{-2/3}. \tag{2.4}$$

Enhanced lifetime As mentioned before, the transition dipole moment between low-lying and Rydberg states scales as $(n^*)^{-3/2}$, resulting in a suppression of the natural decay rate of Rydberg states compared to those of low-lying states.

However, because the energy difference between neighboring Rydberg states reduces to the microwave regime, and the corresponding transition dipole moments are strong, blackbody radiation from the environment can drive these transitions. For highly excited Rydberg atoms, the blackbody-induced decay rate at room temperature is typically comparable to the natural decay rate, whereas it remains negligible for low-lying states [54, 55]. For example, the lifetime of the state $|90\mathrm{S}\rangle$ of ^{87}Rb is 820 µs at 0 K, which is reduced to 270 µs at 300 K [55]—still orders of magnitude longer than the 26 ns lifetime of the lowest-lying excited state $|5\mathrm{P}\rangle$. This extended lifetime (at cryogenic temperatures) is advantageous for implementing quantum protocols involving Rydberg states.

Strong polarizability The diminishing energy spacing and increasing dipole transition moment between adjacent Rydberg states for increasing n leads to a high sensitivity to static external electric fields E_{DC}. The associated quadratic energy shift, the so-called DC Stark shift $\Delta E_n^{\text{DC-Stark}}$, can be obtained by second-order perturbation theory. In the case of $L \in \{\mathrm{S}, \mathrm{P}, \mathrm{D}\}$, the quantum defect of ^{87}Rb breaks the angular-momentum degeneracy, and if the shift remains small compared to the level spacing, the DC Stark shift can be written as

$$\Delta E_{nLJ}^{\text{DC-Stark}} \approx \frac{1}{2}\alpha E_{\mathrm{DC}}^2. \tag{2.5}$$

Here, the polarizability α is [56]

$$\alpha\left[\mathrm{MHz}/(\mathrm{V/cm})^2\right] = 2.202 \times 10^{-9}(n^*)^6 + 5.53 \times 10^{-11}(n^*)^7. \tag{2.6}$$

The strong sensitivity to external electric fields necessitates electric field compensation in many Rydberg experiments [52]. Parasitic stray electric fields from surface charges or adsorbates can significantly perturb Rydberg atoms and must be compensated or mitigated [57–59]. However, this strong polarizability, combined with precise field control, can also serve as a tuning mechanism for the Rydberg transition frequencies, enabling matching with the resonance frequency of HBAR modes.

Rydberg–Rydberg interaction Just as the increased dipole transition moment and reduced energy spacing of neighboring Rydberg atoms enhance their sensitivity to external electric fields, these properties also strengthen the interactions between Rydberg atoms through virtual photon exchange. In ultra-cold atomic clouds, the interatomic distance is typically large compared to the Rydberg wavefunction but small compared to the transition wavelength, allowing the interaction to be modeled quasi-statically with the dipole–dipole interaction as the dominant term [60].

First-order dipole–dipole interactions between two Rydberg atoms in different angular momentum states with dipole-allowed transitions result in state transfer. Here, the interaction strength, for example between Rydberg atoms in states $|n\mathrm{S}_{1/2}\rangle$ and $|(n-1)\mathrm{P}_{3/2}\rangle$, scales as $(n^*)^4/R^3$, where R is the interatomic distance [36].

Second-order dipole–dipole interactions between two Rydberg atoms in the same state (in the absence of a Förster resonance) give rise to the van der Waals interaction, with an interaction potential scaling as $(n^*)^{11}/R^6$ for the state $|n\mathrm{S}_{1/2}\rangle$ [36].

This strong, long-range interaction gives rise to nonlinear collective effects such as the Rydberg blockade. When one atom is excited to a Rydberg state, it shifts the excitation energy of nearby atoms, suppressing additional excitations within a blockaded volume, defined by the so-called blockade radius. With multiple atoms within the blockaded volume, it is unknown which specific atom is excited, and a collective superposition state emerges. This so-called bright state is given by [60, 61]

$$|W\rangle = \frac{1}{\sqrt{N_b}} \sum_{i=1}^{N_b} \beta_i \, |g_1, g_2, \ldots, r_i, \ldots, g_{N_b}\rangle \,, \tag{2.7}$$

where N_b is the number of atoms in the blockaded volume, $|g_i\rangle$ denotes an atom in the ground state, and $|r_i\rangle$ an atom in the Rydberg state. The atom positions are encoded in the phase factors $\beta_j = \exp(i\boldsymbol{k}\boldsymbol{r}_j)$, where $\boldsymbol{k}$ is the wave vector of the excitation laser and $\boldsymbol{r}_j$ is the position of the j-th atom [61]. The corresponding collective ground state is $|G\rangle = |g_1, \ldots, g_{N_b}\rangle$. The transition dipole

moment between the collective ground and bright state is enhanced by $\sqrt{N_b}$, strongly enhancing the coupling to the laser drive.

An important feature is that while the bright state $|W\rangle$ couples to the ground state via laser excitation, there exist $N_b - 1$ collective dark states [60]

$$|D_j\rangle = \sum_{i=1}^{N_b} \gamma_{i,j} \, |g_1, g_2, \ldots, r_i, \ldots, g_{N_b}\rangle \,, \tag{2.8}$$

that do not couple to the ground state. Here, $\gamma_{i,j}$ are phase factors chosen such that $\langle WD_j \rangle = 0$. Within an atomic ensemble, the bright state dephases into the manifold of dark states over time. Dephasing arises from atomic motion, stray fields, inhomogeneous trap depth, and interatomic interactions [**stiesdalCollectiveAtomlightInteractions2022**, 62–64]. While most experiments seek to suppress dephasing, it can be exploited as a resource—for instance, to realize a single-photon absorber [65, 66]. In this case, dephasing is intentionally made fast compared to the Rabi frequency, preventing the excitation laser from driving the state back to the ground state.

This mechanism is also applicable for the hybrid system discussed here. Continuous laser excitation of the ultracold atoms populates the bright state, which then dephases to the manifold of dark states without subsequent de-excitation, providing a persistent reservoir of Rydberg excitations. This property is valuable for coupling to the HBAR and will be utilized in the HBAR mode-cooling scheme presented in Section 5.1.

2.2 High-overtone bulk acoustic resonators

The second constituent of the hybrid platform discussed in this work is the HBAR. The tern high-overtone bulk acoustic resonator refers to a class of acoustic resonators that host standing high overtone sound waves within the bulk. HBARs are typically used as passive radio-frequency devices, operating in the low-GHz (1 to 5 GHz) regime [49], but operation frequencies up 40 GHz have been demonstrated [67]. Specifically, the high achievable quality factors of over 10^5 (at room temperature) at GHz frequencies set HBARs apart from other acoustic resonators commonly used in radio-frequency devices, like surface acoustic wave and bulk acoustic wave resonators [49, 50]. At cryogenic temperatures, intrinsic loss mechanisms like phonon–phonon scattering are suppressed, and the achievable quality factor is further enhanced [47]. Recently values of over 2.4×10^8 at operation frequencies of 12 GHz were reported with a HBAR made from crystalline quartz [51].

Figure 2.1(a) shows an illustration of the HBAR that we plan to use in our hybrid system. It consists of a bulk material with a protruding piezoelectric dome. These devices were originally demonstrated and interfaced with superconducting quibits by Yiwen Chu et al. in the group of Robert J. Schoelkopf [30] in 2017. Afterward, Yiwen Chu developed this platform further in her own research group [32, 68, 69], achieving linewidths below 1 kHz (at cryogenic temperatures) at an operation frequency of 5 GHz corresponding to a quality factor exceeding $Q \sim 10^7$ [32] in 2024. These HBARs have around 400 µm thick sapphire substrates and 1 µm thick piezoelectric domes out of aluminum nitride (AlN).

The piezoelectric dome confines the acoustic (strain) mode similarly to a curved mirror in an optical cavity as sketched in Fig. 2.1(b). The confinement leads to the development of transversal Laguerre-Gaussian modes and a high-overtone longitudinal standing wave in $z-$direction. The

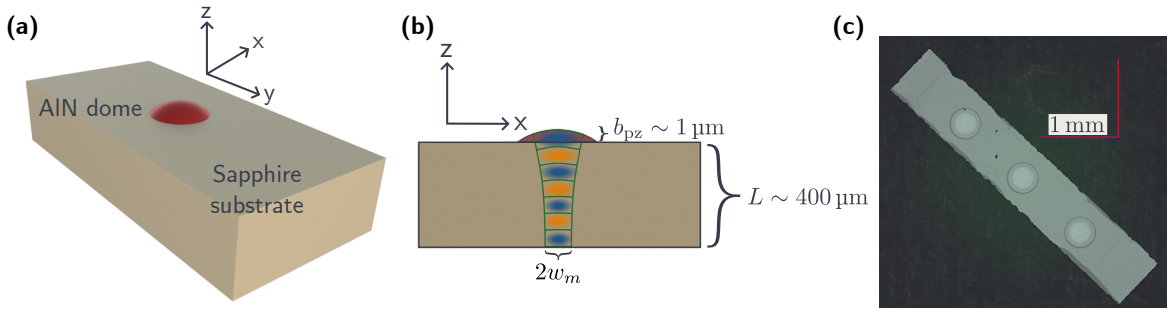

Figure 2.1: **(a):** Schematic illustration of a high-overtone bulk acoustic resonator (HBAR) with piezoelectric AlN dome, not to scale. **(b):** Side view of the HBAR. The longitudinal strain mode profile inside the HBAR is outlined in green. Orange and blue ellipses indicate the strain amplitude. **(c):** Microscope image of a chip dice given to us by the group of Yiwen Chu. The chip dice contains three piezoelectric domes each forming a HBAR as sketched in (a, b).

(single-phonon) strain is mostly directed along the longitudinal direction and can be written as [70]

$$S(z,r,t) = S_0 \sin\left(\frac{m\pi z}{L}\right) \exp\left(-\frac{r^2}{w_m^2}\right)\left(e^{-i\omega_m t} + e^{i\omega_m t}\right). \tag{2.9}$$

Here, S_0 is the single-phonon strain amplitude, r is the radial distance, L is the thickness of the HBAR, ω_m is the resonance frequency, and w_m is the waist of the strain mode.

The piezoelectric material converts the oscillating acoustic mode to an evanescent electric field $\boldsymbol{E}_{\mathrm{HBAR}}$ near the dome's surface. The evanescent electric field enables the coupling of the acoustic mode to, for example, a Rydberg atom in close vicinity to the dome. We describe this coupling mechanism in further detail in Section 2.3.1.

HBARs for the experiment For the production of the HBARs for our experiment, we collaborate with the group of Yiwen Chu. In May 2025, we received ten HBAR chips, each hosting three piezoelectric domes. A photograph of one of these chip dices is shown in Fig. 2.1(c). These chips were diced to avoid clipping the excitation lasers in the experiment. The dimensions for these chips are summarized in Table 2.1. These ten chips have not yet been characterized with regard to their

Table 2.1: Geometric parameters of the HBARs we received from the group of Yiwen Chu.

Parameter	Value / µm
Substrate thickness L	435
Dome height	2.9
Piezoelectric layer height b_{pz}	1.36
Piezoelectric diameter	275
Mode waist w_m (at $\omega_m = 5.8\,\mathrm{GHz}$)	32
Substrate dice width x length	700 x 4000

resonance linewidths. However, the group of Yiwen Chu has performed measurements of other

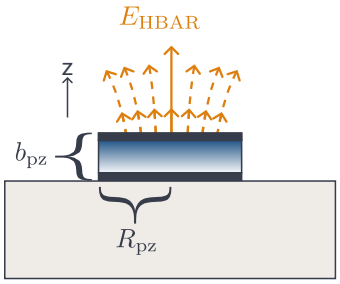

Figure 2.2: Schematic of the simplified piezoelectric disc model for the analytic electric-field calculation.

HBARs from that production batch, achieving linewidths around 1 kHz at 4 K for operation frequencies of 2 to 6 GHz. The corresponding measurement data is shown in Table 2.21 in Ref. [70].

2.2.1 Evanescent electric field of the HBAR

The HBAR can couple to the Rydberg atoms via the evanescent electric field produced by the piezoelectric dome. For the estimation of the coupling strength (see Section 2.3.1), it is necessary to calculate the evanescent (single-phonon) electric field of the HBAR. An analytic expression for the evanescent single-phonon electric field of the HBAR $E_{\mathrm{HBAR}}(z)$ was derived, and the field was also simulated numerically by Samuel Germer in his master thesis [70]. In the following, we summarize the analytic results that reveal the scaling of the field strength with system parameters.

The derivation is carried out in the quasistatic near-field regime, which is valid here, because the distance between the HBAR and the atoms is on the order of $\sim 50\,\mu\mathrm{m}$, whereas the wavelength of the GHz oscillating electric field in vacuum is on the order of $\sim 50\,\mathrm{mm}$.

To derive an analytic expression for the amplitude of the evanescent electric field, we assume a constant strain breathing mode inside the bulk. Furthermore, we assume that the piezoelectric dome can be approximated by a simple flat-disc geometry with radius R_{pz} and thickness b_{pz} for the piezoelectric material, as sketched in Fig. 2.2. This simplified model only approximates the true sinusoidal strain profile in the piezoelectric dome. Additionally, the Laguerre-Gaussian mode shape present in a HBAR with a dome is not taken into account, but the disc radius can approximately be identified with the acoustic-mode waist w_m. This will allow us to infer the scaling behavior of the evanescent electric field.

The single-phonon electric field amplitude for the simplified flat-disc model on the symmetry axis above the disc (normal to the surface) is given by

$$E_{\mathrm{HBAR}}(z) \approx \frac{e_{33} S_0}{2\epsilon_0 \epsilon_r} \frac{R_{\mathrm{pz}}^2 b_{\mathrm{pz}}}{(R_{\mathrm{pz}}^2 + z^2)^{3/2}} + \mathcal{O}(b_{\mathrm{pz}}^2). \tag{2.10}$$

Here, e_{33} is the piezoelectric constant, ϵ_r the relative permittivity, ϵ_0 the vacuum permittivity, and S_0 the single-phonon strain amplitude. Due to symmetry reasons, the field is orientated along the z-axis.

The single-phonon strain amplitude depends on the acoustic mode that forms inside the HBAR.

The dome geometry used in our experiment will result in Laguerre–Gaussian modes with

$$S_0 = \sqrt{\frac{2\hbar\omega_m}{\pi c_{33} L w_m^2}}, \tag{2.11}$$

where c_{33} is the elastic constant of the substrate and L the thickness of the substrate. Here, we have assumed that $b_{\mathrm{pz}} \ll L$ allowing us to neglect the thickness of the dome and the differences in the elastic constant of the substrate and the dome.

In order to maximize the evanescent field and for phase matching at the boundary between the substrate and the dome, the piezoelectric thickness b_{pz} is chosen as half the acoustic wavelength in AlN

$$b_{\mathrm{pz}} = \frac{\lambda_l^{\mathrm{AlN}}}{2} = \frac{v_l^{\mathrm{AlN}}}{2f} = \frac{\pi v_l^{\mathrm{AlN}}}{\omega_m}, \tag{2.12}$$

with v_l^{AlN} the longitudinal acoustic phase velocity in AlN and $f = \omega_m/2\pi$. Using a half-wavelength thickness provides optimal phase matching at the boundary between the AlN dome and the sapphire substrate, as the standing-wave amplitude vanishes at the interface. Moreover, a half-wavelength thickness maximizes the evanescent field, since the strain does not change sign within the AlN layer. For larger thicknesses, the strain reverses sign after half a wavelength, leading to regions of opposite strain polarity. The resulting piezoelectrically induced electric fields then have opposite polarity and partially cancel, thereby reducing the evanescent field.

We now identify the disc radius with the mode waist, using $R_{\mathrm{pz}} \propto w_m$ and insert Eqs. (2.11) and (2.12) into Eq. (2.10) which gives the approximate scaling

$$E_{\mathrm{HBAR}}(z) \propto \frac{e_{33} v_l^{\mathrm{AlN}}}{\epsilon_r} \sqrt{\frac{1}{c_{33} L \omega_m}} \frac{w_m}{(w_m^2 + z^2)^{3/2}}. \tag{2.13}$$

From this relation we can infer, how the geometry of the HBAR should be optimized to increase the produced electric field and thus the coupling strength to the Rydberg atoms. For fixed w_m, z, and material parameters, the single-phonon electric field amplitude decreases as $\omega_m^{-1/2}$ when the mechanical frequency is increased. Increasing the substrate thickness L reduces the field with $L^{-1/2}$. There exists an optimal mode waist that maximized $E_{\mathrm{HBAR}}(z)$ for a given distance, which is $w_m^{\max}(z) = z/\sqrt{2}$. The scaling behavior with ω_m and L were confirmed using finite element simulations in the thesis of Samuel Germer [70], and the relation between the optimal mode waist and distance was found to be slightly different from the prediction by the approximation in Eq. (2.13): $w_m^{\max}(z) \approx 0.6 \cdot z$.

2.2.1.1 Electric field strength of HBARs for the experiment

To quantify the electric field strength expected for the HBARs received from the group of Yiwen Chu, we perform an electrostatic finite-element simulation using COMSOL [71]. In our group, these simulations were first implemented by Samuel Germer, and further details regarding the implementation are given in his thesis [70]. In the simulation, we apply the analytic spatial strain amplitude profile (given in Eq. (2.9)) to the HBAR. The material parameters relevant for the simulation are given in Table 2.3 of [70], and the geometric parameters are in accordance with the values given in Table 2.1.

The resulting electric field is shown in Fig. 2.3. The field exhibits a dipole-like configuration and is

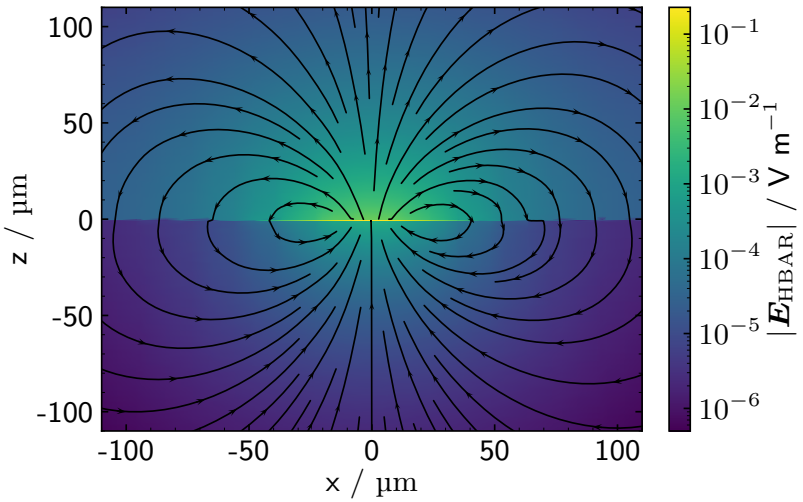

Figure 2.3: Simulated 2D profile of the evanescent electric field amplitude generated by a single-phonon excitation in the HBAR. Streamlines with arrows indicate the electric field orientation for an arbitrarily chosen snapshot in time (the orientation will flip in time after half an oscillation). Simulation parameters correspond to the HBARs received from Yiwen Chu's group. For $z < 0\,\mu\mathrm{m}$, the field is inside the bulk substrate, and for $z > b_{\mathrm{pz}}$ the field is in free space. Irregularities at the surface are artifacts originating from the meshing in the simulation.

strongest at the center directly above the piezoelectric dome. With increasing distance, the field falls off rapidly, approximately with $\propto z^{-3}$ according to Eq. (2.10). The field in the vacuum above the dome is stronger compared to the field in the sapphire substrate. This difference occurs because the induced polarization of the dielectric sapphire counteracts the electric field generated by the piezoelectric dome. As a consequence, the electric field above the dome is stronger compared to a system without a substrate below.

We will use the simulated single-phonon electric field to estimate the coupling strength between a Rydberg atom and a mode of the HBAR in the following Section 2.3.1.

2.3 The hybrid system

We aim to combine the previously discussed Rydberg atoms and HBARs into a novel hybrid system. In this hybrid system, resonant coupling is enabled by the fact that the transition frequencies around 5 to 6 GHz and natural linewidth of approximately 1 kHz of neighboring Rydberg states with principal quantum numbers around 85 to 90 [55] match the parameters of our HBARs, see Section 2.2. Moreover, the increase of the transition dipole moments from $\sim ea_0$ for low-lying atomic states to $\sim 1000ea_0$ for Rydberg states makes the Rydberg atoms sensitive antennas for the evanescent electric field of the HBAR.

The specific architecture that we aim to realize is sketched in Fig. 2.4(a). Here, an ultracold ^{87}Rb atom cloud is trapped close to the surface of a HBAR within a 4 K cryogenic environment. This configuration allows the simultaneous interaction of many Rydberg atoms with the HBAR, which we aim to use for the HBAR mode cooling scheme we elaborate in Section 5.1.

A simplified level-scheme for a single Rydberg atoms interacting with a single HBAR mode is

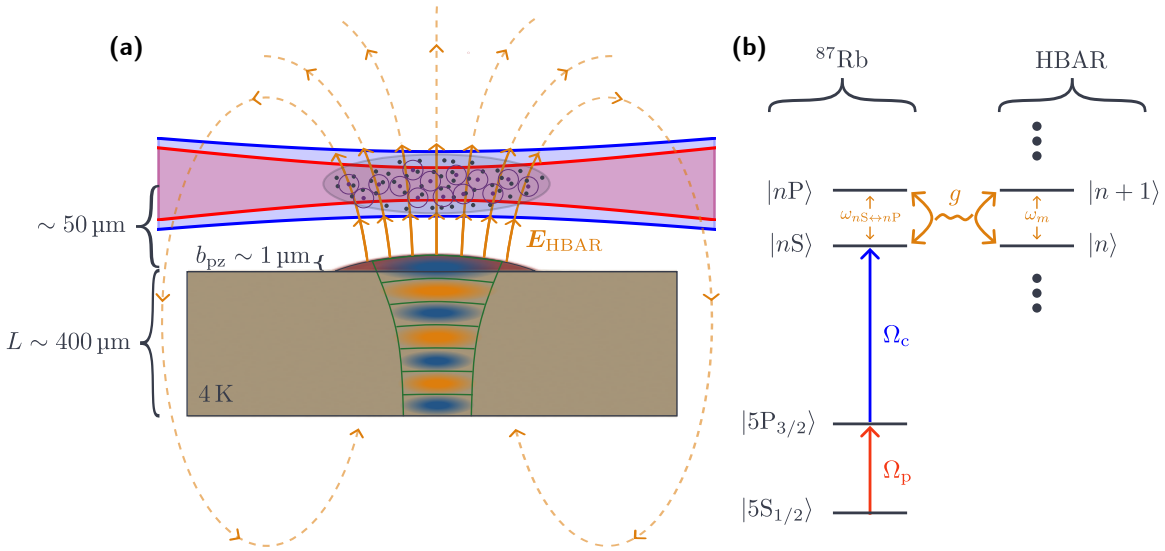

Figure 2.4: **(a):** Schematic overview of the hybrid system. A ^{87}Rb Rydberg atom cloud is coupled to a high-overtone bulk acoustic resonator with a piezoelectric dome on top. The strain profile in the HBAR is indicated by blue and orange ellipses. The dome has a height of half of an acoustic wavelength and converts the mechanical stress to an evanescent electric field $\boldsymbol{E}_{\mathrm{HBAR}}$ indicated by orange arrows (see Fig. 2.3 for the simulated field configuration). The atoms are shown as dark gray dots or violet dots with a circle around them if excited to the Rydberg state. The profile of the Rydberg excitations lasers are indicated by red and blue contours. Atoms in the Rydberg state can interact with the evanescent electric field. **(b):** Schematic level diagram for the hybrid system. The probe and control laser are colored as in (a).

sketched in Fig. 2.4(b). A two photon transition via the intermediate $5P_{3/2}$ state is used to excite the atoms to the high lying Rydberg state $|n\mathrm{S}\rangle$. This transition is driven by one red laser at 780 nm coupling the $|5\mathrm{S}_{1/2}\rangle$ state of rubidium to the $|5\mathrm{P}_{3/2}\rangle$ state, and one blue laser at 480 nm coupling the $|5\mathrm{P}_{3/2}\rangle$ state to the Rydberg state of interest. The two lasers have Rabi frequencies Ω_p and Ω_c respectively. We refer to the red laser as the probe laser and the blue laser as the control laser. Further information regarding the Rydberg excitation is given in Section 3.7.4. The dipole transition between the Rydberg states $|n\mathrm{S}\rangle$ and $|n\mathrm{P}\rangle$—with transition frequency $\omega_{n\mathrm{S}\leftrightarrow n\mathrm{P}}$—is driven by the evanescent electric field of an eigenmode of the HBAR with corresponding coupling strength g. The eigenmode of the HBAR with resonance frequency $\omega_m \approx \omega_{n\mathrm{S}\leftrightarrow n\mathrm{P}}$ is described as a quantum harmonic oscillator with equal level spacing. This description is well-suited for the HBARs with low mode occupation at cryogenic temperatures [30, 72].

Precise control over the atom cloud position relative to the HBAR surface is crucial, as the atom-oscillator interaction strength depends sensitively on the spatial overlap between the Rydberg atoms and the evanescent electric field. Therefore, we employ magnetic wire traps integrated on an atom chip hosting the HBAR (not shown in figure Fig. 2.4). The on-chip wire trap enables dynamic tuning of the atom cloud position, allowing for systematic exploration and optimization of the coupling strength. An additional benefit of this position control is the ability to characterize the spatial dependence and potentially mitigate parasitic evanescent static electric fields arising from charge or adsorbate deposition on the chip and HBAR surfaces. Such fields can strongly perturb Rydberg atoms [39, 57], which are sensitive to stray electric fields as discussed in Section 2.1. The design of the magnetic wire

traps and atom chip are detailed in Section 4.2.

2.3.1 Atom–oscillator coupling

The atomic states participating in the interaction between the HBAR and the Rydberg atom are $|n\mathrm{S}\rangle$ and $|n\mathrm{P}\rangle$, which have an energy separation of $\hbar\omega_{n\mathrm{S}\leftrightarrow n\mathrm{P}}$, as shown in the level scheme in Fig. 2.4(b). As mentioned before, the HBAR resonance frequencies in a range of 5 to 6 GHz can be matched by transitions between Rydberg states with principal quantum numbers around 85 to 90.

We model the atom–HBAR coupling under the assumption that only a single acoustic mode is (near-)resonant with the atomic transition, allowing us to neglect other longitudinal and transverse modes. The Hamiltonian describing a single eigenmode of the HBAR with resonance frequency ω_m can be given in the form of a standard quantum harmonic oscillator [72]

$$H_{\mathrm{HBAR}} = \hbar\omega_m \left(a_m^\dagger a_m + \frac{1}{2} \right), \tag{2.14}$$

with ladder operators $a_m^\dagger$, a_m.

Within the rotating-wave approximation, the Hamiltonian describing the interaction between a single atom and the HBAR eigenmode is given by [43–46]

$$H_{\mathrm{int}} = \hbar g \left(|n\mathrm{P}\rangle \langle n\mathrm{S}| \otimes a_m + |n\mathrm{S}\rangle \langle n\mathrm{P}| \otimes a_m^\dagger \right). \tag{2.15}$$

Here, the single-phonon coupling strength between the Rydberg atom and the mechanical oscillator is

$$g = \frac{1}{2\hbar} \left\langle n\mathrm{P} \left| \boldsymbol{E}_{\mathrm{HBAR}}^{\mathrm{atom}} \cdot \boldsymbol{d} \right| n\mathrm{S} \right\rangle, \tag{2.16}$$

where $\boldsymbol{d}$ is the electric-dipole operator, and $\boldsymbol{E}_{\mathrm{HBAR},0}^{\mathrm{atom}}$ is the evanescent electric field of the HBAR at the atom's position produced by a single phonon.

The electric field can drive π or $\sigma_\pm$ transitions depending on its polarization with respect to the quantization axis, which we define aligned to the external magnetic field. In our experimental setup, the magnetic wire trap constrains the magnetic-field orientation to lie parallel to the HBAR surface (see Section 4.2). For the fundamental transverse mode of the HBAR, the evanescent electric field is oriented perpendicular to the surface, and therefore orthogonal to the magnetic quantization axis.

This orthogonal configuration projects the HBAR field into an equal superposition of left- and right-handed polarization. Therefore, both σ_+ and σ_- transitions can be addressed, but the effective field amplitude coupling to either is suppressed by $1/\sqrt{2}$ compared to the total magnitude.

To obtain a quantitative estimate of the coupling strength, we consider the σ_+ transition $|86\mathrm{S}_{1/2}, m_J = +1/2\rangle \leftrightarrow |86\mathrm{P}_{3/2}, m_J = +3/2\rangle$, which has a transition frequency of 5.8 GHz. We use the single-phonon electric field from the finite-element simulation (Fig. 2.3) at an atom–HBAR distance of 50 µm, where $|\boldsymbol{E}_{\mathrm{HBAR}}(50\,\mu\mathrm{m})| = 1.6 \times 10^{-4}\,\mathrm{V\,m^{-1}}$. With the full dipole matrix element computed using the ARC package [55] and accounting for the $1/\sqrt{2}$ reduction, we obtain a coupling strength of

$$g_{\mathrm{sim}} = 2\pi \times 3.2\,\mathrm{kHz}. \tag{2.17}$$

To assess whether this coupling strength suffices to access the strong-coupling regime, we compare the coherent single-phonon coupling rate g with the relevant dissipation channels. For a single atom

interacting with one mechanical mode, strong coupling requires that coherent exchange of excitations outpaces irreversible loss. A common practical criterion is $g \gg \gamma, \kappa$. A convenient dimensionless figure of merit is the single-photon cooperativity [73]

$$C = \frac{4g^2}{\gamma\kappa}, \tag{2.18}$$

which counts the number of coherent excitation exchanges before decoherence. Strong coupling corresponds to $C \gg 1$. Inserting $g_{\mathrm{sim}}/2\pi = 3.2\,\mathrm{kHz}$, $\gamma/2\pi \sim 1\,\mathrm{kHz}$, and $\kappa/2\pi \sim 1\,\mathrm{kHz}$ [32, 55] yields a cooperativity of $C \approx 10$, indicating operation in the strong-coupling regime.

However, at a temperature of $T = 4\,\mathrm{K}$, the mode of the HBAR is not frozen out but rather thermally occupied according to Bose–Einstein statistics with a mean phonon number of

$$\langle n \rangle_{\mathrm{th}} = \frac{1}{e^{\hbar\omega_m/k_B T} - 1}, \tag{2.19}$$

where k_{B} is the Boltzmann constant. For a resonance frequency of $\omega_m \approx 5.8\,\mathrm{GHz}$ (matching the Rydberg transition $|86\mathrm{S}\rangle \leftrightarrow |86\mathrm{P}\rangle$), this corresponds to an average occupation of $\langle n \rangle_{\mathrm{th}} \approx 14$. Such high thermal occupation precludes the observation of coherent interactions between individual Rydberg atoms and the HBAR [74]. Consequently, a primary experimental objective is to cool the mechanical mode by coupling it to a Rydberg atom ensemble. The envisioned cooling protocol is detailed in Section 5.1.

Several strategies could be employed to increase the coupling strength beyond the estimated $g_{\mathrm{sim}} = 2\pi \times 3.2\,\mathrm{kHz}$. First, reducing the atom–HBAR separation would enhance the evanescent field amplitude, though at the expense of stronger stray-field perturbations and tighter geometric constraints to avoid clipping the Rydberg-addressing beams.

Second, reducing the substrate thickness L in accordance with Eq. (2.13) could increase g, potentially at the cost of degrading the resonator quality factor. For both geometric approaches, the acoustic mode waist must be optimized by adapting the HBAR dome curvature to maximize the field at the atom position.

A third option is to employ higher principle number Rydberg states. The transition dipole moment increases for higher principle quantum numbers and corresponding lower transition frequencies following Eqs. (2.3) and (2.4), while the electric field produced by the HBAR decreases at lower frequencies according to Eq. (2.13). Combining both scalings in the coupling strength formula in Eq. (2.16) yields

$$g \propto \omega^{-7/6}. \tag{2.20}$$

Consequently, increasing the principal quantum number of the Rydberg atoms could improve the coupling strength. However, this comes at the cost of increased polarizability according to Eq. (2.6), potentially worsening the effects of evanescent stray electric fields from the surface.

CHAPTER 3

Cold atom preparation

The hybrid platform pursued in this work combines two ingredients: a mechanical oscillator and a cloud of ultracold rubidium atoms excited to Rydberg states.

In this chapter, the cold atom preparation setup is presented. We start by giving a general overview of the setup, the design choices and the experiment sequence. Next, the working principle of magnetic traps and absorption imaging, employed in the experiment, are introduced, followed by a detailed discussion of the cold atom preparation steps.

3.1 General design choices and setup overview

The goal of the cold-atom preparation setup is to produce an ultracold atomic cloud and position it in close proximity to an HBAR in a cryogenic environment near 4 K. Ultracold neutral-atom physics has matured over the past three decades. In most experiments, like in ours, a magneto-optical trap (MOT)—first demonstrated in 1987 [75]—provides the initial source of cold atoms.

We use rubidium as the working species and chose the isotope ^{87}Rb. Rubidium is particularly attractive for ultracold-atom experiments: the D_2 and D_1 transitions at 780 nm and 795 nm are readily addressed with commercial diode lasers, enabling robust and cost-effective systems. Moreover, ^{87}Rb offers a favorable hyperfine structure for efficient laser cooling, optical pumping, and state preparation, and its atomic properties are well characterized in the literature [76–78]. Another practical advantage is the rubidium vapor pressure at room temperature, which is in the 1×10^{-7} to 1×10^{-6} mbar range. This pressure is low enough to be compatible with the vacuum requirements of ultracold-atom experiments, yet high enough to load a MOT directly from background vapor without an atomic oven or cryogenic pre-cooling.

Figure 3.1 shows a sketched overview of the experiment design. We have chosen a solution with two separate vacuum chambers, connected with a differential pumping tube. This allows us to have a dedicated MOT chamber and a science vacuum chamber. This design is chosen as a compromise that satisfies the requirements for the ultra-cold atom preparation and the HBAR. In the following we will explain these requirements and the resulting design choices we made in detail.

A central design constraint is the requirement to operate the HBAR at a cryogenic temperature near 4 K. Such temperatures can be reached with either flow cryostats or closed-cycle (dry) helium cryostats [79]. Flow cryostats provide superior cooling power and negligible vibration, but they

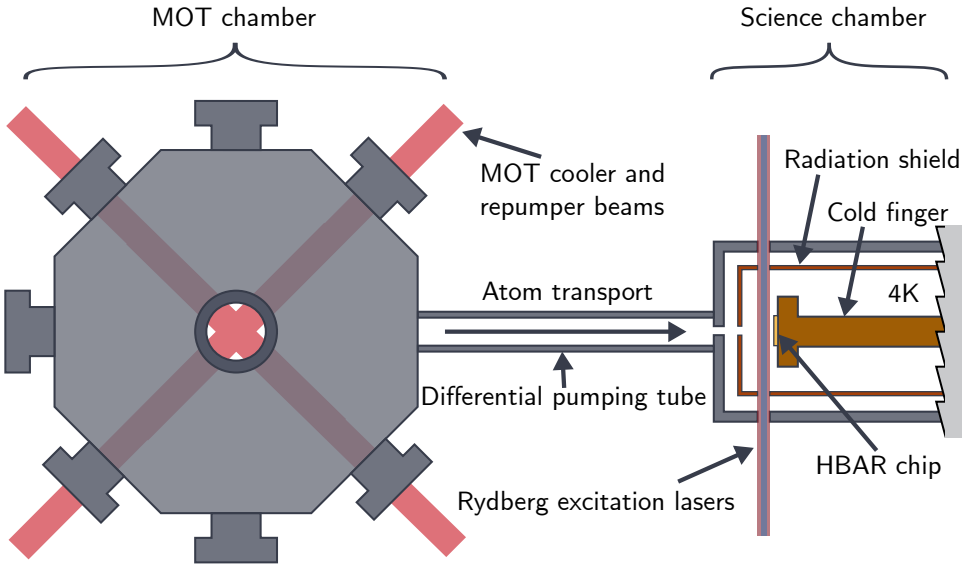

Figure 3.1: Schematic overview of the experimental setup illustrating the two-chamber vacuum system with dedicated MOT and science chamber. The two chambers are connected via a differential pumping tube.

consume liquid helium, making continuous operation costly and logistically demanding due to the need for helium recovery and reliquefaction. By contrast, closed-cycle cryostats compress and expand helium within a sealed loop to transport heat from the cold stage to the ambient environment. This process does not consume helium and is therefore less expensive to operate, at the expense of reduced cooling power and vibrations from moving mechanical components. Because of their lower operating cost, ability to run continuously, and independence from helium-recovery infrastructure, a dry closed-cycle cryostats is our choice for cryocooling in the hybrid system.

The design requirements of a cryogenic experiment are in conflict with those of a MOT region for atom loading. A MOT benefits from large optical access, typically along six axes [80]. In cryogenic environments, optical access should be minimized to reduce radiative heat load from blackbody radiation. When optical access is required, in-vacuum windows—absorbing infrared blackbody radiation but transmitting the target wavelengths—are thermally anchored to a cryogenic heat shield surrounding the experimental region. Higher laser powers generally increase MOT loading rates. However, the MOT laser beams can be a detrimental thermal load on the cryogenic environment by clipping on the cryogenic sample or cryogenic radiation shields. Even when the laser light is incident solely on the cold windows, scattering and absorption by the windows can still introduce unwanted thermal load.

To avoid these thermal-load issues altogether, we chose to spatially separate the atom-loading region from the cryogenic science region. This separation necessitates transporting the atomic cloud after loading, but it also offers important advantages for cold-atom preparation: the vacuum conditions for the loading and science regions can be controlled independently. In particular, with separate vacuum chambers for loading and for the cryogenic environment, a differential pumping tube can be placed between them to decouple the pressures of the two chambers.

In the science region, the pressure should be as low as possible so that residual background gas minimally perturbs the trapped ultracold cloud. Especially, collisions of trapped rubidium atoms with

background atoms or molecules at thermal (room-temperature) velocities typically eject atoms from the trap. This process limits the lifetime of trapped clouds. The background limited trap lifetime is anti-proportional to the background pressure but depends on the composition of the background [81, 82]. As a rule of thumb, lifetimes of 1 s correspond to a pressure of about 1×10^{-9} mbar. Consequently, pressures well below 1×10^{-9} mbar are required for most ultracold-atom experiments.

In contrast, a rubidium MOT loads faster from background vapor at higher Rb pressures [81–83]. By separating the MOT loading region from the science region with a differential pumping tube, one can use a $\sim 1 \times 10^{-9}$ mbar rubidium background pressure for MOT loading without sacrificing the vacuum where the experiments take place. For these reasons, we chose a two-chamber design with a separated MOT-loading and science chamber.

We designed and assembled a room-temperature version of the planned setup, to demonstrate the atom loading and Rydberg excitation before the arrival of the commercial custom cryostat that was bought for the experiment. This setup is designed to be upgradeable to the cryogenic version with minimal alteration and adjustments. Here, a short overview is given, the details of the specific components are discussed in the following sections. A computer assisted drawing (CAD) of the room-temperature setup for the cold atom-preparation is shown in Fig. 3.2. The setup features a commercial steel MOT chamber[1] and a homemade titanium glass cell as science chamber. The titanium glass cell is flanged onto a commercial vacuum octagon[2] that hosts a vacuum ion pump[3], an ion gauge[4] and electrical feedthroughs. Furthermore, electrodes inside the science chamber are mechanically anchored to the octagon. For the cryogenic upgrade, only the inner assembly in the science chamber and the vacuum octagon will need to be exchanged for their cryogenic counterparts that are detailed in Chapter 4.

As shown in Fig. 3.2, two magnetic compensation-coil cages surround the vacuum chambers, one for the MOT and one for the science chamber. An ampoule is the reservoir for rubidium atoms loaded in the MOT chamber. The ampoule is connected via a dosing valve to the MOT chamber. The valve is used as a coarse control knob for the rubidium background pressure in the MOT chamber by regulating the flow of rubidium.

Each vacuum chamber has its own ion pump and a valve that can be connected to a turbo pump. Additionally, a valve between the chambers that can be used to isolate them from each other. This valve allows us to break the vacuum on one side of the setup, without affecting the other, a feature that was useful for the assembly of the room temperature setup. Furthermore, this will also allow us to exchange samples in the science chamber, without interfering with the MOT chamber.

The MOT chamber and the science chamber are separated by a distance of 450 mm, which the atoms have to traverse. There are different ways of transporting the cloud of ultracold atoms from their initial position in the MOT chamber to the science chamber. We picked a magnetic transport, which consists of the chain of magnetic coils visible above and below the vacuum chamber in Fig. 3.2. A detailed description of this magnetic transport is given in Section 3.6.

During the transport, the cloud travels through a differential pumping tube with a length of 105.3 mm and a diameter of 4 mm. With these dimensions, and taking into account the pump rate of the ion pump on the science chamber side ($500\,\mathrm{L\,s^{-1}}$ for H_2), a relative pressure difference of up to $\sim 10^4$ can

[1] VACOM PE KAMMER, 9X CF DN40 1X CF DN16, L=175, ESU/316L
[2] Kimball MCF800-SphOct-G2C8
[3] SAES Getters NexTorr D500
[4] Agilent UHV-24P 9715015

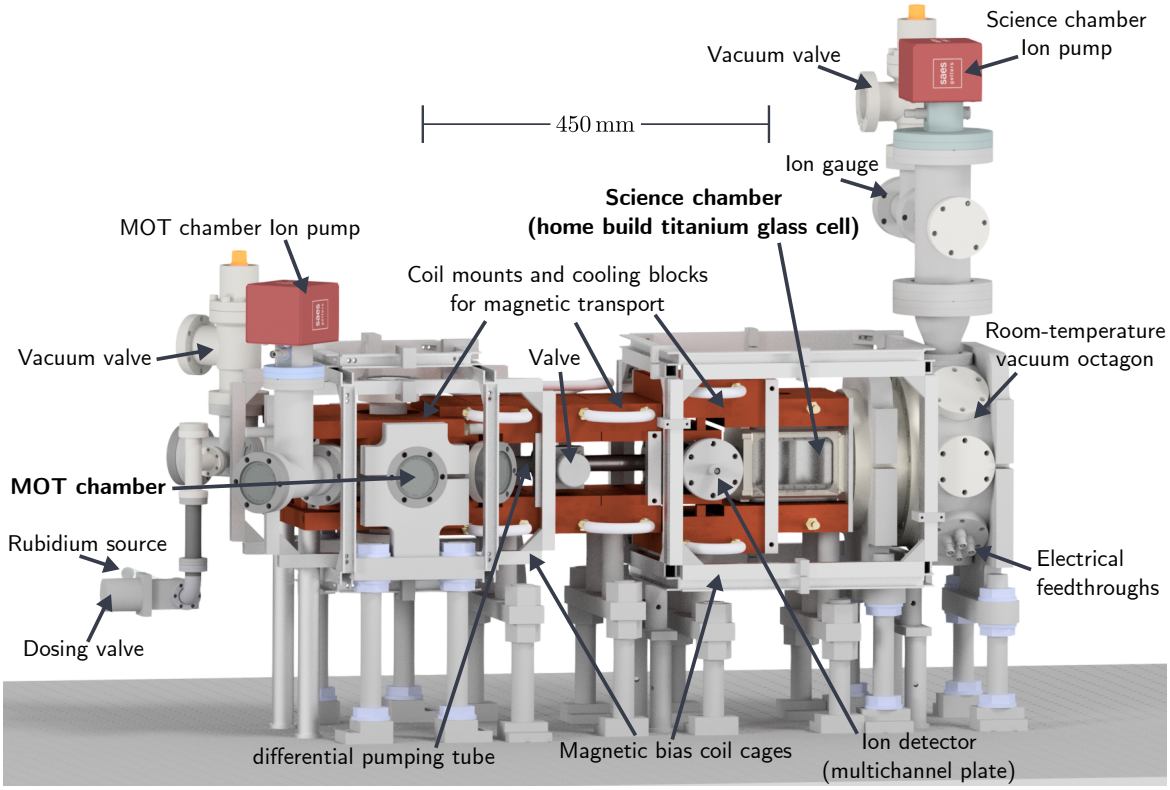

Figure 3.2: CAD rendering of the room-temperature setup with a two-chamber vacuum design. The two vacuum chambers (MOT and science chamber) are connected via a differential pumping tube. Atoms from the MOT chamber are transported to the science chamber via magnetic transport. The rubidium source is a rubidium ampoule that is connected to the MOT chamber via a valve to control the dosing. Electrical feedthroughs on the side of the science chamber are connected to ionization electrodes in the science chamber. An ion detector (multichannel plate) next to the science chamber allows for the detection of ionized Rydberg atoms. For maintenance, the vacuum connection between the two chambers can be closed via a valve and each chamber can be independently vented. A dedicated ion pump for each chamber provides vacuum pumping. For vacuum diagnostics, an ion gauge is connected to the science chamber.

in theory be established between the MOT and the science chamber [84].

Once transported to the science chamber, the atoms are trapped in a magnetic quadrupole field formed with macroscopic magnetic coils outside the vacuum chamber in the room temperature setup, whereas they will be transferred to an atom chip in the cryogenic setup, as detailed in Section 4.2. Therefore, this room-temperature setup allows us to characterize the cold atom preparation up to the atom chip.

The optical setup around the science chamber and MOT chamber (not shown in Fig. 3.2) is placed on breadboards around the experimental setup. This allows for all optics to be removed when the cryostat is set up and then to be put back in place, requiring only minimal realignment.

Two absorption imaging setups are included in the setup. One for imaging the atom cloud in the MOT chamber and one for imaging in the science chamber. Additionally, fluorescence imaging of the MOT is installed. These imaging systems are presented in Sections 3.5.1, 3.5.2 and 3.7.2.

The Rydberg excitation and detection setup and its characterization is presented in Section 3.7.4.

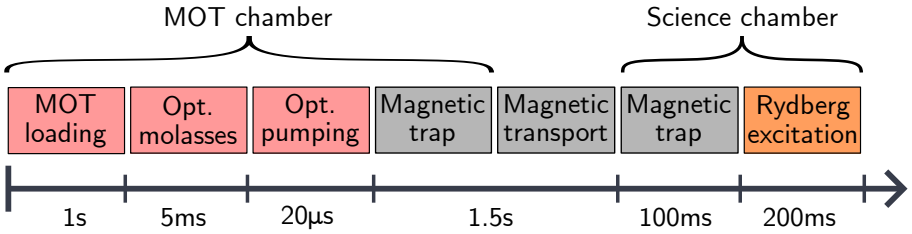

Figure 3.3: Schematic timing overview of the experiment sequence. The stages belonging to atom loading in the MOT chamber are colored in red, the magnetic trapping and transport stages in gray, and the Rydberg excitation in orange.

3.2 Experiment sequence overview

Cold atom preparation and measurements proceed through a fixed set of timed stages that together form an *experiment sequence*. Here, we provide an overview of the sequence, detailed descriptions of individual stages are given in subsequent sections of this chapter. A timing diagram of the room-temperature experiment sequence is shown in Fig. 3.3. The sequence begins with MOT loading of ^{87}Rb from background vapor in the MOT chamber. The captured atoms are further cooled in an optical molasses phase. For efficient magnetic trapping the population is optically pumped into the $|5S_{1/2}, F = 2, m_F = 2\rangle$ Zeeman sublevel and subsequently transferred to a quadrupole magnetic trap. The trapped cloud is then conveyed to the science chamber using the magnetic transport described in Section 3.6. In the science chamber the atoms are held in a quadrupole magnetic trap (room-temperature setup) prior and during the Rydberg excitation and detection.

Absorption imaging in both the MOT and science chambers is set up to characterize the atomic cloud during or after the preparation sequence.

A limitation to the number of measurement repetitions that can be performed on a given atom cloud after the cold atom preparation is determined by the lifetime of the atom cloud. All experimental operations after the atom loading must be completed on a timescale short compared to the cloud lifetime which is on the order of a few seconds in our experiment, limited by the background pressure in the vacuum chamber (see Sections 3.5.6 and 3.7.3). Furthermore, key measurement techniques such as absorption imaging are inherently destructive. Consequently, only a short sequence of measurements or a single destructive measurement can be performed on a given cloud. The experiment sequence is therefore executed repeatedly. We refer to one full repetition as an *experimental cycle*.

Even under nominally identical conditions, experimental observables exhibit irreducible shot-to-shot fluctuations due to quantum-mechanical effects. For example, the excitation of Rydberg atoms is subject to photon-number fluctuations in the excitation laser pulses, as well as to stochastic variations in the number and spatial distribution of excited atoms. Together with technical fluctuations, this necessitates averaging over many repetitions to obtain statistically meaningful results.

In normal operation, the experiment is continuously repeating the experimental cycle. This does not only maximize the data acquisition rate, it also enhances experimental stability by establishing a steady operating point. Because many components—such as magnetic field coils—are powered only during limited portions of each cycle, continuous cycling leads to stable average thermal conditions (after an initial warmup).

The performance of the cold atom preparation fluctuates over weeks to months. A fundamental cause are fluctuations in the rubidium background vapor in the MOT chamber as discussed in Section 3.5.

Table 3.1: Typical performance of the cold atom preparation sequence. Values are representative for standard operating conditions. Fluctuations occur due to variations in rubidium background pressure and other technical factors. The optical pumping is omitted from the table, because it does not affect the atom number or temperature. Also, the magnetic transport is omitted because the values for the magnetic trap in the MOT and science chamber correspond to the start and end condition of the magnetic transport, and the atomic cloud cannot be measured during the transport. The atom cloud is not fully thermalized after the handover to the magnetic trap in the MOT chamber, and the given temperature value is only an approximation.

	MOT loading (1 s)	Optical molasses	Magnetic trap (MOT chamber)	Magnetic trap (science chamber)
Atom number	1×10^9	1×10^9	1×10^9	2.5×10^8
Temperature / µK	370	50	300	200

The characterization measurements we will present in this work were performed at different times throughout the span of three years. As a consequence, the atom numbers will slightly vary between these characterization measurements. In Table 3.1, we summarize the typical atom numbers and temperatures during the cold-atom preparation. The atomic cloud experiences minimal losses in the MOT chamber after the MOT loading, but only about 25% are successfully transferred to the science chamber. In contrast, the temperature increases when the atomic cloud is transferred from the optical molasses to the magnetic trap in the MOT chamber and reduces again during the magnet transport to the science chamber. We discuss the reason for these behaviors in Sections 3.5.6 and 3.6.

Experiment control system Each of the experimental steps requires precise timing and control of many electronic devices simultaneously. Therefore, a sophisticated experiment control system is required. The control system we set up is copied from the mature Rubidium Rydberg experiment in our group and was already developed in Stuttgart, see for example the thesis of Hannes Gorniaczyk [85] for a detailed description.

The experiment control software is run on a dedicated experiment control computer. From there, before every cycle the sequence instructions are fed to a database on a server and to the real time control system ADwin[5]. The ADwin is the central timing unit that triggers other devices and provides analog control voltages with a 20 µs resolution. For the Rydberg excitation and detection stage we require a higher timing precision, and therefore this stage is controlled by a FPGA based pulse generator with a 2 ns precision. The two cameras used for absorption imaging[6] are programmed and read out from a dedicated camera control computer. All other devices are programmed before a cycle starts from a dedicated device control computer.

3.3 Magnetic trap working principle

Magnetic trapping of the atom cloud is employed at several steps during the cold atom preparation. Therefore, we give a short introduction to its working principle here.

[5] Jäger Computergesteuerte Messtechnik GmbH AdWin II Pro

[6] Excelitas Technologies Corp. pco.pixelfly 1.4 USB

Magnetic traps rely on the Zeeman energy shift that magnetic fields induce on atoms with a magnetic moment. The shift is given by [86]

$$\Delta E = \mu_B g_F \boldsymbol{F} \boldsymbol{B}, \tag{3.1}$$

where μ_B is the Bohr magneton, g_F is the Landé g-factor, $\boldsymbol{F}$ is the total angular momentum, and $\boldsymbol{B}$ is the magnetic field. If the change of the field gradient is small compared to the Larmor precession frequency, the magnetic moment of the atom will adiabatically follow the direction of the magnetic field. In this case, the energy shift can be approximated as

$$\Delta E = \mu_B g_F m_F |\boldsymbol{B}|, \tag{3.2}$$

where m_F is the magnetic quantum number. Atoms in low-field-seeking states (where $g_F m_F > 0$) experience a potential minimum at points where the magnetic field strength is lowest, which can be used to trap the atoms. During the cold atom preparation, we optically pump the ^{87}Rb atoms to the low-field-seeking state $|5S_{1/2}, F = 2, m_F = +2\rangle$ to trap them magnetically, as discussed in Section 3.5.5.

In the MOT chamber and in the science chamber as well as during the magnetic transport, we utilize external magnetic field coils in anti-Helmholtz configuration to produce magnetic quadrupole fields with an absolute field minimum at their centers, suitable to trap low-field seeking atoms. However, a magnetic quadrupole has a field zero at its center, where the atoms can undergo transitions to high-field-seeking states, so-called Majorana spin-flips [87]. The associated atom-loss rate from the trap depends on the likelihood of atoms reaching the trap center. Because lower-temperature atoms are confined closer to the center, the loss rate scales with $1/T^2$ [88]. For the temperatures of around 200 µK reached in the magnetic traps during the cold-atom preparation in the room-temperatures setup, this loss mechanism is negligible compared to loss due to collisions with background vapor [89].

The situation changes for the cryogenic version of the experiment, where we plan to employ evaporative cooling to reach temperatures of around 10 µK. A detailed discussion regarding potential spin-flip losses during the evaporative cooling is given in Section 4.2.2. After being cooled, the atom cloud will be transferred to a magnetic Z-wire trap on the atom chip, which is discussed in Section 4.2.1. The Z-wire trap has an Ioffe-Pritchard-like field configuration with a magnetic field offset (~ 1 G) at its minimum that strongly suppresses spin flip losses and renders them negligible [90].

3.4 Absorption imaging working principle

Before describing the individual steps of the cold-atom preparation in the following sections, we introduce the working principle of absorption imaging, which serves as the primary diagnostic tool for characterizing the preparation. Absorption imaging is an imaging technique, where the atom cloud is illuminated with a (near-) resonant laser beam and the "shadow" cast by the atomic cloud on a camera is analyzed to infer quantitative properties such as atom number and temperature.

In the description here, we take the imaging plane to be the x–y plane and the imaging beam to propagate along the z-axis. A magnetic bias field is applied along the z-axis to define the quantization axis. A (near-) resonant circular polarized imaging beam addresses the closed cycling transition in ^{87}Rb, $|5S_{1/2}, F = 2, m_F = 2\rangle \leftrightarrow |5P_{3/2}, F = 3, m_F = 3\rangle$ [91]. On resonance, the effective scattering cross-section is $\sigma_0 = 3\lambda^2/(2\pi)$, with λ the wavelength of the transition. Off resonance, the

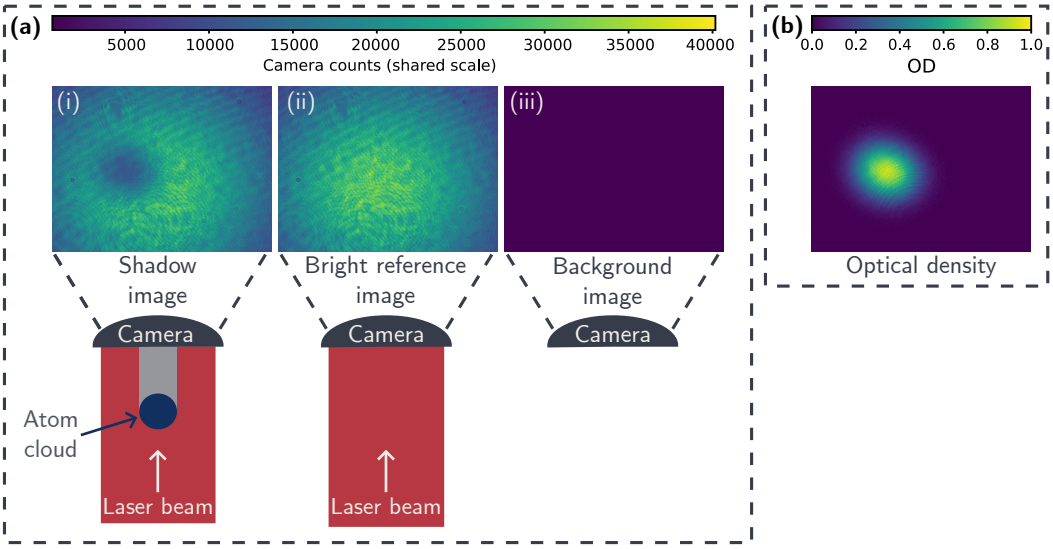

Figure 3.4: Schematic of the working principle of absorption imaging together an exemplary set of absorption images. **(a):** Three images are taken: (i) a (near-)resonant laser beam is shined onto the atomic cloud and the produced shadow is recorded on a camera. (ii) an image without the atoms is taken as reference for the laser intensity. (iii) a background image without laser light is taken to determine background noise. **(b):** The three images in (a) are combined as described in the main text to determine the optical column-density of the atomic cloud.

cross-section is reduced to

$$\sigma(\Delta) = \frac{\sigma_0}{1 + (2\Delta/\gamma)^2}, \tag{3.3}$$

where Δ is the detuning, and γ is the natural linewidth of the transition. The axial transmission through the cloud obeys the Beer–Lambert law

$$T(x,y) = \frac{I(x,y,z=L_c)}{I(x,y,z=0)} = \exp\left(-\int_0^{L_c} n_c(x,y,z)\,\sigma\,dz\right), \tag{3.4}$$

where I is the laser intensity, L_c is the length of the cloud along the z-axis and $n_c(x,y,z)$ denotes the local atom number density.

In practice, three images are recorded, as shown schematically in Fig. 3.4(a): (i) a "shadow" image with atoms, yielding a transmitted intensity of I_{shadow}; (ii) a bright reference image with atoms removed, I_{bright}; and (iii) a background image that captures camera offsets and stray light, I_{bg}. Combining these images allows one to compute the optical column density via Eq. (3.4) as

$$\text{OD}(x,y) = -\ln\left(T(x,y)\right) = -\ln\left(\frac{I_{\text{shadow}}(x,y) - I_{\text{bg}}(x,y)}{I_{\text{bright}}(x,y) - I_{\text{bg}}(x,y)}\right). \tag{3.5}$$

Figure 3.4(b) shows the resulting optical density computed with the images shown in Fig. 3.4(a). From the measured column densities, the atom number follows by spatial integration, and the spatial extent of the cloud is obtained from Gaussian fits to the column-density profile.

The cloud temperature can be extracted from a time-of-flight (TOF) measurement. In a TOF

measurement, the trap is switched off and the cloud expands freely for a variable time t_{TOF}. Assuming a Maxwell–Boltzmann velocity distribution and a ballistic expansion, the root-mean-square width of the cloud σ_{img} in the imaging plane evolves as

$$\sigma_{\mathrm{img}}(t_{\mathrm{TOF}}) = \sqrt{\sigma_{\mathrm{img}}(0)^2 + \frac{k_B T}{m_{^{87}\mathrm{Rb}}} t_{\mathrm{TOF}}^2} \quad , \tag{3.6}$$

where $\sigma_{\mathrm{img}}(0)$ is the cloud root-mean-square width at release, k_{B} is Boltzmann's constant, T is the cloud temperature, and $m_{^{87}\mathrm{Rb}}$ is the atomic mass. By fitting $\sigma_{\mathrm{img}}(t_{\mathrm{TOF}})$ versus t_{TOF}, one extracts the cloud temperature T.

3.5 MOT chamber

As outlined in Section 3.2, the four initial cold-atom preparation stages take place in the MOT chamber: loading the MOT from background vapor, optical molasses, optical pumping, and capture of the atoms in a magnetic trap. The objectives are rapid accumulation of ^{87}Rb atoms in an atom cloud, reduction of the temperature of the atom cloud, and preparation of the atoms spin population for efficient magnetic trapping. Achieving a large atom number at low temperature at this point counteracts potential atom loss and heating during the transfer to the final trap in the science chamber. Absorption and fluorescence imaging implemented in this chamber provide quantitative diagnostics for optimizing each stage.

In the following, we will give an overview of the MOT chamber and the corresponding imaging setup, followed by the description and characterization of the cold-atom preparation steps performed in this chamber.

The MOT chamber is sketched in Fig. 3.5(a) and a corresponding photograph of the chamber with the surrounding experimental setup is shown in Fig. 3.5(b). The chamber is a commercial steel octagon[7] with nine DN40 viewports and one DN16 flange for the differential pumping tube[8] connecting the MOT chamber to the science chamber. Six of the viewports are used for the MOT cooler and repumper beams. An opposite pair of viewports enables the absorption imaging as well as the optical pumping. The final viewport is used for fluorescence imaging of the MOT. Magnetic coils are located above and below the chamber in Anti-Helmholtz configuration to create the magnetic quadrupole fields for the MOT and magnetic trap. A cage of rectangular magnetic field compensation coils surrounds the MOT chamber. These coils are used to compensate stray magnetic fields and to apply magnetic offset fields.

A rubidium ampoule is connected via a valve to the MOT chamber. When the ampoule was first broken in August 2023, the passive absorption of rubidium by the walls of the connecting tube and MOT chamber resulted in too low Rubidium pressures. We utilized additional heating wires, wrapped around the ampoule, to increase the flow of rubidium to reach a pressure of $\sim 1 \times 10^{-9}$ to 3×10^{-9} mbar in the chamber. Over time, the heating wires had to be reduced in power and ultimately turned off after a few months. We assume that all walls got coated with a thin layer of rubidium over that time. Every few weeks to months, the opening of the valve needs to be adjusted a bit, to keep the pressure within the desired range of approximately 1×10^{-9} to 3×10^{-9} mbar.

[7] VACOM PE KAMMER, 9X CF DN40 1X CF DN16, L=175, ESU/316L

[8] Kurt J. Lesker, custom

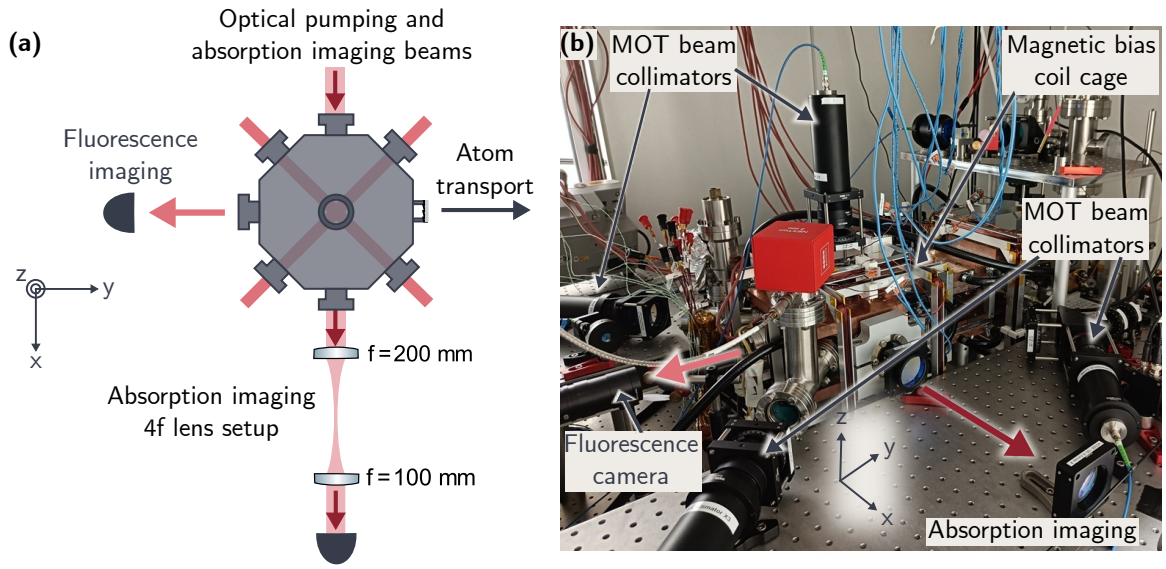

Figure 3.5: **(a):** Sketch of the MOT chamber. The absorption and fluorescence imaging directions are highlighted as well as that of the optical pumping beam. **(b):** Photograph of the MOT chamber with surrounding optics and magnetic coils. The MOT beam collimators, the magnetic bias field coil cage, the fluorescence imaging camera, and the absorption imaging are highlighted. The magnetic field coils in anti-Helmholtz configuration used for the MOT are below the copper cooling plates visible above and below the MOT chamber.

Because the pressure fluctuates over the span of weeks to months, also the experiment performance, especially the atom number undergoes the same fluctuations. The characterization measurements we present in the following sections were performed at different times throughout the span of four years. As a consequence, the absolute atom numbers are not always consistent between these characterization measurements.

3.5.1 Absorption imaging at the MOT chamber

Resonant absorption imaging, as outlined in Section 3.4, is employed as a diagnostic and optimization tool for the cold-atom preparation sequence in the MOT chamber. A standard $4f$ imaging system is used to form the shadow image of the cloud, as sketched in Fig. 3.5(a). The imaging setup was initially implemented during the bachelor thesis of Valerie Mauth, where technical details regarding the imaging laser pulses and camera are discussed [92].

Note, that the strongest absorption of the imaging beam and hence the strongest signal occurs, when the imaging beam is driving the closed cycle transition $|5S_{1/2}, F = 2, m_F = 2\rangle \leftrightarrow |5P_{3/2}, F = 3, m_F = 3\rangle$. However, after the MOT stage, the atoms are distributed over the different m_F states. Therefore, the atom cloud is optically pumped to the state $|5S_{1/2}, F = 2, m_F = 2\rangle$ before imaging, as explained in Section 3.5.5.

A practical challenge for imaging of the MOT cloud is its large atom number, typically $\sim 1 \times 10^9$, which leads to a correspondingly high optical density. For such dense samples, a resonant low-intensity probe beam is almost entirely absorbed near the front of the cloud, leaving too little transmitted light to be reliably detected by the camera. Achieving quantitatively accurate imaging under these conditions

is nontrivial and usually requires techniques such as strong-saturation imaging [93, 94].

Since the primary purpose of absorption imaging in the MOT chamber is to optimize the preparation sequence, small systematic errors are acceptable. We therefore employ off-resonant absorption imaging to mitigate the large optical depth, by reducing the scattering cross-section according to Eq. (3.3). Typically, we use a detuning of $\Delta = 10\,\mathrm{MHz}$.

The reduction in scattering comes at the cost of introducing a nonzero real part of the refractive index [95]. The resulting dispersive phase shift causes the cloud to act as a weak lens, distorting the image. Lensing effects are strongest for clouds with sharp density gradients [95, 96]. In our case, the MOT typically has a comparatively large spatial extent (on the order of $\sim 1\,\mathrm{cm}$), which suppresses such distortions.

To cross-check that off-resonant imaging provides adequate precision for its purpose as an optimization tool, we compared off-resonantly determined atom numbers to resonant measurements of the MOT loading curve. We used fluorescence imaging to determine the full MOT loading curve, from which atom numbers at early loading times—measured with resonant absorption imaging—were extrapolated and compared to off-resonant absorption imaging measurements. These measurements were conducted together with Julia Gamper and the detailed results are presented in her master thesis [97]. The results revealed an approximately 8% lower extrapolated fluorescence-based atom number compared to the off-resonantly measured value. This discrepancy possibly arises from reabsorption effects in fluorescence imaging: At high atomic densities, emitted photons are reabsorbed within the cloud, reducing the fluorescence signal per atom and thus underestimating the true atom number. However, we cannot rule out that instead the off-resonant absorption imaging overestimate the atom number. Nevertheless, the atom-number accuracy is sufficient for optimizing the preparation sequence in the MOT chamber, as the optimization focuses on relative improvements.

This cross-check comparison between fluorescence imaging and off-resonant absorption imaging does not rule out lensing effects influencing time-of-flight measurements and hence affecting temperature measurements. However, as the cloud expands at larger TOF, the density decreases, making any possible lensing effects progressively weaker. Due to eddy current distortions from turning off the magnetic field (see below), we only fit TOF data after waiting for at least 5 ms. At that point, we do not observe deviations from the expected width scaling in Eq. (3.6) when releasing atoms from the MOT or after the molasses phase, which indicates that the influence of the lensing is negligible for our temperature measurements.

Image distortions due to eddy currents Sizable eddy currents are created in our experimental setup when the magnetic quadrupole trap is rapidly turned off from full strength, as is done for absorption imaging after magnetic trapping. This effect is present in both the MOT and the science chamber (more detail are given in Sections 3.5.6, 3.6.3.2 and 3.7.3). The slowly decaying magnetic field (decay time $\sim 20\,\mathrm{ms}$ in the MOT chamber and $\sim 15\,\mathrm{ms}$ in the science chamber) distorts the magnetic offset field the atoms experience. For absorption images, we apply constant bias fields optimized for a specific time of flight $t_{\mathrm{TOF}} = 10\,\mathrm{ms}$. The measurements for the bias field optimization were conducted together with Julia Gamper and are presented in her master thesis [97]. As a consequence of the decaying field, when performing time-of-flight measurements, the perceived atom number varies as a function of time, being lower at earlier and later times compared to $t_{\mathrm{TOF}} = 10\,\mathrm{ms}$.

The precision of the measured atom number, even at the optimized time, is reduced due to the decaying field. The reason is the unknown inhomogeneity of the decaying magnetic field. In the

experiment, we can apply only a constant homogeneous offset field. Therefore, we cannot fully compensate the residual decaying field for absorption imaging. As a result, the magnetic field direction is not properly aligned with the imaging beam over the whole cloud volume.

The decaying field also breaks the free-fall condition assumed for time-of-flight measurements. This effect might alter the expansion of the cloud in time compared to the expected behavior defined in Eq. (3.6). Consequently, the temperature fit can be distorted. In both the MOT and science chamber, the decaying magnetic potential shape is unknown but likely differs from the initial quadrupole field due to the asymmetric slicing in the coil mounts and cooling blocks (discussed later in Section 3.6.2). This results in an unpredictable distortion of the TOF measurements.

The distortions due to eddy currents are only relevant when imaging after magnetically trapping the atoms. Therefore, for most steps during atom preparation in the MOT chamber, this is not a problem. In the science chamber, however, these distortions are problematic for imaging. The mitigation strategy employed in the science chamber is discussed in Section 3.7.2.

3.5.2 MOT fluorescence imaging

Fluorescence imaging provides a complementary diagnostic to absorption imaging, enabling real-time non-destructive monitoring of the MOT loading. The light of the cooler laser during the MOT loading and the optical molasses excites the atoms repeatedly, resulting in a continuous fluorescence signal from the trapped atoms. The intensity of this signal is only approximately proportional to the number of atoms in the cloud and depends on the intensity and detuning of the cooler light (and the repumper light). Therefore, we use the fluorescence imaging mainly as a qualitative diagnostics tool. In our setup, fluorescence from the trapped ^{87}Rb atoms is collected through a dedicated viewport and imaged onto a camera[9] with an objective as shown in Fig. 3.5.

The main purpose of the fluorescence imaging is continuous surveillance of the MOT loading. Should the MOT loading be disrupted, for example because a laser fell out of its frequency or intensity lock or is running multimode, the fluorescence of the MOT will vanish or become unstable, indicating the failure.

Since the fluorescence imaging is continuous and non-destructive, it can be also be used for much more rapid diagnostics compared to absorption imaging, which can only be done at one time per experiment cycle. For example, we used fluorescence imaging for the initial optimization of the magnetic bias fields for the optical molasses phase, as explained in Section 3.5.4.

3.5.3 MOT loading

Magneto-optical trapping of ^{87}Rb is well established for more than three decades [75]. A MOT typically combines a magnetic quadrupole field with six counter-propagating, circularly polarized and red-detuned laser beams to simultaneously cool and confine neutral atoms. The physical mechanism is treated in detail in standard references [86, 98]. We briefly summarize the essentials relevant to this work in the following.

In our ^{87}Rb MOT, the cooling light addresses the transition $|5S_{1/2}, F = 2\rangle \leftrightarrow |5P_{3/2}, F = 3\rangle$. Red detuning ensures that an atom moving toward a beam sees the laser frequency Doppler-shifted closer to resonance, increasing the scattering rate and producing a velocity-damping (optical molasses) force in all three spatial directions. Superimposed on this, the magnetic quadrupole field produces a

[9] Unibrain Fire-i 530b camera with Computar MLH-10X macro/zoom objective

position-dependent Zeeman shift whose magnitude grows linearly with displacement from the field zero. The Zeeman shift renders the σ_+ atomic transitions closer to resonance (and σ_- further from resonance) for atoms displaced from the field center. Thus, with the appropriate choice of circular polarization, the laser beams create a net restoring force toward the field center. The combination of velocity damping and spatially selective scattering yields a trapped, cooled atomic cloud suitable as the starting point for further preparation stages. In ^{87}Rb there is a finite chance, that atoms are excited to the $|5P_{3/2}, F = 2\rangle$ state and decay to $|5S_{1/2}, F = 1\rangle$, thereby being lost from the cooling cycle. Therefore, a repumper laser driving the transition $|5S_{1/2}, F = 1\rangle \rightarrow |5P_{3/2}, F = 2\rangle$, is superimposed with all cooling beams.

The cooling and repumping light are each provided by a diode laser (see Section 3.8). Their outputs are overlapped and distributed into six MOT beam paths using two polarization maintaining fiber beam splitters: a $2 \rightarrow 4$ splitter[10] for the four horizontal beams and a $2 \rightarrow 2$ splitter feeding the two vertical beams. Both cooler and repumper powers are actively intensity-stabilized with acousto–optic modulators (AOMs) in single-pass configuration to suppress intensity drifts and fluctuations.

The maximum available powers per MOT beam are 95 mW for the cooler and 3 mW for the repumper. The $1/e^2$ beam diameter at the MOT position is 37.5 mm, chosen to enlarge the capture volume while remaining compatible with the viewport apertures and optical table geometry.

Five primary control parameters govern the MOT loading characteristics: cooler laser power, cooler detuning, repumper power, repumper detuning, and magnetic field gradient. Note, that the natural scale for the laser detunings here is the linewidth of the cooling transition $|5S_{1/2}, F = 2\rangle \leftrightarrow |5P_{3/2}, F = 3\rangle$ which is $\gamma_{5P_{3/2}} = 6.07\,\text{MHz}$ [91].

In the following we will present characterization measurements we performed to optimize the cold-atom-preparation in the MOT chamber. These measurements were conducted together with Julia Gamper and are also described in her master thesis [97].

The repumper should efficiently deplete population accumulating in $|5S_{1/2}, F = 1\rangle$, yet its intensity should be well below the cooler intensity so that its scattering contribution remains minor. Due to the intrinsically lower power of the rempumper laser in our system, it is sufficient, to operate the repumper on resonance and at the maximum available power. A corresponding measurement demonstrating that repumping on resonance is optimal in our experiment is presented in the master thesis of Julia Gamper [97].

Increasing the cooler power raises the photon scattering rate and thus the MOT loading rate, but also tends to increase the equilibrium temperature. Two-dimensional scans of cooler and repumper power within the available range, shown in Fig. 3.6(a), confirm that the atom number is maximized at the highest accessible powers for both. For the maximum laser powers, the temperature of the cloud was measured using the time-of-flight technique discussed in Section 3.4 to be around 370 µK. While this temperature is quite high, this is unproblematic, because the cloud is cooled down in the subsequent optical molasses stage (see Section 3.5.4). Therefore, we accept the higher temperature in the MOT phase and use the highest laser power settings for the highest atom number.

The interplay between cooler detuning and magnetic field gradient determines the effective trapping volume: The trapping volume approximately extends up to where the Zeeman shift compensates the red detuning. If the detuning is too large, the radiative force may be insufficient to capture and slow thermal atoms. If the detuning is too small, the trapping volume decreases, potentially limiting the atom number. Similarly, a gradient that is too weak yields poor spatial confinement and

[10] Evanescent Optics Inc. Model 954P Coupler

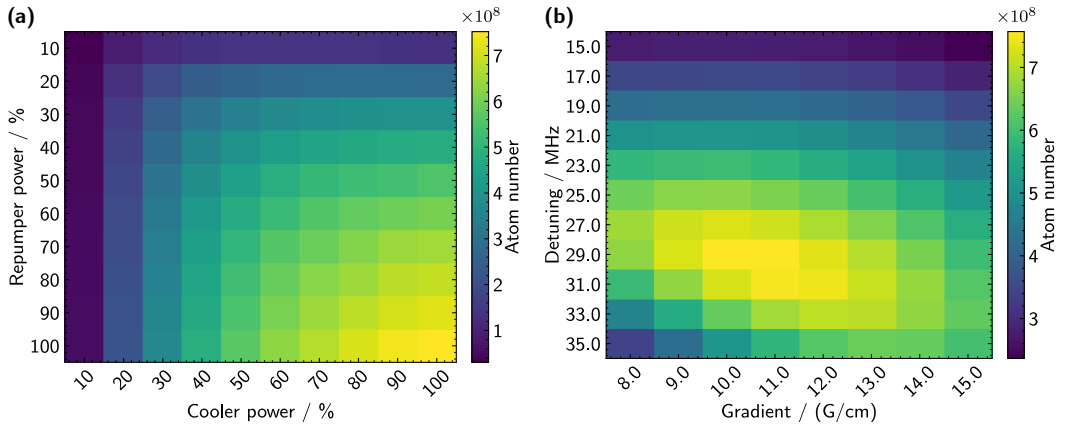

Figure 3.6: Atom number after 1 s MOT loading measured with off-resonant absorption imaging ($\Delta = 5\,\mathrm{MHz}$). **(a):** Cooler and repumper laser power scans. Here, the cooler detuning was 24 MHz and the repumper was on resonance. The MOT coil magnetic field gradient was $10.5\,\mathrm{G\,cm^{-1}}$. **(b):** Cooler detuning and MOT magnetic gradient scans. Here, the cooler and repumper power were set to 100% of the available power. Detuning values are relative to the unshifted transition. The data this figure are also presented in Ref. [97].

reduced density, while an excessively strong gradient compresses the cloud into a small volume where light-assisted collisions limit attainable density and thus total atom number.

The two-dimensional scan over cooler detuning and magnetic field gradient shown in Fig. 3.6(b) reveal a broad optimum at a quadrupole gradient (axial) of about $10.5\,\mathrm{G\,cm^{-1}}$ and a cooler detuning of about 29 MHz (relative to the unshifted $|5S_{1/2}, F = 2\rangle \rightarrow |5P_{3/2}, F = 3\rangle$ transition). We therefore, operate the MOT at these values.

3.5.4 Optical Molasses

The second step in atom preparation is the optical molasses phase, which is employed to reduce the temperature of the atomic cloud. To transition from MOT loading to optical molasses, the magnetic quadrupole field is rapidly switched off and the cooler laser is detuned further to the red. As a result, the atoms are no longer spatially trapped but still experience optical cooling forces. For an ordinary atomic transition, the fundamental temperature limit reachable with optical molasses is the Doppler limit [86] $T_D = \frac{\hbar\Gamma}{2k_\mathrm{B}}$ (146 µK for rubidium). However, due to the hyperfine splitting of the levels in rubidium, the optical molasses also performs polarization gradient cooling, which enables cooling below the Doppler limit. Here the reachable temperature scales as [99]

$$T \propto \frac{I}{|\Delta|}, \tag{3.7}$$

where I is the intensity of the cooler laser and Δ its detuning. This highlights that lower laser power and higher detuning are beneficial for the cooling process. A concise explanation of the working principle of polarization gradient cooling can be found in Refs. [98, 99].

A technical challenge for optical molasses is the influence of residual magnetic fields, for example those caused by eddy currents from the switched-off MOT coils. These fields, together with the optical molasses beams, produce a force similar to that in the MOT, but pointing in an unpredictable

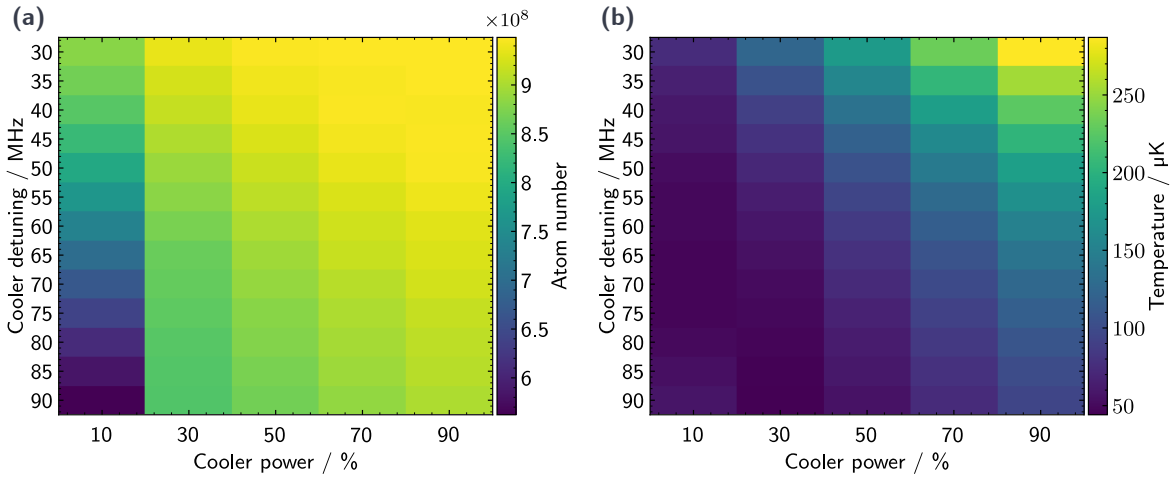

Figure 3.7: Time of flight measurement results after a 10 ms molasses phase showing the atom number **(a)** and temperatures **(b)** dependence on the cooler laser detuning (relative to the unshifted cooling transition) and power during the molasses phase. Before the molasses phase, the MOT was loaded for 1 s according to the description in Section 3.5.3. The data in this figure are also presented in Ref. [97].

direction that can accelerate the atoms away from the trap center. In our experiment sequence, the optical molasses phase lasts only 5 ms. Extending this time to ~ 1 s and observing the fluorescence of the atomic cloud during its slowed expansion in the optical molasses provides quick visual feedback about the movement of the atom cloud. Using this feedback, the magnetic bias fields can be adjusted to compensate the residual magnetic fields. Since our absorption imaging is in a different plane compared to the fluorescence imaging, the final fine adjustment of all three axes is performed using both imaging systems.

For the optical molasses in our setup, we tried out to instantaneously switch the cooler power and detuning at the beginning or to linearly ramp them. We found that the switching results in a better performance which is why we adopted it. From Eq. (3.7) we would expect that going to higher detuning and lower power is optimal for the molasses, but in practice, the reduced velocity capture range and the associated atom loss also needs to be considered. We measured the dependence of atom number and temperature on both parameters for a fixed duration of 10 ms. The results are shown in Fig. 3.7(a, b).

We chose a detuning of $\Delta = 90$ MHz and a cooler power of 50% of the available power as a tradeoff between temperature and atom number. For these settings, the atom cloud temperature is cooled to around 56 µK at the cost of loosing about 10 % of the atoms. With these settings, we found that we can reduce the molasses duration down to 5 ms, without affecting the atom number or temperature. We adopt this shorter duration in the cold atom preparation sequence, because longer durations result in an unwanted expansion of the cloud.

3.5.5 State preparation using optical pumping

After optical molasses, where no magnetic field is applied, the atoms occupy the ground state $|5S_{1/2}, F = 2\rangle$ but are randomly distributed over the different m_F states. Optical pumping is therefore required to transfer the atoms to a low-field-seeking state for the subsequent magnetic trap and

transport (see Section 3.3). For ^{87}Rb, this requires populating the states $|5S_{1/2}, F = 2, m_F = +1\rangle$ or $|5S_{1/2}, F = 2, m_F = +2\rangle$. Optical pumping is also beneficial for absorption imaging, as explained in Section 3.4, where the atom population should be transferred to the state $|5S_{1/2}, F = 2, m_F = 2\rangle$ prior to imaging.

A general description of optical pumping is for example given in Ref. [100]. In the following, we outline our implementation of optical pumping to the state $|5S_{1/2}, F = 2, m_F = 2\rangle$, which is suitable for magnetic trapping and imaging.

As sketched in Fig. 3.5(a), we apply the optical pumping beam along the same beam path through the MOT chamber as the absorption imaging beam. During optical pumping, a magnetic offset field is applied along the beam axis to define the quantization axis. The optical pumping laser beam is circularly polarized and drives the σ^+ transition $|5S_{1/2}, F = 2\rangle \leftrightarrow |5P_{3/2}, F = 2\rangle$. Repeated absorption–emission cycles increase the m_F quantum number on average. Once the atoms reach the dark state $|5S_{1/2}, F = 2, m_F = +2\rangle$, they no longer absorb photons from the σ^+ beam and the optical pumping cycle terminates. A repumper beam is overlapped with the optical pumping beam to drive the $|5S_{1/2}, F = 1\rangle \leftrightarrow |5P_{3/2}, F = 2\rangle$ transition, which recycles any atoms that have decayed to the $F = 1$ manifold back into the pumping cycle. Optical pumping to the dark state requires on the order of 10 absorption–emission cycles. The cycle rate is limited by half the natural decay rate [101] ($\sim 3\,\mathrm{MHz}$), making the total process fast compared to the cooling steps before. In our experiment, optical pumping is completed within $20\,\mu\mathrm{s}$, the time resolution of the experiment control system.

To find suitable power and frequency (detuning) settings for the optical pumping laser for a given magnetic quantization field of 2 G, we image the atomic cloud not only on the standard $|5S_{1/2}, F = 2\rangle \leftrightarrow |5P_{3/2}, F = 3\rangle$ transition but also on the $|5S_{1/2}, F = 2\rangle \leftrightarrow |5P_{3/2}, F = 2\rangle$ transition[11]. Optical pumping increases the perceived atom number for our standard imaging owing to the enhanced cross-section on the cycling transition compared to other transitions. By contrast, for imaging on the $|5S_{1/2}, F = 2\rangle \leftrightarrow |5P_{3/2}, F = 2\rangle$ transition, the optically pumped state $|5S_{1/2}, F = 2, m_F = 2\rangle$ is a dark state that is not addressed, resulting in a vanishing perceived atom number.

The results of a two-dimensional scan over detuning (relative to the unshifted transition) and power, imaged on both transitions, are shown in Fig. 3.8(a, b). We find that the atom number with standard imaging, displayed in Fig. 3.8(a), saturates for an optical pump power settings above 50%, and that the resonance is centered around a detuning of $\sim 2\,\mathrm{MHz}$. As expected, for imaging on the $|5S_{1/2}, F = 2\rangle \leftrightarrow |5P_{3/2}, F = 2\rangle$ transition, shown in Fig. 3.8(b), the results are inverted. However, the perceived atom number does not completely vanish, even at higher powers. This indicates imperfect optical pumping. The likely cause is an imperfect alignment of the magnetic field axis to the beam, or an imperfect polarization of the optical pumping beam. For the measurements presented in Fig. 3.8(b), the magnetic bias fields were already optimized along all three axes to minimize the perceived atom number. We assume that decaying magnetic fields, caused by eddy currents from the MOT coil switch-off, produce a spatially varying magnetic field across the cloud volume, preventing the magnetic field from being uniform for all atoms. Measurements of the magnetic field response to the coil switch-off revealed decay times of approximately 20 ms (see Section 3.6.3.2). The coils are switched off at the beginning of the optical molasses phase, which lasts only 5 ms. Therefore, we assume that the decaying magnetic field influences the optical pumping. Longer waiting times between the molasses phase and optical pumping phase or an extended molasses phase could mitigate this effect, but the cloud would expand during that time. It was ultimately found that for loading into the magnetic

[11] The imaging beams drive σ_+ transitions in both cases.

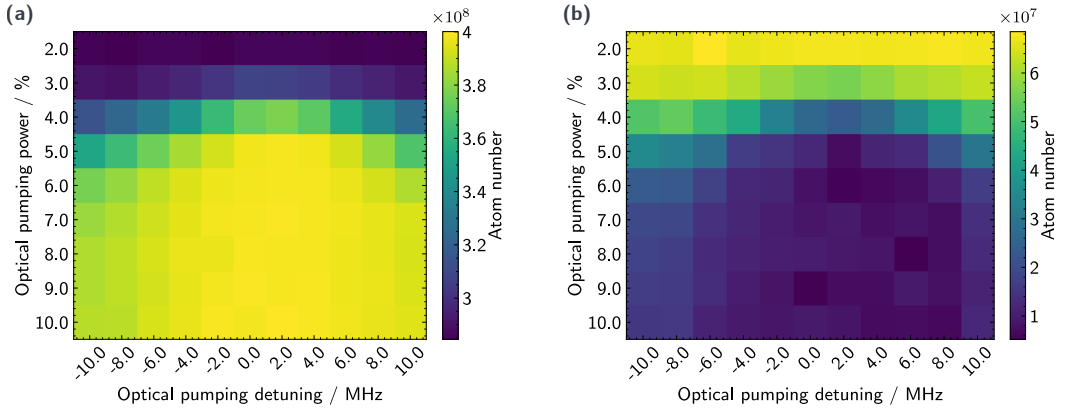

Figure 3.8: Absorption imaging measurements in the MOT chamber after optical pumping for scanned optical pump beam detuning and power. **(a):** Absorption imaging on the $|5S_{1/2}, F = 2\rangle \rightarrow |5P_{3/2}, F = 3\rangle$ (cycling) transition. **(b):** Imaging on the $|5S_{1/2}, F = 2\rangle \rightarrow |5P_{3/2}, F = 2\rangle$ transitions. The displayed absolute atom numbers in (b) are not calibrated. The vanishing perceived atom number indicates the transfer of atoms into the dark state. The MOT loading and optical molasses phases before the optical pumping step are described in Sections 3.5.3 and 3.5.4. Detuning values are relative to the unshifted transition. The data in this figure are also presented in Ref. [97].

trap, the partially imperfect optical pumping is sufficient, and longer molasses or waiting times reduce the overall transfer efficiency.

3.5.6 Magnetic trap in the MOT chamber

The final step of the cold-atom preparation in the MOT chamber is the transfer of the atom cloud to a magnetic trap, which also marks the beginning of the magnetic transport.

An efficient transfer of the loaded atom cloud from the MOT to the magnetic trap with minimal heating requires good spatial overlap and a fast rise time of the magnetic field compared to the acceleration of the atoms due to gravity. Specifically, the atom cloud should not acquire sizable momentum or fall a significant distance compared to its size before the magnetic trap is strong enough to confine the atoms.

In our setup, the relatively long rise time of the magnetic field, when ramping up the coil current, of approximately 15 ms (see Section 3.6.3.2) severely limits the transfer efficiency to the magnetic trap. Assuming free fall for the rise time of 15 ms, the atom cloud would fall by approximately 1 mm and acquire a velocity of approximately $150\,\mathrm{mm\,s^{-1}}$. This velocity exceeds the most probable atom velocity of $90\,\mathrm{mm\,s^{-1}}$ at a temperature of approximately 50 µK after the molasses.

To investigate the behavior of the falling atom cloud during the transfer to the magnetic trap, we scan the magnetic-trap holding time t_{hold} (the time between the turning on and turning off of the magnetic trap) and use absorption images to determine the position of the atomic cloud center. The results of this measurement are shown in Fig. 3.9. In the z-direction, the atomic cloud falls initially before being propelled back after approximately 15 ms, consistent with the time required for the trap to reach full strength. The initial and final positions of the cloud differ because a bias field was applied in the z-direction to shift the magnetic trap relative to the MOT position. Although this offset partially compensates for the gravitational fall, the sloshing is only slightly reduced, because the cloud retains

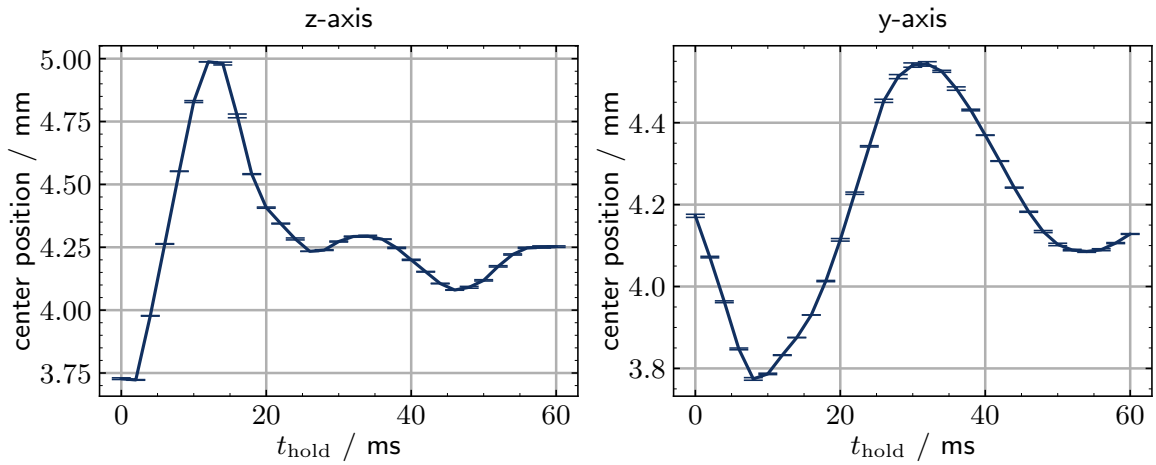

Figure 3.9: Center position of the atomic cloud along the z and y-axis measured with absorption imaging for varied magnetic trap holding times. The center positions are determined via Gaussian fits and by converting camera pixel positions to millimeters via the pixel size and image magnification. Because the image on the camera is inverted, a higher z value here corresponds to a lower position in the imaging plane. The MOT loading, optical molasses and optical pumping before the magnetic trap is engaged, are described in Sections 3.5.3 to 3.5.5. The data in this figure are also presented in [97].

its downward momentum from the initial fall.

Interestingly, sloshing is also observed in the y-direction. Here, the final and initial positions are the same, indicating that eddy currents from the current switching produce a time-dependent deformation of the magnetic trap that shifts the minimum position.

The sloshing affects the cloud temperature when the added kinetic energy is redistributed by atomic collisions and converted to thermal energy. To quantify this impact, we hold the atom cloud for 500 ms in the magnetic trap and then perform TOF measurements. The results are shown in Fig. 3.10. In the first panel, the atom number as a function of the time of flight t_{TOF} is presented. The atom number should be independ on that time. Nevertheless, a strong dependence is observed. The cause are image distortions due to the decaying magnetic field. We have optimized the bias field to compensate the decaying magnetic field as good as possible for $t_{\mathrm{TOF}} = 10\,\mathrm{ms}$. As discussed in Section 3.5.1, we still expect a field inhomogeneity that distorts the image, but the value at $t_{\mathrm{TOF}} = 10\,\mathrm{ms}$, 1×10^9 atoms, is the best estimate of the real atom number. The atom transfer efficiency to the magnetic trap is almost 100%, mainly limited by the lifetime of the magnetic trap that we discuss below.

In the other two panels in Fig. 3.10, the cloud width as a function of t_{TOF} is depicted together with the corresponding temperature fit. We observe a strong increase in the fitted temperature compared to after the molasses phase (56 µK) to 217 µK in the y-direction and 361 µK in the z-direction. The reason for the increased temperature is the sloshing of the atomic cloud in the magnetic trap.

The fact that the fitted expansion curves yield significantly different temperature values along the two axes indicates that the cloud is not fully thermalized at the time of release after 500 ms. In the absence of full thermalization, a unique thermodynamic temperature of the atomic cloud is not well-defined. Nevertheless, the temperature that would be obtained after complete thermalization is expected to lie between the two reconstructed values.

The observed center motion shown in Fig. 3.9 seems to decay within ~ 60 ms. This fast decay of the

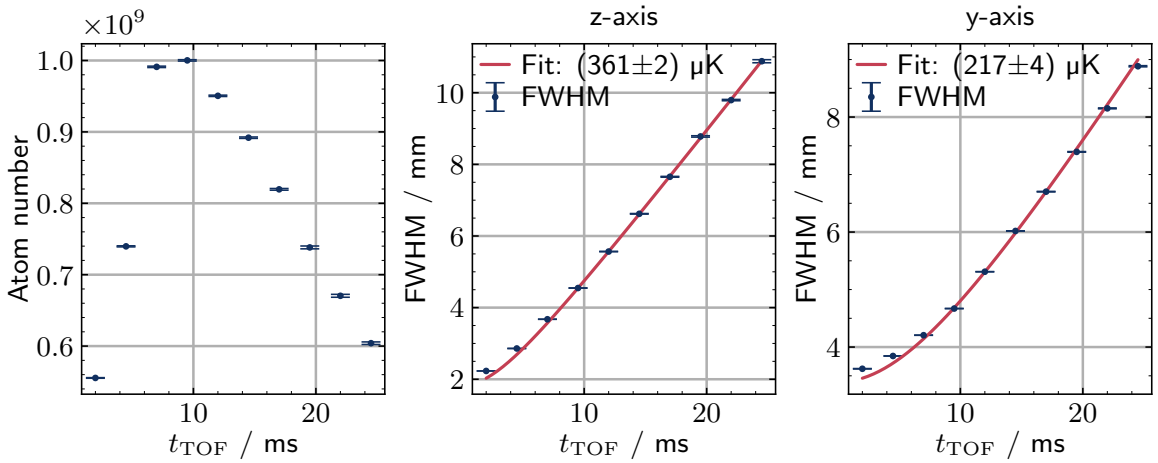

Figure 3.10: Time of flight measurement results after a magnetic trap holding time of 500 ms showing the ballistic expansion of the cloud width and the measured atom number as a function of the fall time. The MOT loading, optical molasses and optical pumping before the magnetic trap is engaged are described in Sections 3.5.3 to 3.5.5

collective motion is due to the fact that no singular trapping frequency exists in the linear quadrupole trap. In particular, the initially collective motion of all atoms washes out not only due to collisions but also because individual atoms oscillate at different frequencies in the trap. This also explains why the apparent temperature in the z-direction is larger than in the y-direction: The initially larger collective velocity in the z-direction results in a broader velocity distribution along that axis.

These measurements demonstrate that the slow rise time of the magnetic field during the handover to the magnetic trap is limiting the achievable temperature of the atom cloud at that stage. We have tried to improve the handover by compressing the MOT before the molasses phase to improve the trap volume overlap. This was unsuccessful, because the sloshing of the cloud in the magnetic trap is not caused by poor trap volume overlap but mainly by the acceleration due to gravity before the magnetic trap reaches sufficient strength together with the induced eddy currents deforming the trap when it is turned on.

One way to speed up the magnetic trap rise time is to utilize a different power supply with higher voltage output. An alternative approach is presented in Ref. [102], where a switching circuit employing capacitors charged at high voltage is used. In this scheme, a high-voltage and low-current supply charges capacitors, which can then provide high current at high voltage for short periods. Such a circuit could significantly reduce the rise time in future implementations. However, faster switching will also produce stronger eddy currents. To mitigate the eddy currents, the copper cooling blocks and mount of the MOT coils (see Section 3.6.2) could be exchanged for lower conductive material.

Nevertheless, an atom number of about 1×10^9 atoms at a temperature of around 300 μK are an acceptable starting condition for the magnetic transport to the science chamber.

Lifetime of the atom cloud in the magnetic trap The lifetime of the magnetic trap in the MOT chamber is limited by collisions with the background gas and therefore serves as a diagnostic for the background pressure in the MOT chamber [81, 82]. An exemplary measurement of the atom number as a function of the holding time is shown Fig. 3.11. We fit an exponential decay

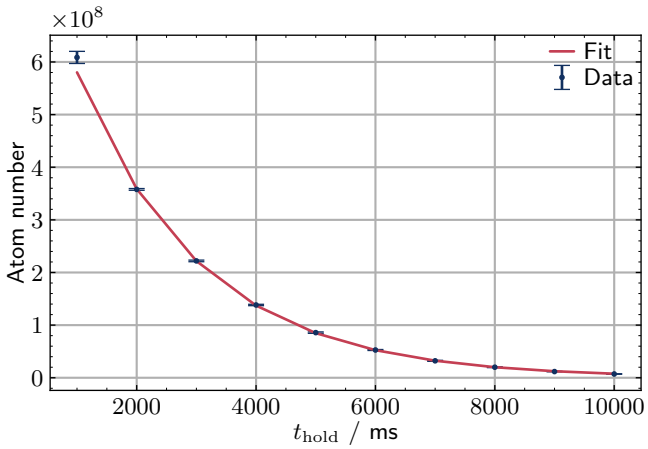

Figure 3.11: Atom number as a function of the holding time in the magnetic trap in the MOT chamber, together with an exponential fit yielding a decay constant of $\tau_{\mathrm{MT}}^{\mathrm{MOT}} = (2.10 \pm 0.01)\,\mathrm{s}$. The MOT loading, optical molasses, and optical pumping steps preceding magnetic trapping are described in Sections 3.5.3 to 3.5.5.

$N(t) = N(0)\exp(-t/\tau_{\mathrm{MT}}^{\mathrm{MOT}})$ to the data and find a lifetime of $\tau_{\mathrm{MT}}^{\mathrm{MOT}} = (2.10 \pm 0.01)\,\mathrm{s}$, consistent with pressures around 1×10^{-9} mbar. A precise absolute pressure estimate is not possible due to the unknown background gas mixture [81, 82], however the lifetime provides a measure for relative pressure changes. This is useful to monitor the pressure in the MOT chamber, because the reading from the ion pump in the MOT chamber—the only other pressure reading available—is not reliable and can drift over time.

3.6 Magnetic transport

The decision to spatially separate the MOT loading from the science region requires the ability to move the atoms after loading. Transport of trapped ultracold atom clouds is usually realized using either a moving optical [103–106] or magnetic trap [107, 108].

We decided to implement a magnetic transport in our setup due to the risk of heating the cryogenic environment with the high-power laser required for an optical trap. We discuss this further in Appendix A. A magnetic transport circumvents the risk of heating the cryogenic environment. Additionally, magnetic traps offer deeper potentials compared to typical optical traps and can therefore trap larger atom numbers. Two different approaches for magnetic transport exist: moving the coils that create the trapping magnetic field [107, 109] or using a series of overlapping stationary coils with time-dependent currents to shift the magnetic field minimum [108]. We chose the latter approach to avoid mechanical moving parts, which can introduce vibrations.

In the following, we explain the working principle of magnetic transport, the design and construction of our system, simulations of the transport dynamics, the electronics implementation, and present characterization measurements.

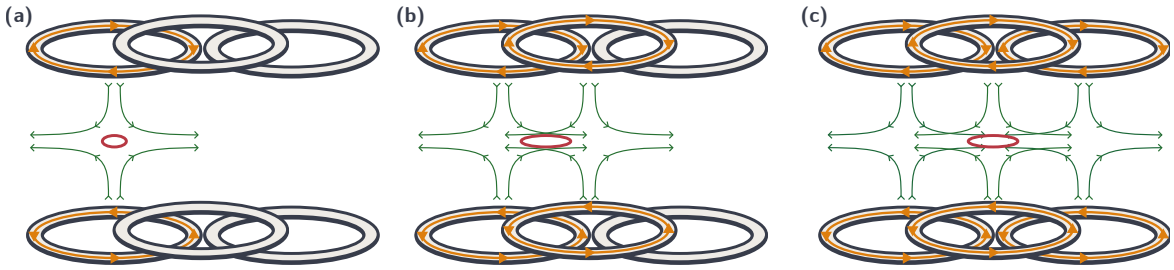

Figure 3.12: Illustration of the principle behind magnetic transport using overlapping anti-Helmholtz coil pairs. Orange lines indicate current flow, green lines show magnetic field lines, and the red line marks a magnetic equipotential corresponding to the spatial extent of a trapped atom cloud. **(a):** Current applied only to the first coil pair creates a magnetic quadrupole trap at its center. **(b):** Gradually applying current to the second coil pair while adjusting the first shifts the trap position but elongates the trap. **(c):** All three coil pairs are energized with the trap forming at the center coil. By carefully tuning the currents, the trap shape can be matched to the configuration in (b). This approach can be used to move the magnetic field minimum—and hence the trapped atom cloud—along the transport axis while maintaining a constant (elongated) trapping potential.

3.6.1 Working principle

Magnetic transport of ultra-cold atoms, as implemented in our setup, was first proposed and realized by Greiner et al. in Ref. [108] as a method to move the atoms from a magneto-optical trap to a spacially separate science region.

The basic principle of the magnetic transport involves creating a moving magnetic potential minimum that can trap and carry the atoms along a predefined path. The trapping magnetic field is generated by current carrying coil pairs arranged in anti-Helmholtz configuration. Such a coil pair creates a quadrupole magnetic field with a zero at its center.

To produce a moving trap we adjust the currents in a series of partially overlapping stationary coils to shift the position of the field minimum. A sketch of the principle is shown in Fig. 3.12. If current is applied to only one coil pair, a quadrupole field with a zero at the center of the coil pair is created. By gradually ramping down the current in this coil pair while simultaneously ramping up the current in the next coil pair, the position of the magnetic field minimum can be shifted towards the center of the second coil pair. Repeating this process with a series of overlapping coil pairs allows for continuous transport of the atoms over large distances.

However, simply using two coil pairs to move the field minimum results in varying field gradients during the transport. This can lead to changes in the trapping potential and possible heating or loss of atoms. To maintain a constant trapping potential, a third coil pair is used. By carefully adjusting the currents in all three coil pairs, the position of the magnetic field minimum can be smoothly moved while keeping the field gradients in all directions constant. Specifically, a magnetic field of the form [110]

$$\boldsymbol{B}(x,y,z) \approx B' \cdot \begin{pmatrix} -\frac{1}{1+\alpha}\, x \\ -\frac{\alpha}{1+\alpha}\, y \\ z \end{pmatrix}, \tag{3.8}$$

can be maintained throughout the transport. Here, B' is the gradient in z-direction and α is the ratio of the magnetic field gradient along the transport direction (y) and perpendicular (x) to it. Due to the overlapping coil geometry, the gradient in transport direction is always the weakest ($\alpha < 1$).

3.6.2 Design and construction

The design of the magnetic transport system was driven by the following considerations and constraints:

- **Magnetic field strength:** A target gradient of at least $130\,\mathrm{G\,cm^{-1}}$ in the axial direction was chosen according to the gradient used by Greiner et al. [108].
- **Current limitations:** The target gradient should be achievable with a maximum current of 100 A per coil pair. Furthermore, the design should only require unidirectional current flow through the coils. This simplifies the coil switching electronics and avoids the need for specialized hardware to handle very high currents.
- **Coil position and geometry**: The coils should be positioned as close as possible to the atomic cloud to achieve the highest possible field gradient for the lowest possible current. In particular, the field gradient scales with the cube of the inverse distance between the atoms and the coils, making this a critical design consideration. The coil geometry must also ensure that the magnetic field maintains a linear gradient over a sufficiently large volume around the trap center, while accommodating the spatial constraints imposed by the vacuum chambers. Improper coil overlap or sizing can cause deviations from the ideal quadrupole field even at small distances ($\sim 1\,\mathrm{cm}$) from the trap center, limiting the effective trapping region.
- **Thermal management and safety:** The heat generated during the transport operation necessitates active cooling. The coils need a good thermal connection to the cooling structure. For safety, overheating must be prevented through an interlock system that shuts down the current supplies in case of a fault.
- **Optical access:** The coils and cooling structures must not obstruct the optical access needed for laser cooling and trapping in the MOT chamber as well as for imaging and Rydberg excitation in the science chamber.
- **Modularity:** The setup should be modular to allow for easy assembly, disassembly, and maintenance of the coils and water cooling.

We used simulations of the magnetic transport (see Section 3.6.4) to determine an appropriate modular coil geometry that fulfills the above-mentioned requirements while minimizing the expected thermal load. The final transport design consists of seven overlapping coil pairs as shown in Fig. 3.13(a). The upper and lower parts of the transport geometry are mirrored. The total magnetic transport length amounts to 450 mm.

Each transport coil consists of two axially stacked coils with 2×32 windings made from rectangular enameled copper wire with a 1.4 mm by 0.8 mm cross-section and an air core. A photograph of a transport coil is shown in Fig. 3.13(b). Three different coil geometries are employed along the transport axis to fulfill the magnetic field gradient requirements while adhering to the physical constraints of the setup and the current limitations. Here, the biggest constraint is the 86 mm height of the science chamber (see Section 3.7.1 for a discussion of the height constraints). The coil geometries are designed such that the magnetic field gradients remain approximately linear up to a distance of at least 5 cm from the field center in transport direction. Their dimensions are summarized in Table 3.2. The sixth coil pair consists of two coils stacked on top of each other to compensate for the increased distance to

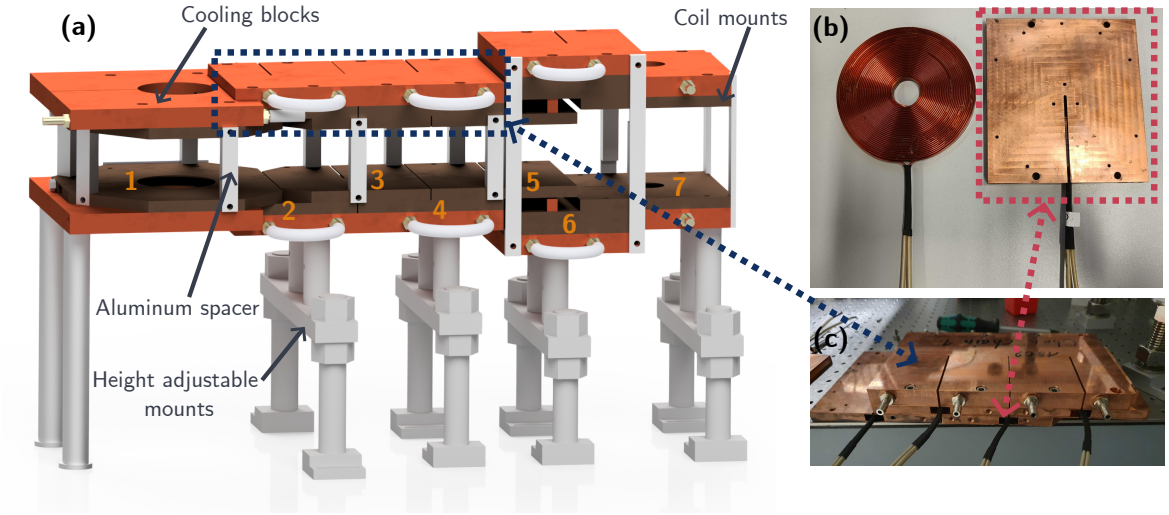

Figure 3.13: **(a):** Rendering of the magnetic transport setup showing seven coil pairs in modular copper coil mounts (brown) and copper cooling plates (orange) screwed to the coil mounts for water cooling. Aluminum spacers separate the upper and lower parts of the transport coils and cooling blocks. The coil pairs are numbered 1–7. **(b):** Photograph of a bare coil and a coil glued into its copper mount. **(c):** Photograph of one of the cooling blocks screwed to the corresponding coil mounts (photograph taken during assembly of the transport). Matching parts between (a), (b), and (c) are marked.

Table 3.2: Dimensions of the three different coil geometries used in the magnetic transport. Coil pairs are counted from start to end.

Coil pair	Inner diameter / mm	Outer diameter / mm
1 (MOT coil)	74.0	172.9
2-5, 7	32.0	130.7
6	25	123.7

the atoms, which arises because the science chamber begins at the position of this coil pair along the transport axis.

For optical access, the magnetic transport coil mounts and the cooling plates above and below the science and MOT chamber include openings that do not obstruct the coil air cores. For the coil pair at the science chamber, we chose an inner free diameter of 32 mm, which is large enough to accommodate a standard 1 inch lens tube. To place the MOT coils as close as possible to the commercial MOT chamber octagon with DN40 viewports, an inner free diameter of 74 mm was necessary. Consequently, the MOT coil has a larger diameter than the rest of the coils.

The coils are glued into modular copper mounts using thermally conductive epoxy[12], as shown in Fig. 3.13(b). The coil mounts are then screwed onto copper cooling plates, as shown in Fig. 3.13(c). Four different cooling plates are used: one for the MOT coil, a shared plate for coils two to five, and individual plates for coil pairs six and seven, respectively. All mounts and cooling plates are sliced to reduce eddy currents during fast switching of the coil currents.

[12] Loctite Stycast 2850; CAT 24VL

Heat-conducting paste is applied between the coil mounts and the cooling plates to improve thermal contact and maximize heat transfer. The cooling plates have holes drilled into them through which cooling water is circulated. The plates are connected in parallel to a closed-loop water cooling system with a commercial water chiller[13] that maintains a constant water temperature of approximately 17 °C and a flow of 8 L min^{-1}. Manual valves are used to control the flow through the individual cooling plates.

During typical operation, the magnetic transport dissipates around 0.5 kW due to Joule heating. For temperature monitoring, dedicated PT100 temperature sensors are screwed into every coil mount. Details regarding the monitoring electronics are presented in Section 3.6.3.3. The different coil mounts have a temperature deviation of up to 2 °C because the inward-facing coils receive less cooling than the outer ones. This temperature deviation is not problematic, as it remains stable over time. However, on timescales shorter than the transport duration (1.5 s), temperature variations of up to 0.3 °C can be observed at the surface of the coil mounts. These are caused by the pulsed operation of the coils and cannot be fully eliminated. Nevertheless, we measured that the air temperature fluctuations near optical elements in the vicinity of the coils are consistent with the general temperature changes on the optical table, indicating that the magnetic transport system itself has negligible influence on the surrounding optics. During continuous operation over the span of weeks, overall temperature drifts remain below these short term fluctuations.

3.6.2.1 Alignment procedure

Here, we briefly outline the alignment procedure for the magnetic transport system. Additional details can be found in the master thesis of Johanna Popp [111], who assisted with the assembly and alignment of the setup.

The main challenge for the alignment is the presence of the differential pumping tube between the MOT and science chambers. The tube, with an inner diameter of 4 mm and a length of 105.3 mm, is welded into a DN16 flange that connects to the MOT chamber. These dimensions restrict the acceptance angle to less than 2°.

To check the alignment of the tube with the transport axis, we used a green laser directed along the transport path and observed the transmission profile with a camera. It quickly became apparent that the tube was welded into the flange at a slight angle, preventing the alignment beam from passing straight through. To compensate for this tilt, we tightened the flange asymmetrically. This adjustment partially corrected the misalignment. We further improved the acceptance angle by slightly adjusting the position and tilt of the MOT chamber. Although it was not possible to fully compensate for the tube's tilt, we achieved an effective acceptance diameter of approximately 3 mm (out of 4 mm).

Afterward, the magnetic transport coil positions were optimized using feedback from absorption imaging in the science chamber. We iteratively altered the coil positions and heights while optimizing the transported atom number.

3.6.3 Magnetic transport electronics

The magnetic transport requires specialized electronics to supply the high currents needed for the coils, switch the currents between different coil pairs, and monitor the temperature of the coils to prevent overheating. At any given time, only three coil pairs are energized, such that three power

[13] Termotek P307-18809-1

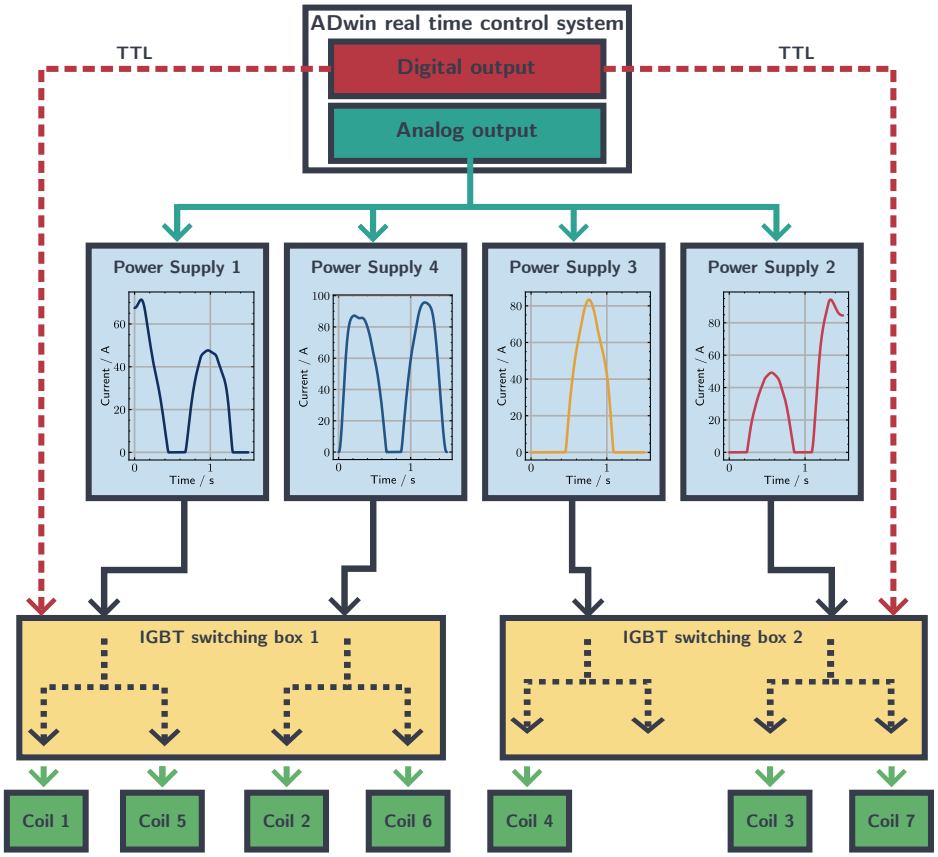

Figure 3.14: Schematic of the magnetic transport electronics. Four power supplies provide current for the magnetic transport. Two insulated-gate bipolar transistor (IGBT) based switching boxes guide the currents to the appropriate coil pairs. The central real time control system ADwin controls all timings and provides the control voltages for the power supplies.

supplies are in principle sufficient to operate the transport. However, this would require instantaneous switching of the power supplies between different coil pairs, which is impractical. Instead, we chose to use four power supplies, allowing for a smooth switching scheme where one power supply can be switched between two coil pairs while it is not in use.

A schematic overview of the control electronics setup is shown in Fig. 3.14. At the heart of the control electronics is the commercial real time control system ADwin that outputs programmed analog traces and digital TTL signals with 20 µs time resolution. The analog voltage output is fed to the analog control input of the programmable current supply units (see Section 3.6.3.1). The high current output is then connected to the appropriate coil via coil switching boxes described in Section 3.6.3.2. The coil switching is controlled via the digital TTL signals from the ADwin that turn the connection to the associated coil on or off.

3.6.3.1 Power supplies

As power supplies we chose the commercially available Delta Elektronika SM15-100 P218 and SM66-AR-110, which provide up to 100 A at 15 V and 30 V respectively (the sixth coil pair requires

larger voltages due to the double stacked coils). These supplies provide a low noise level of less than 15 mA_{rms} and fast analog programming with rise and fall times below 7 ms (10 % ↔ 90 % of the maximum current output). A low noise level is important to prevent fluctuations in the magnetic trap that could heat the atom cloud during the transport.

The power supplies have an interlock that only enables the current output if two specific pins are shorted. We use this feature to turn off the power supplies when the coils overheat. The corresponding interlock circuit we implemented is described in Section 3.6.3.3.

3.6.3.2 Coil switching

The coil switching electronics are based on insulated-gate bipolar transistors[14] (IGBTs), which can handle the high currents required for the transport coils while providing rise and fall times below 100 ns. Two coil pairs are always connected to the same power supply (except for coil pair 4 as illustrated in Fig. 3.14), each via a dedicated IGBT, allowing the current to be routed to the desired coil pair according to the programmed sequence.

The IGBT modules are housed within a custom electronics box built by the electronics workshop of our institute. The box features dedicated driver cards and active temperature control for the IGBT modules to prevent overheating and ensure stable operation. Two of these IGBT boxes, each with four IGBT modules, are used for the magnetic transport.

As discussed in Sections 3.5.1 and 3.5.3 to 3.5.5, the magnetic fields of the MOT coil pair have to be rapidly switched off during absorption imaging, optical molasses, and optical pumping in the MOT chamber. The same applies to coil pair 7 for absorption imaging in the science chamber. In particular, time-of-flight measurements of the atomic cloud require the trapping magnetic field coils to be turned off rapidly to avoid disturbing the free fall. This fast switching capability is provided by the IGBT modules. However, the stored magnetic energy in the coils must be dissipated. When switching off a coil while high currents are running through it, a high voltage spike is generated across the coil terminals. Unavoidable parasitic capacitive coupling to the environment results in crosstalk with other lab equipment. Moreover, the voltage spike can reach several kV, which can potentially damage electronics and is dangerous for humans.

To safely dissipate the energy stored in the coil, we added a coil-switch-off circuit to the two IGBT modules that are connected to the MOT and science chamber coil pairs (coil pairs 1 and 7). A schematic of the circuit is depicted in Fig. 3.15(a). A bypass capacitor is added in parallel to the IGBT module to prevent buildup of the large voltage spike when turning off the coil. The bypass instead allows the current to continue flowing to ground. The capacitor by itself does not dissipate the energy in the coils. Therefore, a power resistor is placed in parallel with the coils, forming a closed loop for energy dissipation. An integrated diode in the IGBT module prevents current flow via the power resistor when the coil is turned on.

A simplified simulation of the circuit that treats the IGBT as an ideal switch was used to estimate appropriate parameters for the power resistor and bypass capacitor. For the simulation, we estimate the inductance of the coils from their geometries to be around 0.3 mH (MOT) and 0.2 mH (science chamber) [112], and the resistance was measured to be 80 mΩ (MOT) and 54 mΩ (science chamber).

We chose a 1 µF bypass capacitor[15] and a 2 Ω power resistor[16]. Such a large capacitance, capable of

[14] IGBT-Module FD150R12RT4

[15] WIMA MKS 4 1 µF 1 kV

[16] Arcol HS100

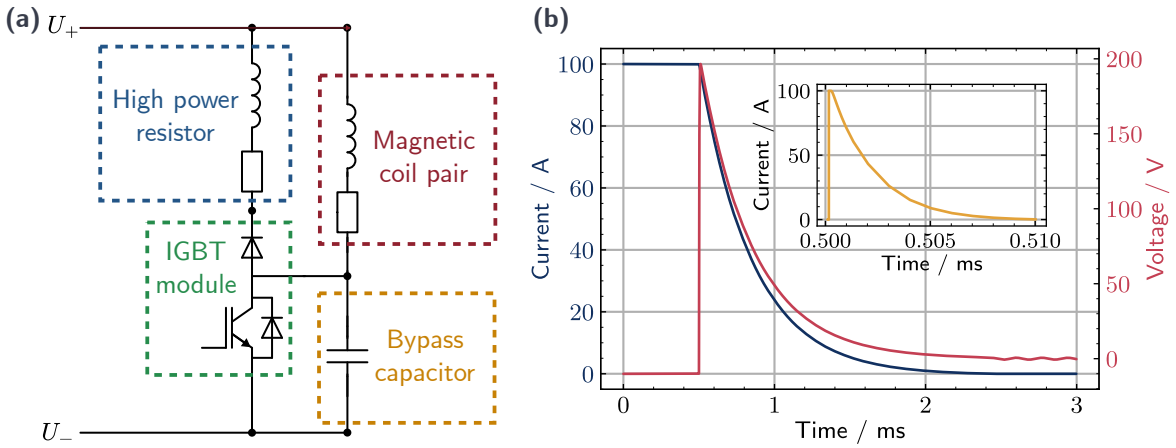

Figure 3.15: **(a):** Schematic of the coil switching electronics. The components are described in the main text. **(b):** Simulation results of the MOT coil switch-off performed with LTspice [**analogdevicesinc.LTspice24092025**]. A current of 100 A is switched off after 0.5 ms. The blue curve shows the current in the MOT coil pair, the red curve shows the voltage drop across the coil pair, and the yellow curve in the inset displays the current flowing via the bypass capacitor to ground when the IGBT is switched off.

dealing with high currents and voltages, is necessary to absorb the initial current flow after switching. The resistance value of the power resistor represents a tradeoff between faster energy dissipation and lower voltage spike.

The resulting simulated current and voltage drop across the MOT coils, together with the current flow via the bypass capacitor, are shown in Fig. 3.15(b). The results show a voltage spike of 200 V, which corresponds to 100 A flowing through the power resistor. The exact parasitic inductance of the power resistor is unknown but can be assumed to be below 10 µH, which has negligible influence on the switching dynamics for the chosen capacitance in the simulations.

A potentially problematic aspect of the cooling and coil mounting design of the magnetic transport (see Fig. 3.13) with large copper blocks are the possibly large eddy currents produced when switching the magnetic coil on or off. The cooling blocks and mounts are sliced to reduce this effect. Nevertheless, parasitic eddy currents will result in an increase of the rise and fall time of the magnetic field. This effect is critical, whenever the field needs to be switched rapidly.

We measured the rise and fall times for the MOT and science chamber coil pairs using a current clamp[17] and a fast magnetic field sensor[18]. The current clamp measured the current flowing through the coil pairs, while the magnetic field sensor was placed in the vicinity of the coil. The switched current during these measurements corresponds to the same axial gradient as in the magnetic transport (130 G cm^{-1}). For the fall time measurement, we utilized the fast switching via the IGBT modules connecting the power supply and the coil pairs. For the rise time measurement we adjusted the current output of the corresponding power supply to the high value, before enabling the current output via the IGBT.

The results for the fall time measurement of the MOT coil pair are shown in Fig. 3.16(a) and for the science chamber coil pair in Fig. 3.16(c). For the MOT coil, we measure a fall time of the current

[17] Hantek AC/AD Current Clamp CC-65
[18] Texas Instruments DRV425EVM

that is slightly longer than simulated of around 3 ms (95% – 5%). The reason is likely the increased inductance due to the metal surrounding the coils and due to the current leads.

The measured magnetic field does not follow the current trace but instead decreases more rapidly in the beginning before slowly rising again and only reaches the steady state after approximately 20 ms. This behavior can be explained by the fact that the eddy currents produced during the coil switch-off create a different magnetic field configuration than the coils themselves, because the coil mounts and cooling blocks are sliced asymmetrically. Therefore, we attribute the measured magnetic field mostly to the field produced by the eddy currents, since the field directly produced by the coils has the same temporal shape as the current trace. We assume that this measurement was more sensitive to the eddy current field because the magnetic field sensor is direction-dependent and was better aligned with the magnetic field produced by the eddy currents. This measurement indicates, that substantial eddy-current-induced magnetic field are created during the switch off that decay only over 20 ms. This strongly affects how fast we can effectively switch of the magnetic field. The consequences for the absorption imaging is discussed in Section 3.5.1.

A similar behavior is observed for the science chamber coil pair. Here, the current fall time of around 2 ms is faster than that of the MOT coil pair due to the lower inductance of the science chamber coils. The measured magnetic field trace roughly follows the shape of the current trace, but decays much slower after about 1 to 2 ms and only reaches the steady state after 15 ms. This indicates, that the magnetic field sensor was aligned to both the eddy-current-induced and the coil field. The magnetic field directly created by the coil pair is responsible for the fast initial decay, while the long decay tail can be attributed to eddy-current-induced fields. Again, such a long decay time of 15 ms impacts the absorption imaging in the science chamber, as discussed in Section 3.7.2.

Figure 3.16(b) shows the results of the MOT coil current rise time measurement. The current reaches its maximum after approximately 15 ms with a slight overshooting that settles 10 ms later. The magnetic field sensor position was not changed between the rise and fall measurements. Therefore, the measurement is more sensitive to the eddy-current-induced field compared to the coil field. This can explain why the magnetic field appears to be ahead of the current trace in time. The rapid switching produces a strong eddy-current-induced field that rises faster than the coil field and then settles down again over 20 ms. A rise time on the order of 15 ms is sufficiently fast for the magnetic transport but is problematic for the initial atom transfer to the magnetic trap in the MOT chamber, as discussed in Section 3.5.6, where we also elaborate possible improvements to the setup to mitigate this problem.

The rise time measurement results for the science chamber coil pair, presented Fig. 3.16(d), reveal a shorter current rise time of about 8 ms. Again, as for the fall time measurement of the science chamber coil, the measured magnetic field trace roughly follows the current trace. The analog to the slower decay of the magnetic field signal, visible in the fall time measurement, is more difficult to detect here due to the overshooting of the current trace. Instead, the field seems to be delayed by about 2 ms compared to the current trace. The measured rise time of about 8 ms is sufficient for the magnetic transport, the only step in the experiment sequence, where this coil pair is relatively quickly ramped up.

We have also measured the current rise time of a shorted power supply without the coils to identify the cause of the slow current rise times. Here, the rise time was approximately 1 ms. This indicates that the power supply simply cannot provide sufficiently high voltage to rapidly drive high currents into the inductive load of the coil pair, which ultimately limits the rise time.

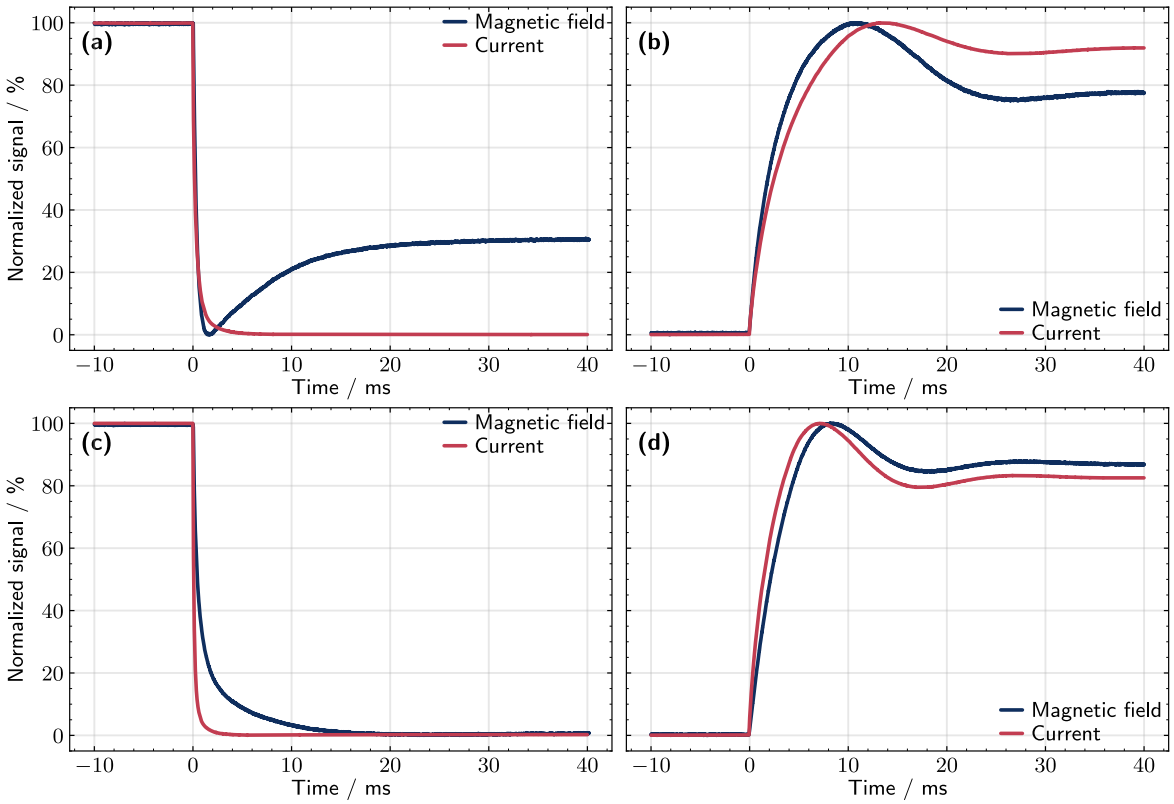

Figure 3.16: Results of the fall **(a)** and rise **(b)** time measurements of the MOT coil pair (a, b) and the coil pair 7 at the science chamber **(c, d)**. The measurement procedure is detailed in the main text.

3.6.3.3 Temperature monitoring and interlock electronics

Overheating of the magnetic-transport coils poses a significant risk due to the large power available from the current supplies. In the worst case, hot coils could ignite surrounding flammable materials and cause a laboratory fire. An obvious cause of overheating is failure of the water-cooling system. In addition, incorrect programming of the coil currents, a software bug in the main experiment control, or a hardware failure of a current supply could drive continuous high current through a coil. The cooling system is designed for pulsed operation during a normal transport sequence and is not sufficiently strong for this failure case.

Given the many potential causes of coil overheating, a temperature-monitoring system is required that can initiate an emergency shutdown. The temperature readings also support debugging and optimization of the magnetic-transport cooling system.

The structure of the temperature-monitoring system we designed and implemented for the magnetic transport is sketched in Fig. 3.17(a). Each coil mount contains a PT100 resistance temperature detector (RTD) with a four-wire connection for accurate readout, resulting in a total of sixteen RTDs for the transport system. The RTDs are housed in threaded mounts and screwed directly into the copper coil mounts to ensure good thermal contact.

An Arduino DUE microcontroller together with commercial RTD readout boards[19] measures and

[19] Adafruit MAX31865

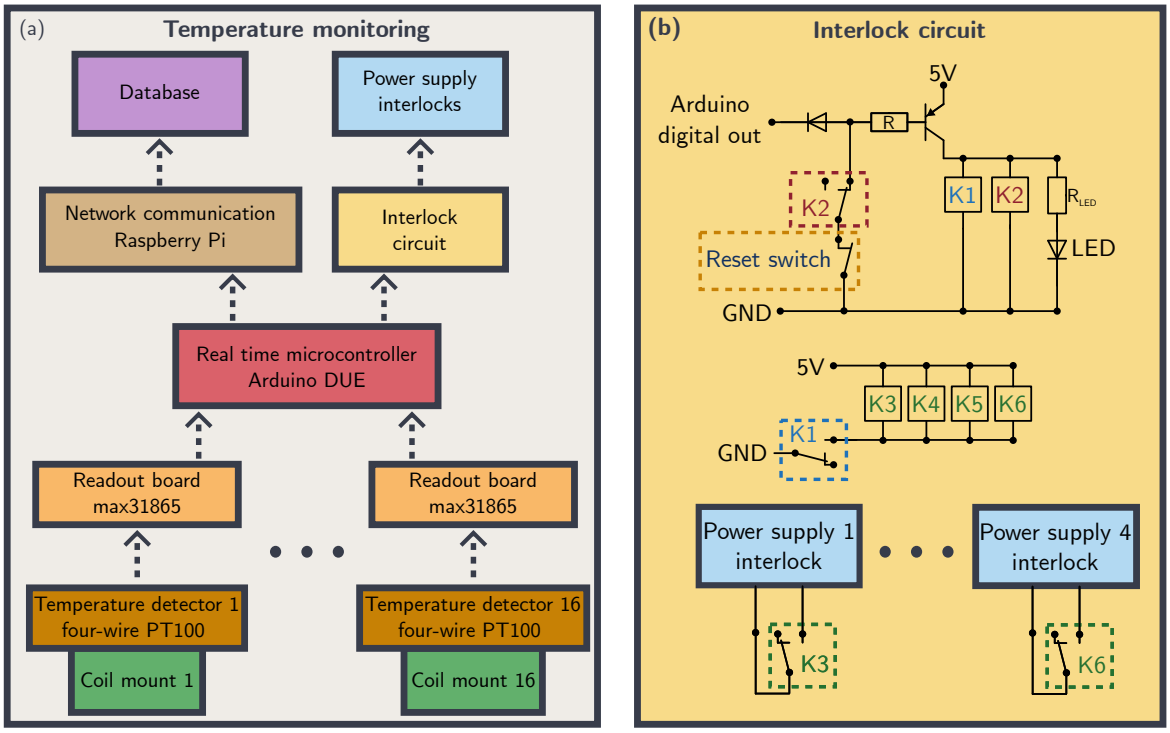

Figure 3.17: **(a):** Schematic of the temperature-monitoring system for the magnetic transport. The functionality of the system is described in the main text. **(b):** Schematic of the interlock circuit. In the nominal state, the Arduino applies a digital high signal (3.3 V) to the circuit, which is forwarded to the gate of a PNP transistor. The transistor then conducts and relays K1 and K2 are energized. Relay K1 in turn energizes the relays connected to the power-supply interlocks, enabling the current outputs. Relay K2 disconnects ground from the transistor gate, keeping the transistor conductive. In a fault condition, the Arduino outputs a digital low signal (0 V), which turns off the transistor and consequently all relays, disabling the power-supply current outputs. Once relay K2 is de-energized, the transistor gate is tied to ground and cannot be reactivated by the Arduino. A physical reset switch must be pressed to disconnect the gate from ground, which clears the fault state. A LED in the circuit indicates that the current outputs are enabled.

monitors the coil temperatures. The Arduino continuously acquires temperature data and compares them against a software-defined threshold of 30 °C. If this threshold is exceeded, the Arduino drives one of its digital output pins from high to low voltage (3.3 to 0 V). This pin is connected to a custom interlock circuit that turns the current supplies off by asserting their interlock inputs (see Section 3.6.3.1) as soon as the Arduino output drops to low voltage.

The schematic of the interlock circuit is shown in Fig. 3.17(b). The circuit is designed to be fail-safe. Any power loss of the interlock circuit itself or of the Arduino automatically shuts down the current supplies. Furthermore, the circuit prevents the current supplies from being turned back on until a physical reset switch is pressed. This guarantees that the system remains off after a fault until manual intervention is performed. For added safety, the watchdog chip of the Arduino is adjusted to reset the Arduino and trigger the fail state if the Arduino crashes or if the temperature measurement loop does not finish within two seconds.

To monitor and save the temperature data, the Arduino is connected to a Raspberry Pi via USB. The

measured temperature values are periodically transmitted to the Raspberry Pi. The Pi is connected to a server via Ethernet and saves the temperature data to an Influx database on it. This database can be accessed, and the data visualized on any computer in the institute network.

3.6.4 Simulation of the magnetic transport

To guide the design process and optimize the coil geometry and current ramps, we implemented a numerical simulation of the magnetic transport in Python that computes the resulting magnetic fields. As a basis for the calculations, we used the package Magpylib [113], a Python library for calculating magnetic fields of current-carrying wires, coils, and permanent magnets. It allows flexible definition of arbitrary coil geometries and efficient computation of the resulting magnetic fields at any point in space.

In the simulation, coils are represented as multiple circular current loops stacked radially and axially to approximate the real coil geometries for the given wire cross-section and number of turns.

We restrict the magnetic transport to unidirectional current flow through the coils and require an axial gradient of $130\,\mathrm{G\,cm^{-1}}$ at any position along the transport. For each position along the transport, this choice defines a system of linear equations relating the currents in the active coil pairs to the desired magnetic-field gradients in the x, y, and z directions. Here, we define the x–y plane as the horizontal plane in the lab, with y aligned with the magnetic-transport direction and the z-axis corresponding to the vertical direction, as depicted in Fig. 3.18(a). Maxwell's equations impose $\nabla \cdot \boldsymbol{B} = 0$, which provides a second constraint. With three active coils, however, the system remains underdetermined.

To obtain a third boundary condition, we impose two requirements: the gradient in the transport direction, $\mathrm{d}B/\mathrm{d}y$, should be as large as possible, and the gradient should not change rapidly or repeatedly along the trajectory. The first requirement stems from the fact that, due to the geometry of the overlapping coils, the gradient in the transport direction is generally the weakest. The associated weaker restoring force of the magnetic trap limits the achievable acceleration of the transport. Consequently, maximizing the gradient along y is desirable. The second requirement is included because rapid variations of the gradient during the transport may result in heating of the atoms.

To properly define the upper bound for the gradient in the transport direction, we first solve the system of linear equations allowing only two active coils at any given position, in which case system is fully determined. The resulting magnetic field gradient in transport direction provides an upper bound, because adding a third coil can only decrease the gradient in the transport direction (assuming unidirectional current flow). Figure 3.18(b) shows the calculated magnetic-field gradients as a function of the transport position, based on a two-active-coil simulation using the coil geometry of the real transport shown in Fig. 3.18(a). The magnetic-field gradient in transport direction oscillates between high values ($65\,\mathrm{G\,cm^{-1}}$) at the coil centers and lower values ($\sim 35\,\mathrm{G\,cm^{-1}}$) between adjacent coil pairs. We create a smooth boundary condition for the gradient by connecting adjacent minima with linear curves. The corresponding gradients along the transport with three active coils—following the set boundary—are depicted alongside the two-active-coil results in Fig. 3.18(b).

The gradients at the start and end of the transport vary more strongly with position because the initial and final traps are formed by only one coil pair. It is in principle possible to start or end with an elongated trap (weaker gradient in the y-direction), by adding a coil pair before and after the transport. We decided against such a solution for the following reason: Neither the initial atom cloud after MOT loading nor the final trap in the science chamber is elongated along the transport direction.

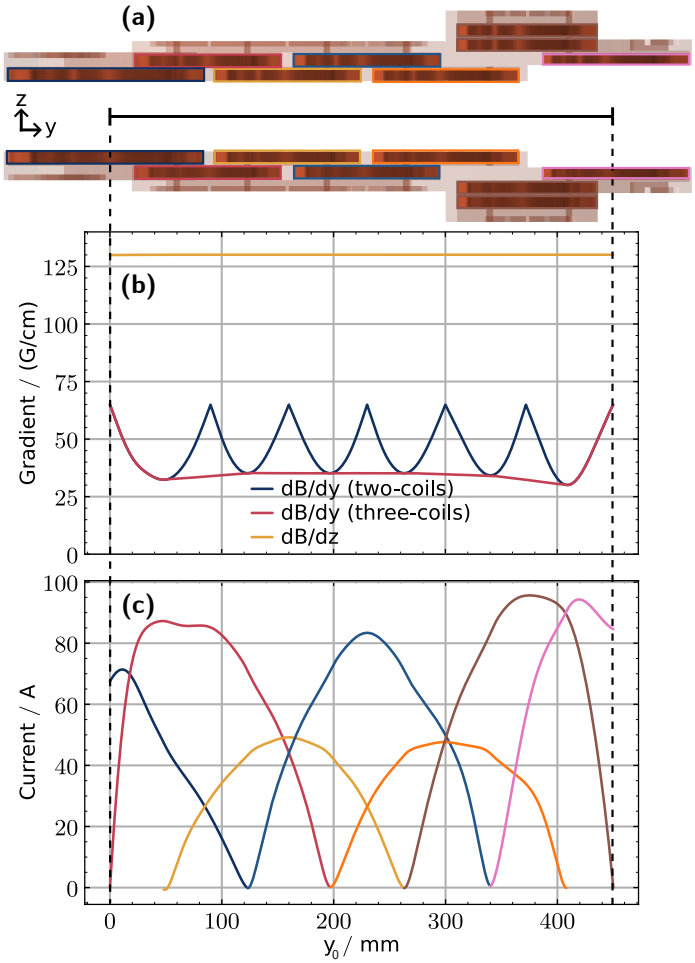

Figure 3.18: **(a):** Cross-section of the magnetic transport coil geometry. The coil pairs are marked with the color of the corresponding current ramps in (c). **(b):** Magnetic-field gradients in the y- and z-directions as a function of the magnetic trap minimum position y_0 during the magnetic transport. Results are calculated with two or three active coils (see main text) for the coil geometry in (a) and a step width of $\Delta y = 0.1$ mm. Boundary conditions for the gradients are described in the main text. **(c):** Current ramps with three active coils calculated for the magnetic transport as a function of the magnetic trap minimum position. The ramps correspond to the three-active-coils gradients in (b).

Hence, starting or ending with an elongated cloud would reduce mode overlap with the initial or final trap. Therefore, the additional coils would add complexity to the setup without a clear benefit to the transport performance.

The current ramps with three active coils, necessary to produce the gradients depicted in Fig. 3.18(b), are shown in Fig. 3.18(c). All current ramps remain below 100 A, as required. Coil pairs three and five, which are closest to the atoms, require lower currents than the other coil pairs.

3.6.4.1 Mapping onto time dependent current traces

The simulation described above calculates the required coil currents for a given magnetic field minimum position along the transport axis. To implement the magnetic transport in the experiment, these position-dependent currents need to be mapped onto time-dependent current ramps.

We implemented this mapping in a Python script. The script loads the simulated current traces for the transport coils as a function of position, as shown in Fig. 3.18, and maps them to the appropriate power supply, with the scaling between analog control voltage and output current applied.

Afterward, a user-defined time-dependent magnetic transport trajectory $y_0(t)$, with y_0 being the position of the magnetic field minimum along the transport axis, is converted to time dependent analog control ramps for the experiment. The script interpolates the individual points of the simulated current traces to calculate the analog control voltages in 20 µs steps, as required by the experiment control system. Furthermore, all coil switching TTL timings (see Section 3.6.3.2) are determined by the script. The analog control voltages and TTL timings are saved to separate csv files that can be loaded by the experiment control software. During the experimental cycle, the power supplies are activated according to the data saved in these csv files.

3.6.5 Characterization and optimization of the magnetic transport

To characterize the performance of the magnetic transport, we use absorption imaging in the MOT and science chambers, as described in Sections 3.5.1 and 3.7.2. These images provide the atom number and spatial extent of the atom cloud before and after the transport. With TOF measurements (see Section 3.4), we determine the temperature of the atom cloud. In our present implementation, only the initial and final states of the transport are observable in this way, leaving the dynamics during the transport itself effectively as a black box.

3.6.5.1 Initial characterization

The choice of an appropriate transport trajectory $y_0(t)$ determines the performance of the magnetic transport. The simplest trajectory is a linear ramp. A disadvantage of this ramp is the abrupt acceleration at the start and end points of the trajectory. This acceleration result in sloshing of the atomic cloud in the trap due to its inertia. When the atoms in the cloud collide and thermalize, the sloshing movement is converted to a higher cloud temperature. Another simple choice is a trajectory with constant acceleration for the first half and constant deceleration for the second half of the transport. This trajectory has a smooth velocity curve at its start and end, but the acceleration has a sign flip after half the transport and is discontinuous at the start and end. This again results in sloshing, reducing the transport performance. An analytic function based on the error function solving these problems was proposed by Badr et al. in [110]. They compared different analytic trajectories and found that a curve of the form

$$y_0(t, T_\mathrm{M}) = \frac{L_\mathrm{M}}{2} \cdot \left[1 - \mathrm{erf}\left(\log\left(\frac{T_\mathrm{M} - t}{t}\right)\right)\right], \tag{3.9}$$

yielded the best performance in their implementation of a magnetic transport. Here, T_M is the transport duration and L_M is the transport length. This trajectory provides smooth acceleration and deceleration without discontinuities in the first three derivatives, maintains a high average velocity for most of the sequence, and thus shortens the transport duration. A short duration mitigates atom loss from

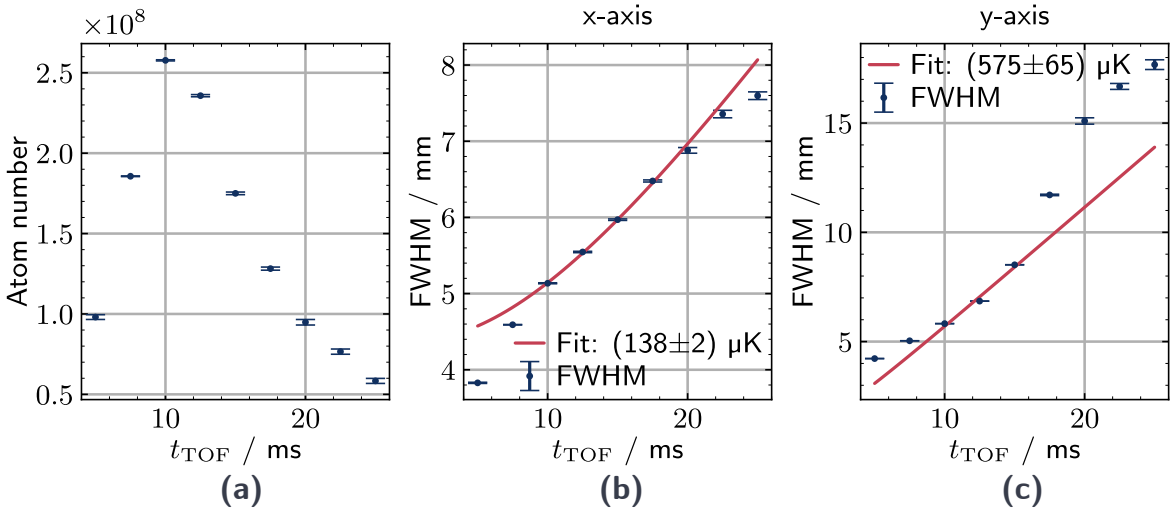

Figure 3.19: TOF measurement results in the science chamber after magnetic transport. **(a):** Reconstructed atom number as a function of the TOF. **(b, c):** Full width half maximum of the atomic cloud as a function of the TOF together with fitted temperature. The final quadrupole trap in the science chamber after the transport is kept at $130\,\mathrm{G\,cm^{-1}}$ for 450 ms before the TOF measurement starts. Each data point is averaged over 20 measurements.

background-gas collisions, and the smooth acceleration limits sloshing of the atom cloud that would results in heating.

We implemented this trajectory in the experiment with a transport duration of $T_\mathrm{M} = 1.5\,\mathrm{s}$ using the trajectory-to-current-trace mapping discussed previously. Exemplary TOF measurement results in the science chamber after magnetic transport are presented in Fig. 3.19. The atomic cloud was held in the final magnetic trap at full strength for 450 ms after the transport before we turned off the trap and started the free fall. Panel (a) shows the reconstructed atom number as a function of the time of flight t_TOF. As discussed in Fig. 3.10, the atom number is independent of t_TOF and the observed dependence is caused by image distortions due to the decaying magnetic field. The best estimate for the real atom number is the maximum in panel (a), because we optimized the imaging bias field for this TOF. Here, the atom number is around 2.6×10^8, corresponding to a transport efficiency of about 25%. A striking observation in panels (b) and (c), which show the temperature fits results in the x- and y-directions, is the large difference between the fitted temperatures. Specifically, the fitted temperature along the transport direction (y) is almost five times higher than in the x-direction. Furthermore, the quality of the fit in the y-direction is poor, with strong deviations from the expected curve defined in Eq. (3.6). As discussed in Fig. 3.10, this indicates that the cloud's velocity distribution is not thermal.

The root cause of these observations is a sloshing of the cloud along the transport direction when the transport ends. This sloshing is caused by residual momentum of the atom cloud upon arrival at the final position. This sloshing becomes clearly visible, when observing the center position of the atom cloud as a function of the holding time in the final quadrupole trap in the science chamber before releasing the cloud. In Fig. 3.20(a, b), we show the results of a corresponding measurement, which was conducted together with Valerie Mauth during her master thesis [114]. Panel (a) shows the center position along the x-axis, and panel (b) along the y-axis. Along the y-axis, decaying oscillations with an initial peak-to-peak amplitude of $S_{y,\mathrm{max}} \sim 0.38\,\mathrm{mm}$ are observed. Sloshing in the x-direction is an order of magnitude weaker, because this axis is perpendicular to the transport

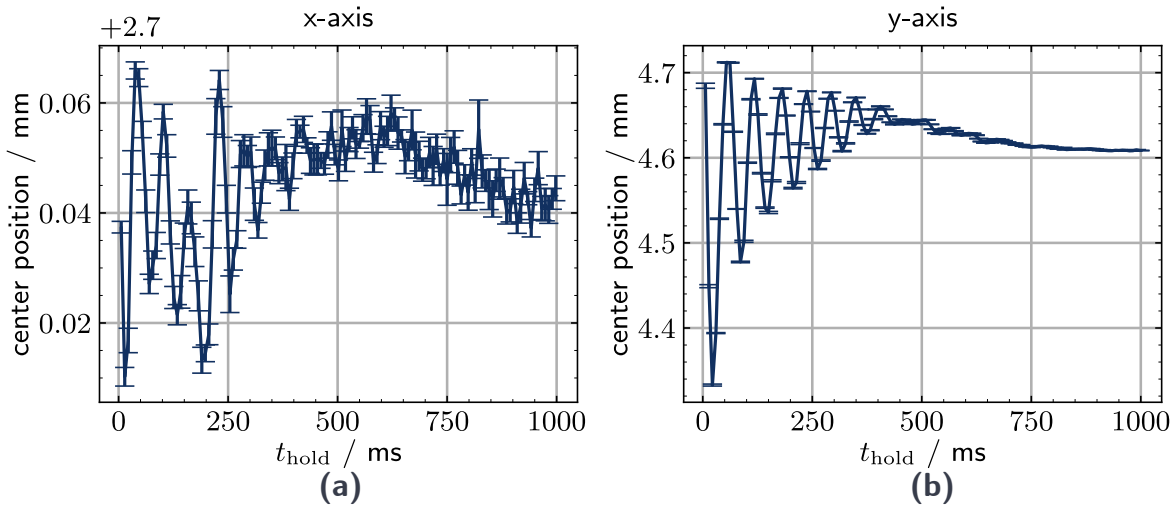

Figure 3.20: Center position of the atom cloud along the x and y-axis measured with absorption imaging for varied magnetic trap holding times in the science chamber after the magnetic transport, using the trajectory defined in Eq. (3.9). The center positions are determined via Gaussian fits, and by converting camera pixel positions to millimeters via the pixel size and image magnification. The data in this figure are also presented in [114].

direction. The oscillations decay within 400 ms. Note that this decay does not mainly result from collisional damping and thermalization. Instead, it is a wash-out of the individual atomic trajectories: In the linear quadrupole trap, there is no well-defined trapping frequency, so atoms with different velocities follow different paths and the collective oscillation dephases. The result is a broader velocity distribution along the y-axis that is no longer Maxwell–Boltzmann distributed. Therefore, we observe a faster expansion along that direction in free fall in Fig. 3.19(c). This also explains, why the cloud is not thermalized, and the cloud expansion in y-direction does not match the temperature fit function defined in Eq. (3.6).

These results show that, although the analytic trajectory is designed to reduce unwanted sloshing of the atom cloud, its performance in our magnetic transport implementation is not satisfactory. Other analytic trajectories (linear, constant acceleration) were tried, but they resulted in worse sloshing. One way to mitigate the sloshing is to slow down the magnetic transport, that is, by choosing a longer transport duration. This comes with the direct downside that the cycle time for the experiment is longer. Furthermore, atom loss due to background collisions becomes problematic when extending the transport time.

These problems motivated us to further optimize the magnetic transport trajectory, which is discussed in the following.

3.6.5.2 Optimization with machine learning algorithm

The optimization of the magnetic transport is nontrivial. Numerous free parameters governs the trajectory, and mid-transport diagnostics are unavailable. In addition, unquantified effects such as eddy currents in chamber walls, coil mounts, and cooling plates perturb the actual magnetic-field evolution in ways not captured by the idealized simulation. Consequently, purely simulation-based

optimization is insufficient.

We therefore employed the Machine-Learning Online Optimization Package (M-LOOP) [115] to optimize the transport. M-LOOP performs unsupervised online optimization of a user-defined set of control parameters. Results from experimental runs are incorporated to refine a model of parameter influence on a user-defined cost function, and subsequent parameter sets are chosen to minimize that cost.

The implementation of M-LOOP into our experiment control system was done by Valerie Mauth and is described in detail in the master thesis [114].

Below, we summarize the optimization procedure—including the choice of the trajectory parameterization and cost function, which was developed together with Valerie Mauth—and highlight the principal results of the optimization.

Trajectory parameterization M-LOOP optimizes a user-defined set of discrete control parameters. For the optimization to converge, the number of parameters should not exceed more than 20 in our experience. This makes direct optimization of all individual coil currents impractical. Therefore, we parameterize the position of the magnetic-field minimum as a function of time (the transport trajectory $y_0(t)$) and deterministically map that trajectory to coil-current ramps as described in Section 3.6.4.1.

The parameterization must satisfy the endpoint constraints $y_0(0, T_\mathrm{M}, \vec{A}) = 0\,\mathrm{mm}$ and $y_0(T_\mathrm{M}, T_\mathrm{M}, \vec{A}) = 450\,\mathrm{mm}$. Because M-LOOP does not enforce algebraic dependencies between different free parameters, these constraints must be built into the functional form from the outset. For that reason, we define the trajectory as a fixed base function $y_{0,\mathrm{base}}$ plus a Fourier sine series whose individual terms vanish at both endpoints:

$$y_0(t, T_\mathrm{M}, \boldsymbol{A}) = y_{0,\mathrm{base}}(t, T_\mathrm{M}) + \sum_{k=k_0}^{k_\mathrm{max}} A_k \cdot \sin\left(\frac{\pi k}{T_\mathrm{M}} t\right). \tag{3.10}$$

Here, T_M is the total transport duration, A_k are the tunable amplitudes, and k_0 and k_max define the included harmonic range. The vector $\boldsymbol{A}$ collects all A_k and constitutes the optimization parameter set passed to M-LOOP.

The base trajectory can in principle be any smooth function that connects the start and end positions within the transport duration. Selecting a base trajectory already close to the optimum accelerates convergence and improves robustness of the optimization. Consequently, we adopt the analytic base function defined in Eq. (3.9).

The added sine series permits systematic exploration of deviations from the base trajectory, while automatically preserving the endpoint constraints (each sine term is zero at $t = 0$ and $t = T_\mathrm{M}$). This yields a compact parameter set, in which low-order terms adjust the overall shape and higher-order terms allow localized refinements.

Cost function The user defined cost function needs to evaluate the performance of a transport sequence with a single number. In our case, the available performance indicators are the atom number, the spacial extent of the atom cloud, and its temperature. The atom number and spacial extend can be computed from a single absorption image after a single measurement cycle, however, a few repetitions are necessary to estimate the uncertainty of the results. A TOF measurement, to determine the temperature, is composed of several absorption images taken in different measurement cycles, each needing to be repeated to estimate the uncertainty. Since each cycle takes around 2 to 3 s, using

the temperature as a part of the performance measure is very costly with regard to measurement time. The spacial extent of the cloud after a certain TOF is correlated with the temperature according to Eq. (3.6). Furthermore, the main contributor to the increased temperature in the transport direction is the sloshing of the atomic cloud after the transport completes, which also results in an increased spacial extend of the atom cloud along that direction. Consequently, optimizing either the temperature or the spacial extent of the cloud also optimizes the other.

For these reasons, we chose a cost function $C(N, \sigma_x, \sigma_y, \boldsymbol{A})$ that only combines the atom number N and spacial extend of the cloud along the x and y-direction σ_x, σ_y after a fixed time of flight $t_{\mathrm{TOF}} = 10\,\mathrm{ms}$. Before releasing the atom cloud, we hold it for 350 ms, just long enough such that the sloshing is mostly washed out, but the cycle time is kept as short as possible.

The cost function that is minimized by M-LOOP is given by

$$C(N, \sigma_x, \sigma_y, \boldsymbol{A}) = -\left(\frac{N(\boldsymbol{A})}{N(0)}\right)^a \cdot \left(\frac{\sigma_x(0)}{\sigma_x(\boldsymbol{A})} \cdot \frac{\sigma_y(0)}{\sigma_y(\boldsymbol{A})}\right)^b, \tag{3.11}$$

where $N(\boldsymbol{A})$, $\sigma_y(\boldsymbol{A})$, $\sigma_x(\boldsymbol{A})$ refer to the measured quantities for a given set of optimization parameters $\boldsymbol{A}$ and $N(0)$, $\sigma_y(0)$, $\sigma_x(0)$ are the default values measured with the base trajectory. The parameters a and b are weights for the atom number and width of the atom cloud. By adjusting these parameters, we can steer the optimization to prioritize increasing atom number over reducing the width or vice versa. The normalization with the default atom number and widths is done, such that relative changes of the atom number and temperature are evaluated.

Optimization results Here, we present the result of the optimization run with $a = 1$, $b = 2$, $k_{\mathrm{max}} = 15$ for a transport duration of $T_{\mathrm{M}} = 1.5\,\mathrm{s}$, which was conducted together with Valerie Mauth. This parameter choice represents a tradeoff between reaching the highest possible atom number and reducing the cloud width and temperature. A systematic study of the influence of the different free parameters a, b, k_{max}, and T_{M} was conducted by Valerie Mauth and is presented in her thesis [114]. The results are tabulated in Tables 4.2 and 4.3 in her thesis.

The optimization run with $a = 1$, $b = 2$, $k_{\mathrm{max}} = 15$ converged after trying approximately 1000 parameter sets, and was stopped after 11 hours when 1500 datasets had been tried. The optimized trajectory and the corresponding velocity profile are shown in Fig. 3.21 together with the curves for the base trajectory. Comparing the velocity profile of the optimized trajectory to that of the base trajectory in Fig. 3.21, we observe multiple periods of acceleration and deceleration during the transport. Notably, the start of the transport is very similar, while the end varies drastically. At the end of the optimized transport, the deceleration of the atomic clouds starts earlier, such that the cloud approaches the final position more slowly than with the base trajectory. This feature is consistently found in different optimization runs [114]. Specifically, the larger b (the weight of the cloud width), the earlier the deceleration starts. This indicates that the earlier deceleration is vital for reducing the temperature and sloshing.

We performed a TOF measurement and a holding time scan, to compare the performance of the base trajectory to the optimized trajectory, as shown for the base trajectory before. The resulting performance metrics of the base and optimized trajectories are given in Table 3.3.

A drastic improvement of the sloshing and temperature in the transport direction with the optimized trajectory is observed, while the atom number is only weakly improved. This indicates that the atom loss during the transport is not caused by atoms spilling out of the trap due to excessively rapid

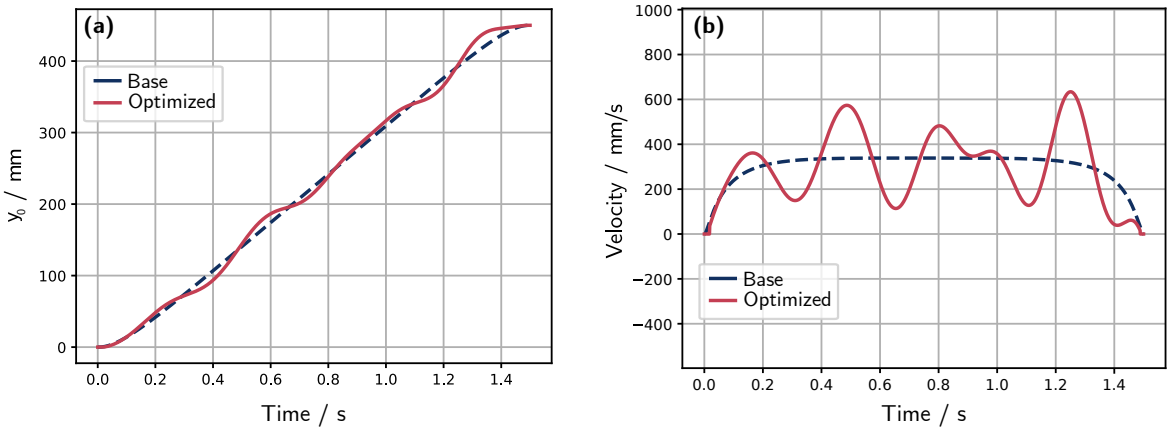

Figure 3.21: **(a):** The magnetic trap minimum position y_0 as a function of time for the optimized and base trajectory of the magnetic transport detailed in the main text. **(b):** The trap-minimum velocity as a function of time corresponding to (a). The data in this figure are also presented in Ref. [114].

acceleration of the transport. Instead, the loss happens at other stages during the transport.

Two loss mechanisms are likely to dominate the total atom loss: losses due to collisions with the background gas and losses due to collisions with the vacuum chamber walls. Specifically, collisions with the walls of the differential pumping tube are likely to contribute to the atom loss. We can estimate the loss due to background gas collisions by comparing the transport duration to the magnetic trap lifetimes measured in the MOT (~ 2 s) and science chamber (~ 7 s), see Sections 3.5.6 and 3.7.3. The trap lifetime and vacuum pressure between the start and end of the transport are not precisely known. Since the differential pumping tube is closer to the MOT than to the science chamber, it is expected that the majority of the trajectory takes place in the better vacuum conditions. We calculate an upper bound for background losses of ~ 50% assuming the lifetime of the magnetic trap during the transport is given by the lifetime in the MOT chamber. The remainder of the loss is likely caused by collisions with the walls of the differential pumping tube. To estimate this loss, we consider the spatial profile of the atomic cloud trapped in the quadrupole-like trap during the transport. The density follows the form

$$n_{\text{dens}}(x,y,z) = n_0 e^{-\Delta E(x,y,z)/k_B T} = n_0 e^{-\mu_B g_F m_F |\boldsymbol{B}(x,y,z)|/k_B T}, \tag{3.12}$$

with n_0 the peak density. $\boldsymbol{B}(x,y,z)$, given in Eq. (3.8), is linear in x, y, z. Therefore, the density profile falls off exponentially from the center of the trap. The differential pumping tube has an inner diameter of 4 mm. However, as discussed before, due to the tilt of the differential pumping tube, its effective free diameter is only approximately 3 mm. To roughly estimate the atom loss due to collisions with the wall, we compute the fraction of the atom cloud that would be outside a 3 mm diameter from its center. To compute this value, we need to input the cloud temperature and gradients into Eq. (3.12), but the temperature at the start of the transport is not well-defined, as detailed before in Section 3.5.6. We choose the lower fitted temperature value, 254 mK, to obtain a lower-bound estimate of the losses due to the differential pumping tube. Under these assumptions, the fraction of the cloud outside the diameter is approximately 6%. This fraction represents only the fraction that is instantaneously lost when the cloud is inside the tube. The cloud will continue to lose atoms until it rethermalizes to a

Table 3.3: Performance metrics of the magnetic transport for the base trajectory and optimized trajectory with different parameters. η_T is the atom number retention, $\sigma_{x,y}(0)$ and $\sigma_{x,y}(\boldsymbol{A})$ are the cloud widths for the base and optimized trajectories, T_x and T_y are the fitted temperatures, and $S_{y,\mathrm{max}}$ is the maximum sloshing amplitude. $\frac{\sigma_{x,y}(0)-\sigma_{x,y}(\boldsymbol{A})}{\sigma_{x,y}(0)}$ describes the relative improvement of the cloud width. The data in this table are also presented in [114].

Trajectory	η_T	$\frac{\sigma_x(0)-\sigma_x(\boldsymbol{A})}{\sigma_x(0)}$	$\frac{\sigma_y(0)-\sigma_y(\boldsymbol{A})}{\sigma_y(0)}$	T_x / µK	T_y / µK	$S_{y,\mathrm{max}}$ / mm
Optimized	$(26.5 \pm 2.6)\%$	10.1%	18.1%	120.6 ± 2.0	189 ± 9	~ 0.20
Base	$(25.0 \pm 2.5)\%$	—	—	117 ± 5	410 ± 70	~ 0.38

temperature where the cloud is confined to an area smaller than the tube. This process is analogous to evaporative cooling. Although care was taken to align the transport as well as possible, small deviations from the symmetry axis cannot be ruled out, which will further increase the atom loss.

Ultimately, we assume that the atom loss due to collisions with the walls makes up at least 50% of the total losses. These collisions would be practically zero, if the temperature in the magnetic trap resembled the temperature after the molasses stage. As of now, we deem the reached atom numbers of over 2×10^8 at temperatures below 200 µK sufficient to conduct the planned experimental steps. If higher atom numbers and lower temperatures will be necessary in the future, the handover to the magnetic trap should be improved, as discussed in Section 3.5.6.

3.7 Science chamber and experiment region

In this section, we present an overview of the room-temperature science region and its key components. We summarize the design of the custom titanium-glass cell that constitutes the science chamber. We further describe the absorption imaging system, and the Rydberg excitation and detection.

3.7.1 Self-build titanium-glass cell

The science chamber is the part of the vacuum system that binds together the atom preparation setup and the cryostat. There are constraints for size and optical access, which led to the decision to not use a commercial piece, but to use a home-built cell instead.

On the one hand the magnetic transport requires the magnetic field coils to be as close together as possible, limiting the height of the chamber. On the other hand, in the cryogenic version of the experiment, two cryogenic radiation shields and a sample holder as well as the electrodes for field ionization will need to fit inside the chamber. Furthermore, the chamber must provide adequate optical access for the Rydberg excitation lasers.

A typical commercial steel chamber requires flange viewports to provide the optical access. These flanges will add to the height of the chamber, which is undesirable due to the magnetic transport. A pure glass cell could solve this problem, but the reduced mechanical stability introduces a new problem for the two-chamber design. Vacuum components need to be connected from both sides to the glass cell, on the one side the cryostat vacuum housing and on the other the connecting vacuum tube between the two chambers. Any misalignment of the attached components might induce stress in the class and could cause it to break. This is especially critical during the assembly of the vacuum system.

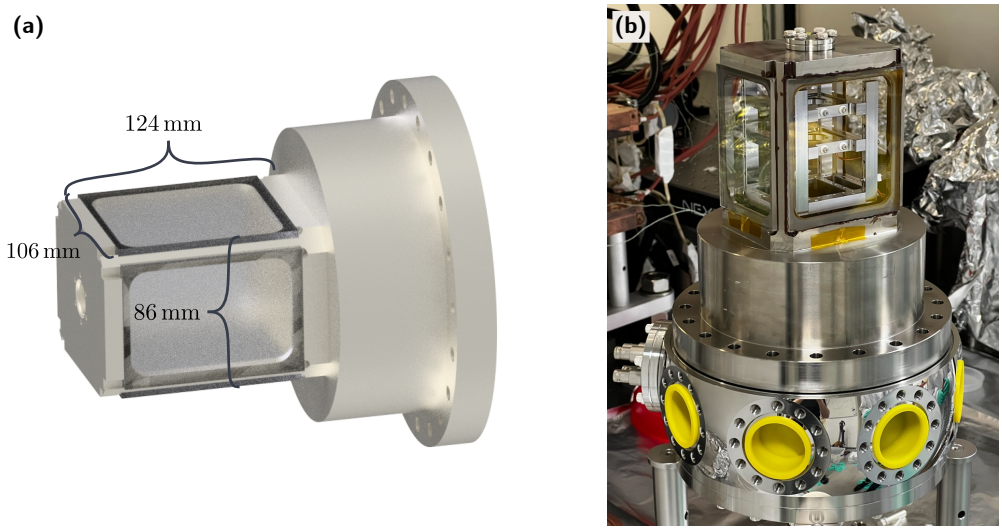

Figure 3.22: **(a):** Rednering of the home built titanium-glass science chamber. **(b):** Photograph of the science chamber during the vacuum assembly of the room temperature setup. The titanium-glass cell is flanged to an octagon that hosts the inner assembly with electrodes for ionization (see Section 3.7.4) that are visible through the glass windows.

These considerations led us to develop and manufacture a home-build vacuum chamber based on a design that has been established in a neighboring experiment in the group [116]. This chamber is planned to also be used for the cryogenic version of the experiment and was designed accordingly.

The cell has a rectangular frame made from titanium housing four rectangular N-BK7 windows that are glued into the frame as shown in Fig. 3.22(a, b). The windows of the chamber are anti-reflection coated for 780 nm and 480 nm, the wavelengths of the probe and control lasers. On one side, the cell ends in a DN16 flange to connect to the MOT chamber, and on the other in a DN100. Such a large flange is required to connect to the vacuum cube of the cryostat. In the room temperature version, we connect a commercial octagon instead, as depicted in the room-temperature setup overview in Fig. 3.2.

The class cell has a length of 124 mm up to the position where the cell widens to accommodate the radial extent of the magnetic field coils positioned above and below for the magnetic transport.

We chose the two materials—titanium and N-BK7 glass—due to their similar thermal expansion coefficients. Titanium [117] (grade 2) has a thermal expansion coefficients of $8.6 \times 10^{-6}\,°C^{-1}$ at 20 to 100 °C while N-BK7 [118] has a coefficient of about $8.4 \times 10^{-6}\,°C^{-1}$ at 50 to 300 °C. A low difference in thermal expansion coefficient reduces the mechanical stress on the windows, when baking the vacuum chamber. This is important to mitigate deformation of the glass, resulting in birefringence, or even worse resulting in a leak that destroys the vacuum. The windows are glued into the frame using the heat curable epoxy glue EPO-TEK®H77S. This glue features low out-gassing, making it compatible with ulta-high vacuum applications. The glue is heat cured in an oven at 150 °C for 1 hour. The gluing and assembly of the chamber was done together with Johanna Popp, and a detailed description of the process can be found in her thesis [111].

Problems when baking the home-built cell Once assembled and glued, the home-built cell was attached to a turbo pump and pumped down to test the vacuum quality. After the pump down, a

bake-out trial was performed. The cell was wrapped in heating wires and isolated with aluminum foil, and heated to 120 °C. During this trial, we discovered that the epoxy bonds between the titanium frame and the glass windows are more sensitive to elevated temperature than anticipated. In the first assembled cell the adhesive began to weaken for bake temperatures above 100 °C and, in one case, adhesion failed completely, rendering the cell unusable. This outcome was unexpected because the chosen adhesive (EPO-TEK® H77S) is heat cured at 150 °C.

A plausible explanation for the observed failures is the polymer glass-transition behavior of the adhesive. The epoxy's glass-transition temperature lies near 80 °C. Temperatures above this threshold potentially lead to softening or partial reflow of the cured bond. Under vacuum the differential pressure exerts an inward mechanical load on the windows. Once the adhesive softens, the bond can no longer reliably sustain that load and the windows may slip or detach, typically starting at the outer edge of the bond and progressing inwards.

To mitigate this problem, we improved the surface preparation and bonding procedure for the second cell, which was subsequently built and is now used in the experiment. Immediately before epoxy application, the titanium mating surfaces were mechanically roughened with fine polishing paper to remove the native oxide layer and increase the effective contact area. The surfaces were then quickly wiped with IPA to remove residual dust and dirt, after which the adhesive was applied.

In addition, the window edges were treated with an oxygen plasma immediately before adhesive application to improve wetting and adhesion. With this enhanced surface preparation, the second cell survived bake-out to 100 °C. Only minor, locally confined signs of bond weakening were observed, and no complete failure occurred. Nevertheless, to reduce the risk of failure during future bake-out procedures, the temperature should be limited to below 80 °C.

Problems with the window quality Interference at the glass windows is one of the problems we faced with the home build science chamber in the experiment. In particular, the collimated imaging beam suffers from interference fringes caused by the glass window. The reason is the anti-reflection coating, which was optimized for two wavelengths 780 nm and 480 nm as well as an angle of incidence from 0° and 45°. As a result of the complex coating, the specified reflectivity per surface is quite high with $R_{\text{coating}} < 1.2\%$. Position dependent constructive and destructive interference between the four consecutive surfaces through which the imaging beam is transmitted, results in a fringe pattern with a relative difference between maximum and minimum of up to 10%. Mechanical vibrations and drifts results in small position changes of the interference pattern which ultimately result in fluctuation for the absorption imaging. Especially for low atom numbers ($\leq 1 \times 10^7$) and small clouds, these fluctuations obscure the imaging fits and atom number measurement results. One way to remove the interference for the imaging beam is to make the beam slightly focused instead of collimated in the science chamber. As a consequence, however, the perceived OD of the atom cloud is slightly changed on the order of $\sim 5\%$ while the shape is unaffected to first order due to the $4f$ imaging lens setup. Note that for the characterization measurements presented in this work, the atom numbers were high enough that this technique was not required and is not used.

3.7.2 Science chamber absorption imaging

As mentioned before, we have installed an absorption imaging system to image the atoms at the end of the magnetic transport. These images are used to optimize the transport, as discussed in Section 3.6.5.2. In the following, we give some additional technical details.

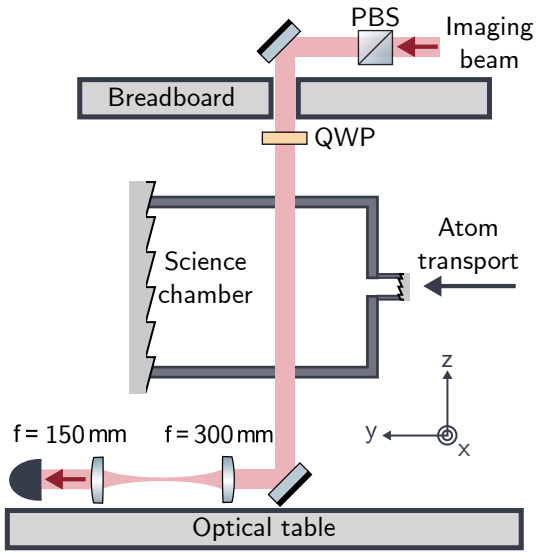

Figure 3.23: Schematic overview of the vertical absorption imaging setup at the science chamber.

Initially, we assembled two absorption imaging systems around the science chamber to image both the horizontal and vertical plane. The horizontal imaging was installed on the probe axis in place of the Rydberg probe and control lasers (see Section 3.7.4). This configuration simplified the alignment of the magnetic transport coils with respect to the probe axis. The horizontal imaging was subsequently removed. Both imaging setups were originally assembled together with Johanna Popp. Details regarding the initial assembly and characterization are presented in her thesis [111]. In the following, we briefly describe the vertical imaging setup and discuss the image distortions that arise due to eddy currents.

The vertical imaging setup at the science chamber is sketched in Fig. 3.23. A breadboard with a central through hole of 5 cm diameter is installed above the science chamber, through which the imaging beam is guided. The imaging beam is delivered via a single-mode fiber (not shown in the figure), passes through a polarizing beam splitter cube (PBS) for polarization correction, and is then circularly polarized using a quarter-wave plate (QWP). Because reflecting a circularly polarized beam from a mirror alters its polarization, we installed the QWP necessary to produce circular polarization after the final mirror on the bottom of the breadboard. After transmission through the chamber, a standard $4f$ lens configuration to image the shadow of the atom cloud in the horizontal plane. As for the MOT absorption imaging, we utilize a CCD camera[20] to take the pictures.

Compared to the imaging in the MOT chamber (see Section 3.5.1), the atom numbers of approximately 2.5×10^8 and the corresponding densities achieved in the science chamber are low enough to permit on-resonance imaging.

Image distortions due to eddy currents Image distortions due to eddy currents, when switching off the magnetic trap in the MOT chamber, were previously discussed in Section 3.5.1. In the science chamber, this problem is also prevalent because imaging always occurs after switching off the final magnetic trap. Therefore, as for the MOT absorption imaging after the magnetic trap, in the science

[20] Excelitas Technologies Corp. pco.pixelfly 1.4 USB

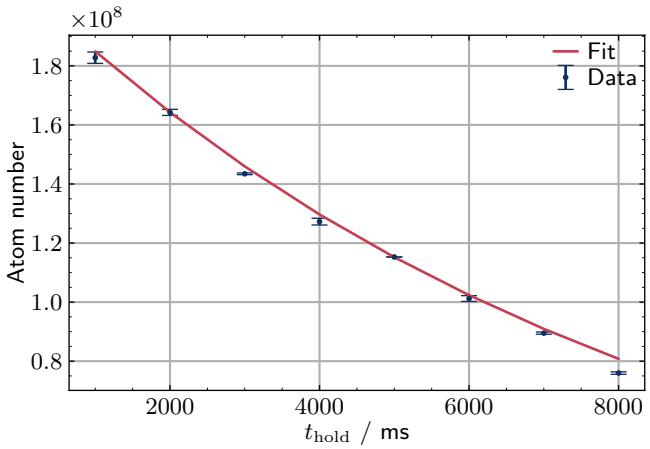

Figure 3.24: Atom number as a function of the holding time in the magnetic trap in the science chamber, together with an exponential fit yielding a decay constant of $\tau_{\mathrm{MT}}^{\mathrm{MOT}} = (8.5 \pm 0.4)\,\mathrm{s}$.

chamber, the atom number and temperature measurements are distorted by the eddy-current-induced magnetic fields.

One technique to mitigate this distortion is to ramp down the magnetic field gradient before turning off the trap completely. Specifically, we employ a ramp from the full strength of $130\,\mathrm{G\,cm^{-1}}$ to $60\,\mathrm{G\,cm^{-1}}$ over a duration of 50 ms. A gradient of $60\,\mathrm{G\,cm^{-1}}$ was chosen because at lower gradients (around $30\,\mathrm{G\,cm^{-1}}$), the magnetic trap becomes weaker than the gravitational force, causing atoms to fall out of the trap and the cloud to deform before the ramp completes. A side effect of ramping down the trap gradient is that the atomic cloud cools slightly, and the measured temperature underestimates the temperature in the initial cloud.

3.7.3 Magnetic trap

After the magnetic transport that brings the atoms from the MOT chamber to the science chamber, the atoms are held in the final magnetic trap, as discussed briefly in Section 3.6. In the room-temperature setup, the final trap in which the atoms are held is the magnetic quadrupole trap in the science chamber generated by the last coil pair of the magnetic transport. As in the MOT chamber and during the magnetic transport, the atoms are held with an axial magnetic field gradient of $130\,\mathrm{G\,cm^{-1}}$.

Although the vacuum condition in the science chamber is better than in the MOT chamber, the dominant loss channel for the magnetic trap remain collisions with background gas. An exemplary measurement of the atom number as a function of the holding time is shown Fig. 3.11. We fit an exponential decay $N(t) = N(0)\exp(-t/\tau_{\mathrm{MT}}^{\mathrm{MOT}})$ to the data and find a lifetime of $\tau_{\mathrm{MT}}^{\mathrm{MOT}} = (8.5 \pm 0.4)\,\mathrm{s}$. The measured lifetime in the science chamber is about 4 times higher than in the MOT chamber (see Section 3.5.6) indicating that the pressure is 4 times lower. The implications of the lifetime for the planned evaporative cooling in the science chamber after the cryogenic upgrade are discussed in Section 4.2.2.

3.7.4 Rydberg excitation and detection

The Rydberg excitation and detection optical setup is assembled on breadboards around the science chamber. It is designed to be compatible with the room-temperature and cryogenic setup without requiring any adaptations. This section describes the implementation of the two-photon Rydberg excitation scheme, the optical setup, and the two detection techniques for the Rydberg excitation: measurement of the probe laser transmission through the atomic cloud using single-photon counters and field ionization of Rydberg atoms followed by ion detection using a microchannel plate (MCP).

3.7.4.1 Two-photon excitation scheme

As outlined in Section 2.3, we utilize a two-photon excitation scheme to coherently drive ground-state atoms to Rydberg states. A weak probe laser at 780 nm drives the σ^+ transition from the ground state $|5S_{1/2}, F = 2, m_F = 2\rangle$ to the intermediate state $|5P_{3/2}, F = 3, m_F = 3\rangle$. This laser is strongly attenuated to only a few photons per pulse. A strong control laser at 480 nm completes the two-photon process by driving the σ^- transition from the intermediate state to the target Rydberg state $|nS_{1/2}, m_J = 1/2\rangle$.

In the following, we will outline the Rydberg excitation and detection sequence. The atom cloud is held in the final magnetic trap while a pulse generator initiates the Rydberg excitation and detection sequence. As described in Section 3.2, the overall experimental sequence timing is controlled by the ADwin real-time control system, which triggers the pulse generator at the appropriate time. The pulse generator is employed here, because the Rydberg excitation requires much higher timing resolution than the ADwin can provide (20 µs). The pulse generator serves as the central timing device for the Rydberg sequence, coordinating all triggers required for excitation and detection with 2 ns precision.

Each measurement cycle contains 1000 Rydberg excitation pulses with atoms present in the trap, followed by 1000 background measurements taken without atoms (after switching off the trap). Within each individual pulse, the pulse generator triggers an arbitrary waveform generator (AWG), which controls the laser power via AOMs to perform the Rydberg excitation with the probe and control lasers. The AWG shapes the probe and control pulses by controlling the RF-power applied to the AOMs. The AWG output is calibrated to compensate for the nonlinear response of the AOM and produce the desired pulse shape (for example, Gaussian or Tukey pulses).

The transmitted probe photons are detected by a single-photon counter module (SPCM). We utilize a commercial time tagger[21] to record the photon arrival times. The time tagger is triggered by the pulse generator to synchronize the time tags to the excitation laser pulses. The probe transmission is computed by dividing the photon counts measured with atoms present by the corresponding background counts.

After each Rydberg excitation pulse, a high voltage is applied to the ionization electrodes to field-ionize all Rydberg atoms present in the cloud. This serves two purposes: first, it enables detection of the Rydberg population via the MCP (see Section 3.7.4.4), and second, it is necessary to remove all Rydberg atoms from the trap before the next excitation pulse to ensure a clean initial state for each measurement. The ion signal from the MCP is recorded using the time tagger.

[21] Swabian Instruments Time Tagger 20

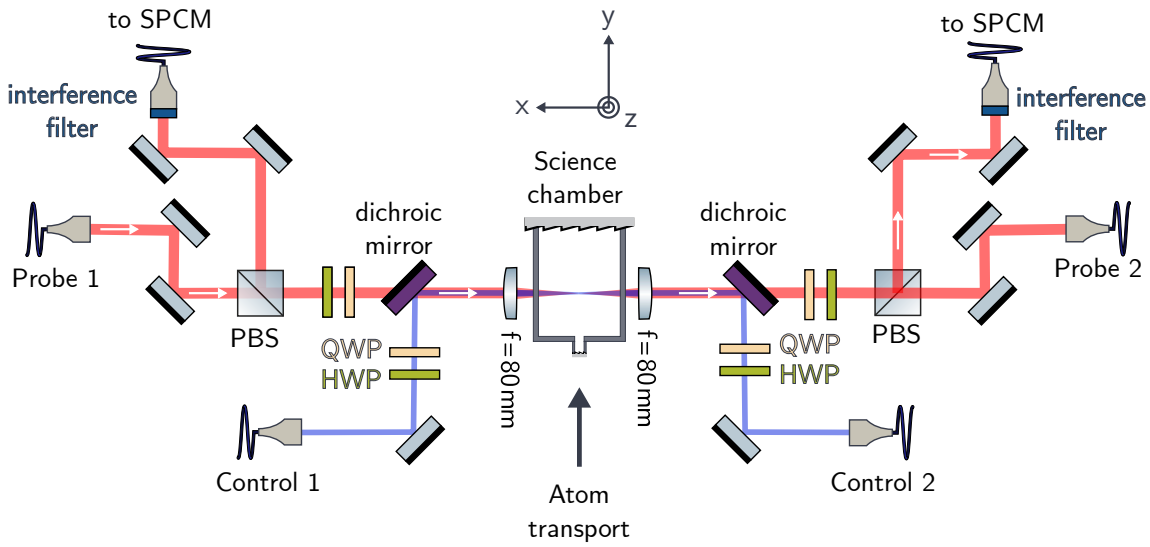

Figure 3.25: Schematic of the optical setup for two-photon Rydberg excitation and detection. The mirrored setup includes two counter-propagating probe (780nm) and control beams (480nm). The beam path of probe 1 is marked with white arrows. The control and probe beams are superimposed using dichroic mirrors. Their polarization is respectively controlled via a half-wave plate (HQP) and a quarter-wave plate (QWP). Achromatic lenses focus the beams at the atom cloud position.

3.7.4.2 Optical setup

The optical setup for Rydberg excitation is depicted in Fig. 3.25. The setup is built in a mirrored configuration with two probe and two control beam paths, providing flexibility to select the propagation directions of the probe and control beams independently. This architecture also enables coupling two control lasers simultaneously, as required for the HBAR cooling scheme presented in Section 5.1. The beam path of probe 1 is marked with white arrows in Fig. 3.25. Linearly polarized probe light exits a fiber collimator and is further filtered by a linear polarizer (not shown in the figure) before being transmitted through a PBS. A combination of a half-wave plate (HWP) and a QWP produces the required circular polarization. The probe beam is then transmitted through a dichroic mirror, where it is overlapped with the control beam 1. Similarly, the control beam is circularly polarized using a combination of an HWP and a QWP before being reflected by the dichroic mirror. Because the dichroic mirror affects polarization in both transmission and reflection, the wave plates are adjusted to precompensate for these polarization changes. The overlapped probe and control beams are focused into the science chamber by a single achromatic lens[22]. We discuss the choice of the focus beam waist below.

On the transmitted side, the setup is mirrored, but the probe 1 beam is reflected by the PBS and directed to a fiber-coupled SPCM for transmission measurements. Interference filters[23] are directly mounted in front of the fiber couplers that guide the probe light to the SPCM, to suppress stray light from the environment. We achieve a probe-to-SPCM fiber coupling efficiency of about 70%.

For the transmission measurements presented in this work, we used SPCMs from Laser Components

[22] Edmund Optics EO #49-33
[23] Thorlabs FL780-10

(COUNT-250C-FC) with a specified quantum efficiency of 51%. We have acquired superconducting nanowire single photon counters from Single Quantum (Eos 810 CS), which were characterized in the bachelor thesis of Max Reicherd [119]. These SPCMs reach detection efficiencies of about 90%, but we have not yet implemented them into the experiment.

The probe and control beams must be carefully aligned both with respect to each other and with respect to the atomic cloud. In the room-temperature setup, we used the probe beam axis as the common reference. To align the atomic cloud to the probe axis, we applied magnetic bias fields to shift the cloud position and maximize the absorption of the probe light. The control laser were then coarsely overlapped with the probe beam by eye. Fine optimization was subsequently performed by maximizing the Rydberg excitation signal.

Probe and control beam waist For compatibility with the cryogenic environment, the excitation lasers must not illuminate the cryogenic sample directly to avoid unwanted heating and scattering. We chose the collimation lenses[24] after the fiber to realize a probe beam waist of $w_{0,\mathrm{probe}} = 8\,\mu\mathrm{m}$ and a control beam waist of $w_{0,\mathrm{control}} = 15\,\mu\mathrm{m}$ at the focus point in the science chamber. The beam center will be located approximately 50 µm from the HBAR surface. With this distance, the beam is always more than two waist radii away from the surface of the HBAR and the atom chip, also when beam divergence away from the focus is taken into account. Scattering of the laser beams is therefore negligible.

These focus dimension allow for the realization of an effective one-dimensional geometry, where the whole probe radius can be blockaded by a Rydberg atom. However, this is not optimal for the cooling scheme we propose in Section 5.1. Instead, it could be beneficial to use a wider probe radius, to be able to create more Rydberg atoms simultaneously in the cloud. This can be achieved by using a shorter focal length collimator after the fiber.

Wavelength adjustment Both the probe and control lasers must be frequency-stabilized and tuned to the two-photon resonance for a targeted Rydberg state. For the probe laser, setting the absolute frequency is straightforward. As described in Section 3.8, the probe laser is locked via a beat-note scheme to a reference laser, which itself is locked to a reference cavity. A rubidium spectroscopy cell allows comparing the laser's absolute frequency to the rubidium D_2 line. This configuration directly provides the required absolute frequency reference for the probe transition.

The control laser is frequency-stabilized to a reference cavity, which provides the required frequency stability but does not serve as an absolute frequency reference. The absolute frequency is roughly determined using a wavemeter with a precision of approximately 100 MHz. Further fine-tuning is necessary to find the resonance, which has a linewidth in the order of only a few kHz. To that end, we illuminate the MOT with the control beam. When the two-photon resonance condition is satisfied, atoms are transferred to the Rydberg state and subsequently lost from the MOT via ionization or other decay channels, resulting in a reduction of the MOT fluorescence signal. This reduction is clearly visible in fluorescence imaging and can be used to optimize the control laser frequency to within a few MHz. The final fine-tuning is done with the Rydberg detection signals in the science chamber with the low-power probe (around 10 photons per pulse) to prevent power broadening and enable use of the SPCM.

[24] Control: Thorlabs A110TM-A Asphere, f = 6.24 mm; Probe: Thorlabs TC25APC-780 Achromat, f=25.08 mm.

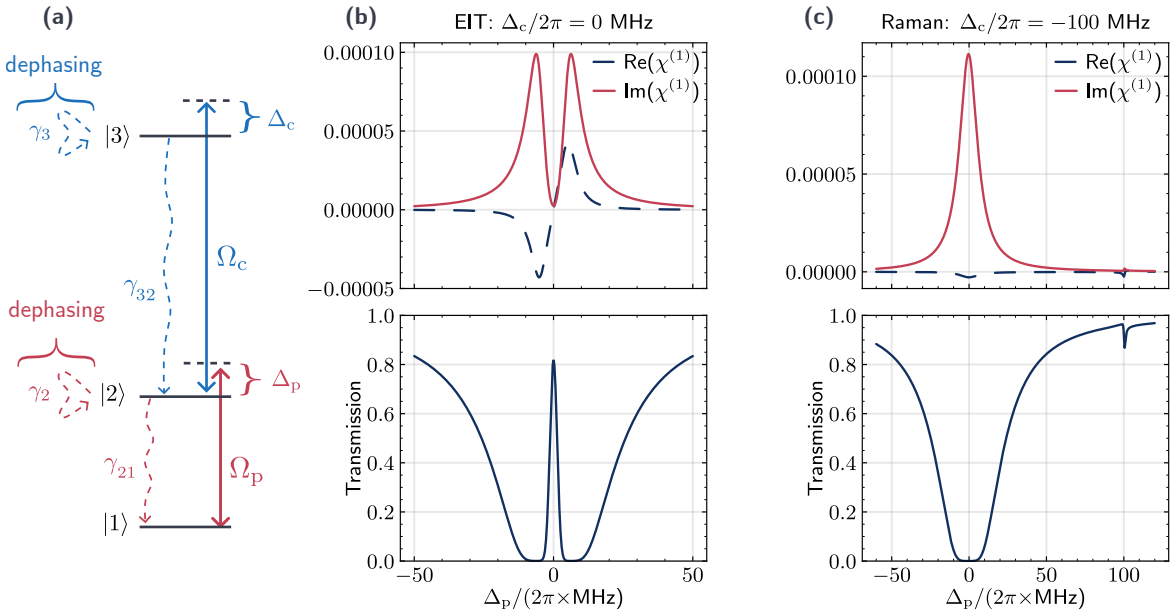

Figure 3.26: **(a):** Effective three level atom model for the calculation of the probe transmission spectrum shown in (b, c). The three levels $|1\rangle$, $|2\rangle$ and $|3\rangle$ are coupled by two laser beams with Rabi frequencies Ω_p and Ω_c and detunings Δ_p and Δ_c respectively. The excited state $|2\rangle$ ($|3\rangle$) decays with rates γ_{21} (γ_{32}) to the ground state $|1\rangle$ and dephases with rate γ_2 (γ_3). **(b, c):** Theoretical calculation of the real (dashed) and imaginary (solid) parts of the susceptibility $\chi^{(1)}$ in the top row, and transmission in the bottom row, as a function of the probe detuning Δ_p. The calculations are performed for a control Rabi frequency $\Omega_c = 2\pi \times 6$ MHz, decoherence rate $\Gamma_2 = \gamma_{21} + \gamma_2 = 2\pi \times 7.07$ MHz and $\Gamma_3 = \gamma_{32} + \gamma_3 = 2\pi \times 0.5$ MHz, atom density $n_{atom} = 9 \times 10^{14}$ m^{-3}, and interaction length $L = 1$ cm. The two panels show (b) electromagnetically induced transparency with $\Delta_c = 2\pi \times 0$ MHz and (c) two-photon Raman resonance with $\Delta_c = -2\pi \times 100$ MHz. In the Raman case, the two-photon resonance at $\Delta_p = -\Delta_c = 2\pi \times 100$ MHz is visible as a transmission dip. The dip would go all the way to zero without decay and dephasing.

3.7.4.3 Rydberg signature in probe light transmission spectrum

Once the atom cloud, the probe and the control beam are all coinciding and the laser frequencies are adjusted properly, it is possible to excite Rydberg atoms, which can be observed by measuring the transmission of the probe light with the SPCM.

The transmission of the probe is strongly modified at two-photon resonance with the control laser. This occurs either through electromagnetically induced transparency (EIT), which involves the Rydberg state when the probe laser is tuned close to the intermediate-state resonance. Alternatively, it occurs through direct two-photon Raman excitation of Rydberg atoms when the probe laser is detuned far beyond the intermediate-state linewidth, such that the intermediate state can be adiabatically eliminated.

To describe the transmission spectrum of the weak probe, we model the rubidium atom as a three-level system, as sketched in Fig. 3.26(a). This approach follows the description in Ref. [120].

We consider the states $|5S_{1/2}, F = 2, m_F = 2\rangle$, $|5P_{3/2}, F = 3, m_F = 3\rangle$, and $|68S_{1/2}, m_J = 1/2\rangle$. The hyperfine splitting of the Rydberg state is not resolved and can be ignored. To shorten the notation, these states are respectively identified with $|1\rangle$, $|2\rangle$, and $|3\rangle$ in the model.

In the rotating wave approximation, the interaction Hamiltonian of this three-level system can be written as [120]

$$H_{\text{int}} = -\hbar\left(\Delta_{\text{p}}\left|2\right\rangle\left\langle 2\right| + (\Delta_{\text{p}} + \Delta_{\text{c}})\left|3\right\rangle\left\langle 3\right| + \frac{\Omega_p}{2}\left(\left|1\right\rangle\left\langle 2\right| + \left|2\right\rangle\left\langle 1\right|\right) + \frac{\Omega_c}{2}\left(\left|2\right\rangle\left\langle 3\right| + \left|3\right\rangle\left\langle 2\right|\right)\right). \tag{3.13}$$

Here, Δ_{p} is the detuning of the probe laser with respect to the transition $|1\rangle \leftrightarrow |2\rangle$ (a positive value corresponds to blue detuning), Δ_{c} is the detuning of the control laser, Ω_{p} is the probe Rabi frequency, and Ω_{c} is the control Rabi frequency.

We utilize the master equation approach to describe the dynamics of the laser-driven system. The time evolution of the density matrix ρ of this system is given by [55]

$$\rho(t) = -\frac{i}{\hbar}\left[H_{\text{int}}(t), \rho(t)\right] + \sum_n \frac{1}{2}\left[2C_n\rho(t)C_n^\dagger - \rho(t)C_n^\dagger C_n - C_n^\dagger C_n\rho(t)\right], \tag{3.14}$$

where C_n are collapse operators. These operators correspond to the decay and dephasing channels of the system:

$$C_n \in \left\{\sqrt{\gamma_{21}}\left|1\right\rangle\left\langle 2\right|, \sqrt{\gamma_{32}}\left|2\right\rangle\left\langle 3\right|, \tag{3.15}$$

$$\sqrt{\gamma_2}\left|2\right\rangle\left\langle 2\right|, \sqrt{\gamma_3}\left|3\right\rangle\left\langle 3\right|\right\}. \tag{3.16}$$

Here, the first line describes the decay of states $|3\rangle$ to $|2\rangle$ and $|2\rangle$ to $|1\rangle$, as illustrated in Fig. 3.26(a), and the second line describes the dephasing of the excited states. Decay from the Rydberg state to the ground state is dipole-forbidden and therefore not included.

The linear susceptibility for the probe of this system is given by [121]

$$\chi^{(1)} = \frac{2\rho_{12}^{\text{ss}} n_{\text{atom}}|d_{1\leftrightarrow 2}|^2}{\hbar\varepsilon_0\Omega_{\text{p}}}, \tag{3.17}$$

where ρ_{12}^{ss} is the steady-state coherence between states $|1\rangle$ and $|2\rangle$, n_{atom} is the atom number density, $d_{1\leftrightarrow 2}$ is the electric dipole moment for the transition $|1\rangle \leftrightarrow |2\rangle$, and ϵ_0 is the vacuum permittivity. The susceptibility can be expressed analytically assuming a weak probe as [120]

$$\begin{aligned}\chi^{(1)} = {} & \frac{n_{\text{atom}}|d_{1\leftrightarrow 2}|^2}{\varepsilon_0\hbar} \\ & \times\left[\frac{4\delta|\Omega_{\text{c}}|^2 - 4\delta\Delta_{\text{p}} - 4\Delta_{\text{p}}\Gamma_3^2}{||\Omega_{\text{c}}|^2 + (\Gamma_2 + i2\Delta_{\text{p}})(\Gamma_3 + i2\delta)|^2}\right. \\ & \left. + i\frac{8\delta^2\Gamma_2 + 2\Gamma_3(|\Omega_{\text{c}}|^2 + \Gamma_3\Gamma_2)}{||\Omega_{\text{c}}|^2 + (\Gamma_2 + i2\Delta_{\text{p}})(\Gamma_3 + i2\delta)|^2}\right],\end{aligned} \tag{3.18}$$

where $\delta = \Delta_{\text{p}} - \Delta_{\text{c}}$ is the two-photon detuning, $\Gamma_3 = \gamma_{32} + \gamma_3$ is the coherence decay of state $|3\rangle$, and $\Gamma_2 = \gamma_{21} + \gamma_2$ is the coherence decay of state $|2\rangle$. For a weak probe, the susceptibility is probe power independent.

The transmission $T_{\text{probe}}(\Delta_{\text{p}})$ through the atomic medium of length L as a function of the probe

detuning follows from the susceptibility as [120, 121]

$$T_{\text{probe}}(\Delta_\text{p}) = \exp\left(-\frac{4\pi}{\lambda_{12}}\int_0^L \text{Im}\left[\sqrt{1+\chi^{(1)}(\Delta_\text{p}, x)}\right] \text{d}x\right). \tag{3.19}$$

Here, we treat the absorption only in one dimension and ignore the spatial extent of the laser. This approximation is valid because variations in the susceptibility are small over the cross-sectional area of the laser beams.

In Fig. 3.26(b, c), we plot the corresponding probe transmission spectrum for two different fixed detunings of the control laser.

In the first case, the control laser is on resonance ($\Delta_\text{c} = 0$). This results in the phenomenon of EIT. On two-photon resonance, the probe is transmitted through the atomic cloud rather than being absorbed. Without decay or dephasing, full transmission would be achieved. When these dissipative processes are taken into account, the transmission is reduced, as shown in Fig. 3.26(b).

In the second case, the control laser is far detuned ($|\Delta_\text{c}| \gg \Gamma_3, \Gamma_2$). As shown in Fig. 3.26(c), the transmission of the probe is modified when two-photon resonance is reached ($\Delta_\text{c} = -\Delta_\text{p}$). Instead of being transmitted through the medium, the probe and control lasers together form a two-photon Raman resonance [122], creating Rydberg atoms in the atomic cloud.

In the room-temperature setup, the transmitted spectra we observe are altered from the theoretical predictions in Fig. 3.26(b, c) by the quadrupole magnetic field in which the atoms are trapped. Specifically, the spatially varying magnetic field results in a position-dependent Zeeman shift of the atomic levels. Furthermore, the orientation of the magnetic field experienced by the atoms flips sign at the trap center. Consequently, the circularly polarized probe (control) laser drives the σ_+ (σ_-) transition in one half of the atomic cloud, as intended in the excitation scheme, but drives the σ_- (σ_+) transition in the other half. Therefore, on one side of the cloud, the excitation path (probe driving σ_+) is

$$|5\text{S}_{1/2}, F = 2, m_F = 2\rangle \rightarrow |5\text{P}_{3/2}, F = 3, m_F = 3\rangle \rightarrow |68\text{S}_{1/2}, m_J = 1/2\rangle\,, \tag{3.20}$$

while on the other side (probe driving σ_-), the excitation path is

$$|5\text{S}_{1/2}, F = 2, m_F = 2\rangle \rightarrow |5\text{P}_{3/2}, F = 3, m_F = 1\rangle \rightarrow |68\text{S}_{1/2}, m_J = -1/2\rangle\,. \tag{3.21}$$

Together with the spatially varying Zeeman shift, the resulting transmitted spectrum becomes asymmetric.

A measured EIT spectrum is shown in Fig. 3.27(a), and a two-photon resonance with a control detuning of 22.4 MHz is shown in Fig. 3.27(b). Theory curves are fitted to both spectra, which are obtained by numerically solving Eq. (3.19) using the Python package SciPy [123]. Here, we include the spatial dependence of the atomic number density, the Zeeman shift, and the excitation path. The fit parameters are the total atom number, the cloud temperature, the detuning and power of the control laser, and the total decoherence rates. The control power is converted into a position-dependent control Rabi frequency Ω_c, depending on the excitation path. For the fits, the magnetic trap center is assumed to be aligned with the focus of the probe and control lasers.

The values of the fit parameters are given in Table 3.4. Because the magnetic transport was only optimized after these spectra were measured, the fitted atom number and temperature differ from the results with absorption imaging presented in Section 3.6. The two spectra were captured on different days, one with the control counter-propagating (detuned control laser), and the other with the

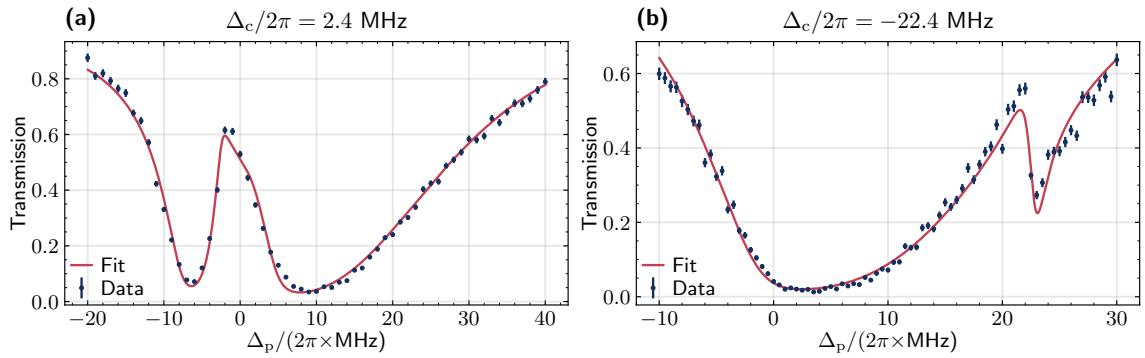

Figure 3.27: Measured probe transmission spectra close to two-photon resonance with the control laser. The Rydberg state $|68S_{1/2}\rangle$ is addressed. **(a):** Spectrum showing an EIT transmission window with a fitted control detuning of $\Delta_c/2\pi = 2.4$ MHz. **(b):** The control is further detuned to (fitted) $\Delta_c/2\pi = -22.4$ MHz creating a dip in transmission on two-photon resonance.

control co-propagating (EIT) with the probe. Therefore, we attribute the deviation of atom number and temperature between both fits to slight changes in the atom preparation, likely caused by a drift of the rubidium background pressure in the MOT chamber. The fitted decoherence rates Γ_2 of the state $|5P_{3/2}, F = 3\rangle$ deviate for the two measurements. The origin of that deviation is unclear. A possible cause is a worsening of the probe frequency lock that could have increased the laser noise during the EIT measurement.

Although the transmission spectrum is distorted due to the magnetic quadrupole trap, these measurements showcase, that the Rydberg excitation and optical detection is successfully implemented in the room-temperature setup. Since the optical setup can be used after the cryogenic upgrade of the experimental apparatus without adjustments, Rydberg excitation and detection will also be directly available, after the cryostat is installed.

3.7.4.4 Ionization of Rydberg atoms and ion detection

So far we have discussed the excitation and optical detection of Rydberg atoms. A second, complementary detection technique for Rydberg atoms, implemented in the room-temperature setup, is the

Table 3.4: Fit parameters extracted from the measured probe transmission spectra shown in Fig. 3.27. Column (a) shows results for the EIT spectrum with near-resonant control laser, column (b) shows results for the control detuned from resonance.

Quantity	Symbol	EIT (a)	Off-resonant (b)
Atom number	N	$(5.04 \pm 0.05) \times 10^7$	$(4.70 \pm 0.05) \times 10^7$
Temperature	T	$(489 \pm 9)\,\mu$K	$(422 \pm 8)\,\mu$K
Control power	-	(34.4 ± 0.7) mW	(7.3 ± 0.7) mW
Control detuning	Δ_c	(2.39 ± 0.08) MHz	(-22.36 ± 0.07) MHz
Rydberg state coherence decay rate	Γ_3	(1.3 ± 0.2) MHz	(1.2 ± 0.2) MHz
Intermediate state coherence decay rate	Γ_2	(7.8 ± 0.4) MHz	(6.3 ± 0.3) MHz

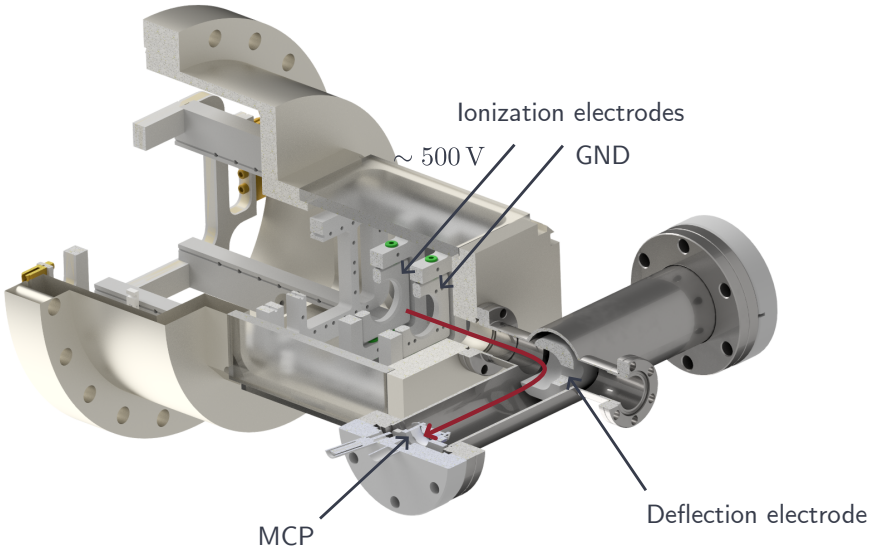

Figure 3.28: Cutaway view of a CAD rendering of the room-temperature ionization and ion-detection setup. The ion trajectory after field ionization is indicated by a red arrow. This figure was adapted with permission in [97].

ionization and subsequent ion detection using an MCP[25].

Here, we utilize the ability to field-ionize Rydberg atoms by applying an electric field. Due to the large distance of the valence electron from the core and the correspondingly weak binding energy, easy to produce electric field on the order of $100\,\mathrm{V\,cm^{-1}}$ are enough to ionize Rydberg atoms. The classical ionization threshold is simply given by the electric field strength, that creates an electric potential for the highly excited valence electron that is equal to its binding energy in Eq. (2.1).

A CAD of the room-temperature ionization and ion-detection setup designed by Hannes Busche is shown in Fig. 3.28. We installed a frame inside the vacuum chamber that hosts two ring electrodes for the field ionization. This simple configuration with two electrodes is used in the room-temperature setup for testing purposes and will be replaced in the cryogenic setup (see Section 4.1.1). The electrodes are symmetrically placed around the magnetic trap center in the science chamber, with an electrode to electrode distance of 1.7 cm. For field ionization, a high positive voltage up to 500 V is applied to one of the electrodes while the other is kept at ground potential. The corresponding electric field of up to $\sim 190\,\mathrm{V\,cm^{-1}}$ is sufficiently strong to ionize rubidium Rydberg atoms with principle quantum number above $n \approx 40$. After ionizing the Rydberg atoms, the electric field produced by the ionization electrodes also accelerates the ions out of the science chamber towards the vacuum cross attached to the science chamber, as illustrated in Fig. 3.28. A third electrode, the deflection electrode, deflects the ions 90° to the side, where they impinge onto the MCP and are detected. To deflect the ions, a high positive voltage around 200 V is applied to the deflection electrode. The exact required deflection voltage depends on the chosen ionization voltage. The small hole in the deflection electrode with a diameter of 4 mm allows the atomic cloud to pass through the electrode during the magnetic transport.

Towards the end of every pulse in the Rydberg excitation and detection pulse sequence, both the ionization and deflection voltage are rapidly switched on, and the ionization is started. For the rapid

[25] Hamamatsu F4655-11 MCP

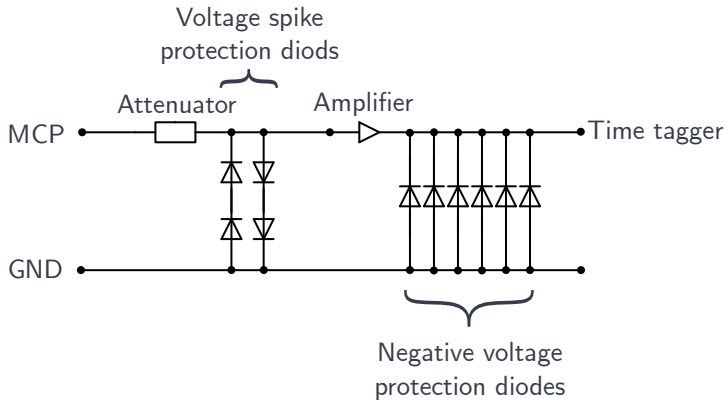

Figure 3.29: Sketch of the ion signal processing and protection circuit. The circuit contains fast-switching schottky diodes with low forward-voltage to protect the time tagger from voltage spikes and negative voltage values. The components and their functionality are specified in the main text.

switching, we utilize a high-voltage switch[26] with a rise time of 60 ns and a voltage rating of up to 500 V. The switch is triggered by the pulse generator.

Detecting ions with the MCP The channels of the MCP are electron multipliers that can create a measurable voltage pulse from just one ion. The gain of the MCP can be adjusted by adjusting the high voltage (< 2 kV) applied to it. We measure and time the ion signal using the time tagger. The pulses from the MCP need to be processed before they can be detected by the time tagger. In particular, the time tagger requires positive voltage input signals but the MCP output signals are negative voltage pulses. To invert the voltage of the short ion signal pulses (~ 500 ps duration) we use an RF-amplifier[27].

Another issue that needs to be addressed is the maximum rated input voltage range of the time tagger, which is −0.3 to 5 V. The pulse height produced by the MCP can vary strongly. In the worst case, a cosmic ray event could produce a signal in many channels simultaneously, creating a pulse that is orders of magnitudes larger than typical for the ion signal. Furthermore, imperfect impedance matching at the amplifier (i.e. due to saturation from a larger than typical signal) results in a reflection signal which can be of opposite polarity. If the reflected signal surpasses −0.3 V in amplitude, it might damage the time tagger. To protect against both, voltage spikes and negative voltage signals, we installed a protection circuit in the signal path from the MCP to the time tagger. The ion signal processing and protection circuit is sketched in Fig. 3.29. We attenuate the signal from the MCP using an RF-attenuator[28]. Any signal reflected by the RF-amplifier will pass the attenuator two more times and is strongly reduced in amplitude. This also prevents false counts at the time tagger. We tried out different combinations of MCP gain and attenuation and found that the best signal-to-noise ratio was achieved with the maximum MCP gain and an attenuation of −12 dB. We protect against voltage spikes using Schottky diodes[29] with fast switching times and a low forward voltage of about 0.25 V.

[26] CGC Instruments AMXT500-4EF
[27] Minicircuit ZX60-6013E-S+
[28] Minicircuit VAT-12+
[29] Toshiba 1SS315(TPH3,F)

Before the amplifier, two of these diodes are put in series in both direction between ground and the signal to cut off pulses exceeding ±0.5 V. After the amplifier, we utilize six of these diodes in parallel to protect the time tagger from potential negative voltages. We use six diodes to make the voltage cutoff sharper around −0.25 V. With the ion signal processing and protection circuit in place, we measured 200 ion signals with an oscilloscope[30] and found that the signals were all in a voltage range of −29 to 600 mV, with only one below −22 mV. This was deemed acceptable, and we connected the MCP to the time tagger.

Performance of ion detection We characterized the performance of the ion detection with focus on two key properties: the total ion detection efficiency and the second-order correlation function $g^{(2)}(\tau)$ of the ion detection signal. These characterization measurements were done together with Valerie Mauth and are also presented in her master thesis [114].

The dark count rate of the MCP is below 0.5 Hz and is therefore negligible on the ≈ 20 µs time-window where the ions arrive at the MCP. Dark counts can be triggered by light shining on the MCP, but due to our experiment geometry—shielding the MCP from direct line of sight to potential light sources—the dark count rate is unaffected by the lasers in our experiment and the room light.

To verify the integrity of the detection chain, including the MCP, signal processing circuit, and time tagger, we measured the second-order temporal correlation function $g^{(2)}(\tau)$ of the ion arrival times. The second-order correlation function quantifies temporal correlations in the ion detection events recorded by the time tagger. For an ideal single-ion detector operating without spurious correlations, we expect $g^{(2)}(\tau) \approx 1$, indicating that detection events are uncorrelated in time.

We compute the second-order correlation function from the discrete time-tagged data as follows. For each measurement pulse in the experimental sequence, the ion detection events are binned into time bins of width $\Delta t = 1$ ns. Each bin i in a given pulse contains either zero or one count, denoted $e_i \in \{0, 1\}$. The measurement is repeated over many pulses (1000 pulses per cycle and multiple cycles), and all quantities are averaged over these repetitions. The average detection rate per bin is $\bar{e} = \frac{1}{N}\sum_{i=1}^{N}\langle e_i\rangle$, where N is the total number of bins per pulse and $\langle\cdot\rangle$ denotes the average over all measurement repetitions. For a time lag $\tau_k = k\,\Delta t$ with integer $k \geq 1$, the correlation function is estimated as

$$\hat{g}^{(2)}(\tau_k) = \frac{\sum_{i=1}^{N-k}\langle e_i\, e_{i+k}\rangle}{(N-k)\,\bar{e}^{\,2}}. \tag{3.22}$$

This expression counts the number of coincident detection events separated by lag k, averaged over all measurement repetitions, and normalizes by the expected number of coincidences for uncorrelated events.

For the ion-detection characterization measurements, we drove Raman transitions to the Rydberg state $|68S_{1/2}\rangle$ with the control laser detuned by $\Delta_c = -45$ MHz and the probe by $\Delta_c = 45$ MHz. To speed up the data-accumulation, the probe laser was operated at above-single-photon power levels for the presented measurements, producing on average 8.5 ions per pulse. The measured correlation data for different ionization voltages is shown in Fig. 3.30(a, b). For any ionization voltage, a dead time of 6 ns is observed in the correlation function, corresponding to the dead time of the time tagger. Beyond the dead time, the ions are antibunching up to a delay of ~ 40 µs, followed by a bunching with $g^{(2)}(\tau)$ peaking at values between 1.05 and 1.10 at a delay of approximately 30 to 100 ns, depending on the ionization voltage. We attribute the antibunching to Coulomb repulsion between ions during their

[30] TELEDYNE LECROY WavePro 735Zi Oscilloscope

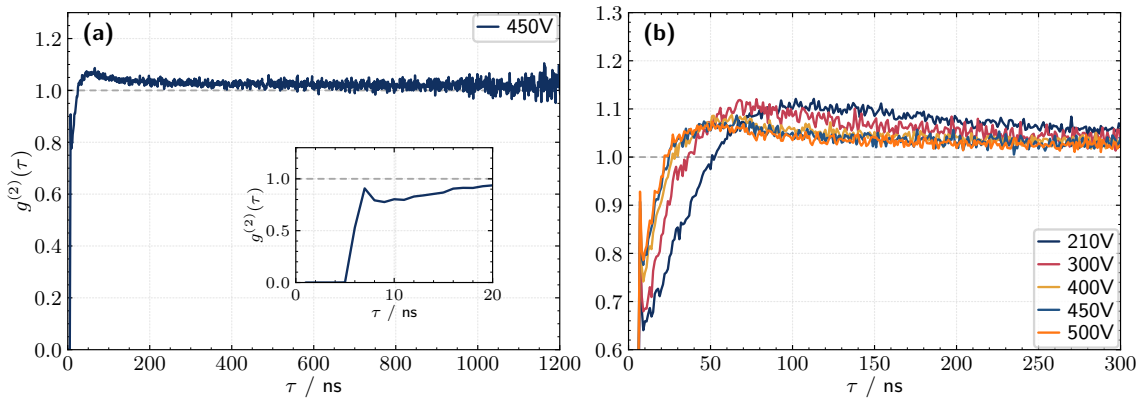

Figure 3.30: Second-order correlation function $g^{(2)}(\tau)$ of the ion detection signal as a function of the time lag τ. **(a):** Measurement results for an ionization voltage of 450 V for time lags of up to 1.2 µs together with a zoom in to the first 20 ns in the inset. **(b):** Zoom in to time lags of 0 to 300 ns with data for different ionization voltages. The deflection voltage was always adapted to the ionization voltage to maximize the overall detection efficiency. The data points are averaged over 240×10^3 Rydberg pulses. The data in this figure are also presented in [114].

flight to the MCP. Lower ionization voltages result in longer ion flight times, which should increase the cumulative effect of Coulomb repulsion and lead to stronger antibunching. This interpretation is supported by the result that lower ionization voltages correspond to stronger antibunching, as shown in Fig. 3.30(b).

In all measured $g^{(2)}(\tau)$ curves, the value at $\tau = 7$ ns is slightly enhanced compared to the subsequent points, as is most clearly visible in the inset of Fig. 3.30(a). Because this peak has a width of only a single bin and occurs immediately after the dead time, we assume that this is a technical artifact related to the time tagger. Otherwise, the measured $g^{(2)}(\tau)$ curves are smooth and no signatures of afterpulsing from the MCP or signal reflections from the RF amplifier—that would manifest as peaks—are visible.

To measure the ion-detection efficiency, we simultaneously record the probe transmission spectrum and the ion detection signal with the probe power reduced to a few photons per pulse. In Fig. 3.31 we present the measured photon counts per pulse in panel (a) and ion counts per pulse in panel (b) as functions of probe detuning, together with their respective background measurements results. To extract the detection efficiency, we compare the number of absorbed photons to the number of detected ions at the two-photon resonance (probe detuning $\Delta_p = 45$ MHz). The photon count with atoms present is offset from the reference due to residual single-photon absorption, as the probe detuning of around 45 MHz is not large enough to completely suppress probe absorption.

At two-photon resonance, the photon count drops from a baseline of approximately 9.0 photons per pulse to 7.8 photons per pulse, indicating that 1.2 photons per pulse are absorbed on average via the two-photon transition. These absorbed photon corresponds to the creation of Rydberg atoms. These Rydberg atoms are subsequently field-ionized by the ionization electrodes, and detected at the MCP. The measured ion signal at resonance, shown in Fig. 3.31(b), yields 0.21 detected ions per pulse. Taking the ratio of detected ions to absorbed photons gives a total ion-detection efficiency of approximately 17%. This value represents the total detection efficiency for the complete chain from Rydberg atom creation to recorded ion signal. Importantly, we cannot differentiate between the

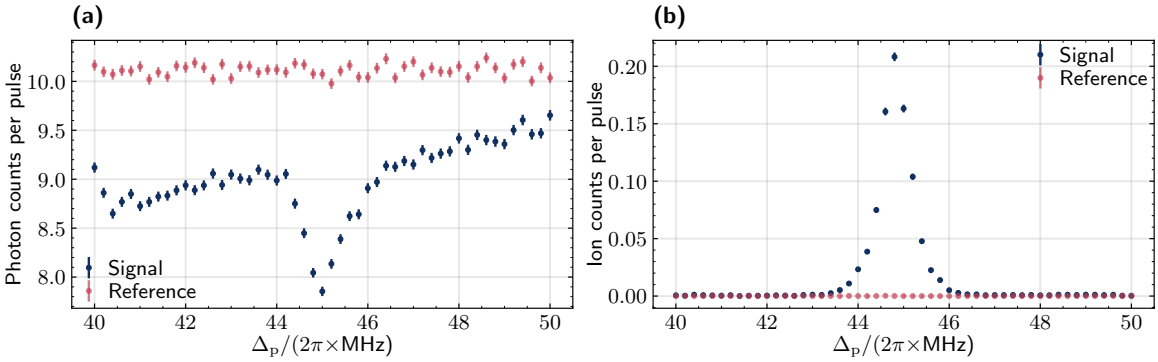

Figure 3.31: Measured photon and ion counts for ion detection efficiency characterization. **(a):** Photon counts per pulse as a function of probe detuning Δ_p with the control laser detuned by $\Delta_c = -45\,\text{MHz}$. The blue dots show measurements with atoms present, while the red dots show reference measurements without atoms. The drop in photon counts at the two-photon resonance ($\Delta_p = 45\,\text{MHz}$) indicates absorption via the Rydberg transition. The shown photon counts are calibrated, accounting for optical losses in the detection path and the SPCM quantum efficiency. **(b):** Ion counts per pulse detected at the MCP measured simultaneously to the probe transmission in (a). The peak at two-photon resonance confirms successful Rydberg excitation followed by field ionization. Data in both panels are averaged over 15×10^3 measurement pulses. The data in this figure are also presented in [114].

efficiencies of the individual processes involved: the field-ionization efficiency, the fraction of ions that successfully reach the MCP (ion collection efficiency), the MCP detection efficiency, as well as the signal counting efficiency at the time tagger. Each of these processes likely contributes losses that compound to produce the observed overall efficiency. An additional loss mechanism is spontaneous decay of the Rydberg state before field ionization can occur. The optical excitation pulses have a duration of 12 µs, and the ionization pulse is triggered 0.5 µs after the optical pulses end. Rydberg atoms are created throughout the excitation pulse and can subsequently decay back to lower-lying states, becoming unavailable for ionization. For the Rydberg state $|68S_{1/2}\rangle$, the lifetime, excluding blackbody radiation-induced transitions to other Rydberg states, is 340 µs [55]. This lifetime is one order of magnitude longer than the pulse duration, therefore spontaneous decay during the excitation and ionization sequence contributes only weakly to the overall detection inefficiency.

We can compare the measured 17% detection efficiency to another mature rubidium Rydberg experiment in our group using the same MCP model, which achieved detection efficiencies of up to 29% [65, 124]. This comparison suggests that substantial improvements are possible.

The detection efficiency could be increased by improving the guiding of the ions from the ionization region to the MCP using additional electrodes. Such electrodes could collimate the ion beam to reduce losses from ions hitting the vacuum chamber walls or electrode surfaces before reaching the MCP. A neighboring ytterbium experiment in our group found that the MCP detection efficiency (using a similar model from the same manufacturer) is strongly dependent on both the impact angle and the position on the detector surface. Consequently, controlled ion steering should be used to optimize the impact angle and position at which ions strike the MCP surface.

However, such optimization is not possible in the current room-temperature setup, as no further electrodes beyond the ionization and deflection electrodes are present. The ionization and deflection voltages have already been optimized for the measurements presented here. In the cryogenic setup,

additional electrodes will be installed, as detailed in Section 4.2.4, which will allow for more sophisticated steering of the ion trajectory to optimize the detection efficiency.

3.8 Laser system

Our ultracold rubidium experiment requires a laser system that provides light at multiple wavelengths with stringent requirements on frequency stability, linewidth, and power control. Specifically for Rydberg excitation, it is desired to have laser linewidths in the kHz regime, matching the narrow Rydberg transition linewidths. The primary wavelengths are 780 nm for addressing the rubidium D_2 line for the cold atom preparation and 480 nm for the two-photon Rydberg excitation scheme.

The laser setup was set up and expanded over the years together with Hannes Busche and several of the supervised master and bachelor students. Detailed description, including characterization measurements can be found in the theses of Julia Gamper [97, 125], Valerie Mauth [92], Florian Pausewang [126], and Samuel Germer [127]. Here, we will only provide an overview of the laser system.

We use commercial diode lasers (Toptica DLpro) as the foundation of the system. For the MOT cooler beam, which requires higher power, we use a commercial diode laser with integrated tapered amplifier (Toptica TApro) to reach the necessary intensity. The 480 nm control laser for Rydberg excitation is generated using a commercial system (Toptica SHGpro) with integrated second harmonic generation from a 960 nm seed.

The commercial diode lasers have free-running linewidths of a few MHz. To achieve the required performance, we implement a hierarchical frequency stabilization scheme. A reference laser at 780 nm is locked to an ultrastable reference cavity (Stable Laser Systems Serial no. 68) using the Pound-Drever-Hall (PDH) technique [128]. The 960 nm seed laser for the blue control laser is similarly locked to the same reference cavity, which is coated for both wavelengths. Before reaching the reference cavity, both beams are phase-modulated using fiber-coupled electro-optic modulators (EOMs) to generate sidebands. The lasers are then locked to these sidebands, allowing frequency tuning by adjusting the sideband modulation frequency. All other 780 nm lasers are locked via beat-note frequency offset locking to the reference laser. The beat-note signal between each laser and the reference is detected with a photodiode and fed, along with a reference offset frequency, into a digital phase-frequency discriminator (ADF4007 High Frequency Divider/PLL Synthesizer from Analog Devices), which converts the frequency and phase difference to an error signal. We use commercial (Toptica FALCpro) and home-built PID controllers to close the feedback loops.

Beyond frequency stabilization, the laser system provides control over timing, intensity, and pulse shaping. All lasers pass through acousto–optic modulators (AOMs) before being fiber-coupled and distributed to the experiment. The AOMs enable fast switching (100 ns timescale) and power adjustment. The MOT cooler and repumper lasers are additionally intensity-stabilized using pick-off beams to ensure consistent atom numbers across experimental cycles. For Rydberg excitation, an arbitrary waveform generator (AWG) controls the AOM drive signals to generate shaped pulses (Gaussian, Tukey, or other profiles). Mechanical shutters are installed in all beam paths to compensate the limited extinction ratio of AOMs.

CHAPTER 4

Preparation of cryogenic experiments

In the previous chapter, we discussed the preparation of cold atoms as well as the creation and detection of Rydberg atoms within a room-temperature version of the final experimental setup. The missing components are a cryostat that provides the cryogenic environment required to operate the HBAR, a chip-based platform that hosts the HBAR, and a trapping mechanism for the ultracold atomic cloud in close proximity to the HBAR surface.

This chapter describes our efforts to realize this cryogenic extension. We begin by describing the originally planned custom cryostat that was to be provided by Cryovac[1] at the end of 2023. After more than two years of delays, it became clear that Cryovac was unable to deliver the system. Therefore, we initiated a redesign with the company Kiutra,[2] which is briefly outlined. This cryostat is scheduled to be delivered in the third quarter of 2026. Subsequently, we describe the superconducting atom chips that we have designed and built.

4.1 Cryogenic setup

As discussed in Chapter 2, a cryogenic environment is a fundamental requirement for the experimental apparatus, because the extraordinary long lifetime of the HBAR at GHz operation frequency is only achieved at low temperatures. More importantly, the mechanical modes at resonance frequencies around 5 GHz are highly occupied at room temperatures according to Eq. (2.19), impeding observation of quantum phenomena. To fully freeze out the mechanical modes, cryogenic temperatures in the 10 mK regime are required. As explained previously in Section 3.1, these temperatures are only achieved within a dilution refrigerator [79], but this type of cryostat is very costly compared to (closed-cycle or flow) helium cryostats operating at temperatures around 4 K. Furthermore, the optical access and the atomic source for ultra-cold atom experiments are difficult to integrate within a dilution refrigerator, increasing the complexity of the experimental setup significantly. That is why, to our knowledge, ultra-cold atom experiments within a dilution refrigerator are rarely pursued [129–132]. To reduce complexity and cost of the experimental apparatus, we decided to use a helium closed-cycle cryostat to produce a 4 K environment for the experiment. We discuss the reason for using a closed-cycle cryostat compared to a flow-cryostat in Section 3.1.

[1] CRYOVAC GmbH & Co. KG, https://www.cryovac.de

[2] kiutra GmbH, https://kiutra.com

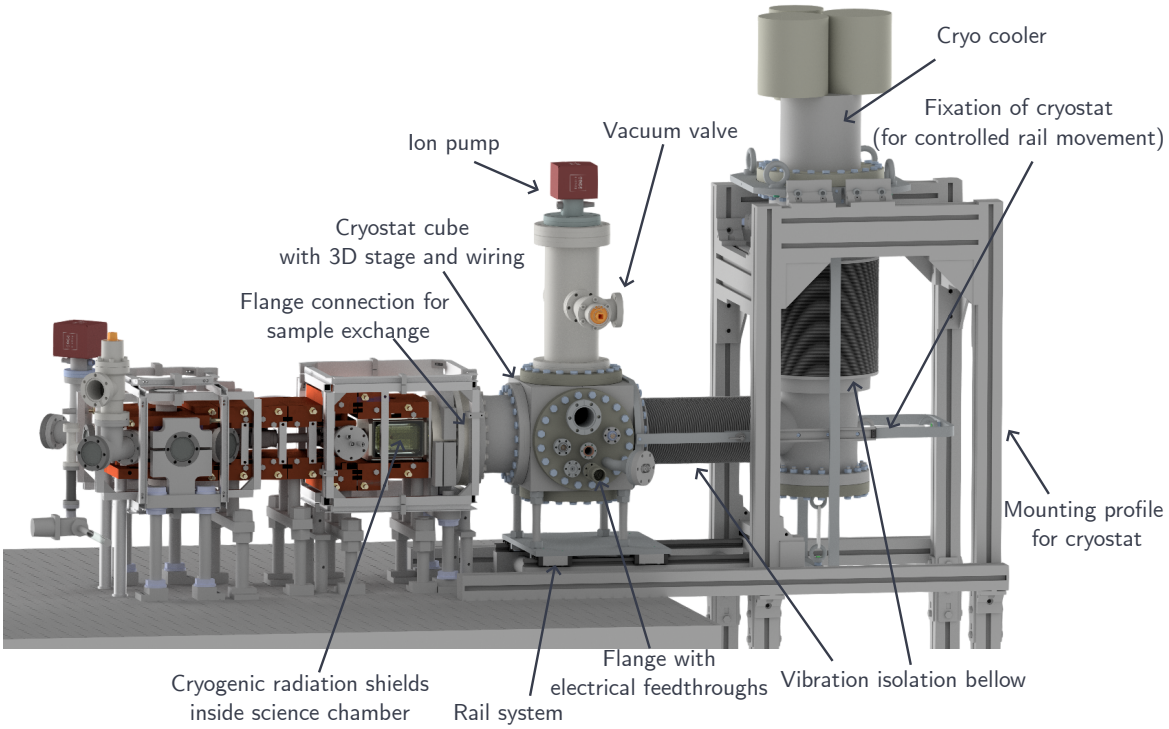

Figure 4.1: CAD rendering of the planned cryogenic experimental setup with Cryovav's cryostat design. The closed-cycle pulse-tube cryocooler is mounted on an aluminum profile and vibrationally isolated from the experimental region via two bellows. The cryostat cube, which contains the three-axis translation stage for the sample, is mounted on a rail system to allow retraction from the science chamber for sample exchange. Electrical feedthroughs provide DC and RF connections to the cryogenic sample. An ion pump provides vacuum pumping during normal operation, while a turbo pump can be connected to the setup via the vacuum valve for initial pumpdown.

4.1.1 Cryogenic extension of room-temperature setup

An overview of the planned experimental apparatus, adapted from the room-temperature version shown in Fig. 3.2 and incorporating the cryostat, is presented in Fig. 4.1. In the following, we discuss the design decisions and specifications of the custom cryostat that was intended to provide the cryogenic environment.

Sample accessibility and exchange To facilitate rapid sample exchange during the experimental development phase, the cryostat should be mounted on rails, as shown in Fig. 4.1. This enables the cryostat to be disconnected and pulled away from the science chamber for sample exchange. As mentioned in Section 3.1, the experimental design is constructed with a valve between the science chamber and the MOT chamber, allowing a maintained vacuum in the MOT region during sample exchange. The heat exchanger hosting the experimental sample and cryogenic shields should be mounted on a three-axis translation stage, allowing fine adjustment of the atom chip position relative to the optical system. This design ensures that the external optics can remain fixed during sample exchanges, avoiding time-consuming realignment procedures. We anticipate that the cryogenic

pumping provided by the cold surfaces will eliminate the need for repeated vacuum baking cycles after sample exchanges.

Cooling requirements and thermal management The cryostat will have to provide sufficient cooling power to maintain the experimental region at approximately 4 K. We specified 1 W of cooling power at the 4.2 K stage, with a guaranteed base temperature below 5 K. This cooling power was chosen to compensate for heat loads from optical access windows, electrical feedthroughs, and thermal radiation from the surrounding structures in the vacuum chamber. To achieve this base temperature and cooling power, the design incorporates two nested radiation shields surrounding the experimental region: An outer shield at 40 to 50 K to minimize thermal radiation from the room-temperature environment, and an inner shield at approximately 4 K that directly encloses the experimental volume. These radiation shields are located around the science region inside the science chamber, as depicted in Fig. 4.2.

Experimental volume and access requirements We defined a minimum cubic experimental volume of 3 cm × 3 cm × 3 cm for the cryogenic region, enclosed by the two nested radiation shields. This volume was chosen as a compromise between providing sufficient space for the ionization electrodes, sample holder, and associated wiring while keeping the region compact enough to position the magnetic transport coils in close proximity to the atoms, as detailed in Section 3.6.2.

The experimental region requires optical and physical access along three orthogonal axes. First, optical access along the horizontal axis is needed for the Rydberg addressing lasers, with unobstructed transmission through the chamber to enable detection. Second, optical access along the vertical axis is required for absorption imaging of the atom cloud. Third, a physical opening in the radiation shields is needed to provide a path for atoms to be magnetically transported into the experimental region.

To realize these access requirements, the radiation shields will have holes with anti-reflection-coated windows on the horizontal and vertical axes, while an opening without a window is located on the transport axis, as shown in Fig. 4.2. To allow absorption imaging along the vertical axis, the atom chip must be oriented facing toward the magnetic transport direction, as shown in Fig. 4.2.

Vibration isolation and vacuum compatibility The strength of the coupling between HBAR and Rydberg atoms depends strongly on the distance between the two constituents, as described approximately by Eq. (2.13). Minimizing mechanical vibrations of the sample position is critical for maintaining stable laser addressing of the trapped atom cloud. Therefore, we specified that vibration amplitudes at the experimental region should not exceed 10 nm. This level of vibration can be compared to the probe focus beam waist of 8 µm, which indicates that this is a conservative estimate of the acceptable level of vibration.

To achieve this stringent requirement, the cryostat design employs a hybrid cooling architecture: A two-stage heat exchanger at the sample stage vaporizes liquid helium to generate the ~ 4 K environment with ultralow vibrations. The inner stage of the heat exchanger cools the 4.2 K radiation shield and experimental region, while the outer stage maintains the 40 to 50 K radiation shield. The helium is cooled and liquefied at the cold head of a standard closed-cycle pulse-tube cryocooler.[3] This combination of a closed-cycle dry cryostat with a closed-cycle wet cryostat for the experimental interface decouples the sample from vibrations produced by the compressor and cold head.

[3] Sumitomo Heavy Industries, Ltd.: RDK-408D2 cryocooler with CSW-71 compressor.

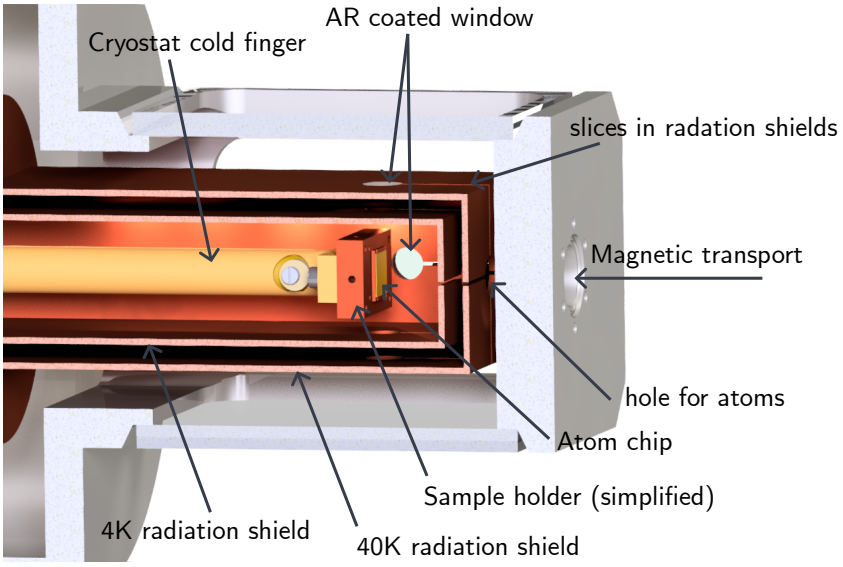

Figure 4.2: Cutaway CAD view of the science chamber, revealing the radiation shields, sample holder, and atom chip. For visual clarity, the electrode cage that is mounted to the sample holder (see Section 4.2.4) is not included in this figure.

The entire system is designed for ultrahigh-vacuum (UHV) compatibility, employing exclusively UHV-compatible materials and conflat (CF) flanges to ensure integration with the ultracold atom apparatus. Additionally, the drift of the sample position during cool-down is designed to be below 1 µm over the entire temperature range from room temperature to 4 K, enabling initial optical alignment at room temperature without significant readjustment upon cooldown.

Electrical connections and feedthroughs The cryostat design incorporates several types of electrical connections between the cryogenic sample and room-temperature electronics. While a single pair of DC wires would be sufficient for the magnetic wire trap on the atom chip (see Section 4.2.1), we specified three pairs of twisted DC wires capable of carrying currents up to 2 A, to provide flexibility for future trap configurations or additional magnetic field control. Similarly, the cryostat was specified to have ten DC wires rated for voltages up to 500 V for electric field compensation and field ionization of the Rydberg atoms, allowing for versatile electrode configurations and optimization of field geometries. Two RF feedthroughs supporting frequencies up to 20 GHz should provide the capability for external driving of the HBAR or direct microwave addressing of the atoms.

4.1.2 Cryostat redesign

After it became apparent early 2025, that Cryovac was unable to deliver the custom cryostat, we started a redesign and reordering process. Our market research in 2025 brought the company Kiutra to our attention. Back in 2022, during the original market research for suitable companies that can provide a custom cryostat fulfilling our requirements, Kiutra did not offer UHV compatible cryostat. In the following years, they developed the cryostat model "T-Type Optical" for trapped ion quantum computing and quantum optics. This off-the-shelf product fulfills our requirements with regard to

vacuum and optical access, and electric wiring but is not directly integrable into our existing vacuum system. A customized solution of the cryostat, fit to our experiment, is available, which we ordered.

This custom cryostat has a specified base temperature of 4.8 K, and a cooling power of 160 mW at 6 K. In contrast to Cryovac's specifications, these values already account for thermal loads from feedlines and thermal radiation. The main heat source that is not included is Joule heating, which will arise from the up to 2 A current delivered to the atom chip. The primary bottlenecks for Joule heating are the non-superconducting wire bonds, and the flexible printed circuit board (PCB) connecting the atom chip to the cryogenic feedlines (see Section 4.2.4).

To estimate the dissipated power in the aluminum wire bonds and the copper conductor on the flexible PCBs, the resistivity of both materials at cryogenic temperatures needs to be known. The residual resistance ratio (RRR) at cryogenic temperatures relative to room-temperature values strongly depends on the material purity [133, 134]. However, the purity of the aluminum and copper is unknown to us. For a rough estimate of the Joule heating, we adopt an RRR of 10 for both materials, which is conservative compared to data found in the literature [133–135]. For the flexible PCB (see Section 4.2.4.2), we consider a rectangular copper conductor with a length of 50 mm, width of 2 mm, and height of 35 µm. Using a resistivity of $1.5 \times 10^{-8}\,\Omega\,\mathrm{m}$ at room-temperature [134] and a contact resistance of 1 mΩ, the total resistance is approximately 3 mΩ at 4 K, yielding a Joule heating of 12 mW. For the wire bonds, we assume a total of 20 cylindrical aluminum bonds per chip side, each with a diameter of 25 µm and length of 5 mm. Using an aluminum resistivity of $2.4 \times 10^{-8}\,\Omega\,\mathrm{m}$ at room-temperature [134] and a contact resistance of 10 mΩ, the resistance of a wire bonds is approximately 44 mΩ at 4 K, resulting in a combined Joule heating of 18 mW. The total Joule heating is therefore estimated to be 30 mW, which is well below the 160 mW cooling capacity available at 6 K, providing sufficient thermal margin for reliable operation. This indicates that the cooling power is sufficient to counteract the joule heating.

Should Joule heating prove problematic in the setup, the wire bonds and copper conductors on the flexible PCB could be replaced by macroscopic solder connections to copper wires, as demonstrated in Ref. [136].

The custom cryostat from Kiutra features a proprietary vibration-damping system that does not rely on a secondary wet closed-cycle stage, thereby reducing the operational and maintenance complexity of the cryostat. This vibration-damping system requires the cryostat to be mounted directly to the optical table.

As a consequence, our requirement to mount the cryostat on rails has to be relaxed. Instead, the vacuum chamber needs to be translated when exchanging the sample. A design, in which the vacuum chamber itself is mounted on rails, is currently being pursued. However, as of the submission date of this thesis, this design is still under development and therefore lies outside the scope of this work. Other groups have demonstrated that vacuum systems mounted on rails can be repositioned with high reproducibility [137].

The cryostat does not include a three-dimensional positioning stage for the sample holder. In the absence of such a stage, it may be necessary to realign the probe and control optics around the chamber after each sample exchange.

4.2 Atom chip for the cryogenic experiments

Interfacing the HBAR with Rydberg atoms, as outlined in Section 2.3, requires positioning of the rubidium atoms close ($\sim 50\,\mu$m) to the HBAR surface to enable strong dipole–dipole coupling. The use of a dedicated trapping mechanism integrated with the HBAR substrate is motivated by the need to achieve this proximity with precise position control. In this section, we describe the design and implementation of a superconducting atom chip—a chip-based device capable of magnetically trapping ultracold atoms—as our chosen approach to fulfill these requirements.

The atomic cloud is transported to the science chamber using a magnetic transport and then held in place by a magnetic quadrupole field generated from the last transport coil. From this starting point, there are different routes for the atom cloud to be positioned above the HBAR. The cloud can either be kept in a magnetic trap or transferred to an optical dipole trap.

The final trap should offer precise control over the atom cloud position relative to the chip surface for two reasons. First, the dipole–dipole coupling strength scales strongly with distance, making fine adjustment of the atom–HBAR separation critical for optimizing the interaction. Second, controllable positioning enables systematic characterization of stray electric fields near the surface by monitoring residual DC Stark shifts of the Rydberg states as a function of position. This capability could be valuable for identifying and mitigating sources of field inhomogeneity that could degrade the coherence of the Rydberg excitation.

We decided against using an optical trap because the high-power laser required for optical trapping could potentially scatter and be absorbed by nearby surfaces and the optical windows, which could cause undesirable heating. Instead, we decided to use magnetic wire traps, which are well established for positioning atoms close to surfaces [138–140]. Using superconducting material enables their implementation in cryogenic environment. In contrast to external magnetic coils, on-chip wires can generate much stronger and more controllable magnetic field gradients close to the surface due to the small spatial scale of the current-carrying structures. In combination with a magnetic bias field—that can be produced by macroscopic coils outside the vacuum chamber—magnetic traps close to the surface can be formed. The strong and controllable gradients make these magnetic wire traps a suitable solution for experiments requiring atom–surface separations in the micrometer to millimeter range.

Another practical advantage of the on-chip approach is that the HBAR already needs a substrate chip to provide mechanical support. Integrating the magnetic trapping structures directly onto this chip ensures that the trap position is automatically coupled to the HBAR position, making the relative atom–HBAR distance insensitive to mechanical drift of the entire assembly. This co-integration simplifies alignment and enhances the stability of the experimental geometry. The magnetic trapping wires can be fabricated from superconducting materials, allowing them to carry the required currents without resistive heating, thereby minimizing the thermal load on the cryogenic system [39, 141, 142].

Figure 4.3 depicts a schematic overview of our atom chip design, which realizes the Rydberg-HBAR hybrid geometry shown in Fig. 2.4. The chip consists of an 11 mm × 11 mm sapphire substrate coated with a gold ground plane. Superconducting niobium wires are patterned on top of the gold layer to form the magnetic Z-wire trap, which provides three-dimensional magnetic confinement for the ultracold atoms (the trap design is discussed in Section 4.2.1). The HBAR is positioned at the center of the chip, elevated above the surface by polymer spacers (SU8 photoresist). This elevation serves to acoustically decouple the HBAR from the substrate. The spacers support the HBAR only at its edges, where the mechanical displacement of the acoustic mode is minimal, thereby preventing dissipation of mechanical energy into the chip substrate. The atoms are trapped approximately 50 µm above the

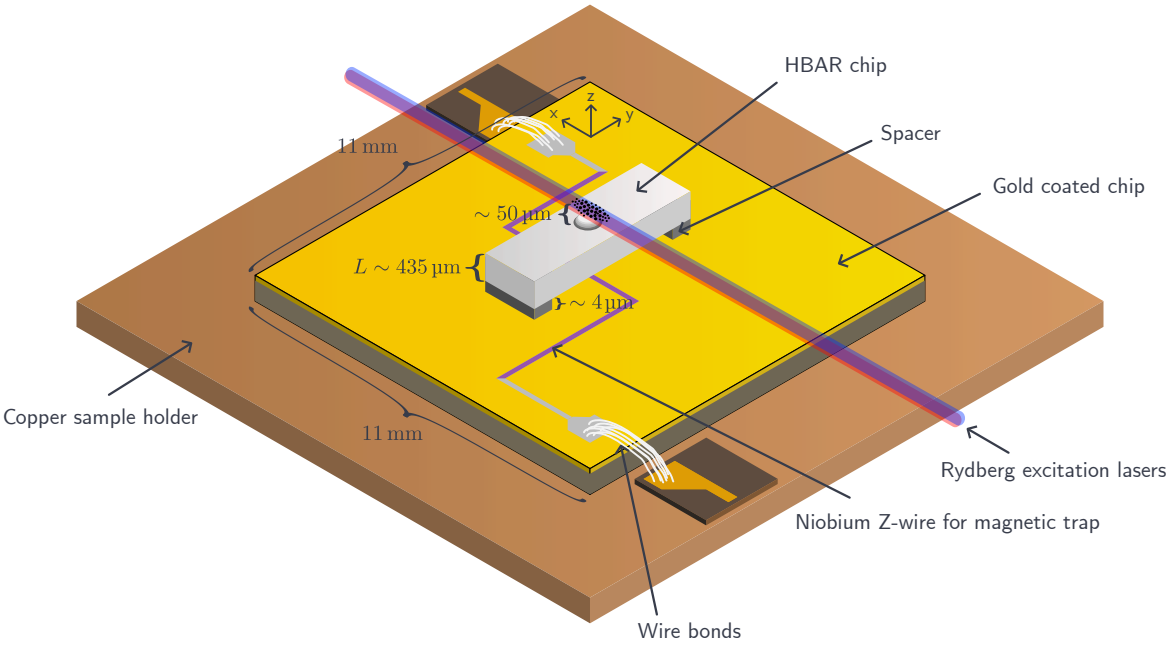

Figure 4.3: Schematic overview of the atom chip design for interfacing ultracold atoms with the HBAR. The 11 mm × 11 mm sapphire substrate is coated with gold and patterned with superconducting niobium wires forming a Z-wire magnetic trap. The Z-part of the niobium structured for the trap is colored in violet for visual clarity. The chip requires a 1 mm clearance at the edges for the lithography processes. Therefore, the niobium structures are constrained to a 9 mm × 9 mm central area. The HBAR (shown at the center) is elevated above the chip surface by polymer spacers. The atom clouded is trapped closely above the HBAR surface. This geometry realizes the experimental configuration sketched in Fig. 2.4. This figure is adapted with permission from [70].

HBAR surface, where they can couple to the evanescent electric field of the resonator. This trap position corresponds to a distance of about 0.5 mm from the chip surface due to the 435 µm height of the HBAR substrate. For the fabrication of the atom chips, we collaborate with the group of Peter Schüffelgen, which has access to the cleanroom facilities at Forschungszentrum Jülich (see Section 4.2.3.3).

Throughout this section, we adopt a coordinate system aligned with the atom chip geometry to maintain consistency with the theoretical discussion in Chapter 2. In this coordinate system, the z-axis points perpendicular to and away from the chip surface (or HBAR surface), matching the coordinate convention used for the hybrid system analysis. However, as described in Section 4.1.1, the atom chip is oriented facing toward the magnetic transport direction in the experimental setup. Consequently, the chip-frame z-axis corresponds to the horizontal direction in the laboratory frame, while the vertical direction in the laboratory aligns with the chip-frame y-axis. This rotation of the coordinate system relative to the lab frame is noted in the relevant figures and must be considered when interpreting gravitational effects on the trap potential.

In the following, we describe the specific implementation of the atom chip approach for our cryogenic experiments. First, the magnetic Z-wire trap design is discussed. We then detail the planned evaporative cooling in the cryogenic experiment. Afterward, we present the first-generation atom chip which incorporates a coplanar waveguide resonator for testing Rydberg atom coupling and readout near the surface. Finally, we discuss the sample holder assembly that provides mechanical support,

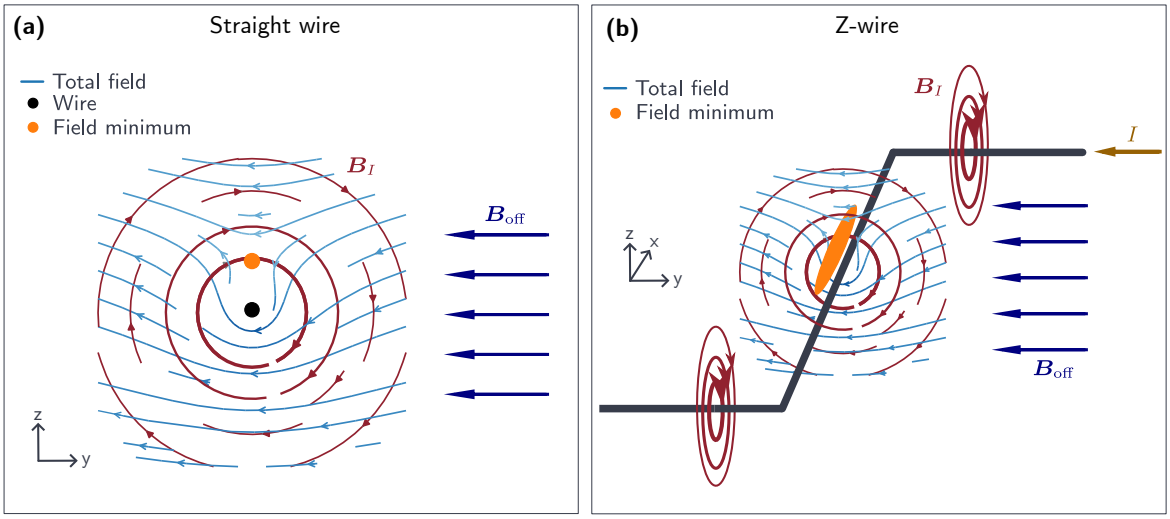

Figure 4.4: **(a):** Schematic of a magnetic trap formed by a straight current-carrying wire combined with a perpendicular bias field. This configuration creates a two-dimensional trapping potential over the wire. **(b):** Bending the wire into a Z-shape adds confinement along the wire axis, forming a three-dimensional trap with a cigar-shaped trapping volume along the central wire.

thermal anchoring, and electrical connectivity for the atom chip within the cryogenic environment.

4.2.1 Magnetic Z-wire trap

As discussed in Section 3.3, magnetic traps for neutral atoms rely on the Zeeman energy shift (see Eq. (3.2)), which is proportional to the magnetic field magnitude. A current I flowing through a straight wire produces a circular magnetic field $\boldsymbol{B}_I$ that decreases with distance from the wire as $1/r^2$. To create a trapping potential with a field minimum, a homogeneous bias field $\boldsymbol{B}_{\text{off}}$ is applied perpendicularly to the wire, as depicted in Fig. 4.4(a). At a specific distance r_0 from the wire, the bias field and the wire-induced field cancel exactly, creating a magnetic field minimum. Rotating $\boldsymbol{B}_{\text{off}}$ about the wire correspondingly rotates the minimum position. This configuration confines low-field-seeking atoms in the plane perpendicular to the wire, but provides no confinement along the wire direction.

To achieve three-dimensional confinement, the wire is shaped into a Z-configuration, as shown in Fig. 4.4(b). The central segment of the Z-wire creates the transverse confinement as described above. The two bent segments generate an additional magnetic field component that produces a quadrupole-like field along the central wire axis. This field has its minimum at the center of the Z-structure, providing the necessary longitudinal confinement. Importantly, because the trap minimum is displaced from the central wire by the distance r_0, the field at the trap center remains finite due to the contributions from the bent segments. This nonzero bias field at the trap minimum prevents Majorana spin-flips (see the magnetic trap discussion in Section 3.3), enabling trapping of colder atom clouds compared to pure quadrupole traps.

For a Z-wire trap with a central wire segment of length L, the magnetic field near the trap center has a harmonic shape and is approximately cylinder symmetric. The scaling behavior of the trap

parameters can be expressed analytically (with $r_0 \ll L$) [143]:

$$r_0 \propto \frac{I}{B_{\text{off}}}, \quad \omega_{\text{rad}} \propto \sqrt{\frac{B_{\text{off}}^5 L^2}{I^4}}, \quad \omega_{\text{ax}} \propto \sqrt{\frac{B_{\text{off}}}{L^2}}, \tag{4.1}$$

where ω_{rad} is the trap frequency in the radial direction and ω_{ax} is the trap frequency along the central wire axis. These scaling relations demonstrate that the trap minimum distance to the wire can be controlled via the current-to-bias-field ratio, while the trap frequencies depend strongly on both B_{off} and L. The axial trap frequency ω_{ax} is typically much weaker than the radial frequencies, resulting in a cigar-shaped atom cloud elongated along the central wire, as illustrated in Fig. 4.4(b). Rotating $\boldsymbol{B}_{\text{off}}$ about the central wire correspondingly rotates the minimum position, but the bend wire segments need to be considered.

To position atoms at larger distances, one must either increase the current I or decrease the bias field B_{off}, according to Eq. (4.1). However, the radial trap frequency scales as $\omega_{\text{rad}} \propto B_{\text{off}}^{5/2} I^{-2}$, meaning that reducing B_{off} weakens the trap more rapidly than increasing I. Consequently, trapping at larger distances is more effectively achieved by operating at higher currents rather than lower bias fields.

To estimate the required current, we simulated the Z-wire magnetic trap numerically using the Python package Magpylib [113], following the same approach as for the magnetic transport system (see Section 3.6.4). We model the superconducting wire as an array of thin parallel current-carrying lines to account for its finite width. Initial simulations revealed that confining atoms at temperatures on the order of 100 µK at a trap distance of approximately 0.5 mm above the wire requires currents of around 2 A.

This current requirement must be compared to the critical current limitations of niobium, the superconducting material used for the wire fabrication. The fabrication process (discussed in Section 4.2.3.3) constrains the maximum niobium film thickness to approximately 500 nm. To estimate the wire width needed to support at least 2 A, we consulted critical current density data for niobium films [144], from which we predict a critical current of approximately 2.9 A for a 100 µm wide wire at 4.2 K. The reduction of the critical current due to magnetic fields does not play a role at the magnetic field strengths on the order of 10 G that are expected at the chip surface.

Although sharp bends in the Z-wire geometry may locally reduce the critical current, the 100 µm width should provide sufficient margin for reliable operation at 2 A. Furthermore, at the target trap distance of around 0.5 mm away from the wire, the 100 µm wire width is sufficiently small that it does not significantly perturb the magnetic field compared to an idealized line current.

Critical current measurements To validate our critical current estimates, we performed direct measurements on dedicated test structures. For that purpose, our collaborators, the group of Peter Schüffelgen, fabricated a test chip hosting five niobium Z-wires with widths ranging from 50 to 700 µm and a thickness of 500 nm, matching the geometry of the atom chip Z-wire. A photograph of the test chip is shown in Fig. 4.5(a). The critical current measurements were conducted together with Samuel Germer and are also described in his master thesis [70]. In the absence of the custom cryostat, we performed the measurements by immersing the test chip in a liquid helium dewar, cooling it to the helium boiling point of 4.15 K.

The chip design allows selective electrical addressing of individual Z-wires. To determine the critical current of a given wire, we continuously increased the applied current while monitoring the voltage

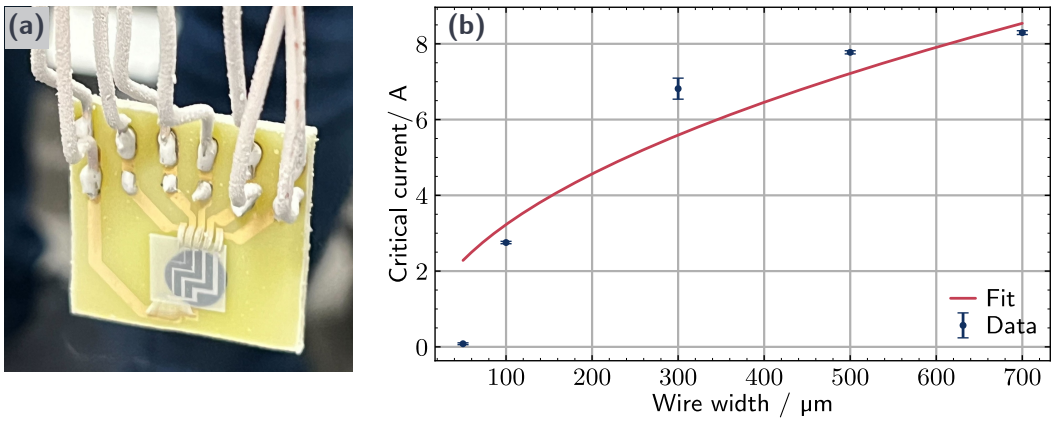

Figure 4.5: **(a):** Photograph of the critical current test chip hosting five niobium Z-wires with widths from 50 to 700 µm. The photo is taken after the chip was taken out of the helium dewar and a thin layer of frozen water from the air is on the chip. **(b):** Measured critical current as a function of the wire thickness. A square root dependence of the critical current on the wire width is fitted to the data excluding the first data point at 50 µm, which is an outlier. The reason for the low critical current of the outlier is not known. It could be attributed to errors during the fabrication or wire bonding. Alternatively, the current crowding at the corners could be more problematic for smaller wires. The data in this figure are also presented in [70].

drop across the Z-wire until superconductivity breaks down. Samuel Germer designed a protection circuit that amplifies the voltage drop for monitoring, detects the voltage spike accompanying the superconducting-to-normal transition, and then rapidly switches off the current in less than 20 µs, as described in his master thesis [70]. This rapid shutoff prevents resistive heating of the wire after the transition, avoiding potential damage and enabling repeated measurements on the same structure.

The results of the critical current measurements are shown in Fig. 4.5(b). We measured a critical current of 2.8 A for a wire width of 100 µm, in good agreement with the theoretical estimate of 2.9 A. A slightly lower measured value is expected due to current crowding at the sharp bends in the Z-wire geometry [145, 146]. This result confirms that the 100 µm wire width provides sufficient margin for reliable operation at 2 A.

The data in Fig. 4.5(b) does not follow a linear dependence but seems to approximately follow a square root dependence of the critical current on the wire width. A square root scaling indicates that the critical current is limited by vortex entry at the wire edges, consistent with a surface-barrier–dominated regime in wide, thin (but wider than the penetration depth) superconducting strips [147, 148].

At larger wire widths, higher currents become possible. Our simulations show that wire widths up to approximately 1 mm remain compatible with the target trap distance of 500 µm, reducing the trap frequencies by only approximately 10 %. This suggests that one could in principle operate at higher currents and bias fields using wider wires. However, the heat load from Joule heating in the non-superconducting current leads and wire bonds must be considered. As discussed in the cryostat redesign section (Section 4.1.2), excessive heat load can be detrimental to the cryogenic system performance. Therefore, we chose to maintain the original 100 µm wire width and limit operating currents to below 2 A, providing a conservative design that minimizes thermal load while ensuring sufficient trapping strength. The measured critical current of 2.8 A for the 100 µm width indicates that this choice provides adequate margin for reliable operation. If, however, the cryostat does not reach temperatures close to 4 K, the wire width should be increased to compensate for the reduced critical

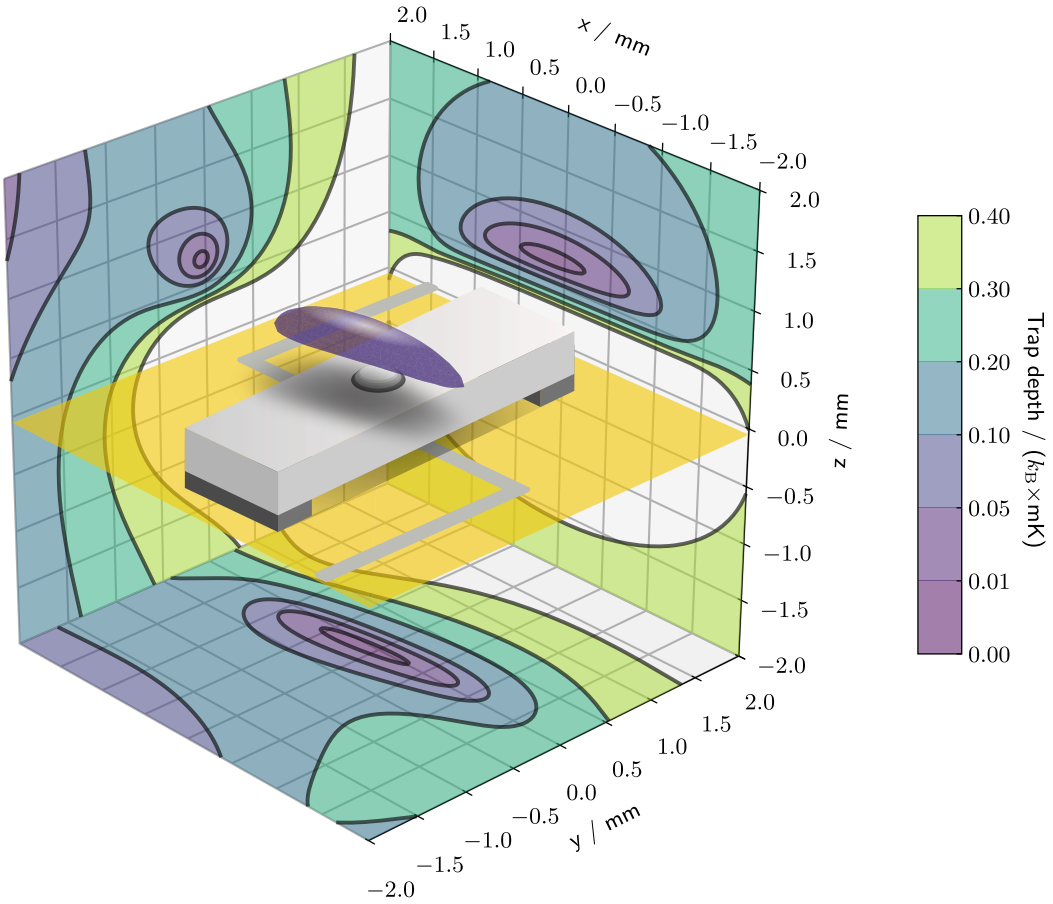

Figure 4.6: Three-dimensional visualization of the magnetic trap potential for the Z-wire configuration. The colored isosurface shows an equipotential surface at 50 µK × k_B trap depth. The three walls display two-dimensional contour plots of the trap depth evaluated at the potential minimum along the respective perpendicular axis: the x–y plane at the minimum z-position, the x–z plane at the minimum y position, and the y–z plane at the minimum x-position. The gold surface represents the chip substrate, and the gray lines resemble the 100 µm wide superconducting niobium Z-wire geometry with a 3 mm central segment. A sketch of the HBAR structure is included to provide geometric context for the experimental configuration.

current.

Beyond the wire width, the choice of the central wire length represents an additional design compromise. According to Eq. (4.1), the axial trapping frequency scales as $\omega_{ax} \propto L^{-1}$, so longer wires lead to weaker axial confinement. Conversely, shorter wires strengthen the axial trap but result in a more tilted trap geometry (see Fig. 4.6), as the magnetic field contributions from the bent segments of the Z-structure become more dominant relative to the central segment. Through iterative simulations exploring different wire lengths within the constraint of the chip size, we selected a central wire length of 3 mm. This length provides sufficient axial confinement while maintaining a trap geometry that is not excessively tilted.

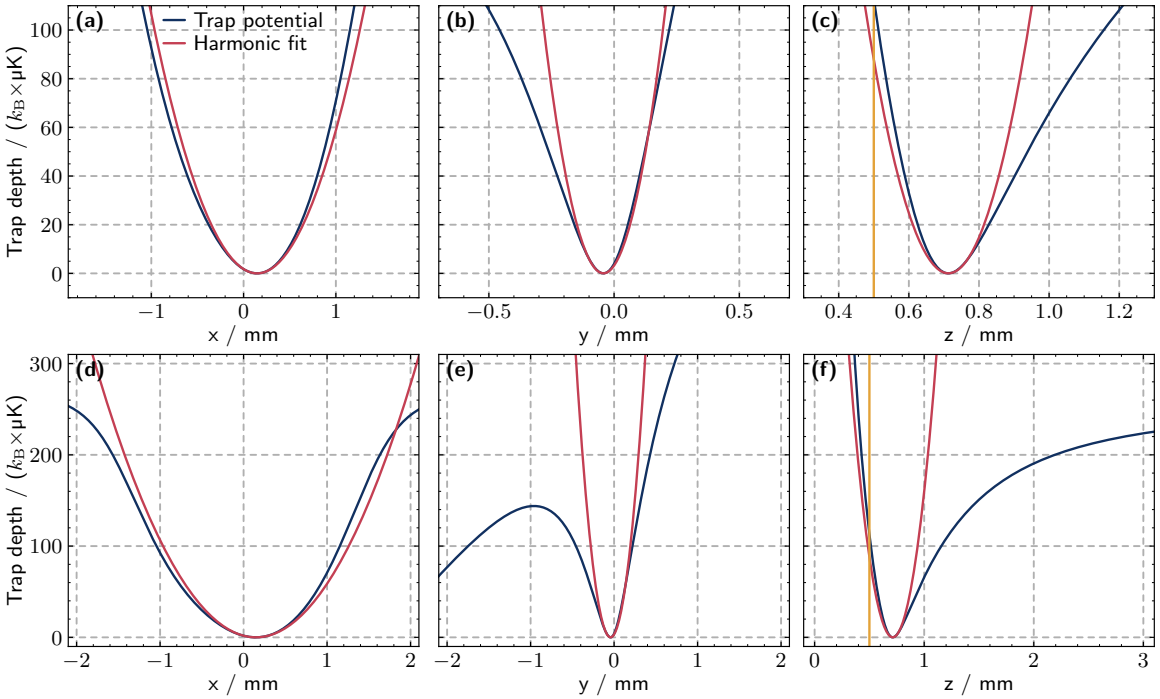

Figure 4.7: One-dimensional cuts of the magnetic trap potential through the trap minimum along the principal axes. Panel **(a)** shows the potential along the x axis (parallel to the central wire segment), panel **(b)** along the y axis (perpendicular to the central wire and parallel to the chip surface), and panel **(c)** along the z axis (perpendicular to the chip surface). Panels **(d-f)** are zoomed-out versions of the panels (a-c). The height of the HABR is highlighted with an orange line in panels (c) and (f). Harmonic fits in the vicinity of the trap center up to a trap depth of $20\,\mu\mathrm{K} \times k_\mathrm{B}$ demonstrate approximately harmonic behavior near the minimum, with significant deviations appearing at larger distances. The simulation parameters are identical to those used in Fig. 4.6. The horizontal axis range differs between panels to accommodate the potential along each respective axis.

Simulated trap geometry and potential Figure 4.6 presents a three-dimensional visualization of the simulated potential including gravity with the final Z-wire trap geometry. The three surrounding walls in Fig. 4.6 show two-dimensional contour plots of the trapping potential. These visualizations illustrate the spatial structure of the trapping potential near the chip surface. The simulation was performed for a wire current of 2 A and a perpendicular bias field in y-direction of 0.5 G, positioning the trap minimum at approximately 0.7 mm above the chip surface. The trap volume has a cigar-like shape with weak confinement approximately along the x direction. However, the weak trap axis is not perfectly aligned with the central wire segment due to the bent wire geometry. The x–y plane contour plot reveals the small rotation of the trap principal axes, primarily about the z-axis.

For completeness, we report the simulated trap frequencies along the slightly rotated principal axes $\tilde{x}\tilde{y}\tilde{z}$ of the magnetic trap. The principal trap frequencies are $\omega_{\tilde{z}} = 2\pi \times 105\,\mathrm{Hz}$, $\omega_{\tilde{y}} = 2\pi \times 108\,\mathrm{Hz}$, and $\omega_{\tilde{x}} = 2\pi \times 15\,\mathrm{Hz}$.

To assess the experimental viability of this trap geometry, we consider the relationship between the trap depth, the atomic cloud temperature, and the proximity to the HBAR surface. The 2D contour plots in Fig. 4.6 indicate that the trapping potential ceases to confine atoms at trap depths exceeding $100\,\mu\mathrm{K} \times k_\mathrm{B}$. Further understanding of the trap geometry is gained from the one-dimensional cuts

through the trap potential along the three principal axes shown in Fig. 4.7. Harmonic fits to the potential cuts near the trap minimum confirm approximate harmonic behavior along all three axes close to the trap center. The zoomed-out cuts in panels (d-f) reveal the strong departure from harmonicity at larger distances from the trap center. Here, panel (e) reveals that gravity—pointing in negative y-direction in the chosen coordinate system—is limiting the trap depth to about $140\,\mu\mathrm{K} \times k_\mathrm{B}$.

As a rule of thumb, atoms remain confined with negligible loss when the trap depth exceeds ten times the thermal energy $k_\mathrm{B}T$. For a three-dimensional harmonic trap—which provides a rough approximation to the Z-wire potential, as visualized in Fig. 4.7—the fraction of atoms with energies exceeding $10 \times k_\mathrm{B}T$ is approximately 0.28 % [149, 150]. Therefore, we expect that the atom cloud in the experiment will need to be cooled to temperatures around 10 µK or below to ensure stable trapping.

However, trap depth alone does not fully characterize the experimental constraints. It is also critical to prevent the rubidium atoms from colliding with the HBAR surface. To quantify this constraint, we examine the one-dimensional cuts through the trap potential along the z-axis shown panels (c) and (f) of Fig. 4.7. At the height of the HBAR surface, $z \approx 0.49\,\mathrm{mm}$, the potential barrier reaches a value slightly above $100\,\mu\mathrm{K} \times k_\mathrm{B}$. To verify this estimate, we computed the minimum potential anywhere on a plane defined by the HBAR surface height by scanning the potential across the x–y plane at $z = 0.49\,\mathrm{mm}$. This calculation yields a minimum barrier height of $105\,\mu\mathrm{K} \times k_\mathrm{B}$, consistent with the one-dimensional cut and confirming that the barrier is indeed lowest directly above the trap center.

For an atomic cloud at 10 µK, this barrier height corresponds to $10.5\,k_\mathrm{B}T$. As discussed before, in a three-dimensional harmonic trap this corresponds to approximately 0.28 % of atoms possessing sufficient energy to reach this barrier. However, as evident from the one-dimensional cuts in Fig. 4.7, the potential deviates significantly from harmonicity at this potential height. Therefore, the harmonic approximation for the density of states provides only a rough estimate of the actual atom distribution at large distances from the trap center. Nevertheless, only a very small fraction of atoms is expected to have enough energy to reach the HBAR surface. This fraction may be small, but contamination of the HBAR surface could add up over time and needs to be monitored when operating the experiment. Lowering the temperature below 10 µK to about 5 µK could remedy this problem entirely, due to the exponentially increasing suppression of high-energy atoms with decreasing temperature. At 5 µK, the barrier height corresponds to $21\,k_\mathrm{B}T$, and within the harmonic approximation, a fraction of less than 10^{-8} of the atoms possess sufficient energy to reach the surface.

These considerations demonstrate that the atom cloud must be cooled substantially after magnetic transport, during which it typically reaches temperatures around 200 µK (see Table 3.3). Therefore, we plan to implement additional evaporative cooling for the cryogenic experiment, which is discussed in Section 4.2.2.

Transfer from quadrupole to Z-wire trap Having established the Z-wire trap characteristics and cooling requirements, we must also ensure that the transfer from the quadrupole transport trap to the on-chip Z-wire trap proceeds efficiently without significant atom loss or collisions with the HBAR surface. An adiabatic transition between these two trap configurations is not feasible due to their fundamentally different geometries. The transfer must therefore rely on rapid switching between the configurations. However, the quadrupole coils outside the vacuum chamber have a characteristic switching time of approximately 15 ms (see Section 3.6.3.2), which constrains the minimum transfer duration.

To simulate the transfer dynamics, we employ a classical Monte Carlo approach in which the atoms

are treated as independent particles evolving in the time-dependent magnetic field. The simulation does not include particle interactions, and therefore only provides an estimate of the real dynamics.

A similar simulation was performed by Leon Sadowski in his master thesis [151], which was supervised during the course of this work. In Leon's simulation, the handover between the two different magnetic traps is performed by changing the fields linearly within a 20 ms time window: The quadrupole coil current is ramped to zero while the Z-wire current and bias field are ramped to their final operating values.

Here, we extend this simulation to allow for a more complex transfer sequence and to correct the initialization of the atomic ensemble. In the previous simulation, the initial spatial distribution of the atomic cloud was constructed by treating the three spatial axes independently. While this approach is valid for separable trapping potentials, such as harmonic traps, it is not appropriate for a quadrupole magnetic trap. As a result, independent Gaussian sampling along each axis does not reproduce the correct Boltzmann distribution. Instead, the atoms are placed approximately 20 to 30 % too close to the trap center. Consequently, the potential energy after initialization is shifted to lower values than expected. With this incorrect initialization, once the simulation starts, the atomic cloud expands and the average velocity decreases, which is unphysical and can impede the interpretation of the simulation results.

In the extended simulation, we instead sample the initial atom positions from the full three-dimensional Boltzmann distribution associated with the quadrupole trap, ensuring a physically consistent initial phase-space distribution at the specified temperature.

Furthermore, we improve upon the transfer sequence by adapting the temporal profile of the current ramps. A simple linear ramp of both traps creates an intermediate time window, where the Z-wire trap and quadrupole trap have comparable strengths, but their field configurations—specifically, the direction of the magnetic field vectors—are incompatible. This incompatibility leads to strong deformation of the trapping potential, imparting a velocity kick to the atom cloud. While rapid switching of the quadrupole trap is not possible, the Z-wire trap can be switched within less than 1 ms. We therefore adopt a two-stage approach: The quadrupole trap is ramped down linearly over 20 ms. For the first 15 ms, the Z-wire trap remains off and is then rapidly switched to full strength. This strategy reduces fluctuations in the trap position during the transfer by avoiding the intermediate regime in which both traps compete. For simplicity, we ramp the Z-wire current and the bias field for the Z-wire trap synchronously.

Reducing the quadrupole magnetic field gradient before increasing the Z-wire current has the drawback that the atomic cloud is less tightly confined during the first 15 ms of the transfer. Thus, it is essential to choose the initial quadrupole trap position sufficiently far from the chip surface to prevent any atoms from colliding with the HBAR. We chose an initial trap distance of 0.8 mm from the chip surface. We show below that this is sufficient to prevent the atoms from reaching the surface during the transfer.

The position fine adjustment between the chip and the quadrupole trap position can be done using the bias field coils. The quadrupole trap center position can be adjusted by about 0.65 mm (at full trap strength) using the magnetic offset field produced by the bias field cage around the science chamber.

The initial distance of 0.8 mm is larger than the final Z-wire trap distance (0.7 mm) discussed previously. To match the trap positions for the transfer, we reduce the Z-wire bias field from 0.5 G to 0.43 G (for the fully activated Z-wire trap), which increases the minimum position of the Z-wire trap to a chip surface distance of approximately 0.8 mm. After the transfer is completed and the cloud has thermalized, the bias field can then be ramped up to reach the final trap position in the experiment.

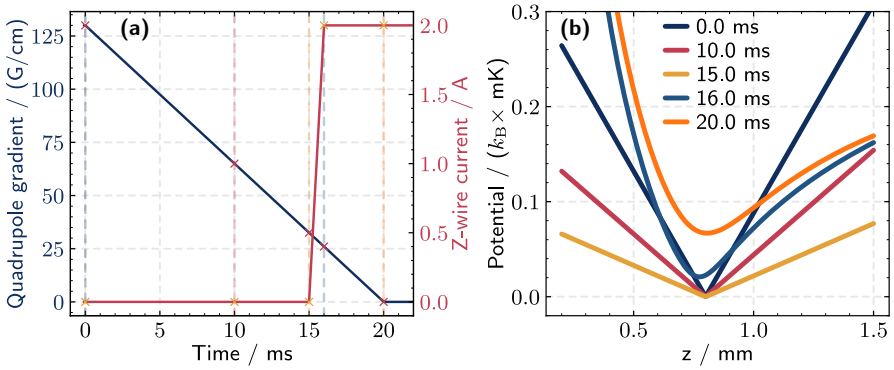

Figure 4.8: Time-dependent profiles of the magnetic trap parameters during the transfer from the quadrupole trap to the Z-wire trap. (a): Calculated magnetic trap potential along the z-axis (atom–chip distance) at selected times during the transfer sequence, illustrating the evolution of the potential minimum and the steeper gradient toward the chip surface in the Z-wire trap. (b): Temporal evolution of the quadrupole gradient and Z-wire current during the transfer. Crosses mark the current and gradient values for the selected times in (a). Not shown is the gradient for the Z-wire trap, that is ramped synchronized with the Z-wire current. The Z-wire trap is rapidly switched on after 15 ms, while the quadrupole gradient is ramped down over 20 ms.

The quadrupole gradient and Z-wire current as a function of time during the transfer sequence is shown in Fig. 4.8(a) together with the corresponding magnetic trap potential along the z-direction in Fig. 4.8(b). The z-axis is the most critical for the transfer, as it directly defines the atom–surface distance and thus the risk of collision with the HBAR.

When the Z-wire trap is switched on after 15 ms, the magnetic field potential minimum is slightly shifted toward smaller chip distances. However, the overall trap shape closely resembles that of the final Z-wire trap, exhibiting a steeper gradient toward the chip surface compared to the ramped-down quadrupole trap. Based on the potential shapes alone, it is difficult to predict whether the trap transfer imparts a momentum kick to the atom cloud or reliably keeps the atoms safely away from the HBAR surface. Therefore, we perform Monte Carlo simulations with 1000 atoms initialized in the quadrupole trap at a temperature of 10 µK. The simulation tracks the position and velocity of each atom throughout the transfer sequence, enabling us to extract the atom–chip surface distance as a function of time. In Fig. 4.9(a), we present the distribution of atom–chip distances during the transfer and for an additional holding time of 80 ms in the Z-wire trap. The absolute maximum and minimum distances reached by the simulated atoms are indicated. Notably, for all 1000 simulated atoms, the minimum distance to the chip surface at any time remained above 0.54 mm, corresponding to a separation of approximately ~ 50 µm from the HBAR. Due to the limited number of only 1000 atoms that were simulated, and with none of the atoms reaching the HBAR surface, the fraction of atoms that could theoretically reach the surface cannot be computed, but is expected to be small.

The mean atom–surface distance and the interval containing 68% of the atoms stays approximately constant during the transfer, as shown in depicted in 4.9(a). Only at the end of the transfer sequence (around 18 to 25 ms), a small kick towards larger distances is observed. This is consistent with the change of the trap potentials shown in Fig. 4.8(b), where the potential minimum at 20 ms is located farther from the chip compared to 16 ms.

Although this fluctuation in trap position does not affect the minimum atom–surface distance in the simulation, it could lead to heating of the atom cloud in the experiment. The change of the trap

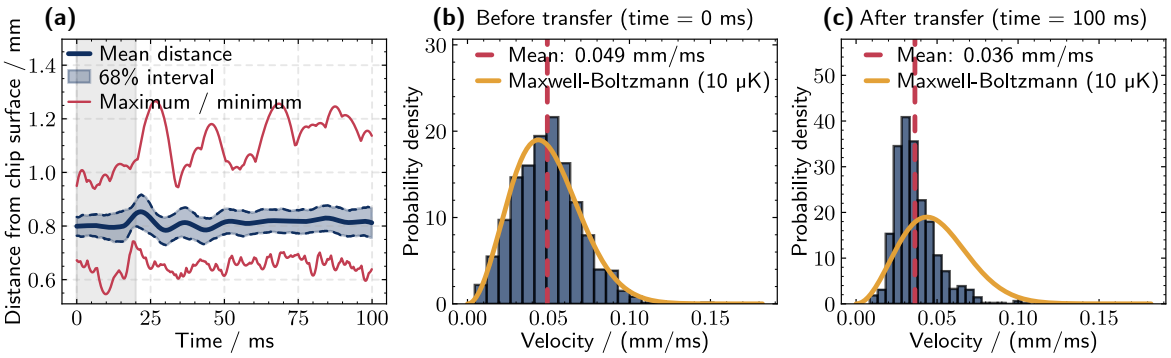

Figure 4.9: Distribution of distances from the atoms to the chip surface and atomic velocities during the transfer from the quadrupole trap to the Z-wire trap, as obtained from the Monte Carlo simulation detailed in the main text. **(a):** Time evolution of the atom–chip distance distribution during the transfer and subsequent holding time in the Z-wire trap. The shaded blue region indicates the interval containing 68% of the atoms, while the solid red lines denote the absolute maximum and minimum distances reached by any atom. No atoms approach the HBAR surface close enough to risk a collision under the simulated conditions. The 20 ms transfer duration is indicated by a gray shaded area. **(b):** Initial velocity distribution of the atomic ensemble in the quadrupole trap, consistent with a Maxwell–Boltzmann distribution at 10 µK. **(c):** Final velocity distribution after the transfer and holding time in the Z-wire trap, showing compression toward lower velocities. The reduction in mean velocity indicates effective cooling of the atomic cloud during the transfer.

position could be prevented by independently optimizing the Z-wire current and bias field during the transfer sequence.

We expect the mean velocity of the atoms to reduce during the transfer, since the Z-wire trap is more shallow compared to the quadrupole trap, especially along the central wire. Conversely, an increase in the mean velocity would indicate that the atoms experience a significant momentum kick during the transfer sequence. The initial and final velocity distributions are shown in Fig. 4.9(b) and (c). The initial velocity distribution is consistent with the Maxwell–Boltzmann distribution at 10 µK, yielding a mean velocity of 49 mm s^{-1}. After the transfer, the velocity distribution is compressed toward lower velocities, with a mean of 36 mm s^{-1}. This observation indicates that the atomic cloud does not experience a strong kick during the transfer.

Although particle interactions are not included in the simulation and, therefore, thermalization cannot occur, the reduction in mean velocity suggests that the atomic cloud is effectively cooled during the transfer from the quadrupole trap to the Z-wire trap. With this additional cooling, it should be possible to move the atomic cloud closer to the chip after the transfer sequence by increasing the bias field of the Z-wire trap, without risking collisions with the HBAR.

4.2.2 On-Chip evaporative cooling

As motivated by the magnetic trap and transfer simulations discussed before, the atom cloud must be cooled from temperatures on the order of 200 µK after the magnetic transport to approximately 10 µK, before it can be efficiently transferred to the Z-wire trap. To achieve this cooling, we plan to implement radio-frequency (RF) evaporative cooling directly in the science chamber. Our approach is to apply an RF current modulation to the Z-wire itself, which generates an oscillating magnetic field that enables evaporative cooling in the quadrupole trap, and in the final Z-wire trap configuration. The

latter can be used to counteract potential heating of the atom cloud due to noise on the Z-wire current and to reach temperatures below ~ 10 µK.

Evaporative cooling relies on the selective removal of high-energy atoms from the trapped ensemble [**ketterleEvaporativeCoolingTrapped1996**, 152]. In a magnetic trap, this cooling technique is realized by applying an additional oscillating magnetic field oriented perpendicular to the trapping magnetic field at least at some location of the trap. Atoms at spatial positions where the trapping magnetic field magnitude satisfies the resonance condition $\Delta E = \mu_B g_F m_F |\boldsymbol{B}| = \hbar\omega_{\mathrm{RF}}$, with ω_{RF} the angular frequency of the oscillating magnetic field, undergo spin-flip transitions to untrapped m_F states, and are subsequently lost from the trap. This resonance condition defines a surface of constant magnetic field magnitude. Only atoms with sufficient total energy to reach this surface are removed, which selectively extracts high-energy atoms from the ensemble. The remaining atoms rethermalize through elastic collisions, redistributing energy and reducing the ensemble temperature. By progressively lowering the RF frequency, the so-called truncation energy $\hbar\omega_{\mathrm{RF}}$ is decreased in a controlled manner, allowing continued cooling. This process is analogous to evaporation from a liquid, where the most energetic molecules escape, cooling the remaining sample.

To determine the appropriate RF frequency range for our system, we follow the optimization criteria established in the evaporative cooling literature, for example in [**ketterleEvaporativeCoolingTrapped1996**, 152]. The RF frequency should be chosen such that the truncation energy satisfies $\hbar\omega_{\mathrm{RF}} = \eta k_B T$, where the dimensionless parameter η determines the energy cutoff, after which atoms are removed. Typically, η ranges from approximately 6 to 10 with the optimum depending on the ratio of inelastic loss rates to elastic collision rates [**ketterleEvaporativeCoolingTrapped1996**, 152] and T is the (changing) cloud temperature during the evaporation. Higher η values (corresponding to higher truncation energies) are optimal when elastic collisions dominate, while lower η values are necessary when inelastic losses become significant.

We plan to use an RF frequency range from 30 MHz down to 1 MHz, which can be provided by the existing arbitrary waveform generator in our experiment[4]. With this frequency range, we can realize $\eta \leq 7.5$ at an initial temperature of 200 µK and $\eta \geq 6$ at the target final temperature of 10 µK. The upper bound $\eta \leq 7.5$ at the beginning of the evaporation may be lower than the optimal truncation parameter, depending on the specific trap condition, which could lead to increased atom loss during the initial stage of the evaporation. The optimal value of η is difficult to predict and must ultimately be determined experimentally. Nevertheless, the available RF frequency range provided by the existing equipment is sufficient for implementing evaporative cooling.

The strength of the RF field determines the probability that an atom in the spatial region satisfying the resonance condition undergoes an adiabatic transition to an untrapped state. In Ref. [152], the oscillating magnetic field amplitude $|B_{\mathrm{RF}}|$ for a transition probability approaching unity is derived:

$$|\boldsymbol{B}_{\mathrm{RF}}| = \sqrt{\frac{\hbar 8 v_T |\boldsymbol{B}'_{\mathrm{rad}}|}{g_F \mu_B}}. \tag{4.2}$$

Here, v_T is the mean thermal velocity of the atoms and $|\boldsymbol{B}'_{\mathrm{rad}}|$ is the radial magnetic field gradient of the trap[5]. Inserting the values for our quadrupole trap ($|\boldsymbol{B}'_{\mathrm{rad}}| = 65\,\mathrm{G\,cm^{-1}}$, $T \approx 200$ µK) we find a

[4] Keysight 33522B

[5] The central part of the Z-wire produces a magnetic field that is (mostly) perpendicular to the radial component of the external quadrupole trap

necessary magnetic field amplitude of $|\boldsymbol{B}_{\mathrm{RF}}| \approx 51\,\mathrm{mG}$.

Since we intend to use the Z-wire to provide the oscillating magnetic field, we estimate the maximum distance from the wire at which the required field strength given in Eq. (4.2) can still be reached. We assume a current amplitude of 0.14 A, corresponding to a 1 W RF drive applied to the Z-wire with a $50\,\Omega$ termination. We plan to use a commercial RF-amplifier from Minicircuit[6] to provide this signal strength. Under these conditions, the magnetic field amplitude exceeds the required threshold of 51 mG up to a distance of approximately 4.5 mm above the chip surface along the z-axis. Beyond this point, the field strength falls below the threshold. This allows us to position the quadrupole trap center at chip-distances $\lesssim 4.5\,\mathrm{mm}$ for the evaporation.

Note that the previously shown simulation of the trap transfer sequence in Section 4.2.1 assumes an initial distance of the quadrupole trap center to the chip surface of 0.8 mm. The currently installed magnetic bias coils at the science chamber provide a maximum bias field of about 10 G, which can move the trap center by about 0.65 mm. Therefore, the initial quadrupole center position should not be further than 1.45 mm from the chip surface. To be sure that atoms at the initial temperature of $\sim 200\,\mu\mathrm{K}$ do not collide with the HBAR, we compute the potential barrier from the quadrupole trap at the HBAR surface position, which is $\gtrsim 30 k_{\mathrm{B}} T$. As a result, the probability of atoms reaching the HBAR surface is practically zero.

Another important criterion, for evaporative cooling is the ratio of elastic collisions to inelastic losses. Specifically, this ratio is required to be at least on the order of 100 to allow the system to enter the runaway regime during the evaporative cooling process [152]. In the runaway regime, the relative reduction in temperature exceeds the relative loss in atom number as the temperature is lowered, rendering the evaporation process increasingly efficient. Therefore, entering the runaway regime is important to reach a low temperature while maintaining a sizable fraction of the initial atom number.

In the quadrupole magnetic trap, collisions with the background gas are the main source of inelastic losses at the initial temperature of $\sim 200\,\mu\mathrm{K}$. For the room-temperature science chamber, the lifetime of the quadrupole trap in the science chamber was measured to be around 8 s (see Section 3.7.3) which is the inverse of the inelastic loss rate. Adding the cryogenic environment to the chamber, we expect that the cryo-pumping of the radiation shields surrounding the experiment region will further reduce the pressure in the chamber and hence the background gas collision rate proportionally. For example, lifetimes of 6 000 s were obtained in an experiment with a similar cryogenic geometry as we plan to implement [153].

We estimate the initial elastic collision rate, τ_{el}^{-1}, in the quadrupole trap using [154]

$$\tau_{\mathrm{el}}^{-1} \approx n_{\mathrm{atom}}^{0} v_T \sigma_{\mathrm{col}} = 620\,\mathrm{s}^{-1}, \tag{4.3}$$

where n_{atom}^{0} is the atom number density at the center of the trap and $\sigma_{\mathrm{col}} = 7.9 \times 10^{-17}\,\mathrm{m}^2$ is the elastic collisional cross-section of ^{87}Rb [154]. To calculate this rate, we use a cloud temperature of $200\,\mu\mathrm{K}$ and an initial atom number of 2×10^8, conservative estimates for the conditions after the magnetic transport (see Table 3.3). In our room-temperature setup, the ratio of elastic collisions to inelastic losses, $620\,\mathrm{s}^{-1} \cdot 8\,\mathrm{s} \approx 5000$, is already comfortably above the threshold required for evaporative cooling to enter the runaway regime. With an improvement in vacuum conditions due to cryo-pumping, the ratio of elastic collisions to inelastic losses due to collisions with the background gas is expected to increase further.

[6] ZHL-5W-1+

So far neglected in this discussion are losses due to Majorana spin-flips. The Majorana loss rate in a quadrupole trap can be estimated as [155]

$$\gamma_{\mathrm{Maj}} \simeq \chi \frac{\hbar}{m_{^{87}\mathrm{Rb}}} \left(\frac{\mu_B |\boldsymbol{B}'_{\mathrm{rad}}|}{k_{\mathrm{B}} T} \right)^2 , \tag{4.4}$$

where $m_{^{87}\mathrm{Rb}}$ is the atomic mass of ^{87}Rb, $|\boldsymbol{B}'_{\mathrm{rad}}|$ is the radial gradient ($65\,\mathrm{G\,cm^{-1}}$) and χ is a numerical proportionality factor that depends on the trap geometry and internal atomic state. Reported values for ^{87}Rb range from $\chi = 0.16$ [156] to $\chi = 0.87$ [**linRapidProduction87Rb2009**]. Assuming a pessimistic $\chi = 1$, we find $\gamma_{\mathrm{Maj}}(T = 10\,\mu\mathrm{K}) = 1.4\,\mathrm{s^{-1}}$, while for an optimistic $\chi = 0.16$ the loss rate is $0.2\,\mathrm{s^{-1}}$. RF evaporation in magnetic traps typically extends over several seconds [52, 145, 152, 154, 157], which is longer than the inverse of the pessimistic loss rate. Accordingly, significant atom loss could be expected. However, the loss rates estimated here correspond only to the final temperature of 10 µK. During most of the evaporation, when the temperature is higher, the spin-flip loss rate is expected to be substantially lower according to Eq. (4.4).

Should spin-flip losses still become a limiting factor during evaporation, they could be mitigated by reducing the magnetic field gradient, or by stopping the cooling at a higher temperature. Both temperature and gradient enter the loss rate given in Eq. (4.4) quadratically. Hence, strong loss rate reduction can be achieved by small changes. Specifically, reducing the gradient during the evaporation is a viable path to reduce spin-flip losses: During the evaporation in the runaway regime, the elastic collision rate will increase while the cloud temperature and size decrease. This gives an added margin to reduce the magnetic field gradient without risking a too low elastic scattering rate (given in Eq. (4.3)), or risking that atoms reach the HBAR. Employing this loss mitigation strategy, we expect that evaporative cooling down to about 10 µK in the quadrupole trap will be possible.

After the evaporation, the atom cloud needs to be transferred from the quadrupole trap to the Z-wire trap, where the magnetic field offset of about 1 G renders spin-flip losses negligible [90].

The relative reduction in atom number during the evaporation is difficult to predict but is typically of a similar size to the relative change in temperatures [152]. Therefore, starting from about 2×10^8 atoms at a temperature of around 200 µK, we estimate that an atom number on the order of 10^7 at 10 µK is reachable in the Z-wire trap.

Current source for the Z-wire trap As power supply for the Z-wire trap, we employ a commercial high-precision bipolar current source[7] with up to 2.5 A output and 5 V voltage compliance. This choice is based on the successful application of a similar model in the atom chip experiments conducted in the research group of professor Fortágh [139], whose work serves as an inspiration for the design of our first-generation atom chip discussed in Section 4.2.3. Operating the current supply around its nominal ratings is optimal for performance according to the manufacturer. Therefore, the current rating is a custom choice we made to closely match the requirements for our experiment. The resistance of the wiring in the cryostat is not precisely known, so we chose a voltage rating of up to 5 V to provide sufficient margin. In the experiment, we can add low-inductance high-current resistors in series with the Z-wire to increase the total resistance. This has the added benefit that the characteristic rise time $\tau = R/L$ of the inductive load is reduced, where L is the inductance and R is the resistance. The manufacturer stated that the current source switching time is typically limited by the inductive load,

[7] Prolan-Mat BCS 2.5/5 power supply.

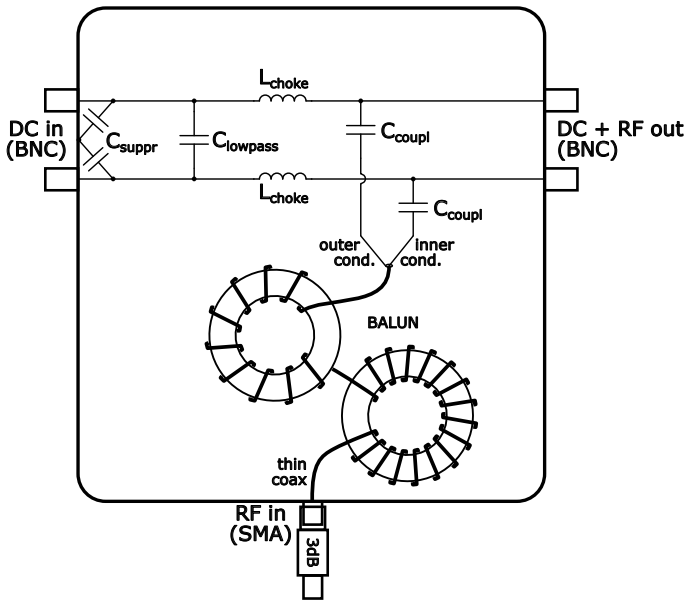

Figure 4.10: Custom-designed RF and DC signal combination circuit inside a grounded box. Details are discussed in the main text. Image courtesy of Wolfgang Alt (unpublished).

with achievable switching times around $5L/R$, based on which we estimate the switching time to be below 1 ms.

Z-wire RF modulation Since we plan to create the oscillating magnetic field for evaporative cooling using the Z-wire itself, the RF signal must be superimposed onto the supplied DC current. Our requirement to switch the Z-wire current rapidly (with frequencies in the low kilohertz regime) places the switching frequency uncomfortably close to the RF modulation range (1 to 30 MHz). Standard commercial bias tees cannot provide sufficient isolation between these regimes, risking interference with the current source feedback loop. To provide the necessary isolation, Wolfgang Alt, a permanent scientific staff member of our group, designed a custom RF and DC signal combination circuit within a grounded box. The circuit, sketched in Fig. 4.10, combines the RF signals from an RF amplifier and the DC current from the high precision current source, while preventing the RF signal from reaching the current source, or the DC current from reaching the amplifier. The incoming RF-signal is first transmitted by a 3 dB attenuator, which attenuates back-reflected signals by 6 dB to protect the RF-amplifier. To combine the RF and DC signals, the circuit contains coupling capacitors C_{coupl} = 100 nF that transmit the RF frequency range while blocking DC, and two series-connected chokes L_{choke} = 22 µH that block RF while passing DC. Together with additional capacitors $C_{lowpass}$ = 50 µF, these chokes form a low-pass filter that blocks RF signals from reaching the current source. A broadband BALUN transformer converts the unbalanced RF amplifier output to balanced anti-symmetric voltages ($+V/2$ and $-V/2$ relative to ground). This balanced configuration prevents RF radiation from the feedlines inside the cryostat leading to the Z-wire, as the anti-symmetric voltages on a twisted wire pair average to zero and their coupling to the environment is strongly suppressed. At the Z-wire position, the RF voltage has a node while the RF current has an antinode,

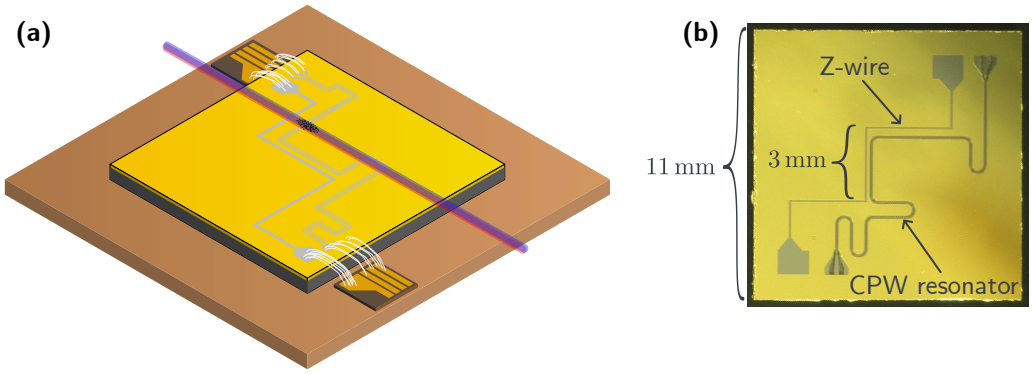

Figure 4.11: The first-generation atom chip hosting a CPW resonator instead of the HBAR. **(a):** Schematic of the atom chip. The design matches that presented in Fig. 4.3 with the HBAR exchanged for a CPW resonator. This figure is adapted with permission from [70]. **(b):** Photograph of the fabricated chip with the Z-wire and CPW resonator highlighted.

providing the desired oscillating magnetic field for evaporative cooling. The BALUN is realized by two series-connected windings of coaxial cable on Fair-Rite ferrite cores[8] (10 and 17 turns, respectively) to achieve broadband common-mode impedance exceeding 5 kΩ across the full frequency range from 1 to 30 MHz. Additional suppression capacitors C_{suppr} dissipate non-balanced noise and RF voltages to ground.

We built the RF and DC signal combination circuit in a grounded box and measured the crosstalk between the RF and current input of the modulation box with a vector network analyzer and found a suppression above 60 dB over the whole frequency range. We also confirmed that the RF-signal is split and 50% is transmitted to each output. These measurement results indicate that the circuit is working as intended and can be used to superimpose the DC and RF signals for the evaporative cooling using the Z-wire as an RF antenna.

4.2.3 First-generation chip with coplanar waveguide resonator

Our planned Rydberg–HBAR hybrid system presents several experimental challenges. For instance, the HBAR resonance frequencies are fixed by the design in our experiment[9], and the Rydberg transition frequencies may be shifted out of resonance due to stray electric fields from surface charges and absorbates on the chip [42, 57, 158, 159]. The Rydberg levels can be tuned by controlled application of electric fields, yet we expect that it will be difficult to maintain the resonance matching condition, given that the atom–HBAR interaction strength is relatively weak, and the resonances are narrow (see Section 2.3.1). Especially so, if the stray electric fields change over time, which will need to be monitored in the experiment. As a consequence, successful operation of the hybrid system requires precise calibration of Rydberg excitation and detection close to the chip surface. Without this calibration, searching for the weak atom-HBAR interaction would be impractical.

[8] FT240-31 Ferrite Toroid from Fair-Rite Material #31

[9] The free spectral range of the HBAR modes depends on the substrate thickness. For our HBARs, we expect a frequency spacing of 12.6 MHz. Frequency tuning is possible by increasing the temperature, which is undesirable for the planned experiments.

To address this challenge, we designed and fabricated a first-generation atom chip featuring a coplanar waveguide (CPW) resonator in place of the HBAR. The chip layout is sketched in Fig. 4.11(a), and a photograph of the fabricated chip is shown in Fig. 4.11(b). This simpler and more controllable system allows us to test and optimize Rydberg atom creation and detection near the chip surface, before attempting the more challenging HBAR experiments. A key advantage of the CPW resonator is that it can be externally driven, providing direct control over the interaction strength with the Rydberg atoms. This tunability greatly simplifies the initial characterization and optimization of the Rydberg excitation and detection. Moreover, by systematically varying the microwave drive parameters, we can investigate how microwave field manifests in the Rydberg detection signal. This characterization will be helpful for identifying and optimizing the atom–HBAR coupling in the subsequent experiments, where the interaction strength cannot be controlled as easily, and resonance identification is more challenging.

The first-generation chip design, inspired by the atom chip work of the Fortágh group [139], incorporates the same Z-wire magnetic trap geometry that we plan to employ for trapping the atom cloud above the HBAR, as discussed in the previous Section 4.2.1. This allows us to develop and optimize the cold atom handling on the atom chip, such as the evaporative cooling, the trap transfer, and the final trap positioning without risking contamination of the HBAR surface with rubidium.

The chip layout consists of three main components fabricated on a sapphire substrate. The first element is the superconducting niobium Z-wire structure (500 nm thick and 100 µm wide) with a 3 mm central segment, matching the geometry defined in Section 4.2.1. Adjacent to the Z-wire is the CPW resonator, positioned such that the magnetically trapped atom cloud sits above the resonator and can interact with its microwave near-field. The design and characterization of the CPW resonator is discussed below. The third component is a 300 nm thick gold ground plane that covers the entire chip surface. This ground plane prevents charge buildup on the chip that would produce stray electric fields affecting the Rydberg atoms. Additionally, by electrically connecting the gold ground plane directly to both the niobium Z-wire and the outer conductor of the coplanar waveguide resonator, we ensure they are grounded. Since the niobium is superconducting during operation, the DC trap current flows exclusively through the Z-wire rather than the gold ground plane. As an added safety feature, if the superconductivity breaks down, the current can flow through the gold layer, protecting the Z-wire from overheating and potential damage.

4.2.3.1 Coplanar waveguide resonator

The CPW resonator serves as a controllable microwave antenna positioned on the chip surface. The resonator is deliberately designed with a low quality factor to produce broad resonances, which simplifies the resonance matching with the Rydberg transition frequencies. We employ a capacitively coupled resonator design, with coupling finger capacitors positioned at both ends of the structure, which corresponds to a $\lambda/2$ resonator. This design follows the geometry proposed by Göppl et al. in Ref. [160]. One limitation of which we became aware of only after fabrication is that the central conductor is not grounded, allowing charge to accumulate on it over time. Future designs could incorporate inductively coupled resonators to mitigate this issue [161].

The resonator is operated at its second harmonic mode, which produces a field maximum at the center of the resonator. It is ideal that the field maximum coincides with the position of the atomic trap to maximize the coupling to the resonator. Thus, we designed the CPW resonator layout such that its center is aligned with the center of the Z-wire. Operation at the fourth harmonic also places

the field maximum at the center, enabling us to probe two different Rydberg states whose transition frequencies are separated by a factor of two. Specifically, we chose the states $n = 68$ and $n = 85$, whose transition frequencies differ by a factor of two plus 32 MHz [55]. The transition frequency for $n = 85$ is $f_{85} = 5.818\,\mathrm{GHz}$ ($85S_{1/2} \leftrightarrow 85P_{3/2}$ transition), and for $n = 68$ is $f_{68} = 11.668\,\mathrm{GHz}$ ($68S_{1/2} \leftrightarrow 68P_{3/2}$ transition).

The CPW resonator was designed by Leon Sadowski during his master thesis work [151] to match these frequencies with the second and fourth harmonic modes, and to achieve a quality factor of approximately 200 for the second harmonic. A critical consideration for the resonator design is the precise choice of the resonance frequency, since the Rydberg atoms must be tuned into resonance with the resonator. In the planned setup, we rely on the DC Stark shift given in Eq. (2.6) to adjust the transition frequencies. However, this tuning mechanism allows only to reduce the transition frequency (for nS↔nP transitions), constraining the allowable mismatch between the resonator and atomic transition. The transition frequency could also be adjusted using microwave dressing [42], but a respective microwave antenna is not included in the current sample holder design.

To quantify the available tuning range using a DC electric field, we calculated Stark maps for the states $|85S_{1/2}, m_J = 1/2\rangle$, $|85P_{3/2}, m_J = 3/2\rangle$, $|68S_{1/2}, m_J = 1/2\rangle$, and $|68P_{3/2}, m_J = 3/2\rangle$ using the ARC package [55] in Python. We focus on the regime in which the eigenstate $|\mu\rangle$ retains more than 90% overlap with the corresponding zero-field (bare) state and where no level crossings with other Stark states occur. Here, the state contribution refers to the projection of the Stark eigenstate onto the bare fine-structure state of interest (e.g. $|\langle 85S_{1/2}, m_J = 1/2\,|\,\mu\rangle|^2$). The 90% threshold is chosen arbitrarily, but corresponds to a regime in which the coupling strength to a microwave drive is expected to remain largely unaffected, with minimal admixture of other Stark components, resulting in a Rabi frequency $\gtrsim 90\%$ of the bare-state value.

For each Stark map calculation, we include states with principal quantum numbers deviating by up to ±5 from the target state and with orbital angular momentum up to $L \leq 20$. The number of included states was varied to verify convergence of the calculated Stark shifts in the regime of interest. As an example, Fig. 4.12(a) displays the calculated Stark map for the $|85S_{1/2}, m_J = 1/2\rangle$ state. The map shows that the first level crossing, corresponding to an intersection between the predominantly $85S_{1/2}$-like Stark state and the nearby high-L manifold ($L > 3$), occurs at an electric field strength of approximately $0.1\,\mathrm{V\,cm^{-1}}$.

To determine the maximum tuning range of the $85S_{1/2} \leftrightarrow 85P_{3/2}$ and $68S_{1/2} \leftrightarrow 68P_{3/2}$ transitions, we compare the DC Stark energy shifts $\Delta E_{nLJ}^{\text{DC-Stark}}$ (Eq. (2.5)) of the respective states as a function of electric field strength, as shown in Fig. 4.12(b). The values are extracted from the calculated Stark maps. Prior to the onset of the first level crossing, the state contribution of all involved states remains close to 100%, as shown exemplarily for the state $|85S_{1/2}, m_J = 1/2\rangle$ in Fig. 4.12(a). The relative difference in $\Delta E_{nLJ}^{\text{DC-Stark}}$, evaluated at the first level crossing, amounts to 90 MHz for the transition with $n = 85$ and 190 MHz for the transition with $n = 68$. These values define the maximum achievable tuning range for the respective transitions, where the states remain only weakly perturbed from the bare states. Beyond this range, the full Stark eigenstates must be considered.

4.2.3.2 Characterization of the coplanar waveguide resonator

To date, we have fabricated two different chips with different CPW resonator lengths. Our collaborators in Peter Schüffelgen's group measured the resonance frequencies of these CPW resonators in a dilution

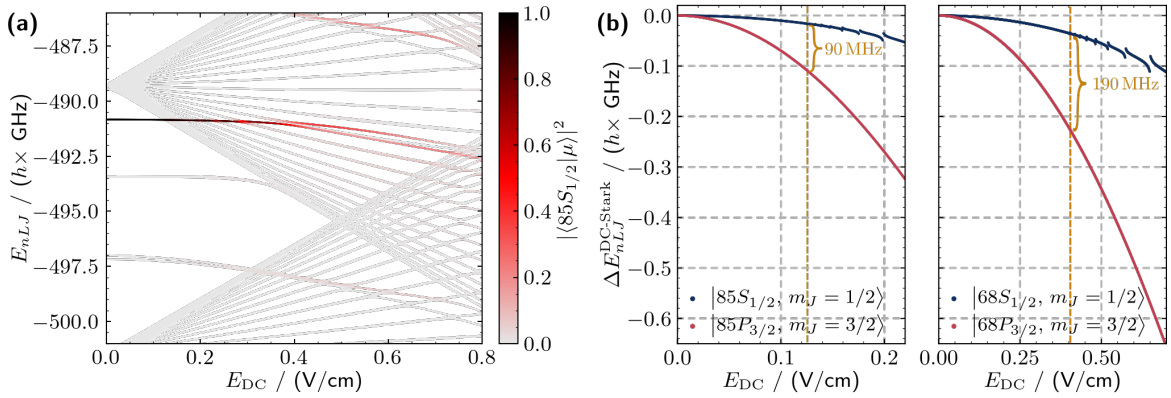

Figure 4.12: **(a):** Calculated Stark map at energies close to the bare state $|85\mathrm{S}_{1/2}, m_J = 1/2\rangle$. The color map indicates the overlap between the eigenstates $|\mu\rangle$ at a given electric field and the bare state $|85\mathrm{S}_{1/2}, m_J = 1/2\rangle$. **(b):** Calculated DC Stark shift $\Delta E_{nLJ}^{\mathrm{DC\text{-}Stark}}$ (Eq. (2.5)) as a function of the applied electric field. The left panel shows the energy shift for the states $|85\mathrm{S}_{1/2}, m_J = 1/2\rangle$ and $|85\mathrm{P}_{3/2}, m_J = 3/2\rangle$, and the right for the states $|68\mathrm{S}_{1/2}, m_J = 1/2\rangle$ and $|68\mathrm{P}_{3/2}, m_J = 3/2\rangle$. The dashed yellow lines indicate the electric field where the respective first level crossing occurs. All values are calculated for zero magnetic field using the software package ARC [55].

refrigerator. We encountered difficulties in achieving the target resonance frequency for both the first and second chip, as not all frequency-shifting effects were properly considered in the initial design. Only after the second chip was measured we gained a more complete understanding of these shifts. The relevant effects were identified by Samuel Germer and described in his master thesis [70] in chapter 4. Specifically, we had previously omitted the variation of the dielectric constant (parallel and orthogonal to the surface) of the sapphire substrate. Additionally, the kinetic inductance and the coupling capacitance were not considered.

The first chip we produced exhibited a resonance frequency that was too high, at approximately 5.955 GHz (second harmonic, $T = 4$ K), while the second chip undershot the target with a resonance at 5.661 GHz (second harmonic, $T = 4$ K). With a too high resonance frequency, the DC-Stark tuning technique cannot bring the Rydberg atoms into resonance, as discussed before. The second chip deviates from the target resonance $f_{85} = 5.818$ GHz by 157 MHz. This deviation lies outside the tuning range of approximately 90 MHz we determined. The same is true for the fourth harmonic (not measured) that will be at twice the freuqency of the second harmonic $2 \cdot 5.661$ GHz = 11.322 GHz. The difference to the target frequency $f_{68} = 11.668$ GHz is larger than the tuning range of 190 MHz. Tuning both transitions into resonance, beyond the first level crossing, may still be possible, albeit at the cost of reduced state purity, which would result in weakened coupling strength.

With the insights gained from the characterization measurements and the improved understanding of CPW resonator design, we expect to improve the resonance frequency precision in future chip designs.

4.2.3.3 Chip fabrication

For the fabrication of the atom chips, we collaborate with the group of Peter Schüffelgen, who has access to the cleanroom facilities at Forschungszentrum Jülich. The chip design is inspired by the

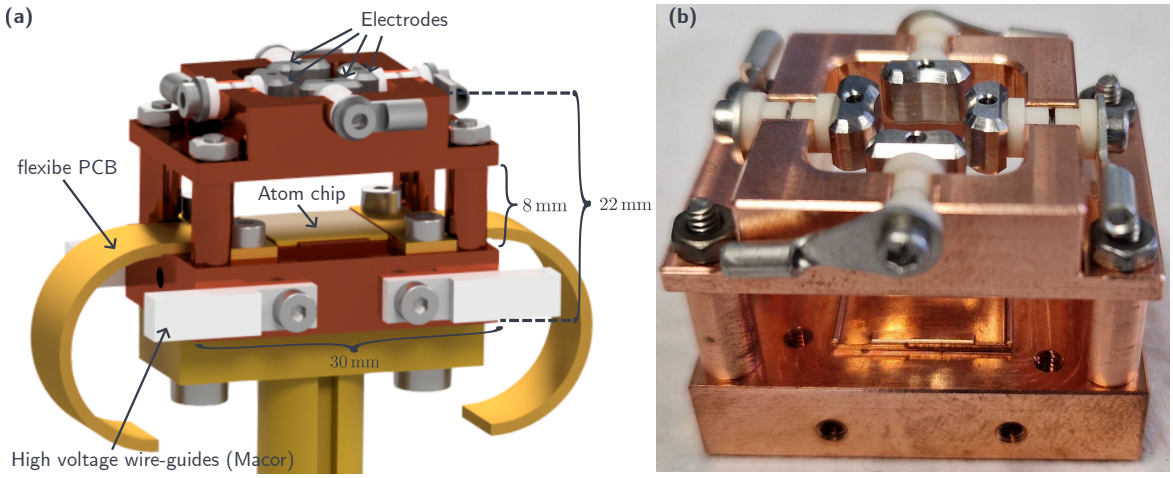

Figure 4.13: **(a):** CAD rendering of the sample holder for the cryogenic atom chip experiment. The holder integrates the atom chip, flexible PCBs for electrical connections, and mounting structures for four electrodes. The copper base of the sample holder has a width of 3 cm and a depth of 22 mm. **(b):** Photograph of the electrode cage and sample holder baseplate after a test assembly (no atom chip, flexible PCBs or high voltage wire guides).

atom chips developed by the group of professor Fortágh [39, 141, 142], and we follow their fabrication procedure, which is detailed, for example, in the supplementary material of Ref. [142].

The fabrication process begins with sputtering a 500 nm thick niobium film onto a c-plane sapphire wafer. The niobium thickness is constrained by the maximum deposition thickness achievable at the facility in Jülich, which is 500 nm. While a thicker niobium layer would be beneficial for achieving higher critical currents as discussed in Section 4.2.1, the 500 nm thickness provides sufficient performance for our application. Following the niobium deposition, the wafer is diced into 11×11 mm individual chip substrates.

The CPW resonator and Z-wire structures are then patterned using photolithography to create a negative mask, followed by reactive ion etching to remove the niobium not protected by the mask. An important fabrication detail is that a small step is etched into the corners of the niobium structure. This ensures that the subsequently deposited gold ground plane not only lies adjacent to the niobium but also overlaps onto it, providing better electrical contact between the gold ground plane and both the niobium Z-wire and the CPW ground strips.

After structuring the niobium layer, a second photolithography step defines the gold ground plane pattern. We first evaporate a 4 nm titanium adhesion layer onto the chip, followed by sputtering 300 nm of gold. The finger capacitors at the ends of the CPW resonator require particularly high fabrication precision and are therefore structured using electron-beam lithography instead of photolithography.

4.2.4 Sample holder

The sample holder serves as the mechanical and electrical interface between the cryogenic environment and the atom chip assembly. We designed and fabricated a custom sample holder to meet the specific requirements of our experiment. Figure 4.13(a) shows a CAD rendering of the complete sample holder assembly and Fig. 4.13(b) a corresponding photograph of a test assembly.

The sample holder—machined from oxygen free copper—provides rigid mechanical support for the atom chip while ensuring efficient thermal contact to the cryostat cold stage for reliable cooling to cryogenic temperatures. It incorporates mounting structures for four electrodes positioned above the chip surface. These electrodes serve two purposes: electric field ionization of Rydberg atoms and compensation of stray electric fields.

The holder integrates flexible printed circuit boards (PCBs) to route electrical signals from the backside of the sample holder to the chip surface. Wire bonds connect the chip to the flexible PCBs. Through the flexible PCBs, we route both the 2 A DC current for the Z-wire trap and the RF signals for the coplanar waveguide resonator. To maintain signal integrity for the RF signals, we bought custom flexible PCBs from Andus Electronics, designed with 50 Ω impedance matching for the RF transmission lines.

The sample holder design incorporates ceramic guiding channels for high-voltage cables to the electrodes, ensuring mechanical stability and preventing electrical shorts. The high voltage wires are guided behind the legs of the electrode mounts, such that the trapped atom cloud on the atom chip has no direct line of sight to the wires. This is important to prevent that the applied voltages or the potential charge build up on the dielectric wire insultation affect the atom cloud.

4.2.4.1 Atom chip mounting and indium soldering technique

Mounting the atom chip to the copper sample holder presents several technical challenges. The mounting technique must be compatible with the UHV environment, provide good thermal contact for efficient cooling to cryogenic temperatures, maintain mechanical stability during thermal cycling between room temperature and 4 K, and avoid protruding above the chip surface plane to prevent clipping of the laser beams used for Rydberg excitation.

We considered three mounting approaches: mechanical clamping with springs, adhesive bonding, and soldering. Mechanical clamping is difficult to implement due to geometric constraints: Any clamping structure extending above the chip surface would obstruct the laser beams or the wire bonding. Adhesive bonding using cryogenic-compatible epoxies such as Stycast (which we use for the magnetic transport coils) is mechanically viable and survives thermal cycling to 4 K, which we verified through dedicated tests. However, based on reports from the group of professor Fortágh [136], we expect adhesive bonds to provide insufficient thermal contact for our application, potentially limiting the achievable chip temperature.

Soldering offers the most promising solution, providing both excellent thermal conductivity and mechanical stability. Conventional soldering in air is problematic because heating the copper sample holder to soldering temperatures causes surface oxidation, which reduces thermal contact and increases outgassing in a vacuum. The group of professor Fortágh successfully addressed this issue using commercial ultrasound soldering equipment. We developed an alternative approach using vacuum soldering with indium without requiring specialized equipment. Indium is suitable for cryogenic and ultra-high vacuum applications. It remains soft and ductile down to cryogenic temperatures, even under repeated thermal cycling, and provides good thermal conductivity [162].

Our vacuum soldering procedure proceeds as follows. We distribute small indium flakes or powder uniformly across the mounting area of the copper sample holder, as shown in Fig. 4.14(a), and position the chip on top. A small weight placed on the chip applies gentle pressure, ensuring good contact between the chip, indium, and copper mount. We then place the entire assembly (sample holder, indium, chip, and weight) onto a vacuum blind flange and connect it via a vacuum bellow to a

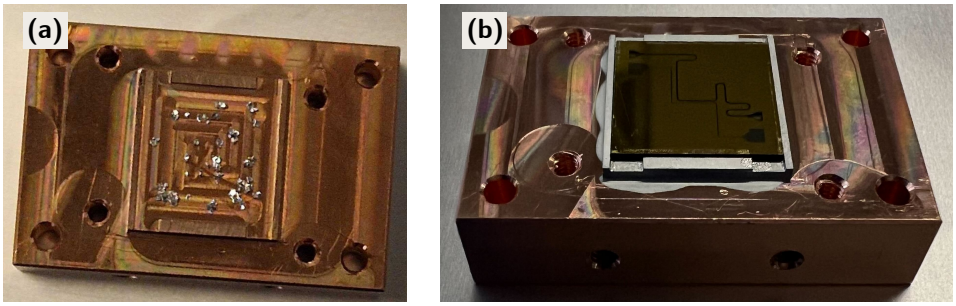

Figure 4.14: **(a):** Photograph of the sample holder with indium flakes for soldering of the atom chip. **(b):** Photograph of the atom chip soldered onto the sample holder. Some indium has flown outside the bonding area because too much was used for soldering.

turbomolecular pump. After evacuating the system, we wrap the blind flange and bellow in heating wire and aluminum foil, employing the same vacuum baking procedure commonly used in ultracold atom experiments. We heat the assembly to approximately 200 °C—above the indium melting point of approximately 157 °C [163]—and maintain this temperature for 12 h to ensure complete thermal equilibration throughout the assembly. At this temperature, the indium melts and bonds to both the chip and the sample holder. After slowly cooling back to room temperature, we vent the vacuum and remove the assembly. A photograph of a chip soldered with this technique is shown in Fig. 4.14(b). We tested, that this technique reliably produces bonds that withstand thermal cycling to cryogenic temperatures around 4 K.

During the development of our soldering technique, we discovered that indium does not bond directly to bare sapphire. To enable bonding, we sputter a thin gold layer onto the back surface of the chip, using a 4 nm titanium adhesion layer between the sapphire and gold, following the same approach used for the front-surface gold ground plane.

4.2.4.2 Flexible PCB integration

The flexible PCBs provide the electrical interconnection between the cryostat wiring and the chip structures. The layout of the flexible PCB is shown in panel (a) of Fig. 4.15, and panels (b) and (c) show photographs of the flexible PCB with wire bonds to the atom chip and soldered connectors on the other end.

The custom flexible PCB from Andus Electronics incorporates a transmission line for the RF signal driving the coplanar waveguide resonator. The transmission line is designed to have 50 Ω impedance to minimize reflections and ensure efficient power transfer.

The flexible PCB is made from a UHV compatible polyimid base material with FR-4 stiffeners at both ends. We chose a UHV compatible SMP connector[10] that is made from copper beryllium without any brass, with LCP E130 as dielectric. The connector is soldered onto the flexible PCB using UHV compatible solder[11].

[10] Amphenol SMP-MSSB-PCS-NM
[11] Allectra 315-LF- SOLDER

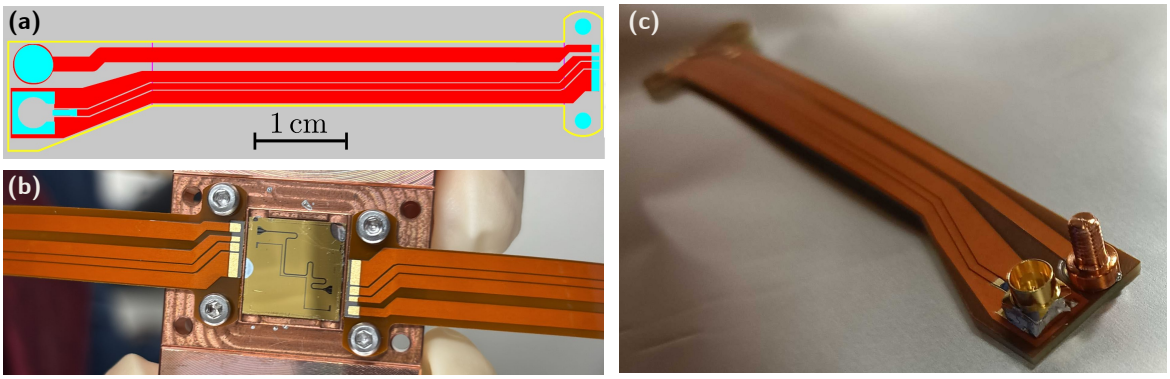

Figure 4.15: **(a):** Layout of the flexible PCB used for electrical connections to the atom chip. The design includes impedance-matched 50 Ω transmission lines for RF signals and a separate trace for the Z-wire DC current. **(b):** Photograph of the flexible PCB with wire bonds to a test atom chip on the sample holder. **(c):** Photograph of the flexible PCB illustrating the SMP connector for the RF-signal and a copper screw for the Z-wire DC current. The respective current-carrying wire is meant to be connected to the screw, with a cable lug and screw nut.

4.2.5 Electrode cage

The electrode cage consists of four electrodes positioned above the chip surface at a horizontal distance of 10.7 mm (chip surface to bottom of electrodes). The electrodes are mounted on the sample holder structure as shown in Fig. 4.13. The electrodes are machined from non-magnetic A4 steel. These electrodes serve two main functions: they generate the electric fields required for field ionization of Rydberg atoms and provide control over electric fields at the atom cloud position.

The ionization scheme for the chip-based experiment differs from the room-temperature configuration discussed in Section 3.7.4.4. Here, the ionization electrodes must pull the ions away from the chip surface toward the MCP detector, instead of pushing them. This pulling configuration is more complex and requires precise timing control of the electrode voltages. The ionization electrodes must be switched off as soon as the ions pass through the electrode plane to avoid being pulled back. Of the four available electrodes, we plan to employ two opposing ones to generate the ionization and acceleration fields, while the remaining two are available for trajectory steering if needed.

Leon Sadowski conducted electrostatic simulations using COMSOL Multiphysics to assess the feasibility of ion detection in the pull configuration in his master thesis [151]. These simulations model the ionization and subsequent acceleration of ions from the atom cloud position toward the MCP detector, assuming instantaneous voltage switching. The simulation results show that successful guiding of all ions could be possible. The finite rise and fall times of the high-voltage switches (60 ns), were not included in the simulation but will likely affect the ion trajectories and may necessitate adjusted voltages and timing sequences to maximize the ion collection efficiency at the MCP.

In addition to their role in field ionization, the four electrodes provide active control over electric fields at the atom cloud position. As discussed before in Section 4.2.3, stray electric fields arising from surface charges and absorbates on the chip or surrounding dielectric materials shift Rydberg energy levels via the DC Stark effect, potentially detuning the atoms from resonance with the CPW resonator or HBAR. The ability to compensate these stray fields is essential for achieving and maintaining the resonance condition required for atom-resonator coupling.

By applying individual voltages to each of the four electrodes, we can generate electric fields with

controllable magnitude and direction at the atom cloud position. Electrostatic simulations show that the electrode geometry provides compensation capabilities of approximately $0.15\,\mathrm{V\,cm^{-1}}$ in the horizontal plane (parallel to the chip surface) and approximately $2.5\,\mathrm{V\,cm^{-1}}$ in the direction perpendicular to the chip surface, using voltages up to $\pm 10\,\mathrm{V}$ on the individual electrodes. The achievable field homogeneity over a distance of 0.5 mm from the trap center is approximately 1 %.

Stray electric fields encountered in chip-based experiments vary considerably between different setups [39, 42, 57, 141, 142, 158, 159] and are difficult to predict. However, we expect that measurements from the chip experiments of the Fortágh group—which employ a similar design to our first-generation atom chip—provide a reasonable indication of the field strengths we can expect in our experiment. In their measurements, stray electric fields decrease approximately exponentially with distance from the chip surface, reaching values around $2\,\mathrm{V\,cm^{-1}}$ at 200 µm surface distance [39, 57].

For our first-generation atom chip, where atoms are trapped at chip-surface distances around 0.5 mm, the expected stray fields will be weak and mostly homogeneous. Therefore, the electrode compensation capabilities should be sufficient to cancel the stray fields.

However, experiments with the HBAR, which is planned to be positioned at distances of only 50 µm from the atoms, present a more challenging scenario. At this closer distance, stray electric fields on the order of 10 to $15\,\mathrm{V\,cm^{-1}}$ have been measured in in the chip experiments of the Fortágh group [39, 57]. Furthermore, because the HBAR surface is dielectric (or piezoelectric) rather than conducting, larger surface charge accumulation is expected compared to the gold-coated chip, likely resulting in stronger stray fields. These larger stray electric fields will necessitate an improved field compensation range.

Several strategies could address this limitation. The most straightforward approach is to increase the applied electrode voltages beyond $\pm 10\,\mathrm{V}$, which will require upgrading the voltage supplies currently installed in the experiment. Alternatively, the electrode cage could be positioned closer to the atom chip to provide stronger fields at the atom position for a given applied voltage. However, this approach introduces additional challenges for ionization: Reducing the electrode-atom distance requires faster voltage switching to prevent ions from being pulled back toward the electrodes, and electrodes positioned closer may deflect ion trajectories more strongly, potentially necessitating additional steering electrodes to maintain efficient ion collection at the MCP.

A more comprehensive solution for future iterations would be to incorporate on-chip electrodes fabricated directly on the chip surface. Such on-chip electrodes positioned closer to the atoms would provide significantly stronger field compensation with lower applied voltages and potentially improved field homogeneity [141]. However, to maintain simplicity in design and fabrication, such electrodes were not included in the first-generation chip.

Beyond hardware modifications, alternative mitigation strategies exist. One promising route is the employment of techniques to prevent charge and adsorbate buildup on the surface, as demonstrated in Ref. [159]. Additionally, microwave dressing schemes can be employed to reduce the sensitivity of Rydberg transitions to stray electric fields [42, 164], effectively making the system more robust without requiring compensation of the fields themselves.

CHAPTER 5

Applications of the hybrid platform

In the previous chapters, we discussed the experimental setup and the problems of the cryostat delivery. While the cryostat is not yet available at the end of this thesis, it is still relevant to consider the first experiments to perform when it is installed, beyond characterizing the cryostat performance.

In this chapter, we first discuss a cooling scheme that utilizes the Rydberg atom–HBAR coupling to cool a mechanical mode of the HBAR. This cooling technique could enable the observation of coherent coupling between the HBAR and the Rydberg atoms, which is otherwise prevented by the residual thermal occupation of the HBARs mechanical mode at 4 K.

Afterward, we discuss a long term perspective for studying Rydberg-tweezer chain mediated coupling between two spatially separated HBARs.

5.1 Cooling of mechanical oscillator mode via Rydberg atoms

In Section 2.3, we established the theoretical foundation for the Rydberg–HBAR hybrid architecture. We analyzed the coupling strength and assessed the prospects of reaching the strong-coupling regime. One of the central challenges to observing coherent coupling was identified as the residual thermal occupation of the HBAR mechanical mode.

In this section, we present a cooling scheme for the HBAR mode that utilizes coupling to Rydberg atoms to extract excitations from the mechanical resonator. Similar mode cooling proposals using Rydberg atoms with mechanical or microwave resonators are proposed in Refs. [45, 74]

An overview of the possible experimental implementation and the corresponding level scheme illustrating the excitation paths is shown in Fig. 5.1. We consider the same experimental configuration as discussed in Section 2.3, but extend the framework. Here, we explicitly model the dissipative coupling of the HBAR to the thermal environment at 4 K. In a thermal environment, the modes of the HBAR are cooled at rate $\kappa_c = \kappa(\langle n \rangle_{\text{th}} + 1)$ and heated at rate $\kappa_h = \kappa \langle n \rangle_{\text{th}}$ [73], with the thermal mean phonon number of a given mode $\langle n \rangle_{\text{th}}$ defined in Eq. (2.19).

We apply a continuous drive between the ground state $|5S_{1/2}\rangle$ and the Rydberg state $|nS_{1/2}\rangle$. This drive utilizes a two-photon excitation process with a 480 nm laser and a 780 nm laser with respective Rabi frequencies Ω_C and Ω_P, as explained before in Section 3.7.4. The intermediate state $|5P_{3/2}\rangle$ is adiabatically eliminated by detuning the lasers from this state while maintaining two-photon resonance. The principal quantum number of state $|nS_{1/2}\rangle$ is selected such that the transition frequency of the

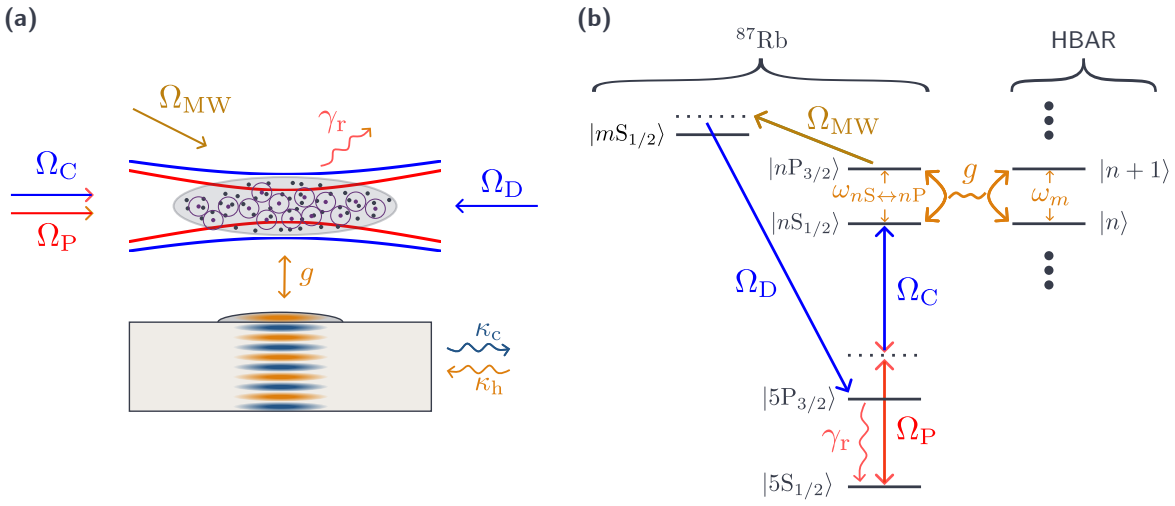

Figure 5.1: **(a):** Schematic of experimental configuration for the cooling scheme for the HBAR mode. The schematic shows the atom cloud trapped near the HBAR surface, with laser and microwave drives and dissipation channels indicated. **(b):** Level scheme for single-atom cooling. The excitation paths and cooling principle are explained in the main text.

transition $|nS_{1/2}\rangle \leftrightarrow |nP_{3/2}\rangle$ matches the resonance frequency of the HBAR mode.

Once an atom in the cloud is excited to the Rydberg state $|nS_{1/2}\rangle$, excitations can be exchanged between the Rydberg atom and the HBAR mode. To make this process irreversible and thereby cool the HBAR, we artificially enhance the decay rate of the state $|nP_{3/2}\rangle$. This decay rate enhancement is realized by dressing the state $|nP_{3/2}\rangle$ with a fast decaying state. The state with the shortest lifetime is $|5P_{3/2}\rangle$ (decay rate $\gamma_r \approx 6\,\mathrm{MHz}$), making it the natural choice. A direct transition between both states is dipole-forbidden. Therefore, a two-photon process is employed, with a microwave drive with Rabi frequency Ω_{MW} and a second 480 nm laser with Rabi frequency Ω_D via an auxiliary Rydberg state $|mS_{1/2}\rangle$, as depicted in Fig. 5.1(b). The auxiliary Rydberg state $|mS_{1/2}\rangle$ is also adiabatically eliminated to effectively dress the state $|nP_{3/2}\rangle$ with the fast-decaying state.

With this engineered decay, the excitation does not undergo Rabi oscillations between that states $|nS_{1/2}\rangle$ and $|nP_{3/2}\rangle$ through exchange of microwave photons with the HBAR, instead the Rydberg atom radiatively decays from the $|nP_{3/2}\rangle$ to the ground state after extracting an excitation from the HBAR. Continuous repetition of this process cools the HBAR mode.

Since both the Rydberg excitation path and the dressing involve the state $|5P_{3/2}\rangle$, care must be taken to avoid that the dressing laser and microwave drive unwanted transitions. This can be prevented by choosing sufficiently different detunings for the two 480 nm lasers relative to their respective transitions.

To increase the efficiency of this cooling scheme, we plan to exploit the collective bright state $|W\rangle_{nS_{1/2}}$ and the manifold of collective dark states $|D\rangle_{nS_{1/2}}$ that form via Rydberg excitation within an atomic cloud due to the Rydberg blockade effect, as introduced in Section 2.1. The adapted level structure of the cooling process with collective ground $|G\rangle_{5S_{1/2}}$ and Rydberg states is shown in Fig. 5.2. With collective states, one might expect a collective enhancement of the coupling strength g between the HBAR and the collective state—analogous to the enhancement between the ground state and the bright state—but such enhancement is in fact absent. This can be verified by inserting the collective

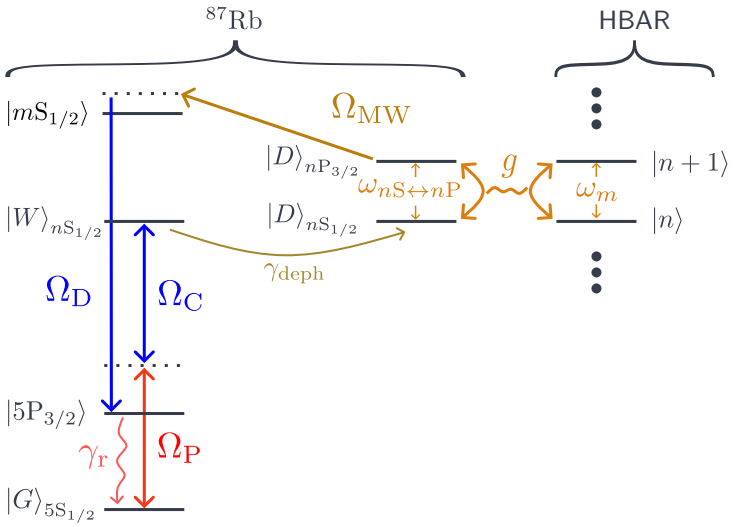

Figure 5.2: Level scheme for the cooling process with collective states. Dephasing into the dark state manifold and the role of collective states are discussed in the main text.

states into the coupling strength formula in Eq. (2.16).

Instead, what is crucial for the cooling scheme is the regime in which dephasing with rate γ_{deph} into the manifold of dark states—which do not couple to the laser drive—occurs rapidly compared to the Rabi frequency of the drive. In this regime, the drive excites Rydberg atoms without subsequently de-exciting them. While the dark states do not couple to the laser drive, they couple normally to the HBAR. Consequently, the drive strength can be increased to rapidly create new Rydberg atoms participating in the cooling process without de-exciting existing Rydberg atoms. The number of Rydberg atoms participating in the cooling process is limited by the ratio of the blockaded volume from a Rydberg atoms to the spatial overlap volume between the laser drive and the atomic cloud close to the HBARs piezoelectric dome.

Numerical simulations for realistic experimental parameters[1] of the proposed cooling scheme were performed by Samuel Germer in his master thesis [70]. The simulated cooling process for different numbers N_{col} of participating collective states reveal an approximate scaling of the steady-state mean phonon occupation with $\langle n\rangle_{\text{ss}} \propto N_{\text{col}}^{-1}$. The simulations are limited to $N_{\text{col}} \leq 4$, but already with only three simultaneous participating collective states, the simulated cooling process reaches a steady-state mean phonon occupation of about 0.5, down from an initial value of around 14.

These results demonstrate the feasibility of cooling a mechanical mode of the HBAR close to its ground state via coupling to an ensemble of Rydberg atoms. Furthermore, they indicate that maximizing the number of simultaneously participating collective states is crucial for improving the cooling performance.

As mentioned above, the number of possibly participating collective states is limited by the ratio of the blockaded volume to the spatial overlap volume between the laser drive and the atomic cloud. In Section 3.7.4.2, we discussed the current optical setup, which is not yet optimized to create a large overlap volume between the excitation lasers and the atomic cloud. However, only the collimator lens after the probe fiber, needs to be exchanged to significantly increase the overlap volume in

[1] The chosen parameters and the numerical implementation are detailed in Chapter 3 of Samuel Germer's thesis [70].

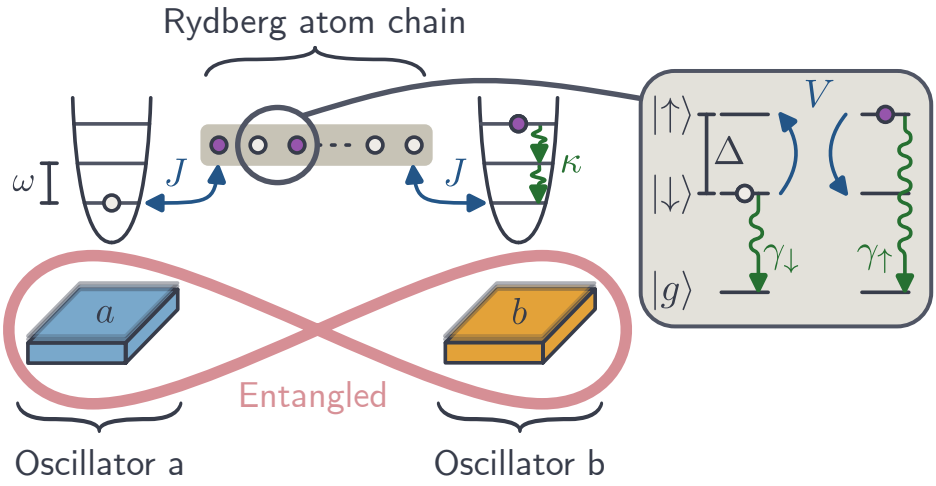

Figure 5.3: Schematic illustration of the model system: Two mechanical oscillators coupled via a chain of Rydberg atoms. The levels, coupling strengths and decay rates introduced in the main text are illustrated. Excitations in the Rydberg spin chain and the oscillators are depicted as violet filled circles, while white filled circles indicate the absence of excitations. This figure is partially reproduced from Ref. [1].

the experiment. Additionally, a microwave antenna needs to be added to the setup, to provide the microwave drive Ω_{MW}.

5.2 Entanglement generation between two mechanical oscillators

If ground state cooling of the oscillator can be established, the hybrid platform could find application in quantum technologies, as outlined in the introduction of this thesis.

In collaboration with Chris Nill and Igor Lesanovsky from the university Tübingen, we explored potential applications of the Rydberg–HBAR hybrid system. Together, we developed the concept of coupling two HBARs via a tweezer chain of Rydberg atoms. This approach not only couples the Rydberg atoms to the oscillators, but also links the two mechanical oscillators, resulting in complex many-body dynamics. These dynamics can be harnessed to entangle the motional states of the two connected oscillators.

Here, we present our study of this system and the many-body dynamics leading to entanglement. First, we introduce the model system used in the theoretical study and then present an analytic investigation of the coherent dynamics. Subsequently, we discuss numerical simulations of the system that include dissipation and present an entanglement scheme that exploits the dissipative dynamics.

Parts of this section have been published on arXiv [1] and are currently under peer review.

5.2.1 Model system

Figure 5.3 shows a schematic representation of the model system under consideration. The two ends of a chain of N equally spaced Rydberg atoms are each coupled to a micro-electromechanical oscillator. The atoms are modeled with three levels, ground state $|g\rangle$ and Rydberg states $|\downarrow\rangle$ and $|\uparrow\rangle$ with energy separation Δ between the Rydberg states. Throughout this section, we set $\hbar = 1$. For ^{87}Rb, the state $|g\rangle$ corresponds to the ground state $|5S_{1/2}\rangle$ while the states $|\downarrow\rangle$ and $|\uparrow\rangle$ correspond to Rydberg states

$|nS_{1/2}\rangle$ and $|nP_{3/2}\rangle$ with a dipole-allowed transition. In experiments, these Rydberg states can be excited using two- or single-photon transitions from the ground state[2].

Atoms in the chain interact via dipolar flip-flop interaction, which is described by the Hamiltonian [14, 165]

$$H_{\text{dipol}} = \sum_{i<j} \frac{\tilde{C}_3}{R_{ij}^3} \left(|\downarrow\rangle\langle\uparrow|_i \otimes |\uparrow\rangle\langle\downarrow|_j + \text{h.c.} \right). \tag{5.1}$$

Here h.c. denotes the Hermitian conjugate, R_{ij} is the distance between atoms i and j, and $\tilde{C}_3 = C_3 \frac{3\cos^2(\theta)-1}{2}$. $\tilde{C}_3$ depends on the angle θ, which is the angle between the quantization axis and the distance vector between two atoms in the chain. To simplify our model, we neglect couplings to next-nearest neighbors and beyond.

The resulting chain Hamiltonian is

$$H_{\text{chain}} = V \sum_{i=1}^{N-1} \left(|\downarrow\rangle\langle\uparrow|_i \otimes |\uparrow\rangle\langle\downarrow|_{i+1} + \text{h.c.} \right) + \Delta \sum_{i=1}^{N} |\uparrow\rangle\langle\uparrow|_i , \tag{5.2}$$

with interatomic coupling strength

$$V = \frac{\tilde{C}_3}{R_{\text{neigh}}^3} \tag{5.3}$$

between neighboring Rydberg atoms with distance R_{neigh}.

The dissipation of the Rydberg atoms in the chain is modeled with two decay channels, $|\downarrow\rangle \to |g\rangle$ and $|\uparrow\rangle \to |g\rangle$ with rates $\gamma_\downarrow$ and $\gamma_\uparrow$ respectively, as depicted in Fig. 5.3. Here, we assume a zero temperature environment such that black-body induced transitions can be neglected. With only two decay channels, the real decay dynamics are simplified and decay to lower excited states is neglected. Because atoms in low-lying excited states do not contribute to the dynamics in the chain, this simplification is justified.

When modeling the oscillators, we focus only on a single mode with frequency ω, which is assumed to be in resonance with the Rydberg transition, i.e., $\Delta = \omega$. Furthermore, the two oscillators are assumed to be identical. The resulting oscillator Hamiltonian is

$$H_{\text{osc}} = \omega(a^\dagger a + b^\dagger b), \tag{5.4}$$

with ladder operators $a, a^\dagger$ and $b, b^\dagger$ corresponding to the respective oscillator mode.

Oscillator damping is modeled with rate κ, and heating is neglected under the zero-temperature approximation.

The oscillators couple to the Rydberg atoms at the chain ends via a dipole interaction, as described in Section 2.3.1. The resulting coupling Hamiltonian is

$$H_{\text{couple}} = J \left(|\downarrow\rangle\langle\uparrow|_1 \otimes a^\dagger + |\downarrow\rangle\langle\uparrow|_N \otimes b^\dagger + \text{h.c.} \right), \tag{5.5}$$

where J quantifies the coupling strength.

The system Hamiltonian is the combination of the chain, oscillator and coupling Hamiltonians in

[2] Alternatively, the state combination $|(n-1)P_{3/2}\rangle$ and $|nS_{1/2}\rangle$ could also be associated with $|\downarrow\rangle$ and $|\uparrow\rangle$, which only slightly changes the energy spacing and decay rates.

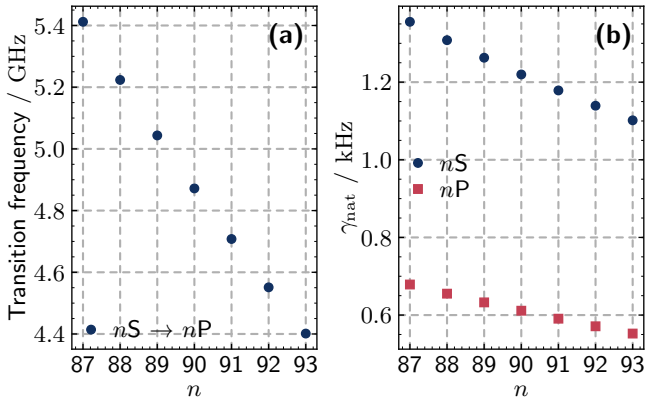

Figure 5.4: **(a):** Transition frequencies between Rydberg states in ^{87}Rb as a function of principal quantum number n. **(b):** Natural decay rate of the corresponding Rydberg states at zero temperature. Transition frequencies and decay rates were calculated using the software package ARC [55].

Eqs. (5.2), (5.4) and (5.5):

$$H_{\mathrm{sys}} = H_{\mathrm{osc}} + H_{\mathrm{chain}} + H_{\mathrm{couple}}. \tag{5.6}$$

This model provides the basis for the subsequent analysis.

5.2.2 Parameter estimates

To analyze the feasibility of the proposed model of coupling the oscillators via a chain of Rydberg atoms, we first estimate the relevant physical parameters for the system components and interactions. In our model, the specific type of micro-electromechanical oscillator is not explicitly defined. However, the chosen platform should maximize the coupling strength to Rydberg atoms while providing GHz resonance frequencies and long lifetimes. We consider HBARs to be the most promising devices, as they typically operate at frequencies around 5 GHz and offer state-of-the-art lifetimes of approximately 1 ms [32, 69, 166] corresponding to[3]

$$\kappa \approx 1\,\mathrm{kHz}. \tag{5.7}$$

Additionally, as discussed in Section 2.3.1, HBARs can couple to Rydberg atoms via the evanescent electric field they generate. Therefore, we estimate parameters for our model considering HBARs as the oscillators.

Regarding the Rydberg atoms, the choice of atomic species is not critical for our model, as highly excited atoms exhibit similar behavior in terms of dipole matrix elements and transition frequencies. They effectively act as a singly positively charged core with an electron in a distant outer shell. To keep the parameter estimation straightforward, and because we have built a rubidium experiment, we calculate explicit values for the states $|n\mathrm{S}_{1/2}\rangle$ and $|n\mathrm{P}_{3/2}\rangle$ in ^{87}Rb.

The principal quantum number n of the Rydberg states must be chosen such that the $|n\mathrm{S}_{1/2}\rangle \rightarrow |n\mathrm{P}_{3/2}\rangle$ transition frequency matches the resonance frequency of the oscillators ($\approx 5\,\mathrm{GHz}$). This yields $n \approx 90$, as shown in Fig. 5.4(a), where the transition frequency is plotted as a function of n. Fig. 5.4(b) shows the natural decay rate γ_{nat} of the Rydberg states at zero temperature. For $n \approx 90$, the decay rate of nS

[3] Throughout this section, all coupling strengths and decay rates are given in units of Hz.

is approximately 1.2 kHz, and that of nP is approximately 0.6 kHz:

The effective decay rates of the Rydberg states may be increased, for example by laser dressing [167–169]. With maximum mixing of up to 50% between the Rydberg states and the state $|5P_{3/2}\rangle$ ($\gamma_{5P_{3/2}} \approx 6\,\mathrm{MHz}$), dressed decay rates of up to $\lesssim 3\,\mathrm{MHz}$ are possible[4]. Consequently, the decay rates are within a range of

$$\gamma_\downarrow,\ \gamma_\uparrow \approx 1\,\mathrm{kHz} \text{ to } 3\,\mathrm{MHz}. \tag{5.8}$$

To estimate the coupling strength V between neighboring Rydberg atoms in the chain, we use Eq. (5.3). We calculate the $\tilde{C}_3$ coefficient using the open source PairInteraction software package [170]. We find $\tilde{C}_3 \approx 31\,\mathrm{GHz}$ for the pair $|90S_{1/2}, m_j = 1/2\rangle$ and $|90P_{3/2}, m_j = 1/2\rangle$, neglecting external magnetic and electric fields and setting $\theta = 0$, such that $\tilde{C}_3 = C_3$. For realistic distances of $R_{\mathrm{neigh}} \approx 15$ to $30\,\mu\mathrm{m}$, this corresponds to coupling strengths of

$$V \approx 1 \text{ to } 10\,\mathrm{MHz}. \tag{5.9}$$

Although not included in our model, we also compute $C_6 \approx 16\,\mathrm{THz}$ for $|90S_{1/2}, m_j = 1/2\rangle$ [55, 170], which corresponds to an energy shift of about 16 kHz at a distance of 30 µm, and up to 1.6 MHz at 15 µm. The shift at larger distances and smaller V is mostly negligible. However, at $R_{\mathrm{neigh}} \approx 15\,\mu\mathrm{m}$, the energy shift reaches 16% of the interaction strength V and could alter the system dynamics. This defines an upper limit for valid interaction strengths, $V \lesssim 10\,\mathrm{MHz}$, within our model.

We estimate the atom–oscillator coupling J analytically following the methods outlined in [46, 70, 72]. For the calculation, the piezoelectric top-layer of the HBAR is assumed to be a flat disc with radius R_{pz}, thickness b_{pz} and density ρ_{pz}. This simplified HBAR model corresponds to the one already discussed in Section 2.2 and depicted in Fig. 2.2. The zero-point displacement of the piezoelectric disc is given by [46]

$$l_0 = \sqrt{\frac{1}{\rho_{\mathrm{pz}}\,\pi R_{\mathrm{pz}}^2 b_{\mathrm{pz}}\,\omega}}. \tag{5.10}$$

Assuming a constant strain in the piezoelectric disc, the single-phonon strain is computed with $S_0 = l_0/b_{\mathrm{pz}}$, which produces a surface charge density

$$\sigma_p = \frac{e_{\mathrm{pz}}\,S_0}{\varepsilon_r}, \tag{5.11}$$

with e_{pz} the piezoelectric constant and ε_r the relative permittivity of the piezoelectric material. We compute the electric field at the atom position z above the HBAR using Coulomb's law [70]

$$E_z(z) = \frac{1}{2\varepsilon_0}\left[-\sigma_p \frac{z}{\sqrt{R_{\mathrm{pz}}^2 + z^2}} + \sigma_p \frac{z + b_{\mathrm{pz}}}{\sqrt{R_{\mathrm{pz}}^2 + (z + b_{\mathrm{pz}})^2}}\right]. \tag{5.12}$$

Here, we assume the atom to be positioned in the center above the piezoelectric disc, such that the full electric field is given by the field component in z direction, due to the radial symmetry. The resulting

[4] Laser dressing would also alter the coupling strengths, however, this could in principle be compensated by adjusting the atom–atom or atom–oscillator spacing accordingly.

Table 5.1: Parameters used for the analytic estimate of the atom–oscillator coupling J.

Quantity	Symbol	Value
Piezo density	ρ_{pz}	$3\,255\,\mathrm{kg/m^3}$ [72]
Piezo radius	R_{pz}	$15\,\mu\mathrm{m}$
Piezo thickness	b_{pz}	$1\,\mu\mathrm{m}$ [72]
Oscillator frequency	$\omega_m/2\pi$	$5\,\mathrm{GHz}$
Atom–surface distance	z	$22\,\mu\mathrm{m}$
Piezoelectric coefficient	e_{pz}	$2.25\,\mathrm{C/m^2}$ [72]
Relative permittivity	ε_r	9 [72]
Dipole matrix element	$d_{n\mathrm{S}\leftrightarrow n\mathrm{P}}$	$3.4\times10^{-26}\,\mathrm{C\,m}$ [55]

Rabi frequency on the Rydberg transition is

$$\Omega = d_{n\mathrm{S}\leftrightarrow n\mathrm{P}}\, E_z, \tag{5.13}$$

where $d_{n\mathrm{S}\leftrightarrow n\mathrm{P}}$ is the transition dipole moment for the $|n\mathrm{S}_{1/2}\rangle \leftrightarrow |n\mathrm{P}_{1/2}\rangle$ transition. The electric field produced by the HBAR is linear polarized in z-direction, such that it drives a π-transition between $|90\mathrm{S}_{1/2}, m_j = 1/2\rangle$ and $|90\mathrm{P}_{3/2}, m_j = 1/2\rangle$ if the quantization axis of the atoms is defined along the z-direction. Using the parameters given in Table 5.1, we compute the coupling strength to be

$$J = \frac{\Omega}{2} \approx 1\,\mathrm{MHz}. \tag{5.14}$$

This analytic estimate indicates that the atom–oscillator coupling can be on the order of 1 MHz, comparable to the interatomic coupling V. However, this constitutes a simplified order-of-magnitude estimation. The predicted coupling strength is significantly larger than expected for the hybrid geometry discussed in Section 2.3, primarily because the assumed atom–surface distance is smaller here and the substrate thickness is neglected. To achieve coupling strengths on the order of 1 MHz in our experiment, the substrate thickness would need to be strongly reduced compared to the 435 µm of our HBARs (see Section 2.2), possibly at the cost of a reduced lifetime of the mechanical modes.

5.2.2.1 Entanglement measure

Our study of the proposed Rydberg chain–oscillator hybrid system focuses on entanglement generation between the motional states of the two oscillators. To obtain the reduced density matrix describing the oscillators, we trace out the atomic chain from the system's density matrix ρ_{sys},

$$\rho_{ab} = \mathrm{tr}_{\mathrm{chain}}(\rho_{\mathrm{sys}}). \tag{5.15}$$

The reduced state ρ_{ab} may be mixed. Accordingly, we quantify bipartite entanglement using the negativity [171, 172].

The negativity for a general bipartite state $|\psi_{AB}\rangle$ with subsystems A and B is given by [171]

$$\mathcal{N}(\rho_{AB}) = \frac{\|\rho_{AB}^{T_A}\|_1 - 1}{2}. \tag{5.16}$$

Here, ρ^{T_A} is the partial transpose of the density matrix $\rho_{AB} = |\psi_{AB}\rangle\langle\psi_{AB}|$ with respect to subsystem A, and $\|\cdot\|_1$ represents the trace norm. $\mathcal{N}(\rho_{AB})$ equals the absolute sum of the negative eigenvalues of $\rho_{AB}^{T_A}$. For any separable state, the partial transpose remains positive semidefinite and $\mathcal{N}(\rho_{AB}) = 0$, while $\mathcal{N}(\rho_{AB}) > 0$ indicates entanglement. The negativity is straightforward to compute numerically, and is suited for the pure or mixed states arising in our system.

Applied to our oscillators,

$$\mathcal{N}(\rho_{ab}) = \frac{\|\mathrm{tr}_{\mathrm{chain}}(\rho_{\mathrm{sys}})^{T_a}\|_1 - 1}{2}. \tag{5.17}$$

5.2.2.2 Negativity bounds

For the interpretation of determined negativities, it is desirable to know the bounds of reachable values in our system. The lower bound of the negativity is zero, which is attained by separable states. The upper bound is not directly known. However, since the negativity is an entanglement monotone, its maximum value is reached by any maximally entangled state.

The maximally entangled oscillator state for a given system size is not unique, but one possible maximally entangled state is given by [172]

$$|\phi_{\max}\rangle = \frac{1}{\sqrt{n_{\max}+1}} \sum_{i=0}^{n_{\max}} |i\rangle_a \otimes |i\rangle_b \,, \tag{5.18}$$

with $n_{\max}$ being an integer number describing the highest occupied Fock state $|i\rangle_{a/b}$ of oscillators a and b. We can compute the negativity and occupation number of the oscillators for this state

$$\mathcal{N}(|\phi_{\max}\rangle\langle\phi_{\max}|) = n_{\max}/2, \tag{5.19}$$

$$\langle\phi_{\max}| a^\dagger a + b^\dagger b |\phi_{\max}\rangle = n_{\max}. \tag{5.20}$$

Using Eqs. (5.19) and (5.20), we can formulate an upper bound for the negativity as a function of the occupation number. For integer occupation numbers, the bound is given by Eq. (5.19). However, also for noninteger occupation numbers a bound can be formulated:

$$\mathcal{N} \leq \frac{\left\lceil \left\langle a^\dagger a + b^\dagger b \right\rangle \right\rceil}{2}, \tag{5.21}$$

where $\lceil\cdot\rceil$ is the ceiling function. This shows, that the occupation number of the oscillators defines the upper bound of the negativity.

Furthermore, we can utilize the fact that the operator

$$\mathcal{M} = a^\dagger a + b^\dagger b + \sum_{i=1}^{N} |\uparrow\rangle\langle\uparrow|_i \tag{5.22}$$

commutes with the system Hamiltonian in Eq. (5.6), and as a consequence, its expectation value $\mu = \langle\mathcal{M}\rangle$ is conserved by the coherent evolution of the system. The operator $\mathcal{M}$ counts the number of atoms in the state $|\uparrow\rangle$ together with the occupation number of the oscillators. We identify atoms in state $|\uparrow\rangle$ as spin excitations and the occupation number of the oscillators as the number of phonon

excitations. Thus, μ represents the total number of excitations in the system. The system Hamiltonian does not create or remove excitations but only converts between phonon and spin excitations.

The total number of excitations in the system provides an upper bound on the number of excitations that can be present in the oscillators. Additionally, the dissipative channels in the system can only reduce the number of excitations and not increase them. This results in an upper bound for the negativity that holds during the system's evolution:

$$\mathcal{N} \leq \frac{\lceil \mu \rceil}{2}. \tag{5.23}$$

In particular, the initial number of excitations defines the upper bound of the reachable negativity.

5.2.3 Effective Hamiltonian for coherent dynamics

We analyze the coherent dynamics of the system to elucidate the mechanisms that govern the system and its capacity to generate entanglement. A purely coherent approximation is valid on timescales for which dissipation is negligible, i.e., $\gamma_\downarrow t$, $\gamma_\uparrow t$, $\kappa t \ll 1$. These timescales are experimentally accessible because the coherent coupling strengths exceed the decay rates, $V, J \gg \gamma_\downarrow$, $\gamma_\uparrow$, κ (see Section 5.2.2).

The coherent dynamics are described by the full system Hamiltonian (Eq. (5.6)). That Hamiltonian couples the oscillators only indirectly via the chain degrees of freedom.

For typical experimental parameters (see Section 5.2.2), the atom–oscillator coupling is much smaller than the inter-atomic coupling, $J \ll V$. This scale separation motivates a perturbative treatment in which the atomic chain is diagonalized and its fast degrees of freedom are eliminated, to yield an effective Hamiltonian acting directly on the oscillator subspace. In general, the diagonalization of H_{chain} can be carried out with the Jordan–Wigner transform [173].

To illustrate the idea, we consider the minimal nontrivial case of a two-atom chain ($N = 2$). The chain eigenbasis contains the spin-singlet $|S\rangle = (|\uparrow\downarrow\rangle - |\downarrow\uparrow\rangle)/\sqrt{2}$ and the triplet manifold $\{|\uparrow\uparrow\rangle, |T\rangle, |\downarrow\downarrow\rangle\}$, with $|T\rangle = (|\uparrow\downarrow\rangle + |\downarrow\uparrow\rangle)/\sqrt{2}$. Performing a Schrieffer-Wolff transformation [174, 175] to eliminate the chain–oscillator couplings to second order in J/V yields the following effective Hamiltonian:

$$\begin{aligned} H_{\text{eff}} = &- \frac{J^2}{V}\left(a^\dagger b + a b^\dagger\right)\left(|\downarrow\downarrow\rangle\langle\downarrow\downarrow| + |\uparrow\uparrow\rangle\langle\uparrow\uparrow| - |S\rangle\langle S| - |T\rangle\langle T|\right) \\ &- \frac{J^2}{V}\left[\left(a^{\dagger 2} + b^{\dagger 2}\right)|\downarrow\downarrow\rangle\langle\uparrow\uparrow| + \left(a^2 + b^2\right)|\uparrow\uparrow\rangle\langle\downarrow\downarrow|\right] \\ &+ \left(V + \frac{J^2\mathcal{M}}{V}\right)\left(|T\rangle\langle T| - |S\rangle\langle S|\right) + \mathcal{M}\omega. \end{aligned} \tag{5.24}$$

The first line contains a beam-splitter-type term, $a^\dagger b + a b^\dagger$, that couples the two oscillators directly. Its sign and strength are conditioned on the chain state through the projector prefactor. Thus, with the chain prepared in an appropriate eigenstate, the effective dynamics reduce to a state-dependent oscillator-oscillator excitation hopping. The second line contains higher-order pair-exchange terms that transfer two excitations at once between the oscillators and the atomic chain. The third line collects energy shifts of the chain eigenstates and the global excitation-energy contribution $\mathcal{M}\omega$.

Equation (5.24) is valid to order $(J/V)^2$ and conserves the total excitation number $\mathcal{M}$.

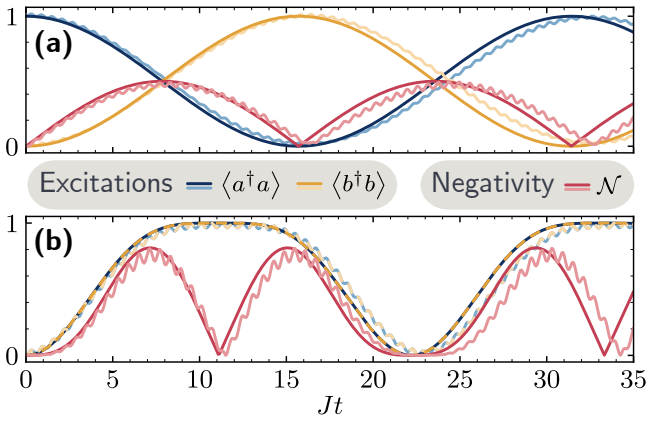

Figure 5.5: Coherent evolution of the number of excitations in the oscillators $\langle a^\dagger a\rangle$, $\langle b^\dagger b\rangle$ and oscillator entanglement quantified by the negativity $\mathcal{N}$ with $N = 2$ atoms and $V = 10J$. In panel **(a)** the system is initialized in $|\psi_1\rangle$ and in panel **(b)** in $|\psi_2\rangle$ (see main text). Dark lines are obtained from the effective Hamiltonian Eq. (5.24), while lighter, semi-transparent lines show the exact dynamics under the full Hamiltonian in Eq. (5.6). In panel (b), $\langle b^\dagger b\rangle$ is shown as a dashed curve to improve visibility. This figure is adapted from [1].

5.2.4 Entanglement generation under coherent evolution

Using the effective two-atom chain Hamiltonian H_{eff} introduced in Eq. (5.24), we study the dynamics starting from two different initial states and quantify the generated entanglement using the negativity. In addition, we compare the predictions of H_{eff} with exact numerical time evolution under the full system Hamiltonian, Eq. (5.6), in order to assess the regime of validity of the effective description.

To elucidate the roles of the different terms in H_{eff}, we consider the two initial states

$$|\psi_1\rangle = |1\rangle_a \otimes |S\rangle \otimes |0\rangle_b\,, \tag{5.25}$$

$$|\psi_2\rangle = |0\rangle_a \otimes |\uparrow\uparrow\rangle \otimes |0\rangle_b\,, \tag{5.26}$$

where $|\cdot\rangle_{a/b}$ denotes a Fock state of oscillator a or b, and $|S\rangle$, $|\uparrow\uparrow\rangle$ are the two-atom states defined above. The state $|\psi_1\rangle$ contains a single phononic excitation and one spin excitation encoded in the singlet state $|S\rangle$, whereas $|\psi_2\rangle$ contains two spin excitations and no phonons. Both initial states have the same total excitation number, $\mu = 2$, and therefore share the same upper bound for the negativity given in Eq. (5.23).

For these initial states the time evolution of the oscillator occupation numbers and the negativity under the effective Hamiltonian can be obtained analytically. Defining the dimensionless time

$$\tau = \frac{2\sqrt{2}J^2}{V}t, \tag{5.27}$$

the analytic solution are

$$\langle\psi_1|\, a^\dagger a\, |\psi_1\rangle = 1 - \langle\psi_1|\, b^\dagger b\, |\psi_1\rangle = \tfrac{1}{2}\left[1 + \cos\left(\frac{\tau}{2\sqrt{2}}\right)\right], \tag{5.28}$$

$$\langle\psi_2|\, a^\dagger a\, |\psi_2\rangle = \langle\psi_2|\, b^\dagger b\, |\psi_2\rangle = 1 - \cos^4\left(\frac{\tau}{2}\right), \tag{5.29}$$

$$\mathcal{N}\big(\,|\psi_1\rangle\,\langle\psi_1|\,\big) = \tfrac{1}{2}\left|\sin\left(\frac{\tau}{2\sqrt{2}}\right)\right|, \tag{5.30}$$

$$\begin{aligned}\mathcal{N}\big(\,|\psi_2\rangle\,\langle\psi_2|\,\big) = {} & \tfrac{1}{2}\big[1 - \cos(\tau)\big]\,\big|\sin(\tau)\big| \\ & + \tfrac{1}{8}\big[1 + \cos(\tau)\big]\Big(\sqrt{5\cos^2(\tau) - 6\cos(\tau) + 5} - 1 - \cos(\tau)\Big).\end{aligned} \tag{5.31}$$

Figure 5.5(a, b) compares these analytic solutions with the numerical evolution generated by the full Hamiltonian in Eq. (5.6). The effective Hamiltonian reproduces the overall dynamics but neglects faster, small-amplitude modulations.

In both cases, entanglement between the oscillators is generated and destroyed periodically, and the oscillator occupation numbers oscillate.

For longer times ($Jt \gg 10$) the full numerical solution lags behind the effective model and exhibits a slightly longer oscillation period. This discrepancy is caused by the omitted higher order corrections.

The larger peak negativity observed for $|\psi_2\rangle$ compared to $|\psi_1\rangle$ can be understood from the allowed exchange processes. For $|\psi_1\rangle$ only single-excitation exchange between the oscillators (the beam-splitter term in H_{eff}, Eq. (5.24)) is allowed. Consequently, the oscillator excitation number $\langle a^\dagger a + b^\dagger b\rangle$ remains fixed at one and the negativity is bounded by $\mathcal{N} \leq 1/2$, according to Eq. (5.21). In contrast, for $|\psi_2\rangle$ pair-exchange processes (the second line of H_{eff}, Eq. (5.24)) enable transfer of the two excitations initially in the chain into the oscillators. This additional channel permits entangled oscillator states with higher phonon occupation and thus a larger attainable negativity.

5.2.5 Quantum-jump trajectory method

While the coherent dynamics of the system discussed so far can be treated analytically, this is not possible for the dissipative dynamics. We simulate the dissipative dynamics numerically using the quantum-jump method pioneered by Dalibard, Castin, and Mølmer [176, 177].

Unlike a master-equation approach, this framework simulates single probabilistic evolutions of the system wave function $|\psi_{\text{sys}}(t)\rangle$, so-called quantum-jump trajectories. Each trajectory corresponds to a single possible realization of the system dynamics, as it would appear in experiments. The ensemble average over the different trajectory realizations is equivalent to the density-matrix solution of the master equation. The initial state $|\psi_{\text{sys}}(0)\rangle$ is evolved by the non-Hermitian Hamiltonian

$$H_{\text{nH}} = H_{\text{sys}} - \frac{i}{2}\sum_\alpha L_\alpha^\dagger L_\alpha, \tag{5.32}$$

with jump operators

$$L_\alpha \in \Big\{ \sqrt{\gamma_\uparrow}\,|g\rangle\langle\uparrow|_1,\ \ldots,\ \sqrt{\gamma_\uparrow}\,|g\rangle\langle\uparrow|_N, \\ \sqrt{\gamma_\downarrow}\,|g\rangle\langle\downarrow|_1,\ \ldots,\ \sqrt{\gamma_\downarrow}\,|g\rangle\langle\downarrow|_N, \\ \sqrt{\kappa}a,\ \sqrt{\kappa}b \Big\}. \tag{5.33}$$

These jump-operators correspond to the decay channels in the system, which are visualized in Fig. 5.3. The first line represents decays from atoms in the state $|\uparrow\rangle$ to $|g\rangle$, the second line decay from atoms in the state $|\downarrow\rangle$ and the third line describes decay of the oscillator modes.

During the evolution under the non-Hermitian Hamiltonian in Eq. (5.32), the system randomly undergoes quantum jumps with the jump operators L_α. The likelihood of any jump occurring during a small time interval δt is given by

$$\delta p = \delta t \sum_\alpha \langle\psi_{\mathrm{sys}}(t)|\, L_\alpha^\dagger L_\alpha\, |\psi_{\mathrm{sys}}(t)\rangle\,. \tag{5.34}$$

If a jump occurs, the likelihood that it is the jump corresponding to a specific L_α is given by its expectation value at the time of the jump

$$P(L_\alpha, t) = \langle\psi_{\mathrm{sys}}(t)|\, L_\alpha^\dagger L_\alpha\, |\psi_{\mathrm{sys}}(t)\rangle\,/\delta p. \tag{5.35}$$

An advantage of the quantum-jump method is that, for a system with a given number of states N_{ss}, evolving the wave function requires only N_{ss} variables, while the density-matrix master-equation approach requires N_{ss}^2 variables [176]. Thus, the quantum-jump approach enables simulation of larger system sizes than the master-equation approach.

5.2.5.1 Numerical implementation

High-level functionality for the simulation of quantum-jump trajectories is available in the open-source software package QuTiP [178] for Python. Initially, we used this package to simulate the hybrid system. However, the implemented quantum-jump trajectory (QJT) solver is not well suited to our system and limited the system size we could simulate to chain lengths of less than $N \lesssim 7$ atoms. Therefore, we developed a new implementation of the quantum-jump method in Python, which is optimized for our system. Our implementation is based on QuTiP's QJT solver, but major changes to both the frontend and backend were made to increase speed and memory efficiency.

At its core, our QJT solver implements the same algorithmic steps as the QuTiP's solver to evolve the system's wave function $|\psi_{\mathrm{sys}}(t)\rangle$. In the following we first outline these steps and then discuss our application specific adaptations. A description of the algorithmic steps is given in the documentation of the QuTiP package [178] and repeated here with adapted notation for completeness:

1. Draw a random number r_1 between zero and one representing the probability for a quantum jump to occur.
2. Integrate the Schrödinger equation with the non-Hermitian Hamiltonian in Eq. (5.32) until a time τ_{jump} at which the wave-function norm satisfies

$$\langle\psi_{\mathrm{sys}}(\tau_{\mathrm{jump}})\,|\,\psi_{\mathrm{sys}}(\tau_{\mathrm{jump}})\rangle = r_1, \tag{5.36}$$

and a jump occurs.

3. Draw a random number r_2 between zero and one. Choose the jump operator L_α such that α is the smallest integer fulfilling
$$\sum_{i=1}^{\alpha} P(L_i, \tau_{\text{jump}}) \geq r_2, \tag{5.37}$$
where the individual probabilities $P(L_i, \tau_{\text{jump}})$ are given by Eq. (5.35). Apply L_α to the state and renormalize the post-jump state.

4. Use the renormalized post-jump state at time τ_{jump} as the new initial state at time τ_{jump}. Repeat all steps until the final simulation time is reached.

Both our solver and the QuTiP solver integrate the Schrödinger equation by passing a matrix representation to an ODE solver implemented in the Python software package SciPy [123]. It is important to choose a sparse representation, otherwise the system size is limited due to the memory requirement when allocating a matrix with a dimensionality of $N_{\text{ss}} \times N_{\text{ss}}$.

Optimization of the implementation To optimize our QJT solver for our specific system, we exploit the fact that an atom in state $|g\rangle$ no longer participates in the dynamics. Furthermore, a jump operator associated with atomic decay projects the atomic subsystem onto its ground state, rendering the atomic subsystem separable from the remaining system state $|\psi_{\text{sys}}^{\text{rest}}\rangle$:

$$\sqrt{\gamma_\uparrow}\,|g\rangle\langle\uparrow|_i\,|\psi_{\text{sys}}\rangle \quad \text{or} \quad \sqrt{\gamma_\downarrow}\,|g\rangle\langle\downarrow|_i\,|\psi_{\text{sys}}\rangle \;\rightarrow\; |g\rangle_i \otimes |\psi_{\text{sys}}^{\text{rest}}\rangle\,, \tag{5.38}$$

where i indexes the atom. Since the atomic subsystem becomes separable and no longer affects the dynamics, it can be discarded from the simulation after a decay event. This reduces the effective Hilbert-space dimension by a factor of two per discarded atom, increasing simulation speed and reducing memory requirements.

More importantly, the fact that a decayed atom no longer affect the dynamics allows us to treat the atoms as effective two-level systems comprising only the states $|\downarrow\rangle$ and $|\uparrow\rangle$. To achieve this, we replace the jump operators to the ground state by jump operators between the Rydberg levels:

$$\sqrt{\gamma_\uparrow}\,|g\rangle\langle\uparrow|_i \rightarrow \sqrt{\gamma_\uparrow}\,|\downarrow\rangle\langle\uparrow|_i\,, \tag{5.39}$$
$$\sqrt{\gamma_\downarrow}\,|g\rangle\langle\downarrow|_i \rightarrow \sqrt{\gamma_\downarrow}\,|\uparrow\rangle\langle\downarrow|_i\,. \tag{5.40}$$

This substitution does not affect the non-Hermitian Hamiltonian in Eq. (5.32) nor the jump selection rule in Eq. (5.37). Steps 1-3 of the QJT solver remain unchanged. After a jump, the renormalized state will be $|\uparrow\rangle_i \otimes |\psi_{\text{sys}}^{\text{rest}}\rangle$ or $|\downarrow\rangle_i \otimes |\psi_{\text{sys}}^{\text{rest}}\rangle$ instead of $|g\rangle_i \otimes |\psi_{\text{sys}}^{\text{rest}}\rangle$. By discarding the atomic subsystem before continuing the evolution, this modification does not alter the simulation results.

Treating the atoms as two-level systems strongly reduces the system size for larger atom numbers N,

$$N_{\text{ss}}^{\text{three-level}} \propto 3^N \quad \rightarrow \quad N_{\text{ss}}^{\text{two-level}} \propto 2^N, \tag{5.41}$$

which improves both speed and memory efficiency of the solver.

One should note that discarding an atom from the system after its decay—which is required to treat the atoms as effective two-level systems—cannot be implemented with QuTiP's solver without

rewriting the backend. This motivated us to develop our own QJT solver, based on NumPy [179] arrays rather than QuTiP's high-level wrappers to represent the Hamiltonian and wave function.

Our QJT solver can optionally save the reduced density matrix ρ_{ab} of the oscillators rather than the full state vector, which strongly reduces required disc space. Here, ρ_{ab} is computed by partial tracing over the chain from a sparse form of the pure system density matrix for memory reasons.

5.2.6 Dissipative entanglement protocol

The coherent protocol discussed before can produce highly correlated oscillator states, but stopping the dynamics precisely at the time of maximum negativity requires accurate timing and detailed knowledge of system parameters. Active interventions—for example removing the atoms with repulsive optical tweezers at the desired instant—are in principle feasible but experimentally demanding.

Here, we consider an alternative approach that uses engineered dissipation in the atomic chain to both generate entanglement, and to halt the subsequent coherent exchange autonomously. For the dissipative protocol, we consider the separable initial state

$$|\psi_{\text{init}}\rangle = |0\rangle_a \otimes |\uparrow\rangle^{\otimes N} \otimes |0\rangle_b \,, \tag{5.42}$$

where all atoms are prepared in the Rydberg state $|\uparrow\rangle$ and the oscillators in the vacuum state.

Enhancing the atomic decay rate steers the system toward a state in which all atoms occupy the ground state, while the oscillators can remain populated and possibly entangled. Once the chain has relaxed, the atom–oscillator coupling vanishes and the oscillators continue to evolve under their individual harmonic Hamiltonians, thereby preserving correlations present at the moment of decoupling. We refer to the state reached after the final atomic decay as the final state. Below, we investigate the entanglement of the final state[5]. Because the sequence and timing of the atomic decay events are probabilistic—each experimental run follows a particular quantum-jump trajectory—the negativity of the final oscillator state is a stochastic quantity.

5.2.6.1 Single trajectory entanglement generation

We investigate an exemplary single trajectory to elucidate the mechanisms that govern the entanglement build-up during the evolution of a trajectory. For this investigation, we choose a system with $N = 5$ atoms, an interaction strength $V = 3J$ and decay rates $\gamma_\uparrow = \gamma_\downarrow = 0.2J$. Decay rates of $0.2J$ correspond to an enhanced decay via laser dressing. We set $\kappa = 0$ to focus on the dissipation in the chain and to simplify the analysis.

In Fig. 5.6(a), the time evolution of the excitation numbers along the chain and in the oscillators are shown for a chosen exemplary trajectory until the final state is reached. The corresponding negativity is shown in Fig. 5.6(b), together with the negativity that would be reached under purely coherent evolution. Comparing both negativities highlight the possibility of the dissipative dynamics to produce final states with much higher negativity than what is reached in the coherent case in the same time. This observation can be explained by considering the decay events in the chosen example trajectory. Here, all jump operators that act on the wave function during its evolution are from the second row in Eq. (5.33). These operators collapse the atomic subspace of the respective atom from the state $|\downarrow\rangle$ to

[5] After reaching the final state, the oscillators remain subject to intrinsic damping, which eventually degrades entanglement. However, this process occurs on a much slower timescale than the engineered atomic decay or the coherent interactions.

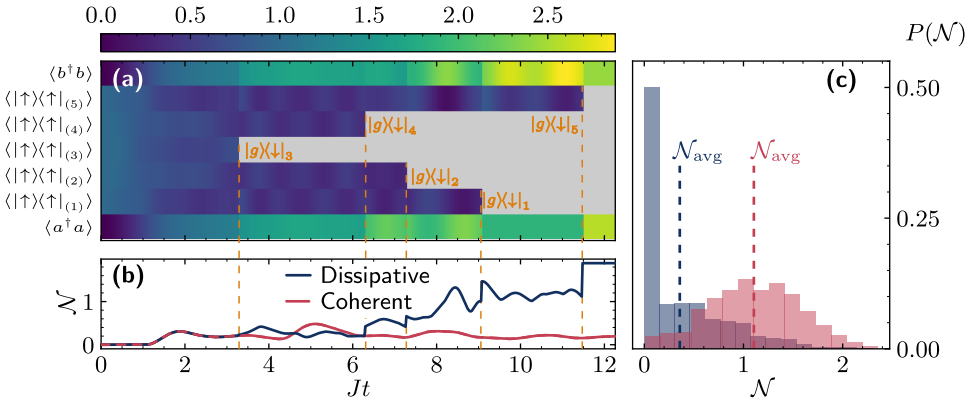

Figure 5.6: **(a)** Time evolution for a single quantum-jump trajectory of the chain site-excitation probabilities $\langle|\uparrow\rangle\langle\uparrow|_{(i)}\rangle$ and the oscillator occupations $\langle a^\dagger a\rangle$, $\langle b^\dagger b\rangle$ for parameters $V = 3J$, $\gamma_\downarrow = \gamma_\uparrow = 0.2J$, and $\kappa = 0$. The system is initialized in $|\psi_{\text{init}}\rangle = |0\rangle_a \otimes |\uparrow\rangle^{\otimes 5} \otimes |0\rangle_b$. Vertical dashed lines mark the times of atomic decay (quantum jumps). Sites that have decayed to the ground state are shown in gray. **(b)** Time evolution of the oscillator negativity $\mathcal{N}$ for the trajectory shown in (a) (blue) compared with the purely coherent evolution (red) for the same parameters. **(c)** Probability distribution $P(\mathcal{N})$ of final-state negativities $\mathcal{N}$ obtained from 2000 trajectories using the parameters from (a) with $\gamma_\uparrow = 0.2J$ (blue) and $\gamma_\uparrow = 0$ (red). Vertical dashed lines indicate the distribution means $\mathcal{N}_{\text{avg}}$. The comparison highlights the role of engineered atomic dissipation in producing entangled final oscillator states. This figure is adapted from [1].

$|g\rangle$[6]. In doing so, the operators preserve the number of excitations in the system. Consequently, when the final state is reached, all excitations are in the oscillators. In Section 5.2.2.2 it was shown, that the negativity is bound by the number of excitations in the oscillators, according to Eq. (5.21). Thus, the final state of the chosen trajectory—with all excitations in the oscillators—allows for the highest negativity. In contrast, during the coherent evolution, excitation hopping between the chain and the oscillators results in some excitations being in the chain, reducing the maximum reachable negativity.

In this example, only decay from $|\downarrow\rangle$ to $|g\rangle$ occurs. However, in general, decay from $|\uparrow\rangle$ to $|g\rangle$ can also occur, which is modeled by the jump operators in the first row of Eq. (5.33). These jumps remove excitations from the system, reducing the number of excitations in the oscillators in the final state and, consequently, reducing the maximum reachable negativity according to Eq. (5.21).

5.2.6.2 Distribution of final-state entanglement

While the chosen trajectory is illustrative, the stochastic nature of the quantum-jump dynamics means that different trajectories will yield different final-state negativities. We simulated 2000 trajectories for the same parameters as in the exemplary trajectory above, to inspect the distribution $P(\mathcal{N})$ of final-state negativities. In Fig. 5.6(c), the distribution of the final-state negativities obtained from the 2000 trajectories is shown. Additionally, the distribution for the case $\gamma_\uparrow = 0$ is shown, where only decays from $|\downarrow\rangle$ to $|g\rangle$ occur. When both decay channels are present ($\gamma_\uparrow = \gamma_\downarrow = 0.2J$), the distribution is centered around a mean negativity of $\mathcal{N}_{\text{avg}} \approx 0.4$. In contrast, when only decays from $|\downarrow\rangle$ to $|g\rangle$ are present ($\gamma_\uparrow = 0$), the mean negativity is increased to $\mathcal{N}_{\text{avg}} \approx 1.1$. This increase can be explained by considering that, with $\gamma_\uparrow = 0$, only decays from state $|\downarrow\rangle$ to $|g\rangle$ can occur, whereas decays from

[6] We specifically present this single trajectory, because it contains only the one kind of decay.

state $|\uparrow\rangle$ to $|g\rangle$ are forbidden. Decay from state $|\uparrow\rangle$ to $|g\rangle$ removes an excitation from the system and, consequently, without this decay channel, more excitations remain in the system until the final state is reached. As explained above, a higher number of excitations in the oscillators allows for a higher negativity according to Eq. (5.21). Thus, by allowing only the decay from $|\downarrow\rangle$ to $|g\rangle$, the distribution is shifted to higher negativities and the average final-state negativity is increased.

Note that in both cases, the distribution of final-state negativities is broad, indicating that while the average negativity can be increased by suppressing certain decay channels, there is still significant variability in the outcomes of individual trajectories. In particular, if decay from state $|\uparrow\rangle$ is present—as is the case in real experiments—the distribution will always include trajectories with zero negativity, corresponding to cases where all excitations are lost from the system. Nevertheless, both distributions shown here, also feature trajectories with high final-state negativities approaching the negativity bound for this initial state of $\mathcal{N} \leq 2.5$.

These results indicate, that the parameter choice is critical for the performance of the dissipative entanglement protocol. Specifically, the decay rate $\gamma_\uparrow$ should be chosen as small as possible to minimize excitation loss from the system. A detailed investigation of the other parameter dependences of the final-state negativity is presented in the following Section 5.2.7.

5.2.7 Parameter dependences of final-state entanglement

Having established the basic functioning of the dissipative entanglement protocol, we now explore how the final-state negativity depends on the system parameters. We study how the final-state negativity can be optimized by tuning the atomic decay rate $\gamma_d ownarrow$, the inter-atomic coupling strength V, the atom-oscillator coupling strength J, and the number of atoms in the chain N.

For this investigation we keep the decay rate $\gamma_\uparrow = 0.001J$ fixed at a value corresponding to the natural linewidth of the Rydberg state. We keep the oscillator decay at $\kappa = 0$ for now and consider the effect of a finite oscillator decay on the final-state negativity later. To keep the analysis tractable, we focus on the average final-state negativity $\mathcal{N}_{\text{avg}}$ obtained from distributions as shown in Fig. 5.6(c).

In Fig. 5.7, we show $\mathcal{N}_{\text{avg}}$ as a function of the atomic decay rate $\gamma_\downarrow$. A non-monotonic behavior is observed, which is well described by a Gaussian in logarithmic scale of the form

$$\mathcal{N}_{\text{avg}}(\gamma_\downarrow) = \frac{A}{\gamma_\downarrow} \exp\left(-\frac{(\ln \gamma_\downarrow - \nu)^2}{2\sigma^2}\right). \tag{5.43}$$

Here, A, ν and σ are fit parameters. This behavior arises from the competition between two opposing mechanisms. On one hand, increasing $\gamma_\downarrow$ decreases the relative likelihood of decay from the state $|\uparrow\rangle$ compared to $|\downarrow\rangle$. As a result, unwanted decays from $|\uparrow\rangle$—which would otherwise remove excitations from the system—become less probable, leading to an increase in the average negativity. On the other hand, a higher decay rate $\gamma_\downarrow$ causes the first decay event to occur earlier, effectively splitting the chain and partitioning the system into two uncoupled subsystems. Following such an event, each sub-chain interacts only with a single mechanical oscillator. While quantum correlations can still develop within each subsystem, entanglement between the two oscillators can no longer be established unless the subsystems were already entangled prior to the first decay. Therefore, a large $\gamma_\downarrow$ suppresses entanglement generation because the system is split before correlations can build up. Notably, the optimal value of $\gamma_\downarrow$—at which $\mathcal{N}_{\text{avg}}$ is maximized—is smaller than J, ensuring that the system has sufficient time to transfer excitations to the oscillators and build up correlations. This underscores the

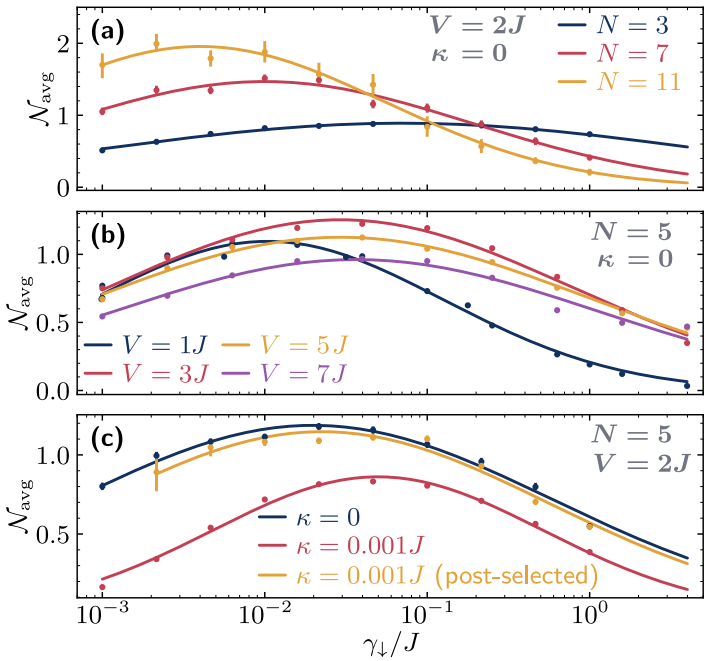

Figure 5.7: Parameter dependence of the average final-state negativity. **(a)** Average final-state negativity $\mathcal{N}_{\mathrm{avg}}$ as a function of the engineered atomic decay rate $\gamma_\downarrow$ for different chain lengths N with fixed $V = 2J$, $\kappa = 0$, and $\gamma_\uparrow = 0.001J$. Data points are averaged over 1000 trajectories for $N = 3$ and $N = 7$, and over 100 trajectories for $N = 11$. **(b)** $\mathcal{N}_{\mathrm{avg}}$ as a function of $\gamma_\downarrow$ for different interatomic couplings V with $N = 5$, $\kappa = 0$, and $\gamma_\uparrow = 0.001J$. Each data point is averaged over 1000 trajectories. **(c)** Comparison of the idealized case ($\kappa = 0$) with a finite oscillator decay ($\kappa = 0.001J$) for $V = 2J$, $N = 5$, and $\gamma_\uparrow = 0.001J$. For the finite-κ data we also show a post-selected subset that contains only trajectories for which all atoms have decayed to $|g\rangle$ within the cutoff time $0.3/\kappa$. The data point at $\gamma_\downarrow = 0.001J$ is omitted because none of the 10^4 simulated trajectories satisfied the post-selection criterion. All averages shown in panel (c) are taken over 10^4 trajectories. Log-normal fits are shown in all panels. This figure is reproduced from [1].

critical role of carefully engineering $\gamma_\downarrow$ for effective dissipative entanglement generation.

In Fig. 5.7(a), we investigate the role of the number of atoms N in the Rydberg chain. We find that increasing N results in a larger maximal average negativity $\mathcal{N}_{\mathrm{avg}}$. This increase can be understood by considering the chosen initial state: The initial product state defined in Eq. (5.42) contains more excitations for longer chains, and the upper bound on the attainable negativity, given in Eq. (5.23), grows with the available excitation number. At the same time, longer chains introduce more potential decay channels, which typically causes the first atomic decay to occur earlier in the time evolution. Moreover, the time required for correlations to build up between the two oscillators increases with N, because excitations must propagate across a longer chain before they can mediate correlations at the ends.

As a consequence of these competing effects, the optimal engineered decay rate $\gamma_\downarrow$ that maximizes $\mathcal{N}_{\mathrm{avg}}$ shifts toward lower values for larger N. Thus, increasing the chain length is beneficial provided the atomic decay rates $\gamma_\downarrow$ can be kept sufficiently small so that there is enough time for correlation buildup. In practice, this decay rate is limited by the natural linewidth of the Rydberg state. We stress that this conclusion also assumes idealized, infinitely long-lived mechanical oscillators ($\kappa = 0$).

With oscillator damping included, the available time window for correlation formation is reduced and increasing the chain length becomes less advantageous or even detrimental.

Next, as shown in figure Fig. 5.7(b), we study the role of the interaction strength V, while keeping $N = 5$ and $\kappa = 0$ fixed. Among the investigated values of V, the largest average final-state negativity $\mathcal{N}_{\text{avg}}$ is reached for $V = 3J$ and $\gamma_\downarrow \approx 0.03J$, as shown in Fig. 5.7(b). For $V = 1J$ the maximum $\mathcal{N}_{\text{avg}}$ shifts toward lower $\gamma_\downarrow$ and attains a smaller value overall. This behaviour is readily explained: A smaller V slows down excitation hopping along the chain, which delays the buildup of correlations between the two oscillators and increases the risk that the sequence of atomic decays interrupts the initial correlation buildup.

We also observe a reduction of the peak value of $\mathcal{N}_{\text{avg}}$ for larger values $V = 5J, 7J$. This effect can be understood by considering the effective Hamiltonian in Eq. (5.24), which is derived in the limit $V \gg J$ and $N = 2$. Up to second order, the chain only couples to the oscillators via terms proportional to J^2/V. Hence, increasing V reduces the effective transfer of spin-excitations from the chain to the oscillators. Consequently, the initially fully excited spin chain remains excited for longer times, which increases the probability of detrimental decays from the state $|\uparrow\rangle$ and thereby reduces the average final-state negativity.

So far we have considered idealized oscillators without internal damping ($\kappa = 0$). To illustrate the effect of a finite oscillator lifetime, we compare in Fig. 5.7(c) the idealized case with a scenario where $\kappa = 0.001J$, a value that is achievable with current state-of-the-art devices (see Section 5.2.2). We find that excitation loss due to oscillator decay reduces the average final-state negativity $\mathcal{N}_{\text{avg}}$ in agreement with the general upper bound in Eq. (5.23). The reduction is most pronounced for small engineered atomic decay rates $\gamma_\downarrow$ and produces a shift of the optimal $\gamma_\downarrow$ toward larger values. Lowering $\gamma_\downarrow$ increases the typical time required for all atoms to decay, thereby increasing the time interval during which oscillator damping can remove excitations from the oscillators and destroy correlations.

A feasible mitigation strategy is post-selection. Experimentally, the atomic population in the ground state $|g\rangle$ can be measured on a timescale short compared to the oscillator lifetime [180]. Selecting only those trajectories in which all atoms have decayed to state $|g\rangle$ within a short time window could restore the average negativity to near the value without oscillator dampening, at the price of a reduced acceptance probability. In Fig. 5.7(c) we show such a post-selected dataset, where only trajectories with all atoms decayed to state $|g\rangle$ within a cutoff time of $0.3/\kappa$ are accepted. While post-selection recovers $\mathcal{N}_{\text{avg}}$ close to the idealized case, the accepted fraction decreases rapidly as $\gamma_\downarrow$ is reduced. For the natural decay rate $\gamma_\downarrow = 0.001J$ no trajectory out of 10,000 meets the post-selection criterion, whereas for the approximately optimal rate $\gamma_\downarrow = 0.02J$ the acceptance fraction is $\approx 6.3\%$. Thus, with oscillator damping, there exists a trade-off between attainable entanglement and fraction of accepted trajectories that must be considered when choosing $\gamma_\downarrow$.

With the presented analysis of the dissipative entanglement protocol and the previously shown analysis of the coherent dynamics of the system, we demonstrated how a chain of Rydberg atoms can be used to entangle the mechanical modes of two distant HBARs.

CHAPTER 6

Conclusion and outlook

In this thesis, we have presented the development of an experimental apparatus designed to realize a novel hybrid architecture interfacing Rydberg atoms with a HBAR. After introducing the theoretical concepts underlying the hybrid system and discussing its individual constituents, we detailed the design and characterization of the experimental platform.

The experimental setup that was assembled during this work comprises a dedicated MOT loading chamber and a separate science chamber connected by a magnetic transport. We described the complete cold-atom preparation sequence, including MOT loading, optical molasses cooling, optical pumping, magnetic transport, and magnetic trapping in the science chamber. Exemplary characterization measurements were presented for each stage of the preparation sequence. In addition, we demonstrated Rydberg excitation and detection in the science chamber using both single-photon detectors and ion detection with a MCP. With these demonstrations, we established that the assembled setup provides an operational cold-atom-preparation platform for future hybrid Rydberg–HBAR experiments.

Using an optimized magnetic transport sequence, we achieve atom numbers of approximately 2×10^8 at temperatures around 200 µK in the science chamber. The temperature is primarily limited by the finite rise time of the magnetic field generated by the MOT coil pair during the transfer from optical molasses into the magnetic trap. This elevated temperature increases the cloud size during transport, leading to collisions with the chamber walls, which we identified as the likely dominant loss mechanism that reduces the atom number from an initial 10^9. We outlined potential ways to speed up the magnetic field rise time, which is expected to simultaneously reduce atom loss and lower the final temperature of the atoms.

At present, cold-atom preparation is performed in a room-temperature version of the apparatus. This setup was designed to require only minimal modifications for the integration of a custom cryostat. We presented the planned upgrade to a cryogenic environment together with the design and fabrication of a first-generation atom chip. The atom chip incorporates a superconducting Z-wire magnetic trap designed to confine and position the atomic cloud close to the chip surface. In future designs, we plan to mount the HBAR directly on the atom chip surface. However, the first-generation chip instead incorporates a coplanar waveguide resonator to simplify the initial characterization of Rydberg excitation, detection, and on-chip atom handling prior to interfacing the atoms with the HBAR. Due to its superconducting structures, this chip has not yet been installed into the room-temperature setup.

The currently achieved temperature of 200 µK in the science chamber is not yet sufficient for successful transfer to the on-chip Z-wire trap. To address this, we will employ evaporative cooling in

the science chamber prior to the transfer, targeting a final temperature of approximately 10 µK. We plan to use the Z-wire itself as the RF antenna for evaporation and have built a custom circuit that combines RF and DC signals for this purpose.

Finally, we investigated potential applications of the hybrid platform. We proposed a cooling scheme that exploits the atom–HBAR coupling to extract thermal excitations from the mechanical mode via a Rydberg atom ensemble. Implementing such a scheme represents an important first experimental step, as the residual thermal occupation of the HBAR at 4 K otherwise prevents observation of coherent interactions. We also studied the possibility of mediating entanglement between two mechanical modes of spatially separated HBARs using a chain of Rydberg atoms.

Outlook Establishing a coherent interface between Rydberg atoms and HBARs would open a range of new experimental directions. Such a hybrid system would combine the long coherence times and precise optical control available in atomic physics with the strong confinement and high quality factors of mechanical resonators.

Analogous to existing hybrid architectures in which superconducting transmon qubits are coupled to HBARs [30, 72], the atomic control toolbox developed for Rydberg atoms could be employed to engineer nonclassical mechanical states. In transmon–HBAR systems, the high degree of qubit control has enabled the preparation of specific mechanical states, including Schrödinger cat states [68] and encoded mechanical qubits [32]. A Rydberg–HBAR interface could similarly leverage optical excitation schemes and state-selective control to manipulate the quantum state of mechanical modes.

Beyond purely mechanical applications, a Rydberg–HBAR interface could also serve as a mediator between atomic (Rydberg) systems and superconducting circuits. Specifically, coupling between Rydberg atoms and transmon qubits could be realized, as proposed in [46].

Many of these applications would benefit from a reduced thermal occupation of the HBAR modes. This can be achieved by operating the hybrid system in a dilution refrigerator [79]. An upgraded experimental platform in which the Rydberg–HBAR interface is embedded in a millikelvin environment would passively cool the mechanical modes close to their ground state, eliminating the need for active mechanical cooling. A similar strategy is for example pursued by the group of professor Fortágh, where earlier Rydberg–microwave resonator chip experiments conducted at 4 K are being extended toward operation in dilution refrigerators [130, 132].

APPENDIX A

Optical trapping close to the chip

We decided to use a magnetic transport to move the atoms from the MOT chamber to the science chamber, as detailed in Section 3.6. A possible alternative are moving optical dipole traps. Here we discuss, why we decided against using an optical trap.

An optical dipole trap is created by tightly focusing a high power laser beam creating a trapping dipole potential at the focus due to the AC-Stark shift [104]. By moving the focus of the beam, for example by moving the focussing lens with a translation stage, the atoms can be transported. We need to transport the atoms very close to the surface of the atom chip in the cryogenic environment such that we can hand them over to the on-chip magnetic trap, as explained in 4.2. To prevent heating of the cryogenic atom chip, the high power laser must not hit the surface of the atom chip. The final trap is planned to be at a distance of only $\approx 50\,\mu\text{m}$ from the HBAR. In principle the handover to the final trap can be done at larger distances, but this is limited by the current carrying capacity of the Z-wire on the chip (see Section 4.2.1).

This is not a problem, when the dipole trap focus is positioned over the chip surface and the Rayleigh length is chosen appropriately. However, at the start of the transport, the focus will need to be at the MOT position. As discussed in Section 3.1, the MOT chamber was chosen to be separated by the science chamber by a differential pumping tube to maintain good vacuum in the science region while allowing for faster MOT loading from a high background pressure. A differential pumping tube that sufficiently isolates the vacuum and has a large enough opening for the atoms to pass through requires a length of several cm. This means that the distance between the MOT position and the atom chip surface needs to be at least on that order. The Rayleigh length of an optical dipole trap beam with an exemplary wavelength of 1 064 nm is $\gtrsim 7.4\,\text{mm}$ for a required focus beam waists of $\lesssim 50\,\mu\text{m}$. Since the distance from the MOT to the chip will be greater than the Rayleigh range, the beam waist will be too large at the position of the chip during the beginning of the transport. This could be mitigated a bit, by choosing a smaller wavelength, but with our geometric constrains, the tradeoff between Rayleigh length and beam waist makes it challenging to design a moving optical dipole trap that can transport the atoms from the MOT position to the atom chip without hitting the chip surface with the high power laser beam, causing unwanted heating.

Bibliography

[1] C. Wind et al.,
Entanglement of Mechanical Oscillators Mediated by a Rydberg Tweezer Chain, 2025,
arXiv: 2510.08371 [quant-ph], (visited on 22/10/2025).

[2] V. Montenegro et al., *Review: Quantum Metrology and Sensing with Many-Body Systems*,
Physics Reports, Review: Quantum Metrology and Sensing with Many-Body Systems **1134**
(2025) 1.

[3] C. L. Degen, F. Reinhard and P. Cappellaro, *Quantum Sensing*,
Rev. Mod. Phys. **89** (2017) 035002.

[4] Y.-A. Chen et al.,
An Integrated Space-to-Ground Quantum Communication Network over 4,600 Kilometres,
Nature **589** (2021) 214.

[5] R. P. Feynman, *Simulating Physics with Computers*, Int J Theor Phys **21** (1982) 467.

[6] I. M. Georgescu, S. Ashhab and F. Nori, *Quantum Simulation*,
Rev. Mod. Phys. **86** (2014) 153.

[7] B. Inglis, J. Ullrich and M. Milton, *Das Internationale Einheitensystem (SI), Deutsche Übersetzung der SI-Broschüre des BIPM 9. Auflage (Update 2024)*, PTB-OAR (2025).

[8] European Space Agency, *GPS Navigation Message - Navipedia*,
https://gssc.esa.int/navipedia/index.php/GPS_Navigation_Message, 2026,
(visited on 27/01/2026).

[9] GOOGLE AI QUANTUM AND COLLABORATORS et al.,
Hartree-Fock on a Superconducting Qubit Quantum Computer, Science **369** (2020) 1084.

[10] D. Bluvstein et al.,
A Fault-Tolerant Neutral-Atom Architecture for Universal Quantum Computation,
Nature **649** (2026) 39.

[11] Y. Cao et al., *Quantum Chemistry in the Age of Quantum Computing*,
Chem. Rev. **119** (2019) 10856.

[12] B. Bauer, S. Bravyi, M. Motta and G. K.-L. Chan,
Quantum Algorithms for Quantum Chemistry and Quantum Materials Science,
Chem. Rev. **120** (2020) 12685.

[13] P. W. Shor, *Polynomial-Time Algorithms for Prime Factorization and Discrete Logarithms on a Quantum Computer*, SIAM J. Comput. **26** (1997) 1484.

[14] D. Barredo et al., *Coherent Excitation Transfer in a Spin Chain of Three Rydberg Atoms*, Phys. Rev. Lett. **114** (2015) 113002.

[15] T. Chalopin et al., *Optical Superlattice for Engineering Hubbard Couplings in Quantum Simulation*, Phys. Rev. Lett. **134** (2025) 053402.

[16] P. Krantz et al., *A Quantum Engineer's Guide to Superconducting Qubits*, Applied Physics Reviews **6** (2019) 021318, arXiv: 1904.06560 [quant-ph].

[17] E. Knill, R. Laflamme and G. J. Milburn, *A Scheme for Efficient Quantum Computation with Linear Optics*, Nature **409** (2001) 46.

[18] T. E. Northup and R. Blatt, *Quantum Information Transfer Using Photons*, Nature Photon **8** (2014) 356.

[19] G. Kurizki et al., *Quantum Technologies with Hybrid Systems*, Proceedings of the National Academy of Sciences **112** (2015) 3866.

[20] A. A. Clerk, K. W. Lehnert, P. Bertet, J. R. Petta and Y. Nakamura, *Hybrid Quantum Systems with Circuit Quantum Electrodynamics*, Nat. Phys. **16** (2020) 257.

[21] J. Koch et al., *Charge-Insensitive Qubit Design Derived from the Cooper Pair Box*, Phys. Rev. A **76** (2007) 042319.

[22] H. J. Kimble, *The Quantum Internet*, Nature **453** (2008) 1023.

[23] N. J. Lambert, A. Rueda, F. Sedlmeir and H. G. L. Schwefel, *Coherent Conversion Between Microwave and Optical Photons—An Overview of Physical Implementations*, Advanced Quantum Technologies **3** (2020) 1900077.

[24] L. Midolo, A. Schliesser and A. Fiore, *Nano-Opto-Electro-Mechanical Systems*, Nature Nanotech **13** (2018) 11.

[25] N. Lauk et al., *Perspectives on Quantum Transduction*, Quantum Sci. Technol. **5** (2020) 020501.

[26] S. Barzanjeh et al., *Optomechanics for Quantum Technologies*, Nat. Phys. **18** (2022) 15.

[27] M. Forsch et al., *Microwave-to-Optics Conversion Using a Mechanical Oscillator in Its Quantum Ground State*, Nat. Phys. **16** (2020) 69.

[28] M. J. Weaver et al., *An Integrated Microwave-to-Optics Interface for Scalable Quantum Computing*, Nat. Nanotechnol. **19** (2024) 166.

[29] T. C. van Thiel et al., *Optical Readout of a Superconducting Qubit Using a Piezo-Optomechanical Transducer*, Nat. Phys. **21** (2025) 401.

[30] Y. Chu et al., *Quantum Acoustics with Superconducting Qubits*, Science **358** (2017) 199.

[31] C. T. Hann et al., *Hardware-Efficient Quantum Random Access Memory with Hybrid Quantum Acoustic Systems*, Phys. Rev. Lett. **123** (2019) 250501.

[32] Y. Yang et al., *A Mechanical Qubit*, Science **386** (2024) 783.

[33] S. Peil, T. G. Akin and J. D. Whalen,
100-Ns-Level Timing Holdover after 12 Years for Rubidium Atomic Fountains,
Phys. Rev. Appl. **24** (2025) 024014.

[34] H. Gorniaczyk, C. Tresp, J. Schmidt, H. Fedder and S. Hofferberth,
Single-Photon Transistor Mediated by Interstate Rydberg Interactions,
Phys. Rev. Lett. **113** (2014) 053601.

[35] T. F. Gallagher, *Rydberg Atoms*, Rep. Prog. Phys. **51** (1988) 143.

[36] N. Šibalić and C. S. Adams, *Rydberg Physics*, IOP Publishing, 2018,
ISBN: 978-0-7503-1635-4.

[37] M. Saffman, T. G. Walker and K. Mølmer, *Quantum Information with Rydberg Atoms*,
Rev. Mod. Phys. **82** (2010) 2313.

[38] D. Petrosyan et al.,
Reversible State Transfer between Superconducting Qubits and Atomic Ensembles,
Phys. Rev. A **79** (2009) 040304.

[39] M. Kaiser et al., *Cavity-Driven Rabi Oscillations between Rydberg States of Atoms Trapped on a Superconducting Atom Chip*, Phys. Rev. Res. **4** (2022) 013207.

[40] C. S. Adams, J. D. Pritchard and J. P. Shaffer, *Rydberg Atom Quantum Technologies*,
J. Phys. B: At. Mol. Opt. Phys. **53** (2019) 012002.

[41] A. A. Morgan and S. D. Hogan, *Coupling Rydberg Atoms to Microwave Fields in a Superconducting Coplanar Waveguide Resonator*, Phys. Rev. Lett. **124** (2020) 193604.

[42] L. L. Brown, J. A. L. Grondin and S. D. Hogan,
Demonstration of a Tunable Interface between Rydberg Atoms and Superconducting Microwave Circuits with Differential Polarizability Nulling, Phys. Rev. A **110** (2024) 022615.

[43] R. Stevenson, J. Minář, S. Hofferberth and I. Lesanovsky,
Prospects of Charged-Oscillator Quantum-State Generation with Rydberg Atoms,
Phys. Rev. A **94** (2016) 043813.

[44] M. Khazali,
Progress towards Macroscopic Spin and Mechanical Superposition via Rydberg Interaction,
Phys. Rev. A **98** (2018) 043836.

[45] F. Bariani, J. Otterbach, H. Tan and P. Meystre,
Single-Atom Quantum Control of Macroscopic Mechanical Oscillators,
Phys. Rev. A **89** (2014) 011801.

[46] M. Gao, Y.-x. Liu and X.-B. Wang,
Coupling Rydberg Atoms to Superconducting Qubits via Nanomechanical Resonator,
Phys. Rev. A **83** (2011) 022309.

[47] R. Lifshitz and M. L. Roukes,
Thermoelastic Damping in Micro- and Nanomechanical Systems,
Phys. Rev. B **61** (2000) 5600.

[48] P. Kharel et al., *Ultra-High-Q Phononic Resonators on-Chip at Cryogenic Temperatures*,
APL Photonics **3** (2018) 066101.

[49] T. Baron et al., "High-Overtone Bulk Acoustic Resonator",
Modeling and Measurement Methods for Acoustic Waves and for Acoustic Microdevices,
IntechOpen, 2013, ISBN: 978-953-51-1189-4.

[50] B. P. Sorokin et al., *Excitation of Hypersonic Acoustic Waves in Diamond-Based Piezoelectric Layered Structure on the Microwave Frequencies up to 20 GHz*, Ultrasonics **78** (2017) 162.

[51] Y. Luo et al., *Lifetime-Limited Gigahertz-frequency Mechanical Oscillators with Millisecond Coherence Times*, 2025, arXiv: 2504.07523 [quant-ph], (visited on 11/09/2025).

[52] R. Löw et al., *An Experimental and Theoretical Guide to Strongly Interacting Rydberg Gases*, J. Phys. B: At. Mol. Opt. Phys. **45** (2012) 113001.

[53] C.-J. Lorenzen and K. Niemax,
Quantum Defects of the n2P1/2,3/2 Levels in 39K I and 85Rb I, Phys. Scr. **27** (1983) 300.

[54] I. I. Beterov, I. I. Ryabtsev, D. B. Tretyakov and V. M. Entin,
Quasiclassical Calculations of Blackbody-Radiation-Induced Depopulation Rates and Effective Lifetimes of Rydberg nS, nP, and nD Alkali-Metal Atoms with N≤80,
Phys. Rev. A **79** (2009) 052504.

[55] N. Šibalić, J. D. Pritchard, C. S. Adams and K. J. Weatherill,
ARC: An Open-Source Library for Calculating Properties of Alkali Rydberg Atoms,
Computer Physics Communications **220** (2017) 319.

[56] M. S. O'Sullivan and B. P. Stoicheff,
Scalar Polarizabilities and Avoided Crossings of High Rydberg States in Rb,
Phys. Rev. A **31** (1985) 2718.

[57] H. Hattermann et al.,
Detrimental Adsorbate Fields in Experiments with Cold Rydberg Gases near Surfaces,
Phys. Rev. A **86** (2012) 022511.

[58] K. S. Chan, M. Siercke, C. Hufnagel and R. Dumke,
Adsorbate Electric Fields on a Cryogenic Atom Chip, Phys. Rev. Lett. **112** (2014) 026101.

[59] D. Maxwell et al., *Microwave Control of the Interaction between Two Optical Photons*,
Phys. Rev. A **89** (2014) 043827.

[60] A. Paris-Mandoki, C. Braun and S. Hofferberth,
Correlations between Interacting Rydberg Atoms, AIP Conf. Proc. **1950** (2018) 020001.

[61] M. O. Scully, E. S. Fry, C. H. R. Ooi and K. Wódkiewicz, *Directed Spontaneous Emission from an Extended Ensemble of N Atoms: Timing Is Everything*,
Phys. Rev. Lett. **96** (2006) 010501.

[62] C. Mewes and M. Fleischhauer, *Decoherence in Collective Quantum Memories for Photons*,
Phys. Rev. A **72** (2005) 022327.

[63] Y. O. Dudin and A. Kuzmich, *Strongly Interacting Rydberg Excitations of a Cold Atomic Gas*,
Science **336** (2012) 887.

[64] H. Busche et al.,
Contactless Nonlinear Optics Mediated by Long-Range Rydberg Interactions,
Nature Phys **13** (2017) 655.

[65] C. Tresp et al., *Single-Photon Absorber Based on Strongly Interacting Rydberg Atoms*, Phys. Rev. Lett. **117** (2016) 223001.

[66] C. R. Murray et al., *Photon Subtraction by Many-Body Decoherence*, Phys. Rev. Lett. **120** (2018) 113601.

[67] B. P. Sorokin et al., *Toward 40 GHz Excitation of Diamond-Based HBAR*, Appl. Phys. Lett. **118** (2021) 083501.

[68] M. Bild et al., *Schrödinger Cat States of a 16-Microgram Mechanical Oscillator*, Science **380** (2023) 274.

[69] U. Von Lüpke, I. C. Rodrigues, Y. Yang, M. Fadel and Y. Chu, *Engineering Multimode Interactions in Circuit Quantum Acoustodynamics*, Nat. Phys. (2024).

[70] S. Germer, *Interfacing Rydberg Atoms with a High Overtone Bulk Acoustic Wave Resonator on an Atom Chip*, MA thesis: Universität Bonn, 2025.

[71] *COMSOL Multiphysics®*, COMSOL AB, Stockholm, Sweden, 2025.

[72] U. von Lüpke, *Quantum Control of a Multimode Bulk Acoustic Wave Resonator*, PhD thesis: ETH Zurich, 2023.

[73] M. Aspelmeyer, T. J. Kippenberg and F. Marquardt, *Cavity Optomechanics*, Rev. Mod. Phys. **86** (2014) 1391.

[74] L. F. Keary and J. D. Pritchard, *Strong Coupling and Active Cooling in a Finite-Temperature Hybrid Atom-Cavity System*, Phys. Rev. A **105** (2022) 013707.

[75] E. L. Raab, M. Prentiss, A. Cable, S. Chu and D. E. Pritchard, *Trapping of Neutral Sodium Atoms with Radiation Pressure*, Phys. Rev. Lett. **59** (1987) 2631.

[76] A. Kramida, *NIST Atomic Energy Levels and Spectra Bibliographic Database*, http://physics.nist.gov/cgi-bin/ASBib1/ELevBib.cgi, 2025, (visited on 05/01/2026).

[77] A. Kramida, *NIST Atomic Transition Probability Database*, http://physics.nist.gov/cgi-bin/ASBib1/TransProbBib.cgi, 2025, (visited on 05/01/2026).

[78] A. Kramida, *Atomic Spectral Line Broadening Bibliographic Database*, http://physics.nist.gov/cgi-bin/ASBib1/LineBroadBib.cgi, 2025, (visited on 05/01/2026).

[79] F. Pobell, *Matter and Methods at Low Temperatures*, Berlin, Heidelberg: Springer, 2007, ISBN: 978-3-540-46356-6 978-3-540-46360-3.

[80] H. J. Metcalf and P. Van Der Straten, *Laser Cooling and Trapping*, ed. by R. S. Berry et al., Graduate Texts in Contemporary Physics, New York, NY: Springer, 1999, ISBN: 978-0-387-98728-6 978-1-4612-1470-0.

[81] T. Arpornthip, C. A. Sackett and K. J. Hughes, *Vacuum-Pressure Measurement Using a Magneto-Optical Trap*, Phys. Rev. A **85** (2012) 033420.

[82] R. W. G. Moore et al., *Measurement of Vacuum Pressure with a Magneto-Optical Trap: A Pressure-Rise Method*, Review of Scientific Instruments **86** (2015) 093108.

[83] A. M. Steane, M. Chowdhury and C. J. Foot, *Radiation Force in the Magneto-Optical Trap*, J. Opt. Soc. Am. B, JOSAB **9** (1992) 2142.

[84] Pfeiffer Vacuum GmbH,
Grundlagen des Vakuums Know-how: Druck- und Gasverhalten | Pfeiffer Global,
https://www.pfeiffer-vacuum.com/global/de/knowledge/vacuum-technology/knowledge-book/1-introduction/1_2_fundamentals/, (visited on 24/01/2026).

[85] Hannes Gorniaczyk,
Single Photon Transistor Mediated by Electrically Tunable Rydberg-Rydberg Interactions,
PhD thesis: Universität Stuttgart, 2016.

[86] C. J. Foot and C. J. Foot, *Atomic Physics*, Oxford Master Series in Physics,
Oxford, New York: Oxford University Press, 2004, ISBN: 978-0-19-850695-9.

[87] E. Majorana, *Atomi orientati in campo magnetico variabile*, Nuovo Cim **9** (1932) 43.

[88] K. B. Davis, M.-O. Mewes, M. A. Joffe, M. R. Andrews and W. Ketterle,
Evaporative Cooling of Sodium Atoms, Phys. Rev. Lett. **74** (1995) 5202.

[89] V. Gomer et al., *Magnetostatic Traps for Charged and Neutral Particles*,
Hyperfine Interactions **109** (1997) 281.

[90] H. Ott, J. Fortagh, G. Schlotterbeck, A. Grossmann and C. Zimmermann,
Bose-Einstein Condensation in a Surface Microtrap, Phys. Rev. Lett. **87** (2001) 230401.

[91] D. A. Steck, *Rubidium 87 D Line Data*,
https://steck.us/alkalidata/rubidium87numbers.1.6.pdf, 2001, (visited on 10/11/2025).

[92] V. Mauth, *Realization of a 87Rb magneto-optical trap*, BA thesis: Univerity Bonn, 2023.

[93] G. Reinaudi, T. Lahaye, Z. Wang and D. Guéry-Odelin,
Strong Saturation Absorption Imaging of Dense Clouds of Ultracold Atoms,
Opt. Lett., OL **32** (2007) 3143.

[94] K. Hueck et al., *Calibrating High Intensity Absorption Imaging of Ultracold Atoms*,
Opt. Express, OE **25** (2017) 8670.

[95] Konstantinidis Gregory-Orfeus,
Diffractive Dark-Ground Imaging of Ultra-Low Atom-Numbers in a MOT,
PhD thesis: University of Crete, 2011.

[96] S. Roof, K. Kemp, M. Havey, I. M. Sokolov and D. V. Kupriyanov,
Microscopic Lensing by a Dense, Cold Atomic Sample, Opt. Lett., OL **40** (2015) 1137.

[97] J. Gamper, *Atom Preparation and Rydberg Excitation of Rubidium Atoms*,
MA thesis: Universität Bonn, 2024.

[98] H. J. Metcalf and P. van der Straten, *Laser Cooling and Trapping of Atoms*,
J. Opt. Soc. Am. B, JOSAB **20** (2003) 887.

[99] J. Dalibard and C. Cohen-Tannoudji,
Laser Cooling below the Doppler Limit by Polarization Gradients: Simple Theoretical Models,
J. Opt. Soc. Am. B, JOSAB **6** (1989) 2023.

[100] W. Happer, *Optical Pumping*, Rev. Mod. Phys. **44** (1972) 169.

[101] M. Fleischhauer, *Optical Pumping in Dense Atomic Media: Limitations Due to Reabsorption of Spontaneously Emitted Photons*, EPL **45** (1999) 659.

[102] L. Uhthoff-Rodríguez et al., *Fast Magnetic Coil Controller for Cold Atom Experiments*, 2025, arXiv: 2503.22554 [physics], (visited on 11/01/2026).

[103] J. Léonard et al., *Optical Transport and Manipulation of an Ultracold Atomic Cloud Using Focus-Tunable Lenses*, New J. Phys. **16** (2014) 093028.

[104] R. Grimm, M. Weidemüller and Y. B. Ovchinnikov, "Optical Dipole Traps for Neutral Atoms", *Advances In Atomic, Molecular, and Optical Physics*, vol. 42, Academic Press, 2000 95.

[105] A. J. Matthies et al., *Long-Distance Optical-Conveyor-Belt Transport of Ultracold Cs 133 and Rb 87 Atoms*, Phys. Rev. A **109** (2024) 023321.

[106] G. Unnikrishnan et al., *Long Distance Optical Transport of Ultracold Atoms: A Compact Setup Using a Moiré Lens*, Rev. Sci. Instrum. **92** (2021) 063205.

[107] J. Goldwin et al., *Measurement of the Interaction Strength in a Bose-Fermi Mixture with ^{87}Rb and ^{40}K*, Phys. Rev. A **70** (2004) 021601.

[108] M. Greiner, I. Bloch, T. W. Hänsch and T. Esslinger, *Magnetic Transport of Trapped Cold Atoms over a Large Distance*, Phys. Rev. A **63** (2001) 031401.

[109] K. Nakagawa, Y. Suzuki, M. Horikoshi and J. Kim, *Simple and Efficient Magnetic Transport of Cold Atoms Using Moving Coils for the Production of Bose–Einstein Condensation*, Appl. Phys. B **81** (2005) 791.

[110] T. Badr et al., *Comparison of Time Profiles for the Magnetic Transport of Cold Atoms*, Appl. Phys. B **125** (2019) 102.

[111] J. Popp, *Construction and Preparation of an Experimental Setup for Excitation and Detection of Rydberg Atoms in a Cryogenic Environment*, MA thesis: Universität Bonn, 2024.

[112] Simon Ramo, John R. Whinnery, Theodore Van Duzer, *Fields and Waves in Communication Electronics, 3rd Edition*, 1994, ISBN: 978-0-471-58551-0.

[113] M. Ortner and L. G. Coliado Bandeira, *Magpylib: A Free Python Package for Magnetic Field Computation*, SoftwareX **11** (2020) 100466.

[114] V. Mauth, *Machine Learning Based Optimization for the Preparation of Rubidium Rydberg Atoms and Characterization of the Detection*, MA thesis: Universität Bonn, 2025.

[115] P. B. Wigley et al., *Fast Machine-Learning Online Optimization of Ultra-Cold-Atom Experiments*, Sci Rep **6** (2016) 25890.

[116] Mogens Henrik From, *Towards Rydberg Quantum Optics with Ultra-Cold Yb Atoms*, MA thesis: Syddansk Universitet, 2021.

[117] Rolled Alloys, *Titanium Grade 2/2H*, https://www.rolledalloys.com/wp-content/uploads/TiGrade2_DS_USA-1.pdf, Data Sheet, 2025, (visited on 08/12/2025).

[118] A. T. Vu, R. d. l. A. Avila Hernandez, T. Grunwald and T. Bergs, *Modeling Nonequilibrium Thermoviscoelastic Material Behaviors of Glass in Nonisothermal Glass Molding*, Journal of the American Ceramic Society **105** (2022) 6799.

[119] Max Reicherd, *Characterization of a Superconducting Nanowire Single Photon Detector*, BA Thesis: Univerity Bonn, 2024.

[120] M. Fleischhauer, *Electromagnetically Induced Transparency: Optics in Coherent Media*, Rev. Mod. Phys. **77** (2005) 633.

[121] D. A. Steck, *Quantum and Atom Optics*, vol. 0.8.3, 2012.

[122] J. Deiglmayr et al., *Coherent Excitation of Rydberg Atoms in an Ultracold Gas*, Optics Communications, Quantum Control of Light and Matter **264** (2006) 293.

[123] P. Virtanen et al., *SciPy 1.0: Fundamental Algorithms for Scientific Computing in Python*, Nat Methods **17** (2020) 261.

[124] N. Stiesdal et al., *Controlled Multi-Photon Subtraction with Cascaded Rydberg Superatoms as Single-Photon Absorbers*, Nat Commun **12** (2021) 4328.

[125] Julia Gamper, *Frequenzstabilisierung Zur Laserkühlung von Rubidium*, BA Thesis: Univerity Bonn, 2022.

[126] F. Pausewang, *Aufbau, Optimierung und Charakterisierung von frequenzstabilisierten Lasersystemen*, BA thesis: Univerity Bonn, 2022.

[127] S. Germer, *Frequency Stabilization of a Laser and a High Resolution Optical Setup for Excitation of Ultracold Rydberg Atoms*, BA Thesis: Univerity Bonn, 2023.

[128] E. D. Black, *An Introduction to Pound–Drever–Hall Laser Frequency Stabilization*, American Journal of Physics **69** (2001) 79.

[129] S. C. Doret, C. B. Connolly, W. Ketterle and J. M. Doyle, *Buffer-Gas Cooled Bose-Einstein Condensate*, Phys. Rev. Lett. **103** (2009) 103005.

[130] F. Jessen et al., *Trapping of Ultracold Atoms in a 3He/4He Dilution Refrigerator*, Appl. Phys. B **116** (2014) 665.

[131] J. Ahokas et al., *A Large Octupole Magnetic Trap for Research with Atomic Hydrogen*, Rev. Sci. Instrum. **93** (2022) 023201.

[132] B. Wilde et al., *A Superconducting On-Chip Microwave Cavity for Tunable Hybrid Systems with Optically Trapped Rydberg Atoms*, 2025, arXiv: 2410.23269 [quant-ph], (visited on 07/04/2025).

[133] P. D. Desai, H. M. James and C. Y. Ho, *Electrical Resistivity of Aluminum and Manganese*, J. Phys. Chem. Ref. Data **13** (1984) 1131.

[134] H. P. R. Frederikse, *CRC Handbook of Chemistry and Physics, 97th Edition, Section 12, TECHNIQUES FOR MATERIALS CHARACTERIZATION*,
Boca Raton: CRC Press Taylor & Francis Group, 2017, ISBN: 13: 978-1-4987-5429-3.

[135] M. Fouaidy and N. Hammoudi, *RRR of Copper Coating and Low Temperature Electrical Resistivity of Material for TTF Couplers*, Physica C: Superconductivity, Proceedings of the 12th International Workshop on RF Superconductivity **441** (2006) 137.

[136] H. Hattermann, *Interfacing Cold Atoms and Superconductors*,
PhD thesis: Universität Tübingen, 2013.

[137] T. Hammel et al., *A Modular Quantum Gas Platform*, 2025,
arXiv: 2501.08211 [cond-mat], (visited on 15/01/2026).

[138] J. Reichel and V. Vuletic, *Trapping and Manipulating Atoms on Chips*,
John Wiley & Sons, Ltd, 2011, chap. 2, ISBN: 978-3-527-63335-7.

[139] J. Fortágh and C. Zimmermann, *Magnetic Microtraps for Ultracold Atoms*,
Rev. Mod. Phys. **79** (2007) 235.

[140] J. Schmiedmayer, *A Wire Trap for Neutral Atoms*, Appl. Phys. B **60** (1995) 169.

[141] L. Y. Ley, *Coupling of Rydberg Atoms to a Superconducting Coplanar Waveguide Resonator for a Quantum Memory Device*, PhD thesis: Universität Tübingen, 2018.

[142] H. Hattermann et al.,
Coupling Ultracold Atoms to a Superconducting Coplanar Waveguide Resonator,
Nat Commun **8** (2017) 2254.

[143] A. Haase, D. Cassettari, B. Hessmo and J. Schmiedmayer,
Trapping Neutral Atoms with a Wire, Phys. Rev. A **64** (2001) 043405.

[144] R. Huebener, R. Kampwirth, R. Martin, T. Barbee and R. Zubeck,
Critical Current Density in Superconducting Niobium Films,
IEEE Transactions on Magnetics **11** (1975) 344.

[145] S. Schneider, *Bose-Einstein Kondensation in einer magnetischen Z-Falle*,
PhD thesis: Universität Heidelberg, 2003.

[146] J. R. Clem and K. K. Berggren,
Geometry-Dependent Critical Currents in Superconducting Nanocircuits,
Phys. Rev. B **84** (2011) 174510.

[147] M. Benkraouda and J. R. Clem,
Critical Current from Surface Barriers in Type-II Superconducting Strips,
Phys. Rev. B **58** (1998) 15103.

[148] A. A. Babaei Brojeny and J. R. Clem,
Self-Field Effects upon the Critical Current Density of Flat Superconducting Strips,
Supercond. Sci. Technol. **18** (2005) 888.

[149] O. J. Luiten, M. W. Reynolds and J. T. M. Walraven,
Kinetic Theory of the Evaporative Cooling of a Trapped Gas, Phys. Rev. A **53** (1996) 381.

[150] H. R. Petry and B. C. Metsch, *Theoretische Mechanik*,
Oldenbourg Wissenschaftsverlag, 2014, ISBN: 978-3-486-79662-9.

[151] L. Sadowski, *Design of a Superconducting Atom Chip for Interfacing Rydberg Atoms with Microwave Resonators*, MA thesis: Universität Bonn, 2024.

[152] Pieter Valkering, *Optimization of Evaporative Cooling of Rubidium Atoms in a Magnetic Trap*, MA thesis: University of Utrecht, 1999.

[153] K.-N. Schymik et al., *Single Atoms with 6000-Second Trapping Lifetimes in Optical-Tweezer Arrays at Cryogenic Temperatures*, Phys. Rev. Appl. **16** (2021) 034013.

[154] Kai Dieckmann,
Bose-Einstein Condensation with High Atom Number in a Deep Magnetic Trap,
PhD thesis: Universiteit van Amsterdam, 2001.

[155] W. Petrich, M. H. Anderson, J. R. Ensher and E. A. Cornell,
Stable, Tightly Confining Magnetic Trap for Evaporative Cooling of Neutral Atoms,
Phys. Rev. Lett. **74** (1995) 3352.

[156] R. Dubessy et al.,
Rubidium-87 Bose-Einstein Condensate in an Optically Plugged Quadrupole Trap,
Phys. Rev. A **85** (2012) 013643.

[157] K. B. Davis et al., *Bose-Einstein Condensation in a Gas of Sodium Atoms*,
Phys. Rev. Lett. **75** (1995) 3969.

[158] A. Tauschinsky, R. M. T. Thijssen, S. Whitlock, H. B. van Linden van den Heuvell and R. J. C. Spreeuw,
Spatially Resolved Excitation of Rydberg Atoms and Surface Effects on an Atom Chip,
Phys. Rev. A **81** (2010) 063411.

[159] D. Davtyan et al.,
Controlling Stray Electric Fields on an Atom Chip for Experiments on Rydberg Atoms,
Phys. Rev. A **97** (2018) 023418.

[160] M. Göppl et al., *Coplanar Waveguide Resonators for Circuit Quantum Electrodynamics*,
J. Appl. Phys. **104** (2008) 113904.

[161] D. M. Walker, L. L. Brown and S. D. Hogan, *Electrometry of a Single Resonator Mode at a Rydberg-atom–superconducting-circuit Interface*, Phys. Rev. A **105** (2022) 022626.

[162] R. W. Chang and F. Patrick McCluskey,
Reliability Assessment of Indium Solder for Low Temperature Electronic Packaging,
Cryogenics, Workshop on Low Temperature Electronics 2008 **49** (2009) 630.

[163] T. J. Quinn, *The International Temperature Scale of 1990 (ITS-90)*, Phys. Scr. **41** (1990) 730.

[164] M. Peper, J. Deiglmayr, F. Merkt, C. Sanna and H. B. v. L. van den Heuvell,
Magic Rydberg-Rydberg Transitions in Electric Fields, Phys. Rev. A **100** (2019) 032512.

[165] S. de Léséleuc et al., *Observation of a Symmetry-Protected Topological Phase of Interacting Bosons with Rydberg Atoms*, Science **365** (2019) 775.

[166] V. J. Gokhale et al., *Epitaxial Bulk Acoustic Wave Resonators as Highly Coherent Multi-Phonon Sources for Quantum Acoustodynamics*, Nat Commun **11** (2020) 2314.

[167] B. Bégoc et al., *Controlled Dissipation for Rydberg Atom Experiments*,
Phys. Rev. A **112** (2025) 023312.

[168] H. Schempp, G. Günter, S. Wüster, M. Weidemüller and S. Whitlock,
Correlated Exciton Transport in Rydberg-Dressed-Atom Spin Chains,
Phys. Rev. Lett. **115** (2015) 093002.

[169] S. Whitlock, H. Wildhagen, H. Weimer and M. Weidemüller,
Diffusive to Nonergodic Dipolar Transport in a Dissipative Atomic Medium,
Phys. Rev. Lett. **123** (2019) 213606.

[170] S. Weber et al., *Calculation of Rydberg Interaction Potentials*,
J. Phys. B: At. Mol. Opt. Phys. **50** (2017) 133001.

[171] G. Vidal and R. F. Werner, *Computable Measure of Entanglement*,
Phys. Rev. A **65** (2002) 032314.

[172] R. Horodecki, P. Horodecki, M. Horodecki and K. Horodecki, *Quantum Entanglement*,
Rev. Mod. Phys. **81** (2009) 865.

[173] P. Coleman, *Introduction to Many Body Physics*,
Cambridge: Cambridge University Press, 2008, ISBN: 978-0-521-86488-6.

[174] J. R. Schrieffer and P. A. Wolff, *Relation between the Anderson and Kondo Hamiltonians*,
Phys. Rev. **149** (1966) 491.

[175] G. T. Landi,
Eigenoperator Approach to Schrieffer-Wolff Perturbation Theory and Dispersive Interactions,
2024, arXiv: 2409.10656 [quant-ph], (visited on 17/02/2025).

[176] J. Dalibard, Y. Castin and K. Mølmer,
Wave-Function Approach to Dissipative Processes in Quantum Optics,
Phys. Rev. Lett. **68** (1992) 580.

[177] M. B. Plenio and P. L. Knight,
The Quantum-Jump Approach to Dissipative Dynamics in Quantum Optics,
Rev. Mod. Phys. **70** (1998) 101.

[178] J. R. Johansson, P. D. Nation and F. Nori,
QuTiP 2: A Python Framework for the Dynamics of Open Quantum Systems,
Computer Physics Communications **184** (2013) 1234.

[179] C. R. Harris et al., *Array Programming with NumPy*, Nature **585** (2020) 357.

[180] A. M. Falconi et al.,
Microsecond-Scale High-Survival and Number-Resolved Detection of Ytterbium Atom Arrays,
2025, arXiv: 2507.01011 [cond-mat], (visited on 21/09/2025).

Acknowledgements

I would like to thank everyone who supported me during my PhD and throughout my studies in general, both professionally and personally. Without you, I would not be where I am today, and I am grateful for that.

First, thank you, Sebastian, for giving me the opportunity and trust to build a new experiment in your group. Starting (twice) in a lab with empty optical tables was an invaluable experience for me. I appreciate your guidance throughout this journey.

I also thank professor Linden for being my second supervisor. I am not sure whether the countless times I was asked where the cryo is and why I am gluing my vacuum chamber again helped my mood in those moments, but I appreciate your persistence nonetheless.

I am grateful for the many awesome colleagues, and dare I say friends, I worked with over the years. Thank you, Hannes, you were the only other person on the team when I started, and I am forever grateful for your guidance and expertise.

Thank you Lukas and Nina. In the beginning, during the pandemic, we shared a lab and I basically only saw you and Hannes, which turned out to be a good thing because you became close friends. I will never forget all the fun we had together in and out of the lab.

Thank you, Chris, for your theoretical insights that helped me understand the experiment I was building from a much more fundamental level.

I want to thank all the Bachelor and Master students who worked with me in my lab team over the years: Julia, Valerie, Valerie (yes, we had two :D), Sam, Leon, Max, Johanna, Alican, Aylin, Tore, and Florian. Working with you was awesome. I hope I was able to teach you one or two things, because I certainly learned a lot from you! Special thanks to Julia, the glue of our team, who has now worked on the experiment for almost as long as I have. I am confident the experiment is in good hands with you taking over, and I look forward to the awesome physics you will do.

Thanks also to the rest of the group: Eduardo, Daniil, Wolfgang, Xin, Tangi, and Lukas (yes, a second Lukas), and of course the staff on the third floor, especially Tina and Dietmar (and all the others I forgot to mention by name—please excuse me). All of you made my time in this group so much better, and I am grateful for the collegial atmosphere and countless shared moments.

Thanks to my study mates from the very beginning: Lukas (yes, a third Lukas), Hajo, Lena and Paul. Who would have thought that we would (soon) all earn our PhDs ten years later?

Finally, I am deeply grateful to my parents, my family, and my personal friends who have supported me throughout this journey. Your encouragement and support have been invaluable. Especially Anica, thank you for being there through all the ups and downs, for your patience during the long hours and stressful moments, and for always believing in me.